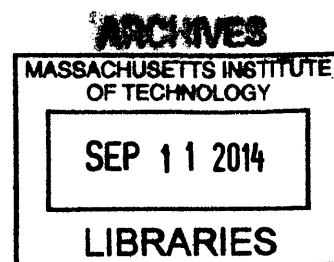


**Reactions of *S*-nitrosothiols with biomimetic iron complexes and other  
transition metals**

by

Eric Victor

B.Sc. Chemistry  
University of Wisconsin - Madison, 2009



Submitted to the Department of Chemistry in Partial Fulfillment of the Requirement for the  
Degree of

DOCTOR OF PHILOSOPHY IN INORGANIC CHEMISTRY

at the  
Massachusetts Institute of Technology

September 2014

© Massachusetts Institute of Technology, 2014  
All Rights Reserved

Signature redacted

Signature of Author: \_\_\_\_\_

\_\_\_\_\_  
Department of Chemistry  
June 4, 2013

Signature redacted

Certified by: \_\_\_\_\_

\_\_\_\_\_  
Stephen J. Lippard  
Arthur Amos Noyes Professor of Chemistry  
Thesis Supervisor

Signature redacted

Accepted by: \_\_\_\_\_

\_\_\_\_\_  
Robert W. Field  
Chairman, Departmental Committee on Graduate Student

This doctoral thesis has been examined by a committee of the Department of Chemistry as follows:

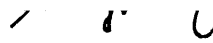
Signature redacted

---

Christopher C. Cummins  
Professor of Chemistry  
Committee Chairperson


Signature redacted

---

 Stephen J. Lippard  
Arthur Amos Noyes Professor of Chemistry  
Thesis Supervisor

Signature redacted

---

 Mircea Dincă  
Assistant Professor of Chemistry

# Reactions of *S*-nitrosothiols with biomimetic iron complexes and other transition metals

by

Eric Victor

Submitted to the Department of Chemistry in Partial Fulfillment of the  
Requirements for the Degree of Doctor of Philosophy in Inorganic Chemistry

## Abstract

### Chapter 1. Bioinorganic Chemistry of Nitric Oxide and *S*-Nitrosothiols

The interplay of nitric oxide (NO), biological thiols, and metals has been a topic of intense study since the discovery of NO as the endothelium-derived relaxation factor. NO is a redox-active diatomic, radical gas that is generated biologically during the conversion of L-arginine to L-citrulline by nitric oxide synthases (NOS), NADH, and O<sub>2</sub>. NOS enzymes have iron-porphyrin and biopterin cofactors that catalyze this conversion. *S*-nitrosothiols form in biology as NO-transport mechanisms, post-translational modifications, or as a cellular protectant against overexposure to NO. Heme and non-heme iron cofactors serve as targets in biology to induce degradation of active sites or to induce conformational changes to inhibit or promote cellular pathways. The only structurally characterized metal complexes containing *S*-nitrosothiols have either iridium or ruthenium centers.

### Chapter 2. Rapid Nitric Oxide and Nitrogen Dioxide Detection and Quantification Assays and Devices based on M(BIPhMe)X<sub>2</sub> Complexes

To explore the release of nitrogen oxide gases from reaction solutions, we developed a series of colorimetric sensors based on the *cis*-nitrogen donating ligand BIPhMe, *bis*-(1-methylimidazol-2-yl)phenylmethoxymethane. The complexes M(BIPhMe)X<sub>2</sub>, where M

is  $\text{Fe}^{2+}$  or  $\text{Co}^{2+}$  and X is  $\text{Cl}^-$ ,  $\text{Br}^-$ , or  $\text{I}^-$ , were prepared, and structurally and spectroscopically characterized. The reactivity of these complexes toward NO (g) and  $\text{NO}_2$  (g) in solution was explored and characterized. These complexes were then incorporated into test strips and syringes to provide devices that can qualitatively, and in the case of the syringes quantitatively, detect  $\text{NO}(\text{g})$  and  $\text{NO}_2(\text{g})$  in a reaction headspace without additional equipment.

### **Chapter 3. Reactions of (PPN)(SNO) and (PPN)(SSNO) with $\text{HBF}_4$ and Biomimetic Iron Complexes.**

The biological relevance of HSNO as a transnitrosating was recently reported. The gas  $\text{H}_2\text{S}$  can perform an  $\text{H}^+ - \text{NO}^+$  exchange with an *S*-nitrosated serum albumin to form HSNO, which can cross the cellular membrane and transnitrosate an exposed cysteine on a hemoglobin protein. With this discovery, we explored the reactivity of the anion  $\text{SNO}^-$  and the related  $\text{SSNO}^-$  toward an acid and the biomimetic iron complexes  $[\text{Fe}^{\text{III}}(\text{TPP})\text{Cl}]$ ,  $[\text{Fe}_2\text{S}_2(\text{SPh})_4]^{2-}$ ,  $[\text{Fe}_2(\text{Et-HPTB})(\text{PhCO}_2)]^{2+}$ ,  $[\text{Fe}_2(\mu\text{-OH})(\text{Ph}_4\text{DBA})(\text{TMEDA})_2(\text{OTf})]$ , and  $[\text{Fe}(\text{BIPhMe})\text{Cl}_2]$ . In all cases HSNO was found to be unstable. The reaction of  $\text{SNO}^-$  with  $\text{HBF}_4$  led to NO (g) release. The reaction of both *S*-nitrosothiols with  $[\text{Fe}^{\text{III}}(\text{TPP})\text{Cl}]$  resulted in reductive nitrosylation of the iron center. The reaction of the  $[\text{2Fe-2S}]$  cluster with both *S*-nitrosothiols led to the formation of reduced Roussin's black anion. The reaction of the mononuclear complex  $[\text{Fe}(\text{BIPhMe})\text{Cl}_2]$  with both *S*-nitrosothiols led to formation of the dinitrosyl iron complex  $[\text{FeS}_5(\text{NO})_2]^-$ . Only with the two diiron complexes was a difference in reactivity between  $\text{SNO}^-$  and  $\text{SSNO}^-$  observed, leading to formation of Roussin's black anion or  $[\text{FeS}_5(\text{NO})_2]^-$ , respectively.

### **Chapter 4. Reactions of Nitrogen Oxide Species with a Monofunctional Platinum Complex**

The structural isomers  $\text{SNO}^-$  and  $\text{NSO}^-$  have both been synthetically prepared, but only the metal-binding reactivity of  $\text{NSO}^-$  has been previously explored. Structural characterization of early first-row, and second and third row transition metals are reported with  $\text{NSO}^-$ , where metal-binding occurs via the terminal nitrogen atom. We attempted to form structurally characterizable Pt-SNO and Pt-SSNO complexes using the “monofunctional” complex  $\text{cis}[\text{Pt}(\text{NH}_3)_2(\text{py})\text{Cl}](\text{OTf})$ , but were not successful. Instead, a new complex formed that we propose to be a polysulfide-bridged diplatinum complex with intact nitrogen-binding of the starting complex and release of  $\text{NO}(\text{g})$ . The vibrational spectra of the proposed complexes were calculated using DFT methods to compare with the experimental data and provides further evidence for the formation of a polysulfide-bridged diplatinum complex. DFT calculations were also performed on possible structural isomers of Pt-SNO and Pt-SSNO complexes. To test whether that the reactivity may not occur by release of  $\text{NO}^+$  from the *S*-nitrosothiols,  $\text{cis}[\text{Pt}(\text{NH}_3)_2(\text{py})\text{Cl}](\text{OTf})$  was found to react with  $\text{NOBF}_4$  to form  $\text{cis}[\text{Pt}(\text{NH}_3)_2(\text{py})(\text{CH}_3\text{CN})]^{2+}$  and  $\text{cis-mer}[\text{Pt}(\text{NH}_3)_2(\text{py})\text{Cl}_3]^+$ .

### **Chapter 5. Synthesis of [3:1] Site-Differentiated [4Fe-4S] Clusters and their Reactivity towards $\text{NO}(\text{g})$ and $\text{Ph}_3\text{CSNO}$**

Previous studies provide evidence that [4Fe-4S] clusters serve as targets of reactive nitrogen oxide species in biology. The products of this reaction range from dinitrosyl iron complexes,  $[\text{Fe}(\text{NO})_2\text{L}_2]^-$ , to Roussin’s Black Anion,  $[\text{Fe}_4\text{S}_3(\text{NO})_7]^-$ . To date, the pathways by which these reactions occur have not been fully elucidated. In this study we prepared the site-differentiated complexes  $[\text{Fe}_4\text{S}_4(\text{LS}_3)\text{L}']^{2-}$  ( $\text{LS}_3 = 1,3,5\text{-tris}(4,6\text{-dimethyl-3-mercaptophenylthio})\text{-}2,4,6\text{-tris}(p\text{-tolylthio})\text{benzene}$ ;  $\text{L}' = \text{Cl}, \text{SEt}, \text{SPh}, \text{N}_3, 2\text{-SPyr}, \text{Tp}, \text{S}_2\text{CNEt}_2$ ) to serve as synthetic models for biological [4Fe-4S] clusters and studied their reactivity toward  $\text{NO}(\text{g})$  and  $\text{Ph}_3\text{CSNO}$ .

The products were characterized by X-ray crystallography, mass spectrometry, and IR, EPR, and  $^1\text{H}$  NMR spectroscopy. In all cases reported here, the reactions proceed via formation of the  $\text{S} = \frac{1}{2}$  species  $[\text{Fe}_4\text{S}_4(\text{NO})_4]^-$ , which ultimately converts to EPR-silent  $[\text{Fe}_4\text{S}_3(\text{NO})_7]^-$ .

#### **Appendix A. M(BIPhMe) Complexes and Reactions with RNOS**

The synthesis and characterization of the metal-BIPhMe complexes  $[\text{Fe}(\text{BIPhMe})\text{I}_2]$ ,  $[\text{Fe}(\text{BIPhMe})(\text{MeCN})_2(\text{OTf})_2]$ ,  $[\text{Fe}_2(\mu\text{-O})(\text{BIPhMe})_2(\text{NO}_3)_4]$ ,  $[\text{Cu}(\text{BIPhMe})_2](\text{OTf})_2$ ,  $[\text{Cu}(\text{BIPhMe})_2][\text{CuCl}_2]$ , and  $[\text{Zn}_2(\mu\text{-OTf})_2(\text{BIPhMe})_2(\text{OTf})_2]$  was reported. These complexes were characterized by X-ray diffraction, FTIR,  $^1\text{H}$  NMR, and ESI-MS. The reaction of  $[\text{Zn}_2(\mu\text{-OTf})_2(\text{BIPhMe})_2(\text{OTf})_2]$  with (PPN)(SNO) results in the release of NO (g) and formation of (PPN)(SSNO) and a zinc-sulfide species. The reaction of (PPN)(SSNO) results in the release of NO (g) and a zinc-sulfide species.

#### **Appendix B. Mass-Spec and FTIR figures of the Reactions of NO (g) and $\text{Ph}_3\text{CSNO}$ with $[\text{Fe}_4\text{S}_4(\text{LS}_3)\text{L}']^{2-}$**

Thesis Supervisor: Stephen J. Lippard

Title: Arthur Amos Noyes Professor of Chemistry

*To Maggie for all the love and support*

*To my parents for letting me know that it is not the end of the world to fail*

*“If someone else has done it before, than you can do it too.” – William C. Victor*

*“Thankfully, dreams can change. If we’d all stuck with our first dream, the world would be  
overrun with cowboys and princesses.” – Stephen Colbert*

## Acknowledgements

I would like to first and foremost thank my advisor Professor Stephen J. Lippard for taking me into his lab and providing me with the resources, support, and guidance to complete my thesis. His persistence to correct my language and force me to provide more clear and concise descriptions of my research will provide the most lasting impact, as well as forcing me to pronounce acetonitrile properly, rather than the germanic way. Being in the lippard lab, I have been exposed to more areas of scientific research, even beyond chemistry, than I think I would've experienced in any other lab. I have also been given access to more instrumentation than I think some entire chemistry departments have. The opportunity to characterize my compounds by mass spectrometry, by ReactIR and Mössbauer spectroscopy, and by X-ray crystallography without having to leave the confines of the lab proved invaluable in my research progress. I would also like to thank the inorganic faculty at MIT, especially my thesis committee chair Professor Kit Cummins who provided me with valuable and encouraging words during our annual meetings. Kit's interest in all things chemistry is inspiring and was always fascinating to observe being manifested in his questions during the inorganic seminars. Rich Girardi deserves thanks for his endless help regarding all things administrative and for his jokes.

I must also thank my undergraduate research advisors Professors John F. Berry, Bassam Shkhashiri, and Philipp Simon. Working in John's lab was a wonderful experience that pushed me towards pursuing graduate school. Learning how to communicate science to the general public from Bassam was amazing. Performing genetic research on carrots for Philipp and the USDA gave me a great wealth of knowledge to share anytime I see people eating carrots. I would also like to give my gratitude to my Berry lab mentor Michael Nippe. I know that he will continue to guide and work with wonderful students as a professor at Texas A&M.

My time in the lippard lab has given me the privilege to work with many great people over the past few years. Ali Liang, aka the Queen of the Stopped Flow, has been a wonderful friend and without whom I would have never had an OKcupid profile worthy of meeting my fiancé. She always served as an outlet for personal discussions and a balance to some of the crazier experiences of graduate school. Tim Johnstone is a great friend and compatriot, and I couldn't choose a better yearmate, if that is a thing - well, it is now. Mik Minier has been an excellent safety officer with a great eye for graphic design. Former lab members Julia Kozhukh and Justin Wilson were both great people to bounce experimental ideas off, or even to discuss crystallography. It was just a joy to hear Semi speak and be very self-conscious of what she would say.

Now for the post-docs as there are many that have come through the lab. I want to thank Zach Tonzetich for pitching the NO project to me during my first year. He was a pleasure to



overlap with and I kind of wish we would've had more time to work together, so that I could pick his brain more. Shanta Dhar taught me the ropes of the lab and I am happy that she is doing great work in Georgia. Daniella Buccella is a wonderful person and I can never forget the long laughs we had about a Sara Lee's croissan'wich. Nakedia Carvalho was a "cool dude" and I am looking forward to meeting her again this summer in Brazil. I want to thank Yang Li for showing me amazing figures of his crystal structures displaying his basic iron (III) acetates. Rui Cao was a great guide in how to not present properly to Steve. Shoutout to Ulf Peter Apfel for being one of the most intense chemists I have ever met, but still having the patience and humor to deal with me, and also for giving me that sweet singing teddy bear in lederhosen. I want to thank Shawn Tsai-Te Lu for being a great lab member with whom I could talk NO chemistry, but mainly for his skills at hitting the Volleyball into the sun so that the other team couldn't hit it. On the topic of volleyball, one of the most fun experiences of graduate school was beating the Nocera lab team with only 4 players (myself, Shawn, Justin, and Tuang). I want to thank Patricia for the beautiful picture of my dog that she took and developed, and also for being a great friend. Amit Majumdar was a great chemist to work with and I am happy for him that he took my advice to further pursue the diiron  $\text{NO}^+$  chemistry, instead of passing on it.

I would like to thank my old roommates, Chris Lemon, Ben Ofori-Okai, and Michael Funk for the great times in the "dudes in chemistry" house. You all made me feel better for coming home much later than me, but also terrible because I would usually try to sleep while you guys would have late-night Smash Bros sessions, especially the night before my oral exams. My best friend and soon-to-be best man Russ Jensen for being an awesome person to hang out with. The 2011-2012 Chemistry Flag Football team for bringing home the intramural championship. My fellow GSC officers Brian Spatocco, Aalap Dighe, and Bomy Lee Chung for a great experience advocating for students, never has there been a better team. I would like to thank the ImprovBoston community for providing me a regular outlet to express my creativity and think about other things than MIT and chemistry. My improv mentors Lori Strauss, Rachel Klein, and Jeff Perry showed me how to roll with the punches and accept whatever comes at me, no matter what. To my cast mates on Intervention! and Abra Cadaver; you all great people to work with even if you try to force science scenes onto me.

I want to give many thanks to my fiancé Maggie Brown. Patience isn't her strongest suit and I know these last two years have really tested it, so thank you for dealing with me. I want to thank my mom for letting me know that it is ok to follow my passions. Last but not least, I need to thank my dad for his wise words that he imparted on me during my time in the Army that I have carried with me since.

## Preface

The field of biological nitric oxide research has matured greatly over the past thirty years. This first chapter serves as a brief introduction into the biological chemistry of nitric oxide and *S*-nitrosothiols. This introductory chapter introduces the reader to the catalytic conversion of L-arginine to NO by the heme cofactor of nitric oxide synthase enzymes. The interactions that biological NO has with different iron active sites, including iron-sulfur clusters and diiron reductases, is presented. The introductory chapter closes with structurally characterized *S*-nitrosothiol ligated metal complexes and a brief discussion of cisplatin resistance that is imparted by *S*-nitrosation in cancer cells.

The second chapter of this thesis presents original research in developing a colorimetric sensor based on the first row transition metals and the BIPhMe ligand. These sensors allow for rapid, “naked eye” detection of NO (g) and NO<sub>2</sub> (g) release into a reaction headspace. The sensors were further developed into test strips capable of providing qualitative detection of these gases, and test syringes that can provide a quantitative assessment of gas release.

The third chapter explores the reactivity of the two *S*-nitrosothiol anions, SNO<sup>-</sup> and SSNO<sup>-</sup>, with an acid and bioinspired iron complexes, ranging from simple mononuclear coordination and iron-heme complexes to carboxylate-bridged diiron and [2Fe–2S] clusters. No new species were prepared from these anionic *S*-nitrosothiols, but they did show rapid NO and electron transfer reactivity. The fourth chapter describes the attempt to form a platinum complex with these two anionic *S*-nitrosothiols, as well as theoretical calculations performed to interrogate the structure of the formed species.

The final chapter describes the nitric oxide chemistry explored using nine [3:1] site-differentiated [4Fe–4S] clusters that are coordinated by the LS<sub>3</sub><sup>3-</sup> ligand. Upon reaction with NO (g), these clusters decompose to form [Fe<sub>4</sub>S<sub>4</sub>]<sup>-</sup> and Roussin’s black anion, [Fe<sub>4</sub>S<sub>3</sub>(NO)<sub>7</sub>]<sup>-</sup>. The

reaction can be performed in a more controlled fashion by using the *S*-nitrosothiol  $\text{Ph}_3\text{CSNO}$ , resulting in initial formation of  $[\text{Fe}_4\text{S}_4]^-$  en route to  $[\text{Fe}_4\text{S}_3(\text{NO})_7]^-$ .

## Table of Contents

Abstract	3
Dedication	7
Acknowledgements	8
Preface	10
Table of Contents	12
List of Figures	16
List of Charts	23
List of Schemes	23
List of Tables	24
List of Equations	25
<b>Chapter 1. Bioinorganic Chemistry of Nitric Oxide and <i>S</i>-Nitrosothiols</b>	<b>26</b>
1.1 Introduction	27
1.2 <i>S</i> -nitrosothiols in biology	31
1.3 Iron-sulfur clusters and dinitrosyl iron complexes in biology	33
1.4 Diiron nitric oxide reductases	36
1.5 Precious metals and nitric oxide	39
1.6 Conclusion	42
1.7 References	43
<b>Chapter 2. Rapid Nitric Oxide and Nitrogen Dioxide Detection and Quantification</b>	
<b>Assays and Devices based on <math>M(\text{BIPhMe})\text{X}_2</math> Complexes</b>	<b>47</b>
2.1 Introduction	48
2.2 Experimental Methods	50
Materials	50
Characterization Methods	50
Synthetic Procedures	51
NO(g)/NO <sub>2</sub> (g) Reaction Procedures	60
NO(g)/NO <sub>2</sub> (g) Test Strip Preparation and Application	60

NO(g)/NO <sub>2</sub> (g) Test Syringe Preparation and Application	61
2.3 Results and Discussion	61
Synthesis and Spectroscopic Characterization of BIPhMe Starting Complexes	61
X-ray Crystallographic Characterization of BIPhMe Starting Complexes	64
Reactions of Fe(BIPhMe)Cl <sub>2</sub> and Fe(BIPhMe)Br <sub>2</sub> with NO(g) and NO <sub>2</sub> (g)	69
Reactions of Co(BIPhMe)Cl <sub>2</sub> and Co(BIPhMe)I <sub>2</sub> with NO(g) and NO <sub>2</sub> (g)	79
Preparation and Utilization of NO(g)/NO <sub>2</sub> (g) Test Strips and Syringes	85
2.4 Summary and Conclusions	88
2.5 References	89
<b>Chapter 3. Reactions of (PPN)(SNO) and (PPN)(SSNO) with HBF<sub>4</sub> and Biomimetic Iron Complexes.</b>	91
3.1 Introduction	92
3.2 Experimental Methods	93
Materials	93
Characterization Methods	93
DFT Calculation Procedure	96
Synthetic Procedures	96
SNO <sup>-</sup> /SSNO <sup>-</sup> Reaction Procedures	97
3.3 Results and Discussion	103
Preparation and characterization of SSNO <sup>-</sup> and SNO <sup>-</sup>	103
HBF <sub>4</sub> ·Et <sub>2</sub> O Reactivity	109
Iron-Porphyrin Reactivity	112
[Fe <sub>2</sub> S <sub>2</sub> ] Reactivity	118
Nitrogen-Rich Carboxylate-Bridged Diiron Reactivity	120
Oxygen-Rich Carboxylate-Bridged Diiron Reactivity	122
Mononuclear Iron Complex Reactivity	130
3.4 Summary and Conclusions	131
3.5 References	133

<b>Chapter 4. Reactions of Nitrogen Oxide Species with a Monofunctional Platinum Complex</b>	136
4.1 Introduction	137
4.2 Experimental Methods	139
Materials	139
Characterization Methods	139
DFT Calculation Procedure	140
SNO <sup>-</sup> /SSNO <sup>-</sup> Reaction Procedures	140
Reaction of <i>cis</i> -[Pt(NH <sub>3</sub> ) <sub>2</sub> (py)Cl](OTf) with NOBF <sub>4</sub>	142
4.3 Results and Discussion	143
Reaction of <i>cis</i> -[Pt(NH <sub>3</sub> ) <sub>2</sub> (py)Cl](OTf) with (PPN)(SSNO) and (PPN)(SNO)	143
DFT Calculations of Polysulfide-Bridged Pt-Species	146
DFT Calculations of <i>cis</i> -[Pt(NH <sub>3</sub> ) <sub>2</sub> (py)(SNO)] <sup>+</sup> and <i>cis</i> -[Pt(NH <sub>3</sub> ) <sub>2</sub> (py)(SSNO)] <sup>+</sup>	149
Reactions of <i>cis</i> -[Pt(NH <sub>3</sub> ) <sub>2</sub> (py)Cl](OTf) with NOBF <sub>4</sub>	152
4.4 Summary and Conclusions	158
4.5 References	159
<b>Chapter 5. Synthesis of [3:1] Site-Differentiated [4Fe-4S] Clusters and their Reactivity towards NO(g) and Ph<sub>3</sub>CSNO</b>	161
5.1 Introduction	162
5.2 Experimental Methods	164
Materials	164
Characterization Methods	164
Synthetic Procedures	166
NO(g)/Ph <sub>3</sub> CSNO Reaction Procedures	181
5.3 Results and Discussion	183
Synthesis of the [3:1] Site-Differentiated Cluster	183
Synthesis and Characterization of Clusters	191
Reactions with NO(g)	199
Reactions with Ph <sub>3</sub> CSNO	200
Reactions with NO(g)/Ph <sub>3</sub> CSNO in the presence of TlPF <sub>6</sub>	206

5.4 Summary and Conclusions	210
5.5 References	211
<b>Appendix A. M(BIPhMe) Complexes and Reactions with RNOS</b>	213
A.1 Introduction	214
A.2 Experimental Methods	214
Materials	214
Characterization Methods	214
Synthetic Procedures	216
SNO <sup>-</sup> /SSNO <sup>-</sup> Reaction Procedures	221
A.3 Results and Discussion	222
Synthesis and Spectroscopic Characterization of M(BIPhMe) Complexes	222
Crystallographic Characterization of M(BIPhMe) Complexes	226
Reactions of M(BIPhMe) Complexes with RNOS	235
A.4 Summary and Conclusions	237
A.5 References	238
<b>Appendix B. Mass-Spec and FTIR figures of the Reactions of NO(g) and Ph<sub>3</sub>CSNO with [Fe<sub>4</sub>S<sub>4</sub>(LS<sub>3</sub>)L']<sup>2-</sup></b>	239
Biographical Note	251
Curriculum vitae	252

## List of Figures

### Chapter 1

Figure 1.1.	Cartoon depictions of the crystal structures of active and NO-inhibited inducible nitric oxide synthase	29
Figure 1.2.	Cartoon depiction of the crystal structure of <i>S</i> -nitrosated HbA	32
Figure 1.3.	Cartoon depiction of the crystal structure of <i>S</i> -nitrosated cNP	33
Figure 1.4.	Cartoon depiction of the crystal structure of protein-bound DNIC to hGST	34
Figure 1.5.	Cartoon depiction of the crystal structure of ACO2	35
Figure 1.6.	Diiron active sites of nitric oxide reductases	37
Figure 1.7.	Ball-and-stick representation of the crystals structures of diiron-nitrosyl complexes	39
Figure 1.8.	Ball-and-stick representation of the crystal structures of iridium and ruthenium <i>S</i> -nitrosothiol complexes	41

### Chapter 2

Figure 2.1.	Metal-halide complexes of the <i>bis</i> -N donor BIPhMe	49
Figure 2.2.	<sup>1</sup> H NMR spectra of [Fe(BIPhMe)Cl <sub>2</sub> ], [Fe(BIPhMe)Br <sub>2</sub> ], and BIPhMe	62
Figure 2.3.	MS Characterization of [Fe(BIPhMe)Cl <sub>2</sub> ] and [Fe(BIPhMe)Br <sub>2</sub> ]	63
Figure 2.4.	<sup>1</sup> H NMR spectra of [Co(BIPhMe)Cl <sub>2</sub> ] and [Co(BIPhMe)I <sub>2</sub> ]	64
Figure 2.5.	MS Characterization of [Co(BIPhMe)Cl <sub>2</sub> ] and [Co(BIPhMe)I <sub>2</sub> ]	64
Figure 2.6.	Drawings of the X-ray crystal structures of mononuclear and dimeric [Fe(BIPhMe)Cl <sub>2</sub> ]	65
Figure 2.7.	Drawing of the X-ray crystal structure of [Fe(BIPhMe)Br <sub>2</sub> ]	66
Figure 2.8.	Drawings of the X-ray crystal structures of [Co(BIPhMe)Cl <sub>2</sub> ] and [Co(BIPhMe)I <sub>2</sub> ]	68
Figure 2.9.	UV-Vis spectra of [Fe(BIPhMe)Cl <sub>2</sub> ] and [Fe(BIPhMe)Br <sub>2</sub> ] and their NO(g) reaction products	69
Figure 2.10.	Solutions of [Fe(BIPhMe)Cl <sub>2</sub> ], [Fe(BIPhMe)Br <sub>2</sub> ], and [Co(BIPhMe)I <sub>2</sub> ] in methylene chloride that were exposed to varying amounts of NO(g)	70



Figure 2.11.	FTIR spectra of $[\text{Fe}(\text{BIPhMe})_2(\text{NO})\text{Cl}][\text{Fe}(\text{NO})\text{Cl}_3]$ and $[\text{Fe}(\text{BIPhMe})_2(\text{NO})\text{Br}][\text{Fe}(\text{NO})\text{Br}_3]$	71
Figure 2.12.	Positive- and negative-mode ESI-MS spectra of $[\text{Fe}(\text{BIPhMe})_2(\text{NO})\text{Cl}][\text{Fe}(\text{NO})\text{Cl}_3]$	72
Figure 2.13.	Positive- and negative-mode ESI-MS spectra of $[\text{Fe}(\text{BIPhMe})_2(\text{NO})\text{Br}][\text{Fe}(\text{NO})\text{Br}_3]$	73
Figure 2.14.	Drawing of the X-ray crystal structure of $(\text{BIPhMe})_2(\text{NO})\text{Cl}][\text{Fe}(\text{NO})\text{Cl}_3]$	74
Figure 2.15.	UV-Vis spectra of $[\text{Fe}(\text{BIPhMe})\text{Cl}_2]$ and $[\text{Fe}(\text{BIPhMe})\text{Br}_2]$ and their $\text{NO}_2(\text{g})$ reaction products	76
Figure 2.16.	FTIR spectra of $[\text{Fe}(\text{BIPhMe})(\text{NO}_3)_2\text{Cl}]$ and $[\text{Fe}(\text{BIPhMe})(\text{NO}_3)_2\text{Br}]$	76
Figure 2.17.	Positive-mode ESI-MS spectra of $[\text{Fe}(\text{BIPhMe})(\text{NO}_3)_2\text{Cl}]$ and $[\text{Fe}(\text{BIPhMe})(\text{NO}_3)_2\text{Br}]$	76
Figure 2.18.	Solutions of $[\text{Fe}(\text{BIPhMe})\text{Cl}_2]$ , $[\text{Fe}(\text{BIPhMe})\text{Br}_2]$ , $[\text{Co}(\text{BIPhMe})\text{Cl}_2]$ , and $[\text{Co}(\text{BIPhMe})\text{I}_2]$ in methylene chloride that were exposed to varying amounts of $\text{NO}_2(\text{g})$	77
Figure 2.19.	Drawing of the X-ray crystal structure of $[\text{Fe}(\text{BIPhMe})(\text{NO}_3)_2\text{Cl}]$	78
Figure 2.20.	Spectroscopic characterization of the product generated by the reaction of $[\text{Co}(\text{BIPhMe})\text{Cl}_2]$ and $\text{NO}_2(\text{g})$	80
Figure 2.21.	Spectroscopic characterization of the product generated by the reaction of $[\text{Co}(\text{BIPhMe})\text{I}_2]$ and $\text{NO}(\text{g})$	81
Figure 2.22.	Positive- and negative-mode ESI-MS spectra of the product generated by the reaction of $[\text{Co}(\text{BIPhMe})\text{I}_2]$ and $\text{NO}(\text{g})$	82
Figure 2.23.	Spectroscopic characterization of the product generated by the reaction of $[\text{Co}(\text{BIPhMe})\text{I}_2]$ and $\text{NO}_2(\text{g})$	83
Figure 2.24.	Drawings of the X-ray crystal structure of $[\text{Co}(\text{BIPhMe})(\text{NO}_3)_2]$	84
Figure 2.25.	Filter paper loaded with $[\text{Fe}(\text{BIPhMe})\text{Cl}_2]$ , $[\text{Fe}(\text{BIPhMe})\text{Br}_2]$ , $[\text{Co}(\text{BIPhMe})\text{Cl}_2]$ , and $[\text{Co}(\text{BIPhMe})\text{I}_2]$ and exposed to $\text{NO}(\text{g})$ and $\text{NO}_2(\text{g})$	85
Figure 2.26.	Silica TLC plates loaded with $[\text{Fe}(\text{BIPhMe})\text{Cl}_2]$ , $[\text{Fe}(\text{BIPhMe})\text{Br}_2]$ , $[\text{Co}(\text{BIPhMe})\text{Cl}_2]$ , and $[\text{Co}(\text{BIPhMe})\text{I}_2]$ complexes and exposed to $\text{NO}(\text{g})$	

	and NO <sub>2</sub> (g)	86
Figure 2.27.	Syringes filled with [Fe(BIPhMe)Cl <sub>2</sub> ], [Fe(BIPhMe)Br <sub>2</sub> ], and [Co(BIPhMe)I <sub>2</sub> ] loaded onto silica gel and exposed to varying amounts of NO(g)	87
Figure 2.28.	Syringes filled with [Fe(BIPhMe)Cl <sub>2</sub> ], [Fe(BIPhMe)Br <sub>2</sub> ], [Co(BIPhMe)Cl <sub>2</sub> ], and [Co(BIPhMe)I <sub>2</sub> ] loaded onto silica gel and exposed to NO <sub>2</sub> (g)	87
<b>Chapter 3</b>		
Figure 3.1.	Diagram of H <sub>2</sub> S-facilitated cross-membrane transnitrosation	92
Figure 3.2.	Spectroscopic characterization of (PPN)(SSNO)	105
Figure 3.3.	Spectroscopic characterization of (PPN)(SNO)	106
Figure 3.4.	Cyclic voltammogram of (PPN)(SNO)	107
Figure 3.5.	Drawings of the X-ray crystal structures of (PPN)(SSNO) and (PPN)(SNO)	108
Figure 3.6.	Crystallographically characterized small molecule organo-S-nitrosothiols	109
Figure 3.7.	UV-Vis spectrum of (PPN)(SNO) + HBF <sub>4</sub> ·Et <sub>2</sub> O	110
Figure 3.8.	Solutions of (PPN)(SNO) and [Fe(BIPhMe)Cl <sub>2</sub> ] before and after addition of HBF <sub>4</sub> ·Et <sub>2</sub> O	111
Figure 3.9.	Calculated energies and structures of the protonated forms of SNO <sup>-</sup>	112
Figure 3.10.	Spectroscopic characterization of [Fe <sup>III</sup> (TPP)Cl] + (PPN)(SNO)	113
Figure 3.11.	<sup>31</sup> P NMR spectrum of the pentane extract of the reaction of [Fe <sup>III</sup> (TPP)Cl] + (PPN)(SSNO)	113
Figure 3.12.	UV-Vis spectrum of the reaction of [Fe <sup>III</sup> (TPP)Cl] with (PPN)(SSNO) and (PPN)(SNO)	115
Figure 3.13.	Stopped-flow kinetic traces and fits of the reaction of [Fe <sup>III</sup> (TPP)Cl] with (PPN)(SSNO)	116
Figure 3.14.	ReactIR spectra of the reaction of [Fe <sup>III</sup> (TPP)Cl] with NO(g) and Ph <sub>3</sub> CSNO	118
Figure 3.15.	FTIR spectra of [Fe <sub>4</sub> S <sub>3</sub> (NO) <sub>7</sub> ] <sup>2-</sup> formed in the reaction of [Fe <sub>2</sub> S <sub>2</sub> (SPh) <sub>4</sub> ] <sup>2-</sup> and (PPN)(SSNO)/(PPN)(SNO)	119
Figure 3.16.	EPR and ESI-MS characterization of [Fe <sub>4</sub> S <sub>3</sub> (NO) <sub>7</sub> ] <sup>2-</sup>	119

Figure 3.17.	FTIR and ESI-MS characterization of $[\text{Fe}_4\text{S}_3(\text{NO})_7]^-$ formed in the reaction of $[\text{Fe}_2(\text{Et-HPTB})(\text{PhCO}_2)](\text{BF}_4)_2$ and $(\text{PPN})(\text{SNO})$	121
Figure 3.18.	FTIR and ESI-MS characterization of $[\text{FeS}_5(\text{NO})_2]^-$ formed in the reaction of $[\text{Fe}_2(\text{Et-HPTB})(\text{PhCO}_2)](\text{BF}_4)_2$ and $(\text{PPN})(\text{SSNO})$	121
Figure 3.19.	EPR spectra of $[\text{FeS}_5(\text{NO})_2]^-$ at RT and 77 K	122
Figure 3.20.	Drawings of the crystal structure of $[\text{Fe}_3(\mu\text{-O})(\text{Ph}_4\text{DBA})_2(\text{TMEDA})_2(\text{NO})_2](\text{OTf})$	124
Figure 3.21.	UV-Vis of the reaction of $[\text{Fe}_2(\mu\text{-OH})(\text{Ph}_4\text{DBA})(\text{TMEDA})_2(\text{OTf})]$ with $\text{NO}(\text{g})$	126
Figure 3.22.	ReactIR of the reaction of $[\text{Fe}_2(\mu\text{-OH})(\text{Ph}_4\text{DBA})(\text{TMEDA})_2(\text{OTf})]$ with $\text{NO}(\text{g})$	127
Figure 3.23.	$^{57}\text{Mössbauer}$ spectrum of $[\text{Fe}_3(\mu\text{-O})_2(\text{Ph}_4\text{DBA})_2(\text{TMEDA})_2(\text{NO})_2](\text{OTf})$	128
Figure 3.24	Drawings of the X-ray crystal structure of $(\text{PPN})_2[\text{FeS}_5(\text{NO})_2](\text{OTf})$	129
Figure 3.25.	Spectroscopic characterization of $[\text{FeS}_5(\text{NO})_2]^-$ formed in the reaction of $[\text{Fe}(\text{BIPhMe})\text{Cl}_2]$ and $(\text{PPN})(\text{SNO})$	131
 <b>Chapter 4</b>		
Figure 4.1.	Known metal complexes containing the $\text{NSO}^-$ ligand	137
Figure 4.2.	$^1\text{H}$ NMR spectra of $\text{cis-}[\text{Pt}(\text{NH}_3)_2(\text{py})\text{Cl}](\text{OTf})$ and the reaction products with $(\text{PPN})(\text{SSNO})$ and $(\text{PPN})(\text{SNO})$	144
Figure 4.3.	FTIR spectra of the reaction of natural abundance and $^{15}\text{N}$ -labeled $(\text{PPN})(\text{SSNO})$ and $(\text{PPN})(\text{SNO})$ with $\text{cis-}[\text{Pt}(\text{NH}_3)_2(\text{py})\text{Cl}](\text{OTf})$	145
Figure 4.4.	Solutions of $\text{cis-}[\text{Pt}(\text{NH}_3)_2(\text{py})\text{Cl}](\text{OTf})$ and $[\text{Fe}(\text{BIPhMe})\text{Cl}_2]$ before and after addition of $(\text{PPN})(\text{SNO})$	145
Figure 4.5.	Calculated structures of $\text{cis-}[\text{Pt}_2(\text{NH}_3)_4(\text{py})_2(\mu\text{-S}_2)]^{2+}$ and $\text{cis-}[\text{Pt}_2(\text{NH}_3)_4(\text{py})_2(\mu\text{-S}_4)]^{2+}$	147
Figure 4.6.	Calculated spectra of $\text{cis-}[\text{Pt}_2(\text{NH}_3)_4(\text{py})_2(\mu\text{-S}_2)]^{2+}$ and $\text{cis-}[\text{Pt}_2(\text{NH}_3)_4(\text{py})_2(\mu\text{-S}_4)]^{2+}$ , and the experimental spectra of the product formed in the reaction of $\text{cis-}[\text{Pt}(\text{NH}_3)_2(\text{py})\text{Cl}](\text{OTf})$ with $(\text{PPN})(\text{SSNO})$ and $(\text{PPN})(\text{SNO})$	148

Figure 4.7.	Calculated energies and structures of <i>cis</i> -[Pt(NH <sub>3</sub> ) <sub>2</sub> (py){SNO}] <sup>+</sup>	150
Figure 4.8.	Calculated vibrational spectra of <i>cis</i> -[Pt(NH <sub>3</sub> ) <sub>2</sub> (py){SNO}] <sup>+</sup>	150
Figure 4.9.	Calculated energies and structures of <i>cis</i> -[Pt(NH <sub>3</sub> ) <sub>2</sub> (py){SSNO}] <sup>+</sup>	151
Figure 4.10.	Calculated vibrational spectra of <i>cis</i> -[Pt(NH <sub>3</sub> ) <sub>2</sub> (py){SSNO}] <sup>+</sup>	152
Figure 4.11.	Drawing of the X-ray crystal structure of <i>cis</i> -[Pt(NH <sub>3</sub> ) <sub>2</sub> (py)(CH <sub>3</sub> CN)](BF <sub>4</sub> ) <sub>2</sub>	153
Figure 4.12.	Drawing of the X-ray crystal structure of <i>cis-mer</i> -[Pt(NH <sub>3</sub> ) <sub>2</sub> (py)Cl <sub>3</sub> ]Cl	154
Figure 4.13.	<sup>1</sup> H NMR spectrum of a mixture of crystalline <i>cis</i> -[Pt(NH <sub>3</sub> ) <sub>2</sub> (py)(CH <sub>3</sub> CN)](BF <sub>4</sub> ) <sub>2</sub> and <i>cis-mer</i> -[Pt(NH <sub>3</sub> ) <sub>2</sub> (py)Cl <sub>3</sub> ]Cl	157
 <b>Chapter 5</b>		
Figure 5.1.	Iron-sulfur nitrosyl compounds	162
Figure 5.2.	<sup>19</sup> F NMR spectra of C <sub>6</sub> Br <sub>3</sub> F <sub>3</sub> , CF <sub>3</sub> (SC <sub>6</sub> H <sub>4</sub> CH <sub>3</sub> ) <sub>3</sub> , and LF(SCH <sub>2</sub> OCH <sub>2</sub> CH <sub>3</sub> ) <sub>2</sub>	186
Figure 5.3.	Gas Chromatogram of crude product when attempting to protect C <sub>6</sub> H <sub>2</sub> (CH <sub>3</sub> ) <sub>2</sub> (SH) <sub>2</sub>	187
Figure 5.4.	Drawings of the X-ray crystal structures of LS <sub>2</sub> (SCH <sub>2</sub> OCH <sub>3</sub> ) <sub>2</sub> and L(SCH <sub>2</sub> OCH <sub>3</sub> ) <sub>3</sub> ·(CH <sub>3</sub> ) <sub>2</sub> CO	188
Figure 5.5.	<sup>1</sup> H NMR spectra of LS <sub>3</sub> and intermediates	190
Figure 5.6.	<sup>57</sup> Fe Mössbauer spectra of [Fe <sub>4</sub> S <sub>4</sub> (LS <sub>3</sub> )L'] <sup>2-</sup> complexes	192
Figure 5.7.	<sup>1</sup> H NMR spectra of [Fe <sub>4</sub> S <sub>4</sub> (LS <sub>3</sub> )L'] <sup>2-</sup> complexes	195
Figure 5.8.	ESI-MS of [Fe <sub>4</sub> S <sub>4</sub> (LS <sub>3</sub> )Cl] <sup>2-</sup> and [Fe <sub>4</sub> S <sub>4</sub> (LS <sub>3</sub> )N <sub>3</sub> ] <sup>2-</sup>	196
Figure 5.9.	Drawings of the X-ray crystal structures of [Fe <sub>4</sub> S <sub>4</sub> (LS <sub>3</sub> )N <sub>3</sub> ] <sup>2-</sup> and [Fe <sub>4</sub> S <sub>4</sub> (LS <sub>3</sub> )(S <sub>2</sub> CNEt <sub>2</sub> )] <sup>2-</sup>	197
Figure 5.10.	Characterization of the products formed between clusters and NO(g)	200
Figure 5.11.	ReactIR spectra of (Et <sub>4</sub> N)[Fe <sub>4</sub> S <sub>4</sub> (SPh) <sub>4</sub> ] and (Ph <sub>4</sub> P) <sub>2</sub> [Fe <sub>4</sub> S <sub>4</sub> (LS <sub>3</sub> )(SPh)] with Ph <sub>3</sub> CSNO	201
Figure 5.12.	80 K <sup>57</sup> Fe Mössbauer spectra of [Fe <sub>4</sub> S <sub>4</sub> (LS <sub>3</sub> )Cl] <sup>2-</sup> , [Fe <sub>4</sub> S <sub>4</sub> (NO) <sub>4</sub> ] <sup>-</sup> , and in a 1:1 ratio	202
Figure 5.13.	Gas chromatogram and EI-MS spectrum of the pentane extract of the reaction of [Fe <sub>4</sub> S <sub>4</sub> (LS <sub>3</sub> )Cl] <sup>2-</sup> and Ph <sub>3</sub> CSNO	203

Figure 5.14.	Drawing of the crystal structure of $(\text{Ph}_3\text{CS})_2$	203
Figure 5.15.	X-band EPR spectra of $[\text{Fe}_4\text{S}_4(\text{NO})_4]^-$ at RT and 77 K	206
Figure 5.16.	$\text{CH}_2\text{Cl}_2$ solution FTIR of the reaction of $[\text{Fe}_4\text{S}_4(\text{LS}_3)\text{Cl}]^{2-}$ with $\text{NO}(\text{g})$ and $\text{Ph}_3\text{CSNO}$ in the presence of $\text{TIPF}_6$	207
Figure 5.17.	Cyclic voltammogram of $[\text{Fe}_4\text{S}_4(\text{NO})_4]$ at ambient temperature at scan speeds from 50 – 1000 mV/s	207
Figure 5.18.	Negative-mode ESI-MS spectrum of $[\text{Fe}_4\text{S}_4(\text{NO})_4]$	208
Figure 5.19.	Drawing of the crystal structure of $[\text{Cp}^*\text{Fe}][\text{Fe}_4\text{S}_4(\text{NO})_4]$	209

## Appendix A

Figure A.1.	$^1\text{H}$ NMR spectrum of $[\text{Fe}(\text{BIPhMe})\text{I}_2]$	222
Figure A.2.	FTIR spectrum of $[\text{Fe}(\text{BIPhMe})(\text{MeCN})_2(\text{OTf})_2]$	223
Figure A.3.	$^1\text{H}$ NMR spectrum of $[\text{Fe}(\text{BIPhMe})(\text{MeCN})_2(\text{OTf})_2]$	224
Figure A.4.	$^{19}\text{F}\{^1\text{H}\}$ NMR spectrum of $[\text{Fe}(\text{BIPhMe})(\text{MeCN})_2(\text{OTf})_2]$	224
Figure A.5.	$^1\text{H}$ NMR spectrum of $[\text{Zn}_2(\mu\text{-OTf})_2(\text{OTf})_2(\text{BIPhMe})_2]$	226
Figure A.6.	Diffraction spot intensities of a single crystal of $[\text{Fe}(\text{BIPhMe})\text{I}_2]$ at varying temperatures	227
Figure A.7.	Drawing of the X-ray crystal structures of $[\text{Fe}(\text{BIPhMe})\text{I}_2]$ at 298 K and 140 K	228
Figure A.8.	Drawing of the X-ray crystal structure of $[\text{Fe}(\text{BIPhMe})(\text{MeCN})_2(\text{OTf})_2]$	230
Figure A.9.	Drawing of the X-ray crystal structure of $[\text{Fe}(\text{BIPhMe})(\text{NO}_3)_2]_2\text{O}$	231
Figure A.10.	Drawing of the X-ray crystal structure of $[\text{Cu}(\text{BIPhMe})_2](\text{OTf})_2$	233
Figure A.11.	Drawing of the X-ray crystal structure of $[\text{Cu}(\text{BIPhMe})_2][\text{CuCl}_2]$	234
Figure A.12.	UV-Vis spectra of the reaction of $[\text{Cu}(\text{BIPhMe})_2](\text{OTf})_2$ with $\text{NO}(\text{g})$ and $\text{NO}_2(\text{g})$	235
Figure A.13.	UV-Vis spectra of the reaction of $[\text{Zn}_2(\mu\text{-OTf})_2(\text{OTf})_2(\text{BIPhMe})_2]$ and $(\text{PPN})(\text{SNO})$	236
Figure A.14.	UV-Vis spectra of the reaction of $[\text{Zn}_2(\mu\text{-OTf})_2(\text{OTf})_2(\text{BIPhMe})_2]$ and $(\text{PPN})(\text{SSNO})$	236
Figure A.15.	Solutions of $[\text{Zn}_2(\mu\text{-OTf})_2(\text{OTf})_2(\text{BIPhMe})_2]$ and $[\text{Fe}(\text{BIPhMe})\text{Cl}_2]$ before and after the addition of $(\text{PPN})(\text{SSNO})$	237

## Appendix B

Figure B.1.	ReactIR of $(\text{Ph}_4\text{P})_2[\text{Fe}_4\text{S}_4(\text{LS}_3)(\text{SPh})]$ with $\text{NO}(\text{g})$	240
Figure B.2.	Negative-mode ESI-MS spectrum of $(\text{Ph}_4\text{P})_2[\text{Fe}_4\text{S}_4(\text{LS}_3)\text{Cl}] + \text{NO}(\text{g})$	240
Figure B.3.	Negative-mode ESI-MS spectrum of $(\text{Ph}_4\text{P})_2[\text{Fe}_4\text{S}_4(\text{LS}_3)(\text{SEt})] + \text{NO}(\text{g})$	241
Figure B.4.	Negative-mode ESI-MS spectrum of $(\text{Ph}_4\text{P})_2[\text{Fe}_4\text{S}_4(\text{LS}_3)(\text{SPh})] + \text{NO}(\text{g})$	241
Figure B.5.	Negative-mode ESI-MS spectrum of $(\text{Ph}_4\text{P})_2[\text{Fe}_4\text{S}_4(\text{LS}_3)(\text{N}_3)] + \text{NO}(\text{g})$	242
Figure B.6.	Negative-mode ESI-MS spectrum of $(\text{Ph}_4\text{P})_2[\text{Fe}_4\text{S}_4(\text{LS}_3)(\text{SPyr})] + \text{NO}(\text{g})$	242
Figure B.7.	Negative-mode ESI-MS spectrum of $(\text{Ph}_4\text{P})_2[\text{Fe}_4\text{S}_4(\text{LS}_3)(\text{Tp})] + \text{NO}(\text{g})$	243
Figure B.8.	Negative-mode ESI-MS spectrum of $(\text{Ph}_4\text{P})_2[\text{Fe}_4\text{S}_4(\text{LS}_3)(\text{S}_2\text{CNEt}_2)] + \text{NO}(\text{g})$	243
Figure B.9.	Negative-mode ESI-MS spectrum of $(\text{Ph}_4\text{P})_2[\text{Fe}_4\text{S}_4(\text{LS}_3)\text{Cl}] + \text{Ph}_3\text{CSNO}$	244
Figure B.10.	Negative-mode ESI-MS spectrum of $(\text{Ph}_4\text{P})_2[\text{Fe}_4\text{S}_4(\text{LS}_3)\text{Cl}] + 4 \text{ Ph}_3\text{CSNO}$	244
Figure B.11.	Negative-mode ESI-MS spectrum of $(\text{Ph}_4\text{P})_2[\text{Fe}_4\text{S}_4(\text{LS}_3)(\text{SPh})] + \text{Ph}_3\text{CSNO}$	245
Figure B.12.	Negative-mode ESI-MS spectrum of $(\text{Ph}_4\text{P})_2[\text{Fe}_4\text{S}_4(\text{LS}_3)(\text{SPyr})] + \text{Ph}_3\text{CSNO}$	245
Figure B.13.	Negative-mode ESI-MS spectrum of $(\text{Ph}_4\text{P})_2[\text{Fe}_4\text{S}_4(\text{LS}_3)(\text{Tp})] + \text{Ph}_3\text{CSNO}$	246
Figure B.14.	$^1\text{H}$ NMR spectrum of pentane extract of $(\text{Ph}_4\text{P})_2[\text{Fe}_4\text{S}_4(\text{LS}_3)\text{Cl}] + \text{Ph}_3\text{CSNO}$	246
Figure B.15.	FTIR spectroscopy of $(\text{Ph}_4\text{P})_2[\text{Fe}_4\text{S}_4(\text{LS}_3)\text{Cl}] + 1-4 \text{ Ph}_3\text{CSNO}$	247
Figure B.16.	FTIR spectroscopy of $(\text{Ph}_4\text{P})_2[\text{Fe}_4\text{S}_4(\text{LS}_3)(\text{SEt})] + \text{Ph}_3\text{CSNO}$	247
Figure B.17.	FTIR spectroscopy of $(\text{Ph}_4\text{P})_2[\text{Fe}_4\text{S}_4(\text{LS}_3)(\text{SPh})] + \text{Ph}_3\text{CSNO}$	248
Figure B.18.	FTIR spectroscopy of $(\text{Ph}_4\text{P})_2[\text{Fe}_4\text{S}_4(\text{LS}_3)(\text{N}_3)] + \text{Ph}_3\text{CSNO}$	248
Figure B.19.	FTIR spectroscopy of $(\text{Ph}_4\text{P})_2[\text{Fe}_4\text{S}_4(\text{LS}_3)(\text{SPyr})] + \text{Ph}_3\text{CSNO}$	249
Figure B.20.	FTIR spectroscopy of $(\text{Ph}_4\text{P})_2[\text{Fe}_4\text{S}_4(\text{LS}_3)(\text{Tp})] + \text{Ph}_3\text{CSNO}$	249
Figure B.21.	FTIR spectroscopy of $(\text{Ph}_4\text{P})_2[\text{Fe}_4\text{S}_4(\text{LS}_3)(\text{S}_2\text{CNEt}_2)] + \text{Ph}_3\text{CSNO}$	250
Figure B.22.	Negative-mode ESI-MS spectrum of $[\text{Cp}^*_2\text{Fe}][\text{Fe}_4\text{S}_4(\text{NO})_4]$	250

## List of Charts

### Chapter 1

- Chart 1.1. Reactivities of the different redox states of NO 27

## List of Schemes

### Chapter 1

- Scheme 1.1. Reaction pathway of L-arginine to L-citrulline conversion with concomitant NO release 30
- Scheme 1.2. Proposed reduction pathways of NO to N<sub>2</sub>O conversion by FprA diiron proteins 38

### Chapter 2

- Scheme 2.1. Known colorimetric and fluorescent probes to detect NO<sup>•</sup> 49

### Chapter 3

- Scheme 3.1. Suggested pathways in the reaction of [Fe<sup>III</sup>(TPP)Cl] and (PPN)(SSNO) 117
- Scheme 3.2. Reaction pathways of [Fe<sub>2</sub>S<sub>2</sub>(SPh)<sub>4</sub>]<sup>2-</sup> to form iron-sulfur-nitrosyl products 120
- Scheme 3.3. Reaction pathways of [Fe<sub>2</sub>(Et-HPTB)(PhCO<sub>2</sub>)](BF<sub>4</sub>)<sub>2</sub> and [Fe<sub>2</sub>(μ-OH)(Ph<sub>4</sub>DBA)(TMEDA)<sub>2</sub>(OTf)] with various RNOS species

### Chapter 4

- Scheme 4.1. Reactions of *cis*-[Pt(NH<sub>3</sub>)<sub>2</sub>(py)Cl](OTf) with (PPN)(SSNO), (PPN)(SNO), and NOBF<sub>4</sub> 138

### Chapter 5

- Scheme 5.1. Reactivity pathways of synthetic [4Fe-4S] clusters with NO(g) and Ph<sub>3</sub>CSNO 163
- Scheme 5.2. Synthesis of the [3:1] site-differentiating ligand L(SH)<sub>3</sub> 185

Scheme 5.3.	Preparation of $[\text{Fe}_4\text{S}_4(\text{LS}_3)\text{L}']^{2-}$ using different alkali metal salts	191
-------------	--	-----

### List of Tables

#### Chapter 2

Table 2.1.	Selected geometrical parameters of $\text{M}(\text{BIPhMe})\text{X}_2$ complexes	66
Table 2.2.	X-ray crystallographic data for mononuclear and chloro-bridged $[\text{Fe}(\text{BIPhMe})\text{Cl}_2]$ , and $[\text{Fe}(\text{BIPhMe})\text{Br}_2]$	67
Table 2.3.	X-ray crystallographic data for $[\text{Co}(\text{BIPhMe})\text{Cl}_2]$ and $[\text{Co}(\text{BIPhMe})\text{I}_2]$	68
Table 2.4.	Selected geometrical parameters and vibrational stretches of $[\text{Fe}(\text{BIPhMe})_2(\text{NO})\text{Cl}][\text{Fe}(\text{NO})\text{Cl}_3]$ and related compounds	74
Table 2.5.	X-ray crystallographic data for $[\text{Fe}(\text{BIPhMe})_2(\text{NO})\text{Cl}][\text{Fe}(\text{NO})\text{Cl}_3]$ and $[\text{Fe}(\text{BIPhMe})(\text{NO}_3)_2\text{Cl}]$	75
Table 2.6.	Selected geometrical parameters of $[\text{Fe}(\text{BIPhMe})(\text{NO}_3)_2\text{Cl}]$ and $[\text{Co}(\text{BIPhMe})(\text{NO}_3)_2]$	79
Table 2.7.	X-ray crystallographic data for $[\text{Co}(\text{BIPhMe})(\text{NO}_3)_2]$	84

#### Chapter 3

Table 3.1.	X-ray crystallographic data for $(\text{PPN})(\text{SSNO})$ and $(\text{PPN})(\text{SNO}) \cdot (\text{CH}_3)_2\text{CO}$	108
Table 3.2.	Selected geometrical parameters of <i>S</i> -nitrosothiols	109
Table 3.3.	Selected geometrical parameters of $[\text{Fe}_3(\mu\text{-O})(\text{Ph}_4\text{DBA})_2(\text{TMEDA})_2(\text{NO})_2](\text{OTf})$ and other diiron-nitrosyl species	123
Table 3.4.	X-ray crystallographic data for $(\text{PPN})_2[\text{FeS}_5(\text{NO})_2](\text{OTf})$ and $[\text{Fe}_3(\mu\text{-O})(\text{Ph}_4\text{DBA})_2(\text{TMEDA})_2(\text{NO})_2](\text{OTf}) \cdot 2\text{Et}_2\text{O} \cdot 0.5\text{CH}_2\text{Cl}_2$	125

#### Chapter 4

Table 4.1.	Selected calculated geometrical parameters for <i>cis</i> - $[\text{Pt}_2(\text{NH}_3)_4(\text{py})_2(\mu\text{-S}_2)]^{2+}$ and <i>cis</i> - $[\text{Pt}_2(\text{NH}_3)_4(\text{py})_2(\mu\text{-S}_4)]^{2+}$	147
Table 4.2.	Vibrational energies used to prepare fitting equation for calculated spectra	149
Table 4.3.	Geometrical parameters of pyriplatin and related complexes	153



Table 4.4.	X-ray crystallographic data for <i>cis</i> -[Pt(NH <sub>3</sub> ) <sub>2</sub> (py)(CH <sub>3</sub> CN)](BF <sub>4</sub> ) <sub>2</sub> and <i>cis-mer</i> -[Pt(NH <sub>3</sub> ) <sub>2</sub> (py)Cl <sub>3</sub> ]Cl	153
------------	--	-----

## Chapter 5

Table 5.1.	X-ray crystallographic data for LS <sub>2</sub> (SCH <sub>2</sub> OCH <sub>2</sub> CH <sub>3</sub> ) and L(SCH <sub>2</sub> OCH <sub>3</sub> )·(CH <sub>3</sub> ) <sub>2</sub> CO	189
Table 5.2.	Mössbauer parameters of relevant iron-sulfur complexes	193
Table 5.3.	X-ray crystallographic data for (Ph <sub>4</sub> P) <sub>2</sub> [Fe <sub>4</sub> S <sub>4</sub> (LS <sub>3</sub> )N <sub>3</sub> ]·4MeCN·Et <sub>2</sub> O·0.5H <sub>2</sub> O and (Ph <sub>4</sub> P) <sub>2</sub> [Fe <sub>4</sub> S <sub>4</sub> (LS <sub>3</sub> )(S <sub>2</sub> CNEt <sub>2</sub> )] 2.5·Et <sub>2</sub> O	198
Table 5.4.	X-ray crystallographic data for (Ph <sub>3</sub> CS) <sub>2</sub> and [Cp <sup>*</sup> <sub>2</sub> Fe][Fe <sub>4</sub> S <sub>4</sub> (NO) <sub>4</sub> ]	204
Table 5.5.	Selected geometric parameters of iron-sulfur clusters capped with mono-nitrosyls	209

## Appendix A

Table A.1.	Selected geometrical parameters for M(BIPhMe) complexes	228
Table A.2.	X-ray crystallographic data for [Fe(BIPhMe)I <sub>2</sub> ] at 296 K and 140 K	229
Table A.3.	X-ray crystallographic data for [Fe(BIPhMe)(OTf) <sub>2</sub> (MeCN) <sub>2</sub> ] and [Fe(BIPhMe)(NO <sub>3</sub> ) <sub>2</sub> ] <sub>2</sub> O	230
Table A.4.	Selected geometrical parameters of hepta-coordinate, μ-oxo diiron complexes	232
Table A.5.	X-ray crystallographic data for [Cu(BIPhMe) <sub>2</sub> ](OTf) <sub>2</sub> , [Cu(BIPhMe) <sub>2</sub> ][CuCl <sub>2</sub> ], and [Zn <sub>2</sub> (μ-OTf) <sub>2</sub> (OTf) <sub>2</sub> (BIPhMe) <sub>2</sub> ]	234

## List of Equations

### Chapter 5

Equation 5.1.	Reaction of [Fe <sub>4</sub> S <sub>4</sub> (LS <sub>3</sub> )Cl] <sup>2-</sup> and 11 equiv NO(g)	199
Equation 5.2.	Reaction of [Fe <sub>4</sub> S <sub>4</sub> (LS <sub>3</sub> )Cl] <sup>2-</sup> and 4 equiv Ph <sub>3</sub> CSNO	202
Equation 5.3.	Reaction of [Fe <sub>4</sub> S <sub>4</sub> (LS <sub>3</sub> )Cl] <sup>2-</sup> and 7 equiv Ph <sub>3</sub> CSNO	202
Equation 5.4.	Reaction of [Fe <sub>4</sub> S <sub>4</sub> (LS <sub>3</sub> )Cl] <sup>2-</sup> , 11 equiv NO(g), and 3 equiv TI <sup>+</sup>	207
Equation 5.5.	Reaction of [Fe <sub>4</sub> S <sub>4</sub> (LS <sub>3</sub> )Cl] <sup>2-</sup> , 4 equiv Ph <sub>3</sub> CSNO, and 2 equiv TI <sup>+</sup>	207

# **CHAPTER 1: BIOINORGANIC CHEMISTRY OF NITRIC OXIDE AND S-NITROSO THIOLS**

**1.1 Introduction.** The chemical composition of the diatomic gas nitric oxide (NO) was discovered in the mid-18<sup>th</sup> century. NO is a radical with one unpaired electron in a  $\pi$ -antibonding orbital, giving the N–O bond an order of 2.5. The radical nature of NO makes it a highly reactive molecule with transition metals and other small-molecule radicals such as  $\text{NO}_2^\bullet$ ,  $\text{O}_2^\bullet$ , and  $\text{RS}^\bullet$  (Chart 1.1).<sup>1</sup>

NO is redox active and can be both oxidized and reduced. NO oxidation to  $\text{NO}^+$  occurs at 1.52 V vs. NHE and reduction to the triplet ground state of  $\text{NO}^-$  occurs at  $-0.8$  V vs. NHE, both potentials were determined in acetonitrile.<sup>2,3</sup> The  $\text{pK}_a$  of  ${}^3\text{NO}^-$  was determined to be 11.6.<sup>3</sup>

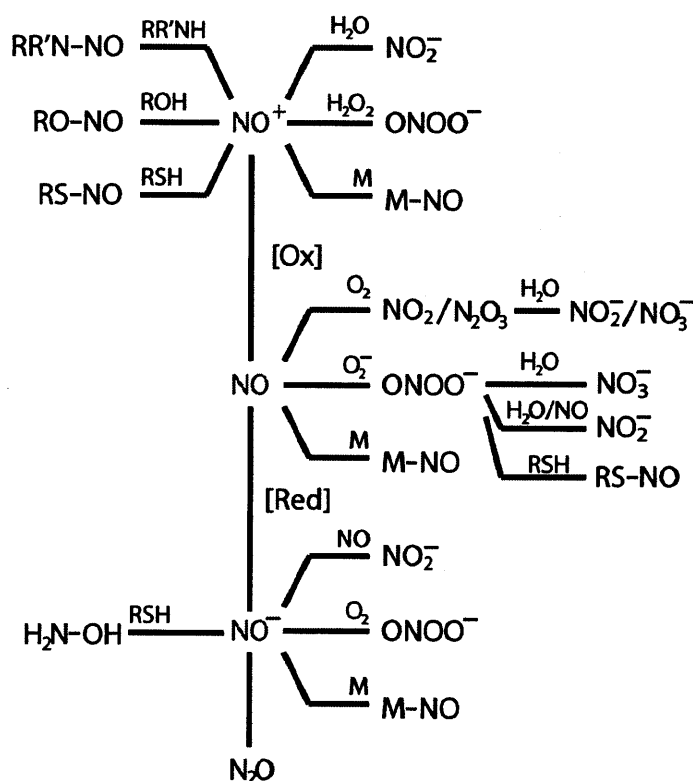


**Chart 1.1.** Reactivities of the different redox states of NO.<sup>1</sup>

Prior to the 1980's, NO was considered a major pollutant with little industrial application.<sup>4</sup> Three decades ago, NO was determined to have a role as the endothelium-derived

relaxation factor in mammals. This discovery led to an entire field of research in the biological sciences being developed with the purpose of determining the role of NO as a signaling agent and microbicide. As NO gained more popularity it was named the Molecule of the Year in 1992 by Science magazine, and the 1998 Nobel Prize in Physiology and Medicine was awarded to Furchgott, Ignarro, and Murad for their discoveries of the role NO serves in biological signaling of the cardiovascular system.<sup>4-7</sup>

NO is produced through multiple pathways in biology.<sup>8</sup> One route of production in mammals involves the conversion of L-arginine to L-citrulline and NO by nitric oxide synthases (NOS), NADPH, and O<sub>2</sub> (Scheme 1.1).<sup>9,10</sup> NOS enzymes are homodimers that require the cofactors (6R)-5,6,7,8-tetrahydrobiopterin (BH<sub>4</sub>), ironprotoporphyrin IX (heme), flavin-adenine dinucleotide (FAD), and flavin mononucleotide (FMN) and the messenger protein calmodulin for full activity.<sup>11,12</sup> The homodimer of NOS enzymes is stabilized by Zn<sup>2+</sup> ions that bind to cysteines C110 and C115 at the dimer interface (Figure 1.1).<sup>11,13</sup>

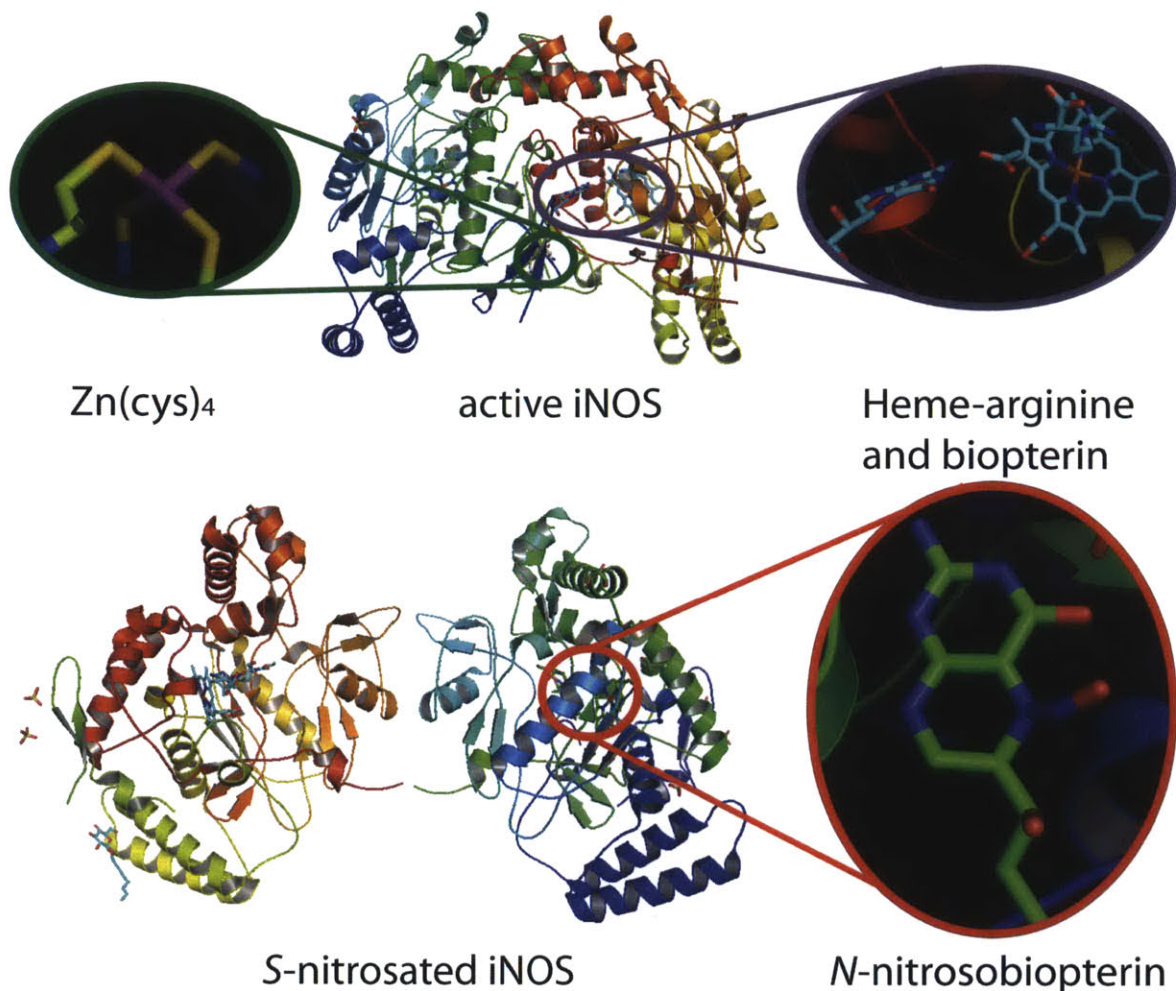
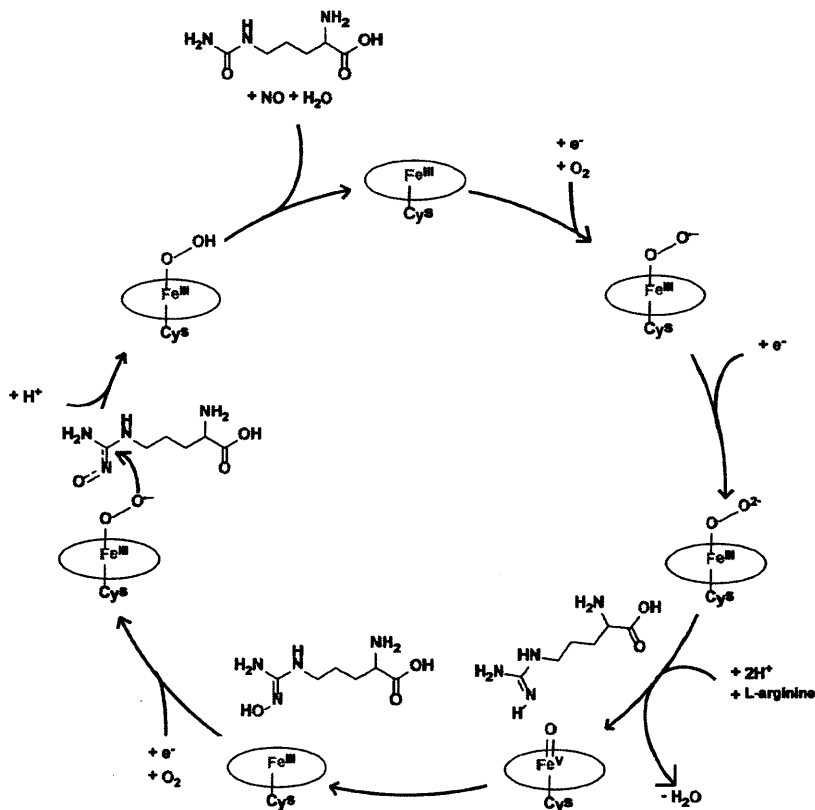


**Figure 1.1.** Cartoon depictions of the crystal structures of active (top; PDB: 1NSI; resolution: 2.55 Å) and NO-inhibited (bottom; PDB: 3NQS; resolution: 2.20 Å) inducible NOS.<sup>11,13</sup> Active iNOS forms a homodimer that is stabilized by a Zn<sup>2+</sup> ion bound by two cysteines of each monomer. When NO concentrations are high, the thiolates of these cysteines are nitrosated and release Zn<sup>2+</sup>, along with nitrosation of the biopterin to prevent further conversion of L-arginine to NO and L-citrulline.

The FAD and FMN cofactors transfer electrons from NADPH to the oxygenase domain where the heme and BH<sub>4</sub> units catalyze the reaction.<sup>14-17</sup> NOS enzymes can be inhibited by high concentrations of NO as a negative feedback mechanism.<sup>13</sup> Nitrosation of C110 and C115 results in the release of Zn<sup>2+</sup>, formation of protein-bound *S*-nitrosocysteine, and destabilization of the homodimer as well as nitrosation of the N5 position of the BH<sub>4</sub> cofactor to form a *N*-nitrosamine.<sup>13</sup> These NO-modifications can be reversed by high concentrations of glutathione

(GSH), which form *S*-nitrosoglutathione (GSNO) by transnitrosation from the protein and cofactor.



**Scheme 1.1.** Reaction pathway of L-arginine to L-citrulline conversion with concomitant NO release.<sup>14</sup>

Three isoforms of NOS enzymes exist: endothelial, neuronal, and inducible. Neuronal (nNOS) and endothelial (eNOS) NOS are Ca<sup>2+</sup>-dependent enzymes that require calmodulin binding, whereas the inducible NOS enzymes (iNOS) are not Ca<sup>2+</sup>-sensitive as calmodulin remains bound.<sup>17</sup> Release of NO from eNOS occurs in endothelial cells to regulate vascular function.<sup>18-21</sup> The nNOS enzymes are present in the of the central and peripheral nervous system.<sup>10</sup> In the central nervous system, NO released by nNOS is linked to cognitive function, sleep control, and neurosecretion.<sup>22,23</sup> Smooth muscle relaxation is controlled by NO released from nNOS in the peripheral nervous system.<sup>24</sup> In these systems, NO serves as a signaling agent

to activate soluble guanylyl cyclase, a heme-containing enzyme that catalyzes the conversion of guanosine triphosphate to 3',5'-cyclic guanosine monophosphate (cGMP), which in turn serves to signal smooth muscle cell relaxation.<sup>25</sup> Macrophages contain iNOS enzymes to release NO in high concentrations and attack bacteria and tumor cells.<sup>9,26</sup> The effect of oxidative stress on target cells and caspase activation can trigger an apoptotic response leading to cell death.<sup>27</sup> To counteract the release of NO as a microbicide by macrophages, some bacteria have developed nitric oxide reductases (NORs) to convert the released NO into N<sub>2</sub>O, a less cytotoxic nitrogen oxide; others such as *Helicobacter pylori* express arginase enzymes to deplete the L-arginine stores of hosts and prevent NO production.<sup>28-31</sup>

The cellular release of NO can perform post-translational modifications, such as protein-bound *S*-nitrosothiol formation or *C*-nitroso DNA modification, degrade metal active sites in enzymes, such as iron-sulfur clusters, or form other reactive nitrogen oxide species (RNOS) that further affect biological pathways.<sup>27,32-34</sup>

**1.2. *S*-nitrosothiols in biology.** Similar to NO, thiols, sulfides, and thioethers can access multiple redox states, from -2 to +6, providing the basis for rich chemistry.<sup>35</sup> *S*-nitrosothiol formation can occur from multiple pathways by reduction of disulfides, copper-mediated oxidation of NO, or reaction with peroxynitrite or dinitrogen.<sup>1,36</sup> Low molecular weight *S*-nitrosothiols, such as GSNO, can transport and shuttle NO throughout the cytosol and perform post-translational modifications.<sup>37-40</sup> Recently, the smallest *S*-nitrosothiol HSNO was proposed to serve as a biologically relevant signaling molecule.<sup>41,42</sup> HSNO is believed to form upon transnitrosation of H<sub>2</sub>S by a Cys-SNO residue on human serum albumin. Due to the small size and neutral charge of HSNO, the molecule crosses the cell membrane and transfers the NO to a surface exposed cysteine of hemoglobin. A crystal structure of SNO-nitrosylHbA (human

hemoglobin A) has been reported and was prepared by exposing crystals of carbonmonoxyl HbA to gaseous NO under anaerobic conditions.<sup>43</sup> The CO ligands of the Fe-heme are replaced by NO and Cys93 is *S*-nitrosated (Figure 1.2).

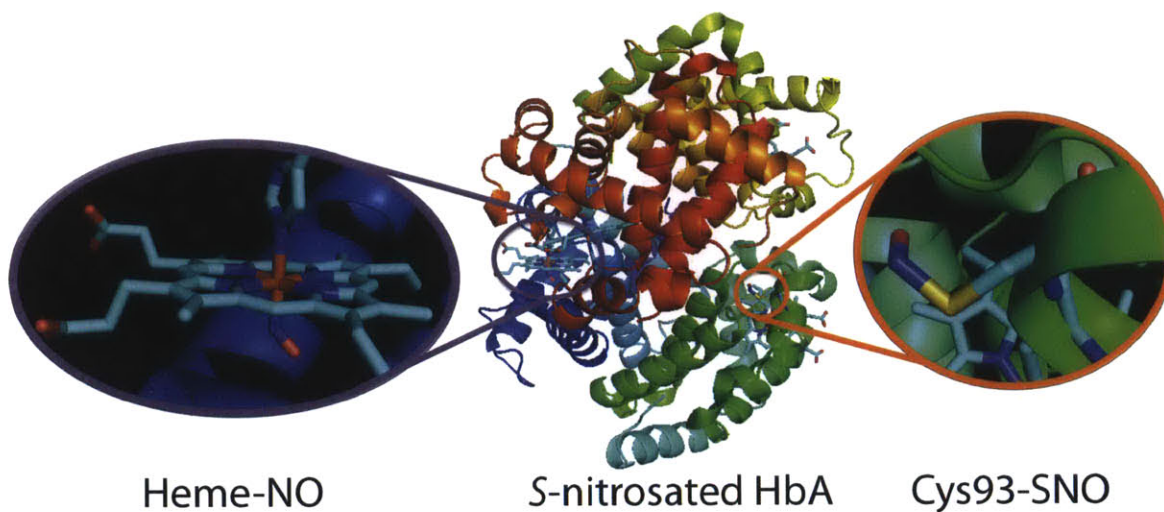
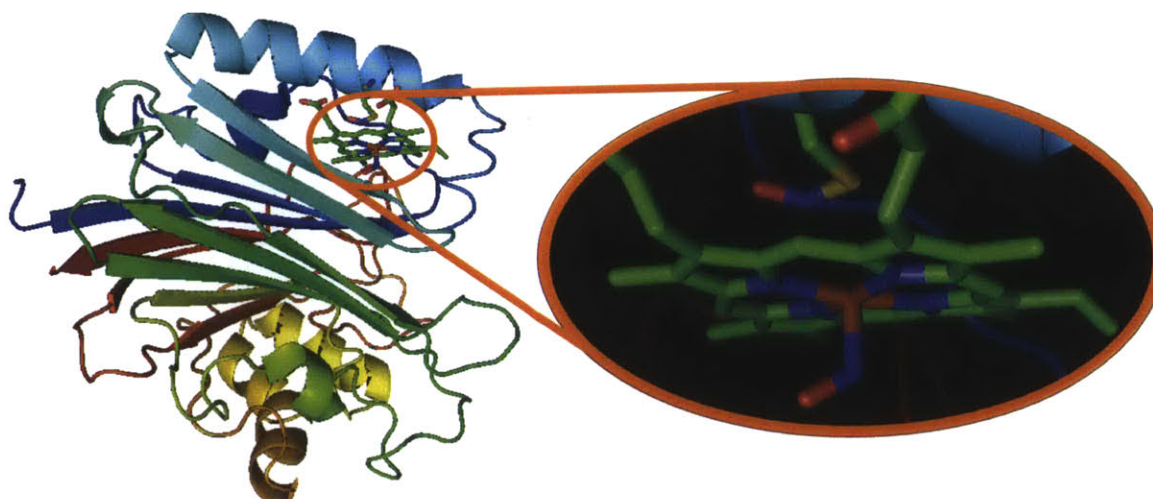


**Figure 1.2.** Cartoon depiction of the 1.90 Å resolution crystal structure of *S*-nitrosated HbA (PDB: 1BUW).<sup>43</sup> The *S*-nitrosocysteine residue has a *syn*-conformation.

Protein-bound *S*-nitrosothiols can also serve as intercellular and interspecies NO transporters, such as the NO transport protein nitrophorin (cNP) from the insect *Climex lectularius*, commonly known as the bedbug. The cNP protein binds NO at Cys60 as well as its heme cofactor (Figure 1.3).<sup>44</sup> The low pH in the saliva of *C. lectularius* prevents the release of NO from nitrosated-cNP. When the protein is injected into the feeding site on the victim, the NO is released in the higher pH environment. The release of NO induces vasodilation at the site of injection and improves feeding for the insect.





**S-nitrosated nitrophorin**

**Heme-NO and Cys60-SNO**

**Figure 1.3.** Cartoon depiction of the 1.75 Å resolution crystal structure of *S*-nitrosated cNP from *C. lectularius* (PDB: 1Y21).<sup>44</sup> Prior to nitrosation, the proximal cysteine is bound to the heme cofactor. The CSNO moiety has a *syn*-conformation and is oriented away from the heme cofactor.

**1.3. Iron-sulfur clusters and dinitrosyl iron complexes in biology.** The NO released by iNOS during the immune response can proliferate other reactive oxygen/nitrogen species and react with other biological components such as the non-heme iron cofactor [4Fe–4S] cluster.<sup>26,45-47</sup> Protein-bound [4Fe–4S] clusters can serve as sensor domains in cells for oxidative stress and cytosolic iron levels, among other uses.<sup>48</sup> Dinitrosyl iron complexes (DNICs) are mononuclear iron species that form upon nitrosation of labile iron.<sup>14,37,45,49</sup> NO released into the cytosol of cells will react with cytosolic iron to form DNICs that can provide long-term storage for NO and either transfer NO to other metal centers within cells or to bind proteins and inhibit function (Figure 1.4).<sup>34,49-52</sup> DNICs are also formed during the degradation process of iron-sulfur proteins and are thought to be the major iron-containing product of these transformations.<sup>52-57</sup>

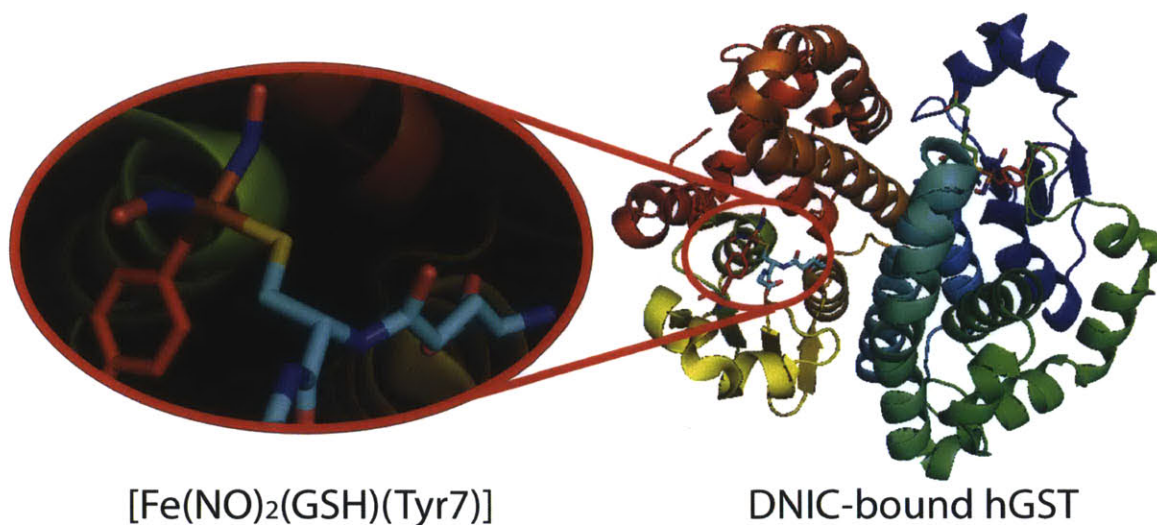


**Figure 1.4.** Cartoon depiction of the 2.10 Å resolution crystal structure of protein bound DNIC to human glutathione transferase (PDB: 1ZGN).<sup>51</sup> The complex was formed by soaking of wild-type crystals of hGST in a solution containing  $[\text{Fe}(\text{NO})_2(\text{GS})_2]$ . Ligand metathesis occurs between the DNIC and Tyr7 resulting in the protein-bound DNIC and GSH.

One of the non-heme iron cofactor targets is the active site of aconitase.<sup>58</sup> Aconitase hydratases, metalloproteins containing a [3:1] site-differentiated [4Fe–4S] cofactor, is present in both the cytosol (ACO1) and the mitochondrial membrane (ACO2).<sup>59,60</sup> Aconitase hydratases catalyze the isomerization of citrate to isocitrate within the citric acid cycle, and ACO1 also serves as a sensing domain in iron-responsive protein-binding protein (IRE-BP) to regulate intracellular iron concentrations.<sup>61-64</sup> These cluster are unique by comparison to common biological [4Fe–4S] clusters in that they do not contain four cysteine ligands, but rather maintain three iron atoms ligated to cysteine (Figure 1.5).<sup>61</sup> The fourth iron site is usually occupied by either hydroxide or bound substrate. ACO2 is inactivated and catalytic activity is inhibited upon removal of the apical iron.<sup>58,65</sup> An apical iron atom is extruded from the core of these clusters to form [3Fe–4S] units and DNICs, as evidenced by the representative  $g_{\text{avg}} = 2.03$  rhombic EPR spectrum.<sup>58</sup> Protein-bound DNICs form when NO reacts with ACO2 with inhibition of enzymatic activity resulting in disruption of the citric acid cycle that can eventually lead to either

cellular apoptosis or necrosis.<sup>66</sup> Complete degradation of the [4Fe–4S] active site in ACO1 by NO has been implicated in the regulation of intracellular iron levels by changing the conformation of iron regulatory protein 1 (IRP1) to its IRE-binding conformation.<sup>67</sup>

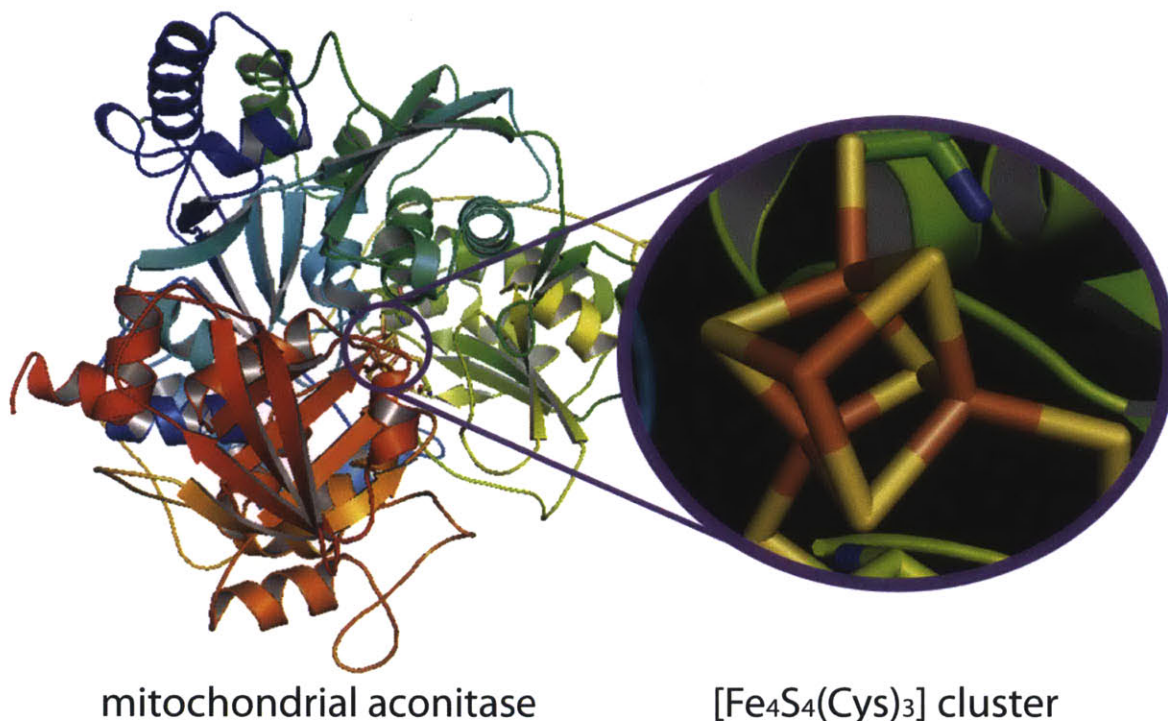


**Figure 1.5.** A cartoon depiction of the 2.50 Å resolution crystal structure of the [Fe<sub>4</sub>S<sub>4</sub>] active site of ACO2 isolated from pig heart mitochondria (PDB: 6ACN). The cluster is ligated by three cysteine residues and a H<sub>2</sub>O/OH<sup>-</sup>.

The [4Fe–4S] clusters of the fumarate nitrate reduction (FNR) regulator in *Escherichia coli* reacts with O<sub>2</sub> and NO to control anaerobic and aerobic respiration as well as the cellular oxidative stress response.<sup>68</sup> Exposure of *E. coli* cells to ~5 μM of NO in an aerobic environment leads to inactivation of FNR by degradation of the [4Fe–4S] cluster, resulting in formation of DNICs and Roussin's red ester (RRE), and leads to monomerization of the enzyme. This monomerization reduces DNA binding affinity and removes transcriptional repression of the *hmp* gene. The *hmp* gene regulates expression of Hmp, a flavohemoglobin protein that detoxifies cells of NO by conversion to N<sub>2</sub>O (anaerobic) or NO<sub>3</sub><sup>-</sup> (aerobic).<sup>69</sup>

The [4Fe-4S]-containing Wbl proteins induce sporulation in actinomycetes upon degradation by NO, resulting in the formation of two equivalents of RRE as the major product with only <3% DNIC formation.<sup>70</sup> The formation of RRE was postulated based on reaction completion at eight equivalents NO and the release of S<sup>0</sup>.

**1.4. Flavodiiron nitric oxide reductases.** NO is encountered by bacteria due to reduction of nitrate and nitrite during denitrification or as a host immune response during infection.<sup>71-77</sup> There are multiple forms of nitric oxide reductases (NORs) that involve heme and/or non-heme iron active sites (Figure 1.6).<sup>28,78</sup> These NORs can be membrane-bound or dissolved in the cytosol. A-type flavoproteins (FprA) have been proposed to serve as scavenging NORs in the cytosol to reduce NO to N<sub>2</sub>O.<sup>79,80</sup> FprA proteins contain non-heme, non-sulfur diiron sites where the iron atoms are five-coordinate and bridged by a solvent molecule (OH/H<sub>2</sub>O) and an aspartate.<sup>81,82</sup> Each iron site contains two histidines and a terminal carboxylate ligand from either an aspartate or a glutamate. The open coordination sites on the irons are *syn* with one another. These proteins also contain a FMN cofactor for electron transport.

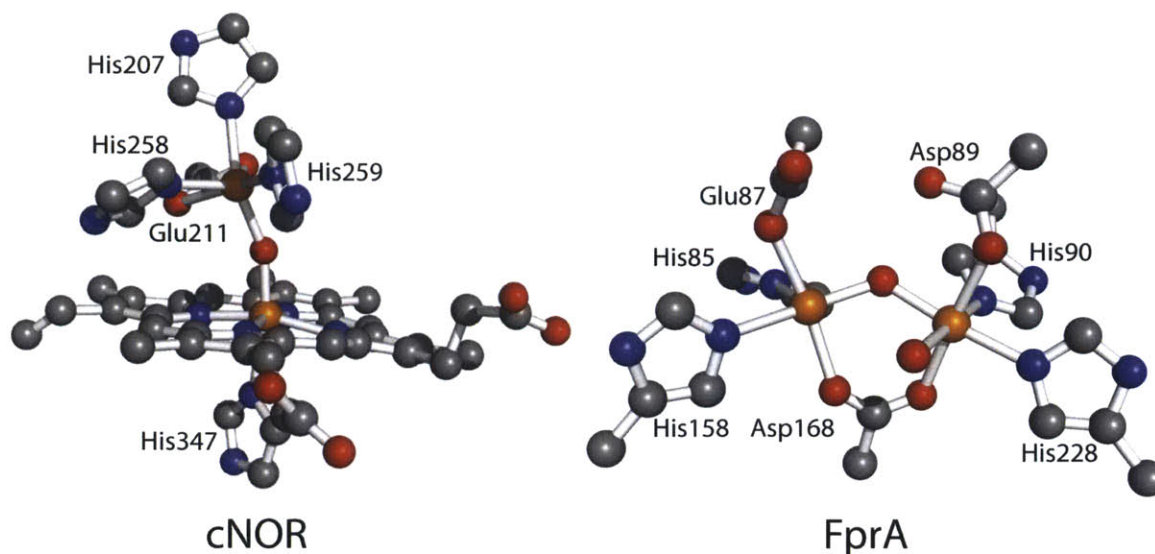
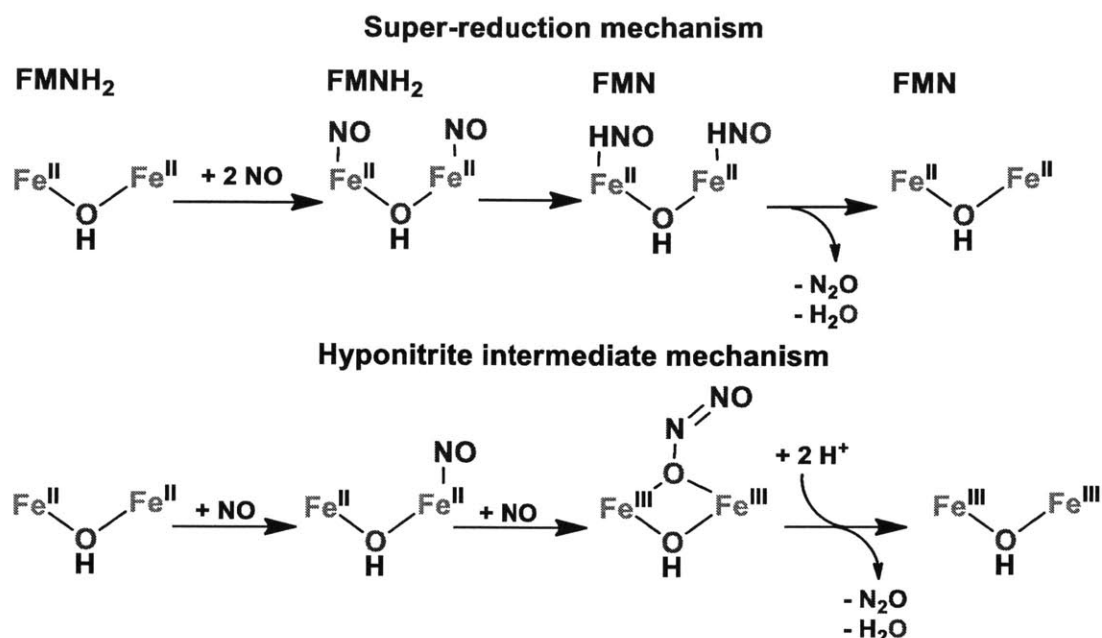


**Figure 1.6.** Diiron active sites of nitric oxide reductases from *Pseudomonas aeruginosa* (left; PDB: 3O0R) and *Thermotoga maritima* (right; PDB: 1VME). The active site of cNOR from *P. aeruginosa* consists of an Fe-heme-his and FeN<sub>3</sub>O<sub>2</sub> oxo-bridged active site. The FprA diiron active site of *T. maritima* consists of both an oxo-bridge as well as a carboxylate-bridge. In both NORs, the two irons have different coordination environments, and in the case of FprA may also have different coordination numbers.<sup>30,83</sup>

**1.5 Proposed flavodiiron nitric oxide reductase pathways.** The reduction mechanism of NO by FprA proteins has not been fully elucidated.<sup>29,30,78</sup> Two mechanistic pathways have been proposed and partially proven via biochemical methods (Scheme 1.2).<sup>30</sup> The super-reduction pathway involves concomitant binding of NO to both iron sites to form a diferrous-dinitrosyl species. The nitrosyls are protonated to nitroxyls, followed by N=N bond formation to yield N<sub>2</sub>O and H<sub>2</sub>O. In the hyponitrite intermediate pathway, NO initially binds to a single iron within the active site. An additional NO couples to the bound-NO to form an N=N bond and the oxygen forms a bridge to the second iron. N<sub>2</sub>O dissociation occurs, followed by protonation of the bridging oxygen to form and release H<sub>2</sub>O.



**Scheme 1.2.** Proposed reduction pathways of NO to N<sub>2</sub>O by FprA diiron proteins.<sup>30</sup>

**1.6 Synthetic flavodiiron nitric oxide reductase models.** Synthetic analogues capable of reproducing this chemistry have not been well explored. Our lab was the first to publish a carboxylate-bridged diiron(II)-dinitrosyl species, [Fe<sub>2</sub>(*N*-Et-HPTB)(O<sub>2</sub>CPh)(NO)<sub>2</sub>](BF<sub>4</sub>)<sub>2</sub>; the related compound [Fe<sub>2</sub>(BPMP)(O<sub>2</sub>Pr)(NO)<sub>2</sub>](BPh<sub>4</sub>)<sub>2</sub> was shown to form N<sub>2</sub>O upon bulk two-electron reduction, making it the first functional FprA model (Figure 1.7).<sup>84,85</sup> Our lab recently published the first synthetic diiron-mononitrosyl species [Fe<sub>2</sub>(*N*-Et-HPTB)(L)(NO)(DMF)<sub>2</sub>]<sup>3-</sup>, where L is either hydroxide or *N*-coordinated DMF.<sup>86</sup> This species was formed by the one-electron oxidation with NOBF<sub>4</sub> or by addition of ferrocenium and Ph<sub>3</sub>CSNO. A hydroxo-bridged tetra-iron-nitrosyl cube, Fe<sub>4</sub>(Mes<sub>2</sub>ArCO<sub>2</sub>)<sub>4</sub>(NO)(μ<sub>3</sub>-OH)<sub>4</sub>, forms upon addition of NO to a toluene solution containing FeOTf<sub>2</sub>, 2,6-dimesitylbenzoate, and water.<sup>87</sup> The [Fe<sub>4</sub>(OH)<sub>4</sub>] core resembles a [Fe<sub>4</sub>S<sub>4</sub>] cluster, but the iron atoms have an octahedral geometry instead of the typical tetrahedral geometry.

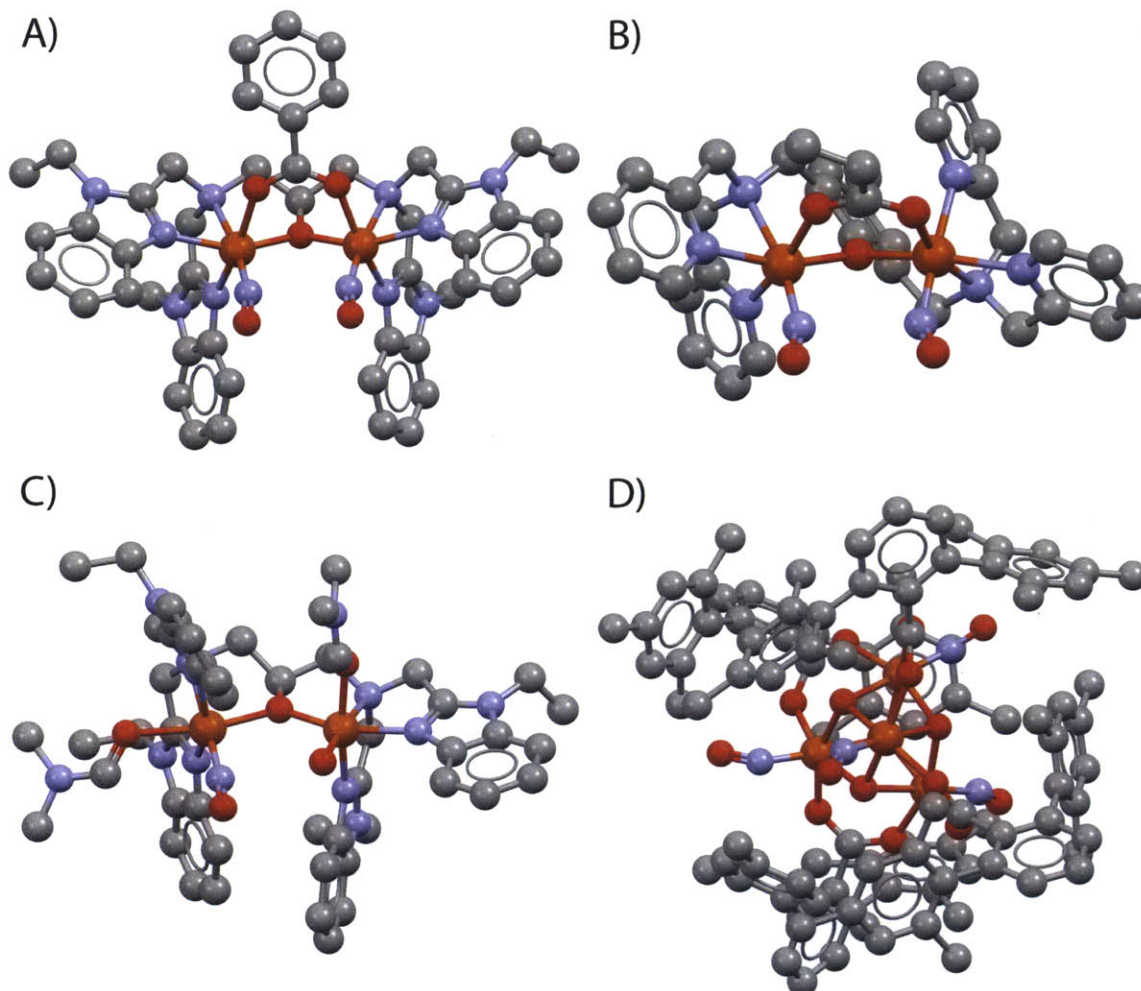


**Figure 1.7.** Ball-and-stick representation of the crystal structures of A)  $[\text{Fe}_2(\text{N-Et-HPTB})(\text{O}_2\text{CPh})(\text{NO})_2]^{2+}$ ,<sup>84</sup> B)  $[\text{Fe}_2(\text{BPMP})(\text{O}_2\text{Pr})(\text{NO})_2]^{2+}$ ,<sup>85</sup> C)  $[\text{Fe}_2(\text{N-Et-HPTB})(\text{L})(\text{NO})(\text{DMF})_2]^{3-}$ ,<sup>86</sup> and D)  $\text{Fe}_4(\text{Mes}_2\text{ArCO}_2)_4(\text{NO})(\mu_3\text{-OH})_4$ .<sup>87</sup> Color scheme: iron, orange; nitrogen, blue; oxygen, red; carbon; grey.

**1.7. Precious metals and nitric oxide.** The first crystallographically characterized bent metal-nitrosyl species was *trans*- $[\text{IrCl}(\text{CO})(\text{NO})(\text{PPh}_3)_2](\text{BF}_4)$  (Figure 1.8A).<sup>88,89</sup> This species was prepared by addition of 1.5 equiv of  $\text{NOBF}_4$  to Vaska's complex, *trans*- $[\text{IrCl}(\text{CO})(\text{PPh}_3)_2]$ . This species is thought to be formally Ir(III) by oxidative addition of  $\text{NO}^+$  to the Ir(I) starting material. Studies of Vaska's complex with  $\text{O}_2$  and  $\text{I}_2$  are also characterized to occur by oxidative addition of these substrates.<sup>90</sup> In all cases, the  $\nu_{\text{CO}}$  stretch increases in energy from  $1967\text{ cm}^{-1}$  to  $2015$

$\text{cm}^{-1}$  ( $\text{O}_2$ ),  $2050 \text{ cm}^{-1}$  ( $\text{NO}$ ), and  $2067 \text{ cm}^{-1}$  ( $\text{I}_2$ ), due to a decrease in  $\pi$ -backbonding of Ir to C upon oxidation from 1+ to 3+.

The first crystallographically characterized metal-SNO complex was *cis*- $[\text{RuCl}(\text{bpy})_2\{\text{N}(\text{O})\text{SO}_3\}]$  (Figure 1.8B).<sup>91</sup> Only spectroscopic characterization of similar complexes of iron or ruthenium are available owing to the instability of the formed complexes and their subsequent decomposition.<sup>92-94</sup> This ruthenium species provided the first structural evidence for the product formed in the analogous reaction of  $[\text{Fe}(\text{CN})_5(\text{NO})]^{2-}$  with  $\text{SO}_3^{2-}$ , originally reported by Boedeker in 1861 that forms a deep red solution.<sup>95</sup> It was later established by spectroscopic means that that the species is  $[\text{Fe}(\text{CN})_5\{\text{N}(\text{O})\text{SO}_3\}]^{4-}$ , but no structural characterization was performed.<sup>93</sup>

The first crystallographically characterized metal-bound organo-*S*-nitrosothiol was an iridium complex, *trans*- $\text{K}[\text{IrCl}_4(\text{CH}_3\text{CN})\{\text{N}(\text{O})\text{SCH}_2\text{Ph}\}]$  (Figure 1.8C).<sup>96</sup> This species was formed by addition of benzyl mercaptan to  $\text{K}[\text{IrCl}_5(\text{NO})]$  in acetonitrile to form the *S*-nitrosothiol. The formation of the *S*-nitrosothiol labilizes the *trans*-chloride and results in ligand metathesis with the solvent to release HCl. This method was employed to form analogous complexes using mercaptanobenzene, mercaptosuccinic acid, *N*-acetyl-L-cysteine, and L-cysteine ethyl ester, but these compounds were characterized only by  $^1\text{H}$  NMR and other spectroscopies.<sup>97</sup>



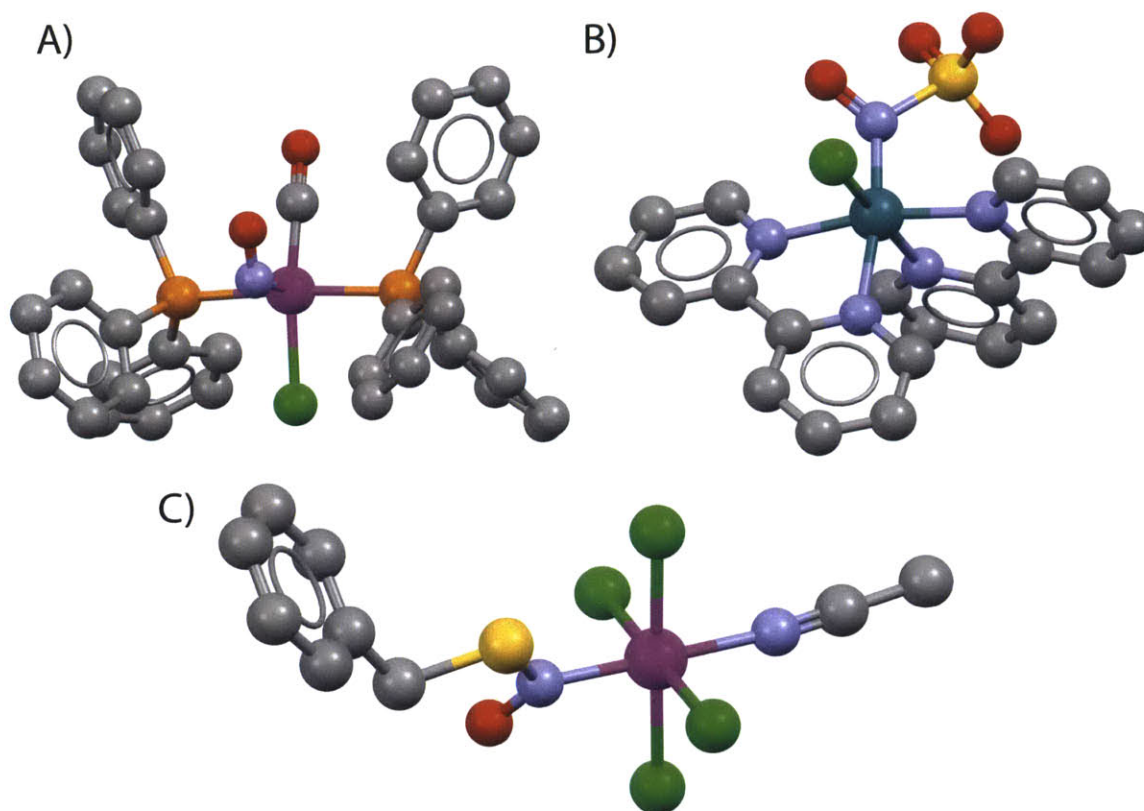


**Figure 1.8.** Ball-and-stick representation of the crystal structures of A) *trans*-[IrCl(CO)(NO)(PPh<sub>3</sub>)<sub>2</sub>]<sup>+</sup>,<sup>88</sup> B) *cis*-[RuCl(bpy)<sub>2</sub>{N(O)SO<sub>3</sub>}],<sup>91</sup> and C) *trans*-[IrCl<sub>4</sub>(CH<sub>3</sub>CN){N(O)SCH<sub>2</sub>Ph}]<sup>-</sup>.<sup>96</sup> Color scheme: iridium, magenta; ruthenium, dark green; chloride, light green; phosphorous, orange; sulfur, yellow; nitrogen, blue; oxygen, red; carbon, grey.

NO plays an important role in cisplatin, *cis*-[Pt(NH<sub>3</sub>)<sub>2</sub>Cl<sub>2</sub>], resistance of H-460 (human lung carcinoma) cells by *S*-nitrosating the protein Bcl-2.<sup>98</sup> H-460 cells express iNOS enzymes and produce NO to prevent apoptosis and promote tumor growth.<sup>99-101</sup> Bcl-2 suppresses cell death and is therefore targeted during the cellular pathway triggering apoptosis.<sup>102</sup> *S*-nitrosation of Bcl-2 prevents ubiquitin binding and the subsequent degradation of the protein by ubiquitin-proteasome.<sup>98</sup> Cisplatin-induced cell death also relies on formation of reactive oxygen species, which can react with NO and *S*-nitrosothiols to form less reactive species.<sup>103,104</sup> This behavior was also observed in human melanoma cell lines A375, which also express iNOS enzymes and maintain a nanomolar concentration of NO intracellularly.<sup>105</sup> *S*-nitrosation of caspase-3 in this

cell line interferes with apoptosis. In both cases, inhibition of iNOS activity or addition of NO scavengers increased cisplatin sensitivity.<sup>98,105</sup> No evidence in either study was presented for NO interacting directly with cisplatin to cause the displayed resistance.

**1.8. Conclusion.** NO and *S*-nitrosothiols play an important role in biology and bioinorganic chemistry. Further understanding their interactions with metal active sites requires multiple approaches. The approach taken in this thesis the use of small molecule analogues of iron-sulfur clusters, hemes, non-heme NORs, and a platinum complex, and studies of their reactivity toward NO and three *S*-nitrosothiols: Ph<sub>3</sub>CSNO, SSNO<sup>-</sup>, and SNO<sup>-</sup>.

## 1.7. References.

1. Torday, L. L.; Santillan, M. B.; Ciuffo, G. M.; Jauregui, E. A.; Pataricza, J.; Papp, J. G.; Csizmadia, I. G., *J. Mol. Struct. - Theochem* **1999**, *465*, 69.
2. Kochi, J. K., *Acc. Chem. Res.* **1992**, *25*, 39.
3. Bartberger, M. D.; Liu, W.; Ford, E.; Miranda, K. M.; Switzer, C.; Fukuto, J. M.; Farmer, P. J.; Wink, D. A.; Houk, K. N., *Proc. Natl. Acad. Sci. U.S.A.* **2002**, *99*, 10958.
4. Koshland, D., *Science* **1992**, *258*, 1861.
5. Furchgott, R. F., *Angew. Chem. Int. Ed.* **1999**, *38*, 1870.
6. Ignarro, L. J., *Angew. Chem. Int. Ed.* **1999**, *38*, 1882.
7. Murad, F., *Angew. Chem. Int. Ed.* **1999**, *38*, 1857.
8. Shiva, S., *Redox Biol.* **2013**, *1*, 40.
9. Bronte, V.; Zanovello, P., *Nat. Rev. Immunol.* **2005**, *5*, 641.
10. Calabrese, V.; Mancuso, C.; Calvani, M.; Rizzarelli, E.; Butterfield, D. A.; Stella, A. M., *Nat. Rev. Neurosci.* **2007**, *8*, 766.
11. Li, H.; Raman, C. S.; Glaser, C. B.; Blasko, E.; Young, T. A.; Parkinson, J. F.; Whitlow, M.; Poulos, T. L., *J. Biol. Chem.* **1999**, *274*, 21276.
12. Knowles, R. G.; Moncada, S., *Biochem. J.* **1994**, *298 (Pt 2)*, 249.
13. Rosenfeld, R. J.; Bonaventura, J.; Szymczyzna, B. R.; MacCoss, M. J.; Arvai, A. S.; Yates, J. R.; Tainer, J. A.; Getzoff, E. D., *J. Biol. Chem.* **2010**, *285*, 31581.
14. Szaciłowski, K.; Chmura, A.; Stasicka, Z., *Coord. Chem. Rev.* **2005**, *249*, 2408.
15. Andrew, P. J.; Mayer, B., *Cardiovasc. Res.* **1999**, *43*, 521.
16. Wasielewska, E.; Witko, M.; Stochel, G.; Stasicka, Z., *Chem. Eur. J.* **1997**, *3*, 609.
17. Stuehr, D. J., *Biochim. Biophys. Acta, Bioenerg.* **1999**, *1411*, 217.
18. Furchgott, R. F.; Vanhoutte, P. M., *FASEB J.* **1989**, *3*, 2007.
19. Ignarro, L. J.; Buga, G. M.; Wood, K. S.; Byrns, R. E.; Chaudhuri, G., *Proc. Natl. Acad. Sci. U.S.A.* **1987**, *84*, 9265.
20. Rapoport, R. M.; Draznin, M. B.; Murad, F., *Nature* **1983**, *306*, 174.
21. Ignarro, L. J., *Nitric Oxide: Biology and Pathobiology*. Academic Press: San Diego, 2000.
22. McCann, S. M., *Experimental Gerontology* **1997**, *32*, 431.
23. Guix, F. X.; Uribealago, I.; Coma, M.; Muñoz, F. J., *Prog. Neurobiol.* **2005**, *76*, 126.
24. Toda, N.; Ayajiki, K.; Okamura, T., *Pharmacol. Ther.* **2005**, *106*, 233.
25. Krumenacker, J. S.; Hanafy, K. A.; Murad, F., *Brain Res. Bull.* **2004**, *62*, 505.
26. Bogdan, C., *Nat. Immunol.* **2001**, *2*, 907.
27. Wink, D. A.; Mitchell, J. B., *Free Radical Biol. Med.* **1998**, *25*, 434.
28. Wasser, I. M.; de Vries, S.; Moënné-Loccoz, P.; Schröder, I.; Karlin, K. D., *Chem. Rev.* **2002**, *102*, 1201.
29. Kurtz, D. M., *Dalton Trans.* **2007**, 4115.
30. Hayashi, T.; Caranto, J. D.; Wampler, D. A.; Kurtz, D. M.; Moënné-Loccoz, P., *Biochemistry* **2010**, *49*, 7040.
31. Gobert, A. P.; McGee, D. J.; Akhtar, M.; Mendz, G. L.; Newton, J. C.; Cheng, Y.; Mobley, H. L. T.; Wilson, K. T., *Proc. Natl. Acad. Sci. U.S.A.* **2001**, *98*, 13844.
32. Gaston, B., *Biochim. Biophys. Acta, Bioenerg.* **1999**, *1411*, 323.
33. Howard-Flanders, P., *Nature* **1957**, *180*, 1191.

34. McCleverty, J. A., *Chem. Rev.* **2004**, *104*, 403.
35. Meyer, B., *Chem. Rev.* **1976**, *76*, 367.
36. Zhang, S.; Çelebi-Ölçüm, N.; Melzer, M. M.; Houk, K. N.; Warren, T. H., *J. Am. Chem. Soc.* **2013**, *135*, 16746.
37. Tennyson, A. G.; Dhar, S.; Lippard, S. J., *J. Am. Chem. Soc.* **2008**, *130*, 15087.
38. Ramachandran, N.; Root, P.; Jiang, X.-M.; Hogg, P. J.; Mutus, B., *Proc. Natl. Acad. Sci. U.S.A.* **2001**, *98*, 9539.
39. Singh, S. P.; Wishnok, J. S.; Keshive, M.; Deen, W. M.; Tannenbaum, S. R., *Proc. Natl. Acad. Sci. U.S.A.* **1996**, *93*, 14428.
40. Myers, P. R.; Minor, R. L.; Guerra, R.; Bates, J. N.; Harrison, D. G., *Nature* **1990**, *345*, 161.
41. Filipovic, M. R.; Miljkovic, J. L.; Nauser, T.; Royzen, M.; Klos, K.; Shubina, T.; Koppenol, W. H.; Lippard, S. J.; Ivanović-Burmazović, I., *J. Am. Chem. Soc.* **2012**, *134*, 12016.
42. Miljkovic, J. L.; Kenkel, I.; Ivanović-Burmazović, I.; Filipovic, M. R., *Angew. Chem. Int. Ed.* **2013**, *52*, 12061.
43. Chan, N.-L.; Rogers, P. H.; Arnone, A., *Biochemistry* **1998**, *37*, 16459.
44. Weichsel, A.; Maes, E. M.; Andersen, J. F.; Valenzuela, J. G.; Shokhireva, T. K.; Walker, F. A.; Montfort, W. R., *Proc. Natl. Acad. Sci. U.S.A.* **2005**, *102*, 594.
45. Tonzetich, Z. J.; McQuade, L. E.; Lippard, S. J., *Inorg. Chem.* **2010**, *49*, 6338.
46. Saini, V.; Farhana, A.; Glasgow, J. N.; Steyn, A. J. C., *Curr. Opin. Chem. Biol.* **2012**, *16*, 45.
47. Crack, J. C.; Green, J.; Thomson, A. J.; Le Brun, N. E., *Curr. Opin. Chem. Biol.* **2012**, *16*, 35.
48. Crack, J. C.; Green, J.; Hutchings, M. I.; Thomson, A. J.; Le Brun, N. E., *Antioxid. Redox Signaling* **2012**, *17*, 1215.
49. Vanin, A. F., *Nitric Oxide* **2009**, *21*, 1.
50. Vanin, A. F., *Biochemistry (Moscow)* **1998**, *63*, 782.
51. Cesareo, E.; Parker, L. J.; Pedersen, J. Z.; Nuccetelli, M.; Mazzetti, A. P.; Pastore, A.; Federici, G.; Caccuri, A. M.; Ricci, G.; Adams, J. J.; Parker, M. W.; Bello, M. L., *J. Biol. Chem.* **2005**, *280*, 42172.
52. Richardson, D. R.; Lok, H. C., *Biochim. Biophys. Acta* **2008**, *1780*, 638.
53. Harrop, T. C.; Tonzetich, Z. J.; Reisner, E.; Lippard, S. J., *J. Am. Chem. Soc.* **2008**, *130*, 15602.
54. Chen, Y.-J.; Ku, W.-C.; Feng, L.-T.; Tsai, M.-L.; Hsieh, C.-H.; Hsu, W.-H.; Liaw, W.-F.; Hung, C.-H.; Chen, Y.-J., *J. Am. Chem. Soc.* **2008**, *130*, 10929.
55. Tsai, F.-T.; Chiou, S.-J.; Tsai, M.-C.; Tsai, M.-L.; Huang, H.-W.; Chiang, M.-H.; Liaw, W.-F., *Inorg. Chem.* **2005**, *44*, 5872.
56. Lu, T.-T.; Huang, H.-W.; Liaw, W.-F., *Inorg. Chem.* **2009**, *48*, 9027.
57. Lu, T.-T.; Chiou, S.-J.; Chen, C.-Y.; Liaw, W.-F., *Inorg. Chem.* **2006**, *45*, 8799.
58. Kennedy, M. C.; Antholine, W. E.; Beinert, H., *J. Biol. Chem.* **1997**, *272*, 20340.
59. Dupuy, J.; Volbeda, A.; Carpentier, P.; Darnault, C.; Moulis, J. M.; Fontecilla-Camps, J. C., *Structure* **2006**, *14*, 129.
60. Robbins, A. H.; Stout, C. D., *Proc. Natl. Acad. Sci. U.S.A.* **1989**, *86*, 3639.
61. Rao, P. V.; Holm, R. H., *Chem. Rev.* **2004**, *104*, 527.
62. Drapier, J.-C., *Methods* **1997**, *11*, 319.

63. Beinert, H.; Kennedy, M. C.; Stout, C. D., *Chem. Rev.* **1996**, *96*, 2335.
64. Beinert, H.; Kennedy, M. C., *FASEB J.* **1993**, *7*, 1442.
65. Foster, M. W.; Cowan, J. A., *J. Am. Chem. Soc.* **1999**, *121*, 4093.
66. Han, D.; Canali, R.; Garcia, J.; Aguilera, R.; Gallaher, T. K.; Cadenas, E., *Biochemistry* **2005**, *44*, 11986.
67. Styś, A.; Galy, B.; Starzyński, R. R.; Smuda, E.; Drapier, J.-C.; Lipiński, P.; Bouton, C., *J. Biol. Chem.* **2011**.
68. Cruz-Ramos, H.; Crack, J.; Wu, G. G.; Hughes, M. N.; Scott, C.; Thomson, A. J.; Green, J.; Poole, R. K., *EMBO J.* **2002**, *21*, 3235.
69. Bang, I. S.; Liu, L. M.; Vazquez-Torres, A.; Crouch, M. L.; Stamler, J. S.; Fang, F. C., *J. Biol. Chem.* **2006**, *281*, 28039.
70. Crack, J. C.; Smith, L. J.; Stapleton, M. R.; Peck, J.; Watmough, N. J.; Buttner, M. J.; Buxton, R. S.; Green, J.; Oganessian, V. S.; Thomson, A. J.; Le Brun, N. E., *J. Am. Chem. Soc.* **2010**, *133*, 1112.
71. Watmough, N. J.; Butland, G.; Cheesman, M. R.; Moir, J. W.; Richardson, D. J.; Spiro, S., *Biochim. Biophys. Acta* **1999**, *1411*, 456.
72. Sarti, P.; Fiori, P. L.; Forte, E.; Rappelli, P.; Teixeira, M.; Mastronicola, D.; Sancier, G.; Giuffrè, A.; Brunori, M., *Cell. Mol. Life Sci.* **2004**, *61*, 618.
73. Gardner, A. M.; Helmick, R. A.; Gardner, P. R., *J. Biol. Chem.* **2002**, *277*, 8172.
74. Gomes, C. M.; Giuffrè, A.; Forte, E.; Vicente, J. B.; Saraiva, L. g. M.; Brunori, M.; Teixeira, M., *J. Biol. Chem.* **2002**, *277*, 25273.
75. Anjum, M. F.; Stevanin, T. M.; Read, R. C.; Moir, J. W. B., *J. Bacteriol.* **2002**, *184*, 2987.
76. Stevanin, T. M.; Moir, J. W. B.; Read, R. C., *Infect. Immun.* **2005**, *73*, 3322.
77. Moëgne-Loccoz, P.; Fee, J. A., *Science* **2010**, *330*, 1632.
78. Hayashi, T.; Caranto, J. D.; Matsumura, H.; Kurtz, D. M.; Moëgne-Loccoz, P., *J. Am. Chem. Soc.* **2012**, *134*, 6878.
79. Pooch, S. R.; Leach, E. R.; Moir, J. W.; Cole, J. A.; Richardson, D. J., *J. Biol. Chem.* **2002**, *277*, 23664.
80. Corker, H.; Poole, R. K., *J. Biol. Chem.* **2003**, *278*, 31584.
81. Silaghi-Dumitrescu, R.; Kurtz, D. M.; Ljungdahl, L. G.; Lanzilotta, W. N., *Biochemistry* **2005**, *44*, 6492.
82. Silaghi-Dumitrescu, R.; Coulter, E. D.; Das, A.; Ljungdahl, L. G.; Jameson, G. N.; Huynh, B. H.; Kurtz, D. M., Jr., *Biochemistry* **2003**, *42*, 2806.
83. Hino, T.; Matsumoto, Y.; Nagano, S.; Sugimoto, H.; Fukumori, Y.; Murata, T.; Iwata, S.; Shiro, Y., *Science* **2010**, *330*, 1666.
84. Feig, A. L.; Bautista, M. T.; Lippard, S. J., *Inorg. Chem.* **1996**, *35*, 6892.
85. Zheng, S.; Berto, T. C.; Dahl, E. W.; Hoffman, M. B.; Speelman, A. L.; Lehnert, N., *J. Am. Chem. Soc.* **2013**, *135*, 4902.
86. Majumdar, A.; Lippard, S. J., *Inorg. Chem.* **2013**, *52*, 13292.
87. Klein, D. P.; Young, V. G.; Tolman, W. B.; Que, L., *Inorg. Chem.* **2006**, *45*, 8006.
88. Hodgson, D. J.; Ibers, J. A., *Inorg. Chem.* **1968**, *7*, 2345.
89. Hodgson, D. J.; Payne, N. C.; McGinnety, J. A.; Pearson, R. G.; Ibers, J. A., *J. Am. Chem. Soc.* **1968**, *90*, 4486.
90. Crabtree, R. H., *The Organometallic Chemistry of the Transition Metals*. 5th ed.; John Wiley & Sons, Inc.: 2009; p 505.

91. Bottomley, F.; Brooks, W. V. F.; Paez, D. E.; White, P. S.; Mukaida, M., *J. Chem. Soc., Dalton Trans.* **1983**, 2465.
92. Swinehart, J. H., *Coord. Chem. Rev.* **1967**, 2, 385.
93. Moser, W.; Chalmers, R. A.; Fogg, A. G., *J. Inorg. Nucl. Chem.* **1965**, 27, 831.
94. Hofmann, K. A., *Z. Anorg. Chem.* **1896**, 11, 31.
95. Boedeker, C., *Liebigs Ann. Chem.* **1861**, 117, 193.
96. Perissinotti, L. L.; Estrin, D. A.; Leitun, G.; Doctorovich, F., *J. Am. Chem. Soc.* **2006**, 128, 2512.
97. Perissinotti, L. L.; Leitun, G.; Shimon, L.; Estrin, D.; Doctorovich, F., *Inorg. Chem.* **2008**, 47, 4723.
98. Chanvorachote, P.; Nimmannit, U.; Stehlik, C.; Wang, L.; Jiang, B.-H.; Ongpipatanakul, B.; Rojanasakul, Y., *Cancer Res.* **2006**, 66, 6353.
99. Kolb, J. P., *Leukemia* **2000**, 14, 1685.
100. Liu, C. Y.; Wang, C. H.; Chen, T. C.; Lin, H. C.; Yu, C. T.; Kuo, H. P., *Br. J. Cancer* **1998**, 78, 534.
101. Puhakka, A.; Kinnula, V.; Näpänkangas, U.; Säily, M.; Koistinen, P.; Pääkkö, P.; Soini, Y., *APMIS* **2003**, 111, 1137.
102. Xie, K.; Huang, S., *Free Radical Biol. Med.* **2003**, 34, 969.
103. Miyajima, A.; Nakashima, J.; Yoshioka, K.; Tachibana, M.; Tazaki, H.; Murai, M., *Br. J. Cancer* **1997**, 76, 206.
104. Schweyer, S.; Soruri, A.; Heintze, A.; Radzun, H. J.; Fayyazi, A., *Int. J. Oncol.* **2004**, 25, 1671.
105. Godoy, L. C.; Anderson, C. T. M.; Chowdhury, R.; Trudel, L. J.; Wogan, G. N., *Proc. Natl. Acad. Sci. U.S.A.* **2012**, 109, 20373.

**CHAPTER 2: RAPID NITRIC OXIDE AND  
NITROGEN DIOXIDE DETECTION AND  
QUANTIFICATION ASSAYS AND DEVICES  
BASED ON M(BIPhMe)<sub>2</sub> COMPLEXES**

## 2.1 Introduction.

It is often desirable to observe and quantify the release of NO (g) or NO<sub>2</sub> (g) from a reaction, both in biology and chemistry. There currently exist multiple methods to perform these experiments either using electrochemistry or spectroscopy.

Electrochemical methods oxidize NO• to NO<sup>+</sup> and monitor the change in amperage using Clark electrode.<sup>1</sup> These setups can provide solution concentrations of NO•, but cannot measure the release of NO (g) to the surrounding headspace and require an additional instrument that may not be commonly available or can alter the observed reaction.

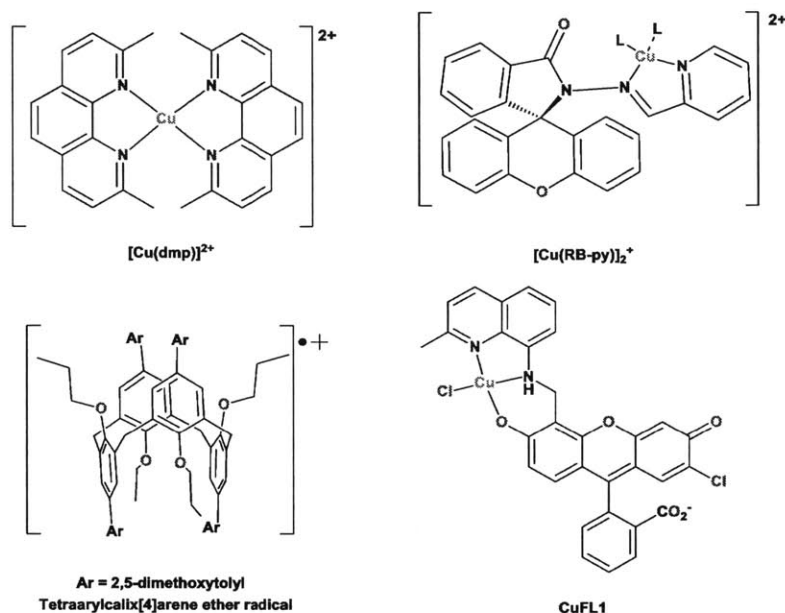
[Fe<sup>II</sup>(porphyrin)] compounds have been used to detect and quantify the release of NO (g) by IR, UV-Vis, and EPR spectroscopy follow capture as [Fe<sup>II</sup>(porphyrin)(NO)].<sup>2,3</sup> These methods provide a rapid method to detect the release of NO (g) using instruments available in most chemistry departments, but, due to the strong intensity of porphyrin absorbance bands, do not provide a rapid method for observing the release by the naked eye.

Commercial NO colorimetric detection kits are available, however, which indirectly measure NO by oxidation to a higher NO<sub>x</sub> species and subsequently quantification of the concentration of nitrate and nitrite present in solution using the Griess reagent.<sup>4,5</sup> This method can result in incorrect measurements due to NO<sub>2</sub><sup>-</sup> contamination or loss of NO (g) to the surrounding headspace.

The complexes [Cu(dmp)<sub>2</sub>]<sup>2+</sup> and [Cu(RB-Py)]<sup>2+</sup>, and a tetraarylcalix[4]arene ether radical (Scheme 2.1), exhibit colorimetric responses upon NO• exposure.<sup>6-8</sup> The mechanism of response of the Cu<sup>2+</sup> complexes occurs by reduction to Cu<sup>+</sup>, resulting in a change from pale green to bright yellow/orange and colorless to pink, respectively for the two compounds noted.



This response mechanism is similar to that of the fluorescent NO probe CuFL1.<sup>9,10</sup> The tetraarylcallyx[4]arene radical binds NO<sup>•</sup>, eliciting a color change from bright green to dark blue.



**Scheme 2.1.** Known colorimetric and fluorescent probes to detect NO<sup>•</sup>.

In the present work we report a set of colorimetric sensors (Figure 2.1) using Fe<sup>2+</sup> and Co<sup>2+</sup> halide complexes of *bis*-(1-methylimidazol-2-yl)phenylmethoxymethane, BIPhMe, which is a *bis*-N donor ligand.<sup>11</sup> The NO (g) and NO<sub>2</sub> (g) chemistry of these complexes was explored, and they were characterized by X-ray crystallography, ESI-MS spectrometry, and FT-IR, UV-Vis, EPR, and <sup>1</sup>H NMR spectroscopy. We developed these compounds into colorimetric test strips and headspace analyzers capable of providing simple and rapid methods to observe the release of NO (g) and NO<sub>2</sub> (g) from chemical and biological reactions.

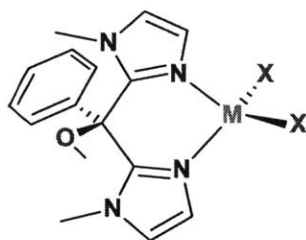


**Figure 2.1.** Metal-halide complexes of the *bis*-N donor BIPhMe, where M = Fe<sup>2+</sup> or Co<sup>2+</sup>, and X = Cl<sup>-</sup>, Br<sup>-</sup>, or I<sup>-</sup>.

### 3.2 Experimental Methods

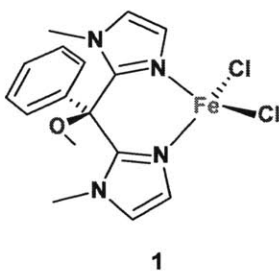
**General.** All manipulations were performed under an atmosphere of nitrogen gas using standard Schlenk techniques or in an MBraun glovebox under an atmosphere of purified nitrogen. NO (Airgas, 99%) was purified by a literature procedure.<sup>12</sup> The NO gas stream was passed through an Ascarite column (NaOH fused on silica gel) and a 6 ft. coil filled with silica gel that was cooled to  $-78\text{ }^{\circ}\text{C}$  using a dry ice/acetone bath. Nitric oxide was stored using standard gas bulbs and transferred via gastight syringes. Diethyl ether, pentane, methylene chloride, and acetonitrile were purified using a Glass Contour solvent system.<sup>13</sup> Deuterated solvents were purchased from Cambridge Isotope Labs Inc. (Tewksbury, MA). BIPhMe was synthesized according to a literature procedure.<sup>11</sup> All organic chemicals were purchased from Sigma-Aldrich and used as received. Metal salts were purchased from Strem Chemicals and used as received.

**Physical Measurements.** NMR spectra were recorded on a Bruker Avance spectrometer operating at 400 MHz at ambient temperature and referenced to residual signals in the deuterated solvent. MALDI-TOF mass spectra were obtained with a Bruker Omnix MALDI-TOF with a Reflectron accessory. Low-resolution ESI mass spectra were obtained with an Agilent 1100 Series LC/MSD mass spectrometer using degassed acetonitrile as the carrier solvent. FT-IR spectra were recorded on a Thermo Nicolet Avatar 360 spectrometer running the OMNIC software package; solid samples were pressed into KBr disks and solution samples were prepared in an airtight Graseby-Specac solution cell with  $\text{CaF}_2$  windows and 0.1 mm spacers.

**Mössbauer Measurements.** Samples for  $^{57}\text{Fe}$  Mössbauer studies were prepared by grinding a solid sample with Apiezon-N grease. These  $^{57}\text{Fe}$  Mössbauer samples were placed in an 80 K cryostat during measurement. A  $^{57}\text{Co/Rh}$  source was moved at a constant acceleration at room temperature against the absorber sample. All isomer shift ( $\delta$ ) and quadrupole splitting ( $\Delta E_Q$ )

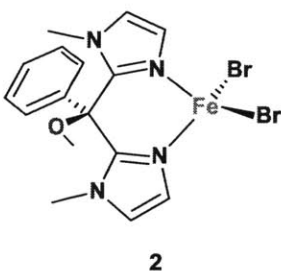
values are reported with respect to  $^{57}\text{Fe}$ -enriched metallic iron foil that was used for velocity calibration. The displayed spectrum was folded to enhance the signal-to-noise ratio. Fits of the data were calculated by the *WMOSS* plot-and-fit program, version 2.5.<sup>14</sup>

**X-ray Data Collection, Structure, and Solution Refinement.** Crystals of **1** – **9** suitable for X-ray diffraction were mounted in Paratone N oil and frozen under a nitrogen cold stream maintained at 100 K by a KRYO-FLEX low-temperature apparatus. Data were collected on a Bruker APEX CCD X-ray diffractometer with Mo  $K\alpha$  radiation ( $\lambda = 0.71073 \text{ \AA}$ ) controlled by the *APEX2* software package.<sup>15</sup> Empirical absorption corrections were calculated with *SADABS*.<sup>16</sup> The structures were solved by direct methods with refinement by full-matrix least-squares based on  $F^2$  using *SHELXTL-97*.<sup>17,18</sup> All non-hydrogen atoms were located and refined anisotropically. Hydrogen atoms were assigned to idealized positions and given thermal parameters equal to either 1.5 (methyl hydrogen atoms) or 1.2 (non-methyl hydrogen atoms) times the thermal parameters of the atoms to which they were attached. Figures were generated using the *Olex2.1* Graphical User Interface.<sup>19</sup> See Tables 2.2, 2.3, 2.5, and 2.7 below for crystallographic data and refinement details.



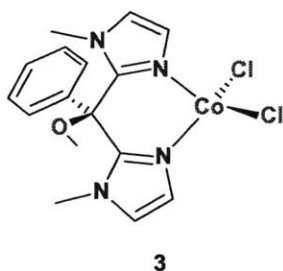
**Fe(BIPhMe)Cl<sub>2</sub>, 1.** A 50 mL Erlenmeyer flask was charged with  $\text{FeCl}_2 \cdot 4\text{H}_2\text{O}$  (227.5 mg, 1.144 mmol) and BIPhMe (336.0 mg, 1.190 mmol). Tetrahydrofuran (20 mL) was added to the flask and the reacting solution was stirred for 1 h, during which time a white precipitate formed. The precipitate was filtered and the solid was washed with tetrahydrofuran (3 x 10 mL) and diethyl

ether (3 x 20 mL), and dried in vacuo. The solid was collected to yield 417.6 mg (1.021 mmol, 74%) of **1**. X-ray quality crystals were grown by vapor diffusion of diethyl ether into a methylene chloride solution of **1**. Anal. Calc'd for C<sub>16</sub>H<sub>18</sub>Cl<sub>2</sub>FeN<sub>4</sub>O: C, 46.98; H, 4.43; N, 13.70. Found: C, 47.12; H, 4.45; N, 13.51. MALDI-TOF MS (anthracene, m/z): 408.17 (calc'd [M]<sup>+</sup>: 408.02), 373.12 (calc'd [M-Cl]<sup>+</sup>: 373.05). ESI-MS (MeCN, m/z): 373.1 (calc'd [M-Cl]<sup>+</sup>: 373.1), 655.2 (calc'd [M+BIPhMe-Cl]<sup>+</sup>: 655.2). <sup>1</sup>H NMR (400 MHz, CDCl<sub>3</sub>, ppm): 1.88 (s), 3.77 (s), 9.42 (s), 10.93 (s), 18.82 (s), 21.90 (br), 29.15 (s), 37.27 (s). FT-IR (KBr, cm<sup>-1</sup>): 3156 (w), 3139 (w), 3118 (m), 3067 (w), 3009 (w), 2954 (m), 2834 (m), 1630 (w), 1603 (w), 1541 (m), 1500 (s), 1470 (m), 1449 (s), 1400 (m), 1350 (w), 1323 (m), 1284 (s), 1225 (w), 1212 (w), 1174 (m), 1174 (s), 1146 (s), 1090 (sh), 1071 (s), 1032 (w), 990 (s), 940 (w), 898 (s), 760 (s), 733 (s), 703 (s), 688 (w), 645 (m), 558 (w), 512 (w), 465 (w). <sup>57</sup>Mössbauer (mm/s) (80 K, δ mm/s, ΔE<sub>Q</sub> mm/s, Γ mm/s): 0.929(2), 3.127(2), 0.354(2).



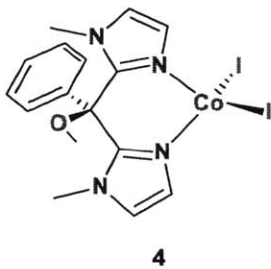
**Fe(BIPhMe)Br<sub>2</sub>, 2.** In a 20 mL vial FeBr<sub>2</sub> (330.2 mg, 1.531 mmol) was dissolved in THF (10 mL) and a solution of BIPhMe (422.0 mg, 1.495 mmol) in tetrahydrofuran (10 mL) was added dropwise over one min. The solution was stirred for 1 h, during which time a pale brown precipitate formed and was collected on an F-grade frit. The precipitate was washed with THF (3 x 10 mL), diethyl ether (3 x 20 mL), dried in vacuo and collected to yield 569.1 mg (1.143 mmol, 77 %) of **2**. X-ray quality crystals were grown by vapor diffusion of diethyl ether into a

methylene chloride solution of **2**. Anal. Calc'd for  $C_{16}H_{18}Br_2FeN_4O$ : C, 38.59; H, 3.64; N, 11.25. Found: C, 38.39; H, 3.34; N, 11.06. ESI-MS (MeCN, m/z): 417.0 (calc'd  $[M-Br]^+$ : 417.0), 699.2 (calc'd  $[M+BIPhMe-Br]^+$ : 699.1).  $^1H$  NMR (400 MHz,  $CDCl_3$ , ppm): 2.82 (br), 9.72 (s), 11.03 (s), 23.09 (br), 23.36 (s), 33.59 (s), 38.54 (s). FT-IR (KBr,  $cm^{-1}$ ): 3153 (w), 3143 (w), 3120 (m), 3056 (w), 3005 (w), 2954 (w), 2833 (w), 1709 (w), 1691 (w), 1603 (m), 1542 (m), 1498 (s), 1468 (m), 1448 (s), 1398 (w), 1349 (w), 1322 (w), 1284 (s), 1225 (w), 1212 (w), 1174 (m), 1145 (m), 1089 (m), 1070 (s), 988 (s), 939 (w), 898 (s), 759 (s), 723 (s), 702 (s), 645 (m), 627 (w), 556 (w), 511 (w), 465 (w).  $^{57}Mössbauer$  (mm/s) (80 K,  $\delta$  mm/s,  $\Delta E_Q$  mm/s,  $\Gamma$  mm/s): 0.901(2), 3.322(2), 0.255(2).



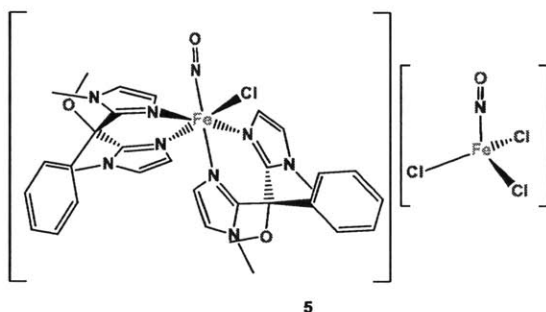
**Co(BIPhMe)Cl<sub>2</sub>, 3.** To a 20 mL vial anhydrous  $CoCl_2$  (212.0 mg, 1.633 mmol) and BIPhMe (460.0 mg, 1.629 mmol) was added. The mixture was dissolved in a mixture of tetrahydrofuran (12 mL) and methylene chloride (4 mL). The solution was stirred for 1 h, resulting in a deep blue precipitate. The precipitate was collected by filtration, washed with tetrahydrofuran (2 x 5 mL) and diethyl ether (3 x 20 mL), and dried in vacuo to afford 619.6 mg (1.503 mmol, 92 %) of **3**. X-ray quality crystals of **3** were grown by vapor diffusion of diethyl ether into an acetonitrile solution. Anal. Calc'd for  $C_{16}H_{18}Cl_2CoN_4O$ : C, 46.62; H, 4.40; N, 13.59. Found: C, 46.28; H, 4.15; N, 13.39. ESI-MS (MeCN, m/z): 376.1 (calc'd  $[M-Cl]^+$ : 376.1), 658.3 (calc'd  $[M+BIPhMe-Cl]^+$ : 658.2).  $^1H$  NMR (400 MHz,  $CDCl_3$ , ppm): 9.12 (s, 1H), 10.56 (s, 2H), 13.08

(s, 3H), 17.75 (s, 6H), 19.70 (br, 1H), 33.78 (s, 2H), 37.93 (br, 2H). FT-IR (KBr,  $\text{cm}^{-1}$ ): 3143 (w), 3116 (m), 3056 (w), 2999 (w), 2956 (m), 2928 (w), 2889 (w), 2823 (w), 1679 (w), 1594 (w), 1533 (w), 1493 (s), 1461 (m), 1446 (s), 1393 (w), 1348 (w), 1317 (w), 1283 (s), 1222 (m), 1207 (w), 1182 (m), 1168 (m), 1142 (m), 1085 (s), 1066 (s), 1031 (w), 985 (s), 949 (w), 932 (w), 891 (s), 841 (w), 755 (s), 719 (s), 702 (s), 642 (m), 554 (w), 508 (w), 461 (w). UV-Vis (MeCN, nm,  $\epsilon$ ,  $\text{M}^{-1}\text{cm}^{-1}$ ): 531 ( $155 \pm 4$ ), 555( $259 \pm 5$ ), 611( $422 \pm 5$ ), 631( $490 \pm 4$ ).

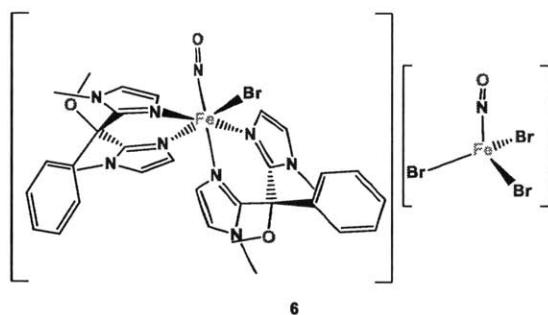


**Co(BIPhMe)I<sub>2</sub>, 4.** To a 50 mL Erlenmeyer flask, anhydrous CoI<sub>2</sub> (325.5 mg, 1.041 mmol) and BIPhMe (306.6 mg, 1.083 mmol) was added. The mixture was dissolved in a mixture of tetrahydrofuran (20 mL) and methylene chloride (2 mL). The solution was stirred for 1 h, resulting in a green solution. Pentanes (30 mL) were added to precipitate the product as a green microcrystalline solid. The precipitate was filtered, washed with pentanes (3 x 10 mL), and dried under vacuum for 5 h, affording 579.8 mg (0.973 mmol, 93 %) of **4**. X-ray quality crystals of **4** were grown by vapor diffusion of diethyl ether into the methylene chloride solution. Anal. Calc'd for C<sub>16</sub>H<sub>18</sub>I<sub>2</sub>CoN<sub>4</sub>O: C, 32.29; H, 3.05; N, 9.41. Found: C, 31.98; H, 2.81; N, 9.32. ESI-MS (MeCN, m/z): 750.2 (calc'd [M+BIPhMe-I]<sup>+</sup>: 750.1), 468.0 (calc'd [M-I]<sup>+</sup>: 468.0), 579.6 (calc'd [M-CH<sub>3</sub>]<sup>-</sup>: 579.9), 126.8 (calc'd [I]<sup>-</sup>: 126.9). <sup>1</sup>H NMR (400 MHz, CDCl<sub>3</sub>, ppm): 9.60 (s, 1H), 11.20 (s, 2H), 17.01 (s, 2H), 22.30 (s, 6H), 28.13 (br, 1H), 34.64 (s, 2H). FT-IR (KBr,  $\text{cm}^{-1}$ ): 3162 (w), 3130 (m), 3079 (w), 2973 (w), 2928 (w), 2898 (w), 2863 (w), 2829 (w), 1649 (w), 1550 (w), 1505 (s), 1449 (m), 1408 (w), 1355 (w), 1285 (s), 1224 (m), 1150 (s), 1090 (m),

1072 (m), 1031 (s), 992 (m), 938 (w), 900 (m), 762 (s), 725 (s), 704 (m), 637 (s), 572 (m), 517 (m), 472 (w). UV-Vis (MeCN, nm,  $\epsilon$ ,  $M^{-1}cm^{-1}$ ): 310 ( $2123 \pm 105$ ), 373 ( $1506 \pm 69$ ), 583 ( $289 \pm 16$ ), 607 ( $424 \pm 21$ ), 639 ( $596 \pm 28$ ), 668 ( $449 \pm 22$ ).

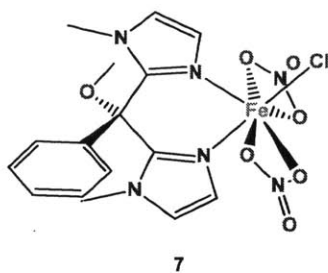


**[Fe(BIPhMe)<sub>2</sub>(NO)Cl][Fe(NO)Cl<sub>3</sub>], 5.** In a 20 mL vial, **1** (58.2 mg, 0.143 mmol) was dissolved in methylene chloride (2 mL). The reaction vessel was capped with a rubber septum and NO (g) (7.5 mL, 0.30 mmol) was injected under vigorous stirring. The solution instantly turned from colorless to dark green. The solution was stirred for an additional 1 h and filtered through glass microfiber filter paper. X-ray quality crystals of the product were formed upon vapor diffusion of diethyl ether over the course of 2 days. These dark green crystals were collected by filtration and washed with diethyl ether (3 x 5 mL), resulting in a yield of 41.6 mg (47.4  $\mu$ mol, 33%) of **5**. Anal. Calc'd for C<sub>32</sub>H<sub>36</sub>Cl<sub>4</sub>Fe<sub>2</sub>N<sub>10</sub>O<sub>4</sub>: C, 43.77; H, 4.13; N, 15.95. Found: C, 43.42; H, 4.34; N, 16.13. ESI-MS (MeCN, m/z): 655.2 ([CAT-NO]<sup>+</sup>, calc'd 655.2), 125.8 ([AN-NOCl]<sup>-</sup>, calc'd 125.9), 160.6 ([AN-NO]<sup>-</sup>, calc'd 160.8). FT-IR (KBr, cm<sup>-1</sup>): 3121 (m), 3054 (w), 2958 (m), 2928 (m), 2829 (w), 1792 ( $\nu_{NO}$ ), 1709 ( $\nu_{NO}$ ), 1656 (s), 1606 (w), 1542 (w), 1498 (s), 1468 (w), 1448 (m), 1400 (w), 1351 (w), 1322 (w), 1282 (s), 1226 (w), 1171 (m), 1143 (m), 1089 (m), 1072 (s), 1032 (w), 988 (s), 935 (w), 898 (s), 761 (s), 723 (s), 702 (s), 644 (m), 510 (w), 466 (w). UV-Vis (MeCN, nm,  $\epsilon$ ,  $M^{-1}cm^{-1}$ ): 363 ( $850 \pm 40$ ), 473 ( $340 \pm 30$ ), 699 ( $220 \pm 10$ ).

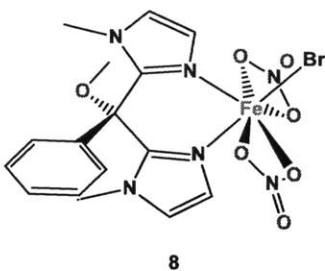


**[Fe(BIPhMe)<sub>2</sub>(NO)Br][Fe(NO)Br<sub>3</sub>], 6.** In a 20 mL vial, **2** (20.4 mg, 0.0371 mmol) was dissolved in methylene chloride (2 mL). The reaction vessel was capped with a rubber septum and NO (g) (3.7 mL, 0.15 mmol) was injected under vigorous stirring. The solution instantly turned from colorless to dark red. The solution was stirred for an additional hour and filtered through a piece of glass microfiber filter paper. Dark red crystals were grown by vapor diffusion of diethyl ether into the methylene chloride solution, collected by filtration, and washed with diethyl ether (3 x 5 mL), resulting in a yield of 7.2 mg (6.8 μmol, 18%) of **6**. Anal. Calc'd for C<sub>32</sub>H<sub>36</sub>Br<sub>4</sub>Fe<sub>2</sub>N<sub>10</sub>O<sub>4</sub>: C, 36.40; H, 3.44; N, 13.26. Found: C, 36.55; H, 3.57; N, 13.33. ESI-MS (MeCN, m/z): 701.1 ([Cat-NO]<sup>+</sup>, calc'd 701.2), 213.6 ([An-NOBr]<sup>-</sup>, calc'd 213.8), 296.5 ([An-NO]<sup>-</sup>, calc'd 296.7). FT-IR (KBr, cm<sup>-1</sup>): 3120 (m), 3061 (w), 3006 (w), 2955 (m), 2928 (m), 2829 (m), 1791 (ν<sub>NO</sub>), 1705 (ν<sub>NO</sub>), 1656 (m), 1597 (w), 1542 (w), 1497 (s), 1468 (m), 1448 (m), 1399 (w), 1350 (w), 1322 (w), 1282 (s), 1226 (w), 1208 (w), 1171 (m), 1143 (m), 1089 (m), 1071 (s), 1032 (w), 988 (s), 935 (w), 897 (s), 761 (s), 723 (s), 702 (m), 645 (m), 557 (w), 510 (w), 466 (w). UV-Vis (MeCN, nm, ε, M<sup>-1</sup>cm<sup>-1</sup>): 370 (2780 ± 200), 490 (750 ± 30), 701 (360 ± 20).





**Synthesis of Fe(BIPhMe)(NO<sub>3</sub>)<sub>2</sub>Cl, 7.** In a 20 mL vial, **1** (20.0 mg, 0.0489 mmol) was dissolved in methylene chloride (2 mL). The reaction vessel was capped with a rubber septum and NO<sub>2</sub>(g) (3.7 mL, 0.15 mmol) was injected under vigorous stirring. The solution instantly turned from colorless to yellow. The solution was stirred for an additional hour and filtered through a piece of glass filter paper in a Pasteur pipette. X-ray quality crystals of the product were formed upon vapor diffusion of diethyl ether over the course of 2 days. The crystals were collected by filtration and washed with diethyl ether (3 x 5 mL), resulting in a yield of 9.7 mg (0.018 mmol, 37 %) of **7**. Anal. Calc'd for C<sub>16</sub>H<sub>18</sub>ClFeN<sub>6</sub>O<sub>7</sub>: C, 38.62; H, 3.65; N, 16.89. Found: C, 38.79; H, 3.81; N, 16.90. ESI-MS (MeCN, m/z): 682.2 (calc'd [M+BIPhMe-NO<sub>3</sub>-Cl]<sup>+</sup>: 682.2), 655.2 (calc'd [M+BIPhMe-2NO<sub>3</sub>]<sup>+</sup>: 655.2). FT-IR (KBr, cm<sup>-1</sup>): 3120 (m), 3058 (w), 2997 (w), 2954 (m), 2931 (m), 2824 (w), 1653 (w), 1546 (w), 1493 (s), 1467 (s), 1448 (m), 1384 (m), 1352 (m), 1282 (w), 1227 (w), 1208 (m), 1169 (w), 1153 (w), 1132 (m), 1090 (m), 1073 (m), 1032 (w), 987 (m), 949 (w), 936 (w), 900 (s), 846 (m), 761 (s), 722 (s), 702 (s), 644 (w), 556 (w), 511 (w). UV-Vis (MeCN, nm, ε, M<sup>-1</sup>cm<sup>-1</sup>): 335 (570 ± 40).

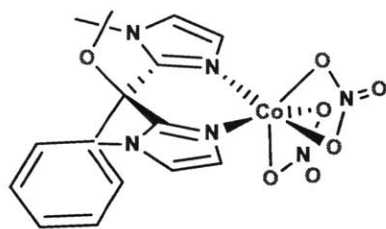


**Synthesis of Fe(BIPhMe)(NO<sub>3</sub>)<sub>2</sub>Br, 8.** In a 20 mL vial, **2** (20.0 mg, 0.0489 mmol) was dissolved in methylene chloride (2 mL). The reaction vessel was capped with a rubber septum and NO<sub>2</sub>(g) (3.7 mL, 0.15 mmol) was injected under vigorous stirring. The solution instantly turned from colorless to yellow. The solution was stirred for an additional hour and filtered through a piece of glass filter paper in a Pasteur pipette. The crystals were collected by filtration and washed with diethyl ether (3 x 5 mL), resulting in a yield of 9.7 mg (0.018 mmol, 37 %) of **8**. Anal. Calc'd for C<sub>16</sub>H<sub>18</sub>ClFeN<sub>6</sub>O<sub>7</sub>: C, 38.62; H, 3.65; N, 16.89. Found: C, 38.79; H, 3.81; N, 16.90. ESI-MS (MeCN, m/z): 701.1 (calc'd [M+BIPhMe-2NO<sub>3</sub>]<sup>+</sup>: 701.1), 682.1 (calc'd [M+BIPhMe-NO<sub>3</sub>-Br]<sup>+</sup>: 682.2). FT-IR (KBr, cm<sup>-1</sup>): 3129 (m), 3062 (w), 2997 (w), 2954 (m), 2929 (m), 2829 (w), 1635 (w), 1545 (w), 1495 (s), 1468 (m), 1448 (m), 1384 (s), 1353 (s), 1282 (s), 1169 (m), 1154 (m), 1134 (m), 1090 (m), 1072 (s), 1032(w), 897 (m), 932 (w), 899 (s), 834 (m), 760 (s), 721 (s), 702 (m), 634 (w), 555 (w), 511 (w). UV-Vis (MeCN, nm): 290 (5800 ± 300), 360 (3500 ± 220).

**Reaction of Co(BIPhMe)Cl<sub>2</sub> and NO<sub>2</sub>(g).** In a 20 mL vial **3** (27.7 mg, 0.0672 mmol) was dissolved in methylene chloride (2 mL). The reaction vessel was capped with a rubber septum and NO<sub>2</sub> (g) injected until no further color change was observed. The solution turned from deep blue to dark green. The solution was stirred for 1 h and subsequently filtered through glass microfiber filter paper. The product was precipitated by addition of diethyl ether (10 mL), collected by filtration, and dried under vacuum. The final product was a dark green solid and the

collected yield was 17 mg. The exact structure of the product is currently unknown. ESI-MS (m/z): 660.7 (calc'd  $[\text{Co}(\text{BIPhMe})_2\text{H}_2\text{Cl}]^+$ : 660.2); 685.4 (calc'd  $[\text{Co}(\text{BIPhMe})_2\text{NO}_3]^+$ : 685.2); 780.3 (calc'd  $[\text{Co}_2(\text{BIPhMe})(\text{NO}_3)\text{HCl}]^+$ : 780.1). FT-IR (KBr,  $\text{cm}^{-1}$ ): 3122 (m), 3058 (w), 2997 (w), 2935 (m), 2830 (w), 1652 (w), 1501 (s), 1471 (m), 1448 (s), 1385 (m), 1314 (s), 1286 (s), 1169 (s), 1149 (s), 1090 (m), 1072 (s), 1033 (w), 992 (s), 960 (w), 899 (s), 819 (m), 760 (s), 721 (s), 703 (s), 644 (m), 556 (w), 510 (w).

**Reaction of  $\text{Co}(\text{BIPhMe})\text{I}_2$  and NO (g).** In a 20 mL vial, **4** (44.5 mg, 0.0748 mmol) was dissolved in tetrahydrofuran (2 mL). The reaction vessel was capped with a rubber septum and NO (g) injected until no further color change was observed. The solution turned from emerald green to dark green. The solution was stirred for 1 h and subsequently filtered through glass microfiber filter paper. The product was precipitated by addition of diethyl ether (10 mL), collected by filtration, and dried under vacuum. The final product was a dark green solid and the collected yield was 38 mg. The exact structural nature of the product is currently unknown. ESI-MS (m/z): 668.2 (calc'd  $[\text{Co}(\text{BIPhMe})_2(\text{NO})_2]^+$ : 668.2); 371.1 (calc'd  $[\text{Co}(\text{BIPhMe})(\text{NO})]^+$ : 371.1); 341.1 (calc'd  $[\text{Co}(\text{BIPhMe})]^+$ : 341.1); 439.6 (calc'd  $[\text{CoI}_3]^-$ : 439.6); 380.5 (calc'd  $[\text{I}_3]^-$ : 380.7); 312.6 (calc'd  $[\text{CoI}_2]^-$ : 312.7). FT-IR (KBr,  $\text{cm}^{-1}$ ): 3112 (m), 3058 (w), 3002 (w), 2993 (m), 2863 (w), 2826 (w), 1866 (s), 1818 (s), 1748 (s), 1748 (s), 1596 (w), 1542 (m), 1503 (s), 1447 (s), 1404 (m), 1319 (w), 1283 (s), 1226 (w), 1184 (m), 1170 (m), 1134 (w), 1088 (m), 1071 (s), 1031 (w), 986 (m), 934 (w), 897 (s), 759 (s), 721 (s), 701 (s), 645 (w), 626 (w), 556 (w), 509 (w), 468 (w).



9

**Synthesis of Co(BIPhMe)(NO<sub>3</sub>)<sub>2</sub>, 9.** In a 20 mL vial, **4** (37.5 mg, 0.0630 mmol) was dissolved in methylene chloride (2 mL). The reaction vessel was capped with a rubber septum and NO<sub>2</sub> (g) injected until no further color change was observed. The solution turned from emerald green to purple-red. The solution was stirred for 1 h and filtered through glass microfiber filter paper. X-ray quality crystals of the product were formed upon vapor diffusion of diethyl ether over the course of one week. The crystals were collected by filtration and washed with diethyl ether (3 x 5 mL), resulting in a yield of 6.1 mg (0.0131 mmol, 21 %) of **9**. Anal. Calc'd for C<sub>16</sub>H<sub>18</sub>ClFeN<sub>6</sub>O<sub>7</sub>: C, 38.62; H, 3.65; N, 16.89. Found: C, 38.79; H, 3.81; N, 16.90. ESI-MS (m/z): 685.4 (calc'd [M+BIPhMe-NO<sub>3</sub>]<sup>+</sup>: 685.2). FT-IR (KBr, cm<sup>-1</sup>): 3128 (m), 3058 (w), 2993 (w), 2932 (m), 2824 (w), 1597 (w), 1500 (s), 1448 (s), 1384 (m), 1315 (s), 1284 (m), 1164 (s), 1089 (m), 1070 (s), 1032 (w), 990 (m), 958 (w), 898 (m), 856 (w), 819 (m), 758 (s), 720 (s), 702 (s), 644 (w), 556 (w), 510 (w).

**NO (g)/NO<sub>2</sub> (g) reactions monitored by UV-Vis spectroscopy.** Solutions of **1** – **4** (102 – 1120 μM) in acetonitrile were prepared in the glove box, removed, and placed into the Cary 50 UV-Vis spectrometer. After an initial scan, a syringe of 500 μL gas was injected, and the cuvette shaken for 10 - 20 sec, and returned into the spectrometer. Scans were collected every 30 sec for the first 10 min, 1 min for the next 20 min, and every 5 min for the final 90 min.

**Sensor loaded filter paper NO/NO<sub>2</sub> test strips.** Strips of filter paper were dipped into separate methylene chloride solutions of **1** – **4** (30 – 50 mM). The methylene chloride was allowed to

evaporate. These integrated filter paper strips were placed in 20 mL vials that were sealed with a septum. NO (g) or NO<sub>2</sub> (g) (1 mL) was injected into the vial and color changes were observed instantly and recorded.

**Sensor loaded silica TLC NO/NO<sub>2</sub> test strips.** Methylene chloride solutions of 1 – 4 (30 – 50 mM) were spotted onto TLC plates and the methylene chloride was allowed to evaporate. These TLC plates were placed in a 20 mL vial and the vial was sealed with a septum. NO (g) or NO<sub>2</sub> (g) (1 mL) was injected into the vial and color changes were observed within 1 min.

**Sensor loaded silica syringe NO/NO<sub>2</sub> headspace gas analyzers.** Solutions of 1 – 4 (30-50 mM) in methylene chloride were loaded onto 250 – 300 mg of silica gel and dried under vacuum. The integrated silica gel was poured into 1 mL plastic syringes fitted with 16 gauge stainless steel needles. NO (g) or NO<sub>2</sub> (g) was pulled into the syringe headspace and color changes were observed instantly.

### 3.3 Results and Discussion

**Synthesis and spectroscopic of BIPhMe starting complexes.** The BIPhMe ligand was previously used to impart preorganization of two *cis*-histidine donors within diiron-carboxylate complexes.<sup>11</sup> We originally intended to use this ligand to prepare models of Rieske-type [2Fe–2S], but no successful synthetic route was found to install this ligand onto a prepared [2Fe–2S] cluster. While trying to develop starting materials for these Rieske-models, a variety of metal halide complexes were prepared.

Compounds 1 – 3 are fairly insoluble in THF whereas their starting materials are soluble. This property allows for easy preparation and purification of the target complexes. Addition of BIPhMe to the metal halide solution affords rapid precipitation of microcrystalline material. Stirring for an additional hour was performed to allow for completion and improve overall

yields. Purification of compounds **1** – **3** was performed by washing with additional THF and Et<sub>2</sub>O and subsequently drying under vacuum.

The <sup>1</sup>H NMR spectrum of **1** has eight peaks and the spectrum of **2** has seven (Figure 2.2). All of these peaks are shifted downfield from the spectrum of BIPhMe. The peaks are fairly similar to one another. The differences are that, in the spectrum of **1**, there are peaks at 1.86 ppm and 3.76 ppm, whereas in the spectrum of **2** there is a single broad peak at 2.83 ppm. This result suggests that the two peaks at for **1** maybe be related and are collapsed into a single broad peak in **2**, which is why **1** has an additional peak. The other difference between the two spectra is that the broad peak at 21.81 ppm and the sharp peak at 18.83 ppm in the spectrum of **1** shift downfield and overlap in the spectrum of **2**.

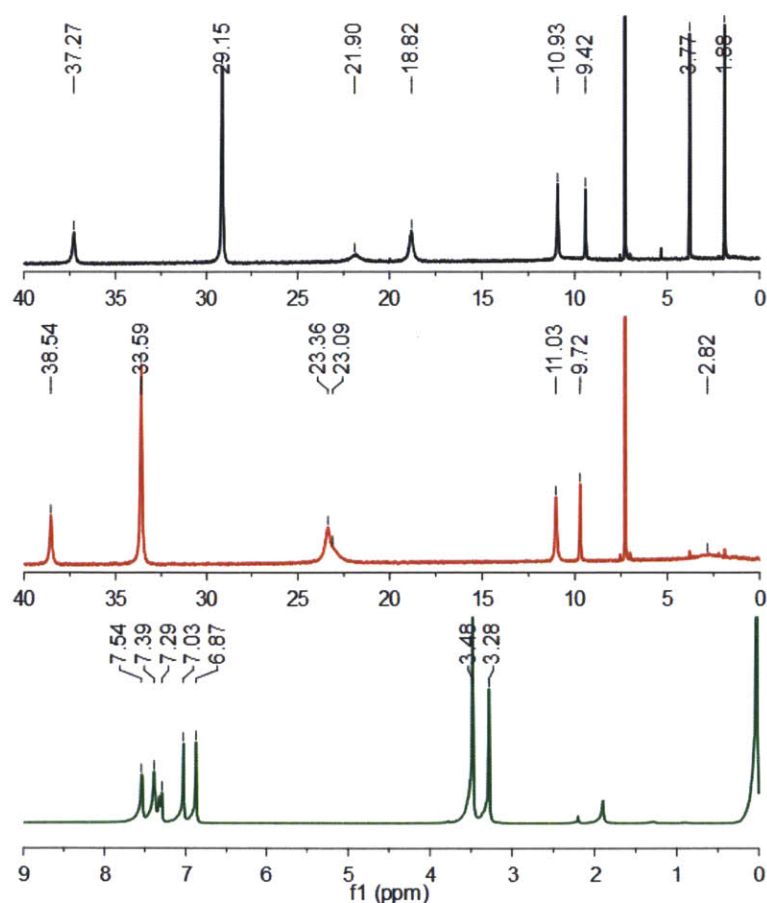


**Figure 2.2.** <sup>1</sup>H NMR spectra of **1** (black), **2** (red), and BIPhMe (green) in CDCl<sub>3</sub> collected at 400 MHz. The spectra are references to the residual CHCl<sub>3</sub> peak at 7.29 ppm

Complex **1** was observed in a MALDI-TOF experiment using recrystallized anthracene as the matrix (Figure 2.3). We were also able to observe **1** and **2** losing a halide in the ESI-MS experiment using acetonitrile as the carrier solvent. During the ESI-MS experiment we also observed the binding of an additional BIPhMe ligand to iron. Since there was not a second set of peaks in the  $^1\text{H}$  NMR experiment, we doubt that an equilibrium exists in solution where dissociation and binding of an additional BIPhMe ligand occur.

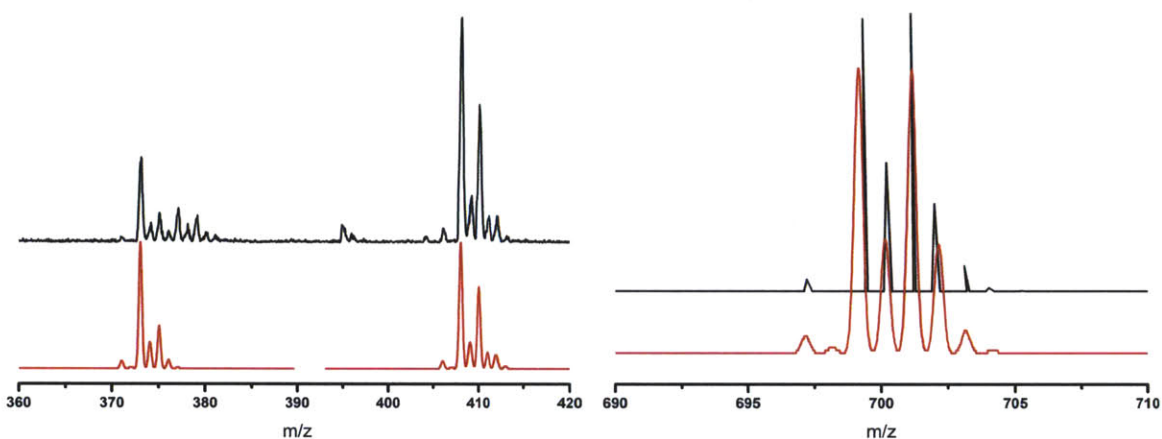


**Figure 2.3.** Left: MALDI-TOF spectrum of **1** using anthracene as the matrix. Right: Positive mode ESI-MS spectrum of  $[\mathbf{2}+\text{BIPhMe}-\text{Br}]$  using acetonitrile as the carrier solvent. Color scheme: black, experimental; red, simulated.

Preparation of pure **4** is not as simple owing to its high solubility in THF, requiring the addition of a 1.5 equivolume of pentanes to precipitate the intended product. The compound was washed with pentane to remove any residual solvent and subsequently dried under vacuum.

In the  $^1\text{H}$  NMR spectrum of **3**, seven peaks are present, whereas we only observe six peaks in the spectrum of **4** (Figure 2.4). The BIPhMe peaks are all shifted downfield as in the iron complexes. The farthest downfield peak for **3** occurs at 37.95 ppm, but this resonance is not observed in the spectrum of **4**. We hypothesize that the peak has been broadened enough to be observed under these experimental conditions.

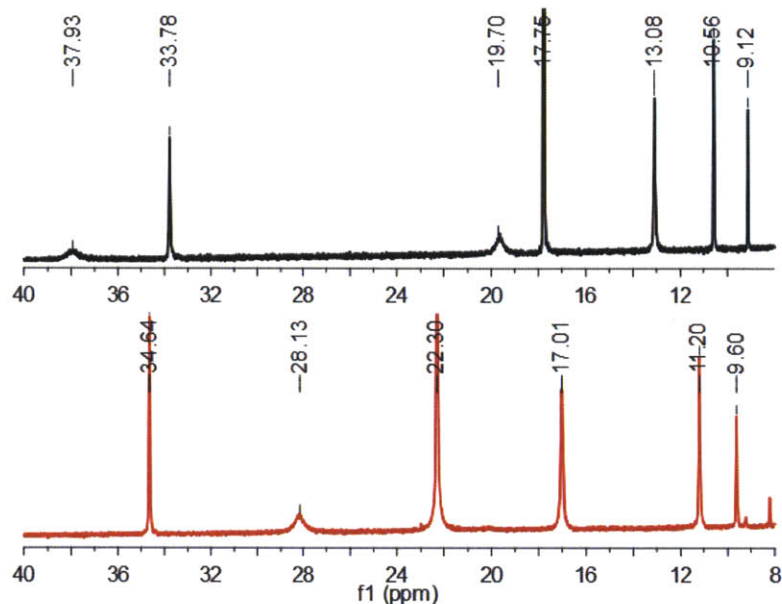


**Figure 2.4.**  $^1\text{H}$  NMR spectra of **3** (black) and **4** (red) in  $\text{CDCl}_3$  collected at 400 MHz.

As in the ESI-MS spectra of the iron containing compounds, **3** and **4** show peaks corresponding to the complexes minus a halide (Figure 2.5). These spectra also have peaks that correspond to the binding of an additional BIPhMe ligand to the complex. The  $^1\text{H}$  NMR spectra of **3** and **4** do not suggest that a *bis*-BIPhMe complex exists in solution.

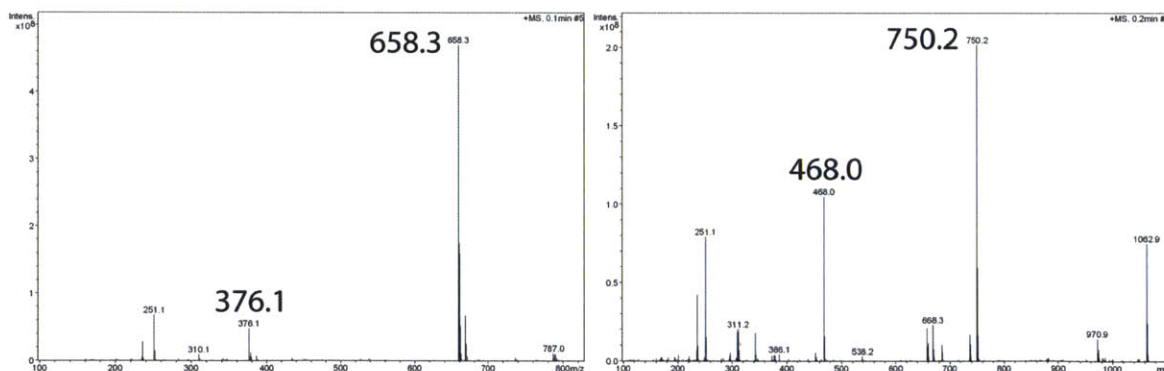


**Figure 2.5.** Positive mode ESI-MS spectra of **3** (left) and **4** (right) using acetonitrile as the carrier solvent. Peak assignments ( $m/z$ ): 376.1 ( $[\mathbf{3}-\text{Cl}]^+$ , calc'd 376.1); 658.3 ( $[\mathbf{3}+\text{BIPhMe}-\text{Cl}]^+$ , calc'd 658.2); 750.2 ( $[\mathbf{4}+\text{BIPhMe}-\text{I}]^+$ , calc'd 750.1); 468.0 ( $[\mathbf{4}-\text{I}]^+$ , calc'd 468.0).

**X-ray crystallographic characterization of BIPhMe starting complexes.** Crystallization of compound **1** resulted in two different structures, a mononuclear complex and two chloro-bridged dimers co-crystallized with two molecules of methylene chloride (Figure 2.6). Both crystals were



grown by vapor diffusion of diethyl ether into a methylene chloride solution of the compound at ambient temperature. Crystals of the mononuclear species form as colorless rods while the dimer complex forms colorless block crystals. The mononuclear species contains a pseudo-tetrahedral iron with a Cl–Fe–Cl angle of  $119.778(14)^\circ$  and Fe–Cl bond distances of  $2.2405(4)$  Å and  $2.2638(4)$  Å (Table 2.1).

The chloride-bridged dimer has two pseudo-square pyramidal iron centers with axial chlorides. The average Cl–Fe–Cl angles are  $82.134(11)^\circ$ ,  $98.476(13)^\circ$ , and  $110.630(15)^\circ$ . The average Fe–Cl bond distances are  $2.4336(4)$  Å and  $2.5025(4)$  Å for the bridging chlorides, and  $2.2931(4)$  Å for the axial chloride. The average Fe–Cl–Fe angles are  $97.124(13)^\circ$  and  $98.369(13)^\circ$ . The average N–Fe–N bond angle is more acute in the dimer,  $83.18(4)^\circ$ , compared to the mononuclear complex,  $86.53(4)^\circ$ , resulting in elongation of the Fe–N bond by more than  $0.5$  Å. Compound **2** also crystallizes as a pseudo-tetrahedral complex (Figure 2.7) with a Br–Fe–Br bond angle of  $118.618(13)^\circ$  and Fe–Br bond distances of  $2.3800(3)$  Å and  $2.4058(3)$  Å.

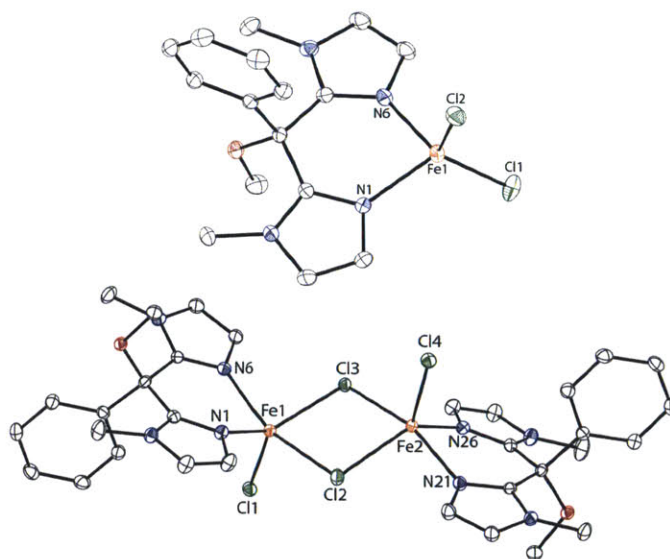


**Figure 2.6.** Drawings of the X-ray crystal structures of **1**, mononuclear (top) and dimer (bottom), with ellipsoids shown at 50% probability. Solvent molecules and hydrogen atoms are omitted for clarity. Color scheme: iron, orange; chloride, dark green; nitrogen, blue; oxygen, red; carbon, colorless.

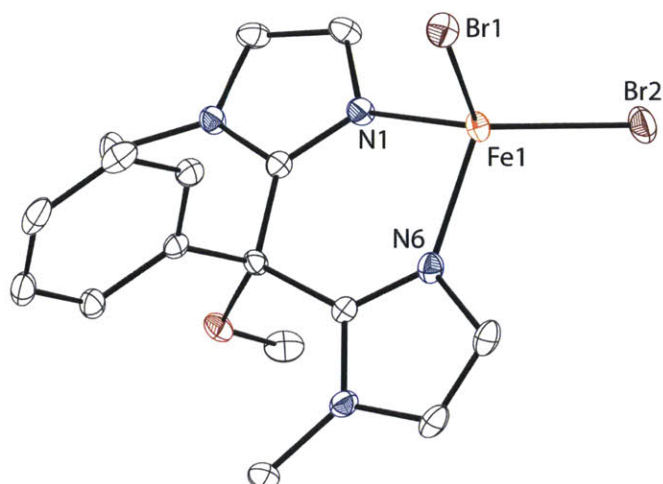


**Figure 2.7.** Drawing of the X-ray crystal structure of **2** with ellipsoids shown at 50% probability. Hydrogen atoms are omitted for clarity. Color scheme: iron, orange; bromide, dark red; nitrogen, blue; oxygen, red; carbon – colorless.

**Table 2.1.** Selected geometrical parameters of **1 – 4**.

Compound	M–N, (Å)	N–M–N, (°)	M–X, (Å)	X–M–X, (°)	N–M–X, (°)	
Fe(BIPhMe)Cl <sub>2</sub> , <b>1</b>	2.0601(10)	86.53(4)	2.2405(4)	119.778(14)	111.81(3)	
	2.0644(10)		2.2638(4)		116.57(3)	
Fe <sub>2</sub> (μ–Cl) <sub>2</sub> (BIPhMe) <sub>2</sub> Cl <sub>2</sub> , average values of equivalent atoms	2.1162(11)	83.18(4)	Axial:	82.134(11)	89.58(3)	
	2.1314(11)		2.2931(4)	98.476(13)	91.20(3)	
			Bridge:	110.630(15)	99.33(3)	
			2.4336(4)		115.70(3)	
			2.5025(4)		133.65(3)	
Fe(BIPhMe)Br <sub>2</sub> , <b>2</b>	2.0539(16)	86.75(6)	2.3800(3)	118.618(13)	162.06(3)	
	2.0612(16)		2.4058(3)		108.09(4)	
					110.44(4)	
					110.55(4)	
Co(BIPhMe)Cl <sub>2</sub> , <b>3</b>	1.9996(10)	91.13(4)	2.2269(4)	114.903(14)	117.88(4)	
	1.9961(11)		2.2494(4)		108.32(3)	
					110.51(3)	
					112.36(3)	
Co(BIPhMe)I <sub>2</sub> , <b>4</b>	1.990(4)	90.93(15)	2.5510(8)	113.62(3)	117.18(3)	
	1.991(4)		2.5594(8)		106.28(10)	
						106.14(11)
						118.48(11)
				120.01(11)		

**Table 2.2.** X-ray crystallographic data for mononuclear **1**, chloro-bridged dimer **1**, and **2** at 100K.

compounds	Fe(BIPhMe)Cl <sub>2</sub> , <b>1</b>	Fe <sub>2</sub> (μ-Cl) <sub>2</sub> (BIPhMe) <sub>2</sub> Cl <sub>2</sub> ·2CH <sub>2</sub> Cl <sub>2</sub> , <b>1</b>	Fe(BIPhMe)Br <sub>2</sub> , <b>2</b>
formula	C <sub>16</sub> H <sub>18</sub> Cl <sub>2</sub> FeN <sub>4</sub> O	C <sub>37</sub> H <sub>38</sub> Cl <sub>6</sub> Fe <sub>2</sub> N <sub>8</sub> O <sub>2</sub>	C <sub>16</sub> H <sub>18</sub> Br <sub>2</sub> FeN <sub>4</sub> O
formula weight	409.09	903.12	498.01
crystal system	monoclinic	monoclinic	monoclinic
space group	P2 <sub>1</sub> /n	P2 <sub>1</sub> /n	P2 <sub>1</sub> /n
a, Å	10.2647(5)	16.4602(8)	10.4213(4)
b, Å	14.0114(8)	18.1395(9)	14.3580(5)
c, Å	13.2275(7)	25.8784(13)	13.3271(5)
β, deg	104.5200(10)	93.9280(10)	104.8480(10)
V, Å <sup>3</sup>	1841.65(17)	7708.6(7)	1927.54(12)
Z	4	8	4
ρ <sub>calcd</sub> , g/cm <sup>3</sup>	1.475	1.556	1.716
μ, mm <sup>-1</sup>	1.119	1.211	4.938
θ range, deg	2.15 to 30.91	1.37 to 30.79	2.12 to 31.16
completeness to θ, %	96.1	99.2	92.7
reflections collected	39933	180470	27105
independent reflections	5589	23955	5782
R(int)	0.0302	0.0335	0.0270
restraints	0	0	0
parameters	220	931	220
Max., min. transmission	0.7461, 0.6798	0.7461, 0.6556	0.7462, 0.5320
R1(wR2) [I>2σ(I)]	0.0269 (0.0758)	0.0285 (0.0736)	0.0248 (0.0698)
R1(wR2)	0.0338 (0.0782)	0.0385 (0.0779)	0.0329 (0.0718)
GoF(F <sup>2</sup> )	1.397	1.457	1.304
max, min peaks, e.Å <sup>-3</sup>	0.495, -0.226	0.760, -0.890	0.965, -0.368

Compounds **3** and **4** both crystallize as pseudo-tetrahedral mononuclear complexes (Figure 2.8). Compound **3** has a Cl–Co–Cl bond angle of 114.903(14)° and Co–Cl bond distances of 2.2269(4) Å and 2.2494(4) Å. Compound **4** has a I–Co–I bond angle of 113.62(3)° and Co–I bond distances of 2.5510(8) Å and 2.5594(8) Å. The N–M–N bond angles of these cobalt complexes are larger by ~5° compared to the iron analogues.

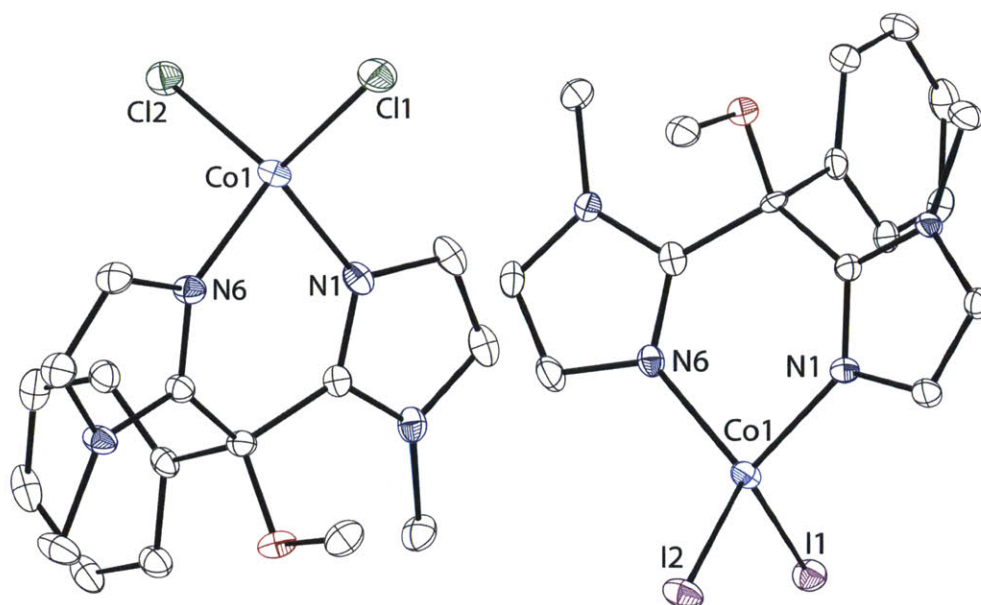


**Figure 2.8.** Drawings of the X-ray crystal structures of **3** and **4** with ellipsoids shown at 50% probability. Solvent molecules and hydrogen atoms are omitted for clarity. Color scheme: cobalt, light blue; chloride, dark green; iodine, purple; nitrogen, blue; oxygen, red; carbon, colorless.

**Table 2.3.** X-ray crystallographic data for **3** and **4** at 100K.

compounds	Co(BIPhMe)Cl <sub>2</sub> , <b>3</b>	Co(BIPhMe)I <sub>2</sub> , <b>4</b>
formula	C <sub>16</sub> H <sub>18</sub> Cl <sub>2</sub> CoN <sub>4</sub> O	C <sub>16</sub> H <sub>18</sub> CoI <sub>2</sub> N <sub>4</sub> O
formula weight	412.17	595.07
crystal system	monoclinic	monoclinic
space group	P2 <sub>1</sub> /n	P2 <sub>1</sub> /n
a, Å	10.2452(5)	10.7833(18)
b, Å	13.9041(6)	13.324(2)
c, Å	13.2165(6)	14.141(2)
β, deg	104.3620(10)	100.339(3)
V, Å <sup>3</sup>	1823.86(14)	1998.8(6)
Z	4	4
ρ <sub>calcd</sub> , g/cm <sup>3</sup>	1.501	1.977
μ, mm <sup>-1</sup>	1.244	3.958
θ range, deg	2.16 to 30.93	2.12 to 27.19
completeness to θ, %	95.7	99.8
reflections collected	39351	35044
independent reflections	5515	4428
R(int)	0.0309	0.0735
restraints	0	0
parameters	220	220
Max., min. transmission	0.7462, 0.6618	0.7455, 0.6137
R1(wR2) [I>2σ(I)]	0.0265 (0.0733)	0.0347 (0.0549)
R1(wR2)	0.0324 (0.0755)	0.0530 (0.0571)
GoF(F <sup>2</sup> )	1.577	1.536
max, min peaks, e.Å <sup>-3</sup>	0.420, -0.301	1.012, -0.712

**Reactions of Fe(BIPhMe)Cl<sub>2</sub> and Fe(BIPhMe)Br<sub>2</sub> with NO (g) and NO<sub>2</sub> (g).** The reaction of colorless **1** with NO (g) results in the formation of the MNICs [Fe(BIPhMe)<sub>2</sub>(NO)Cl]<sup>+</sup> and [Fe(NO)Cl<sub>3</sub>]<sup>-</sup>, **5**. The reaction occurs rapidly in methylene chloride, acetonitrile, and methanol, and forms a dark green solution. The UV-Vis spectrum (Figure 2.9) shows absorption bands at 363 nm, 473 nm, and 699 nm. The band at 363 nm is ascribed to [Fe(NO)Cl<sub>3</sub>]<sup>-</sup> based on the published literature value of 360 nm.<sup>20</sup> The two bands at 473 nm and 699 nm are assigned to the octahedral [Fe(BIPhMe)<sub>2</sub>(NO)Cl]<sup>+</sup> cation. These values are similar to the absorption bands of the published complex [Fe(TPA)(O<sub>2</sub>CCH<sub>3</sub>)(NO)]<sup>+</sup>, which are 430 nm and 650 nm and have extinction coefficients of 730 M<sup>-1</sup>cm<sup>-1</sup> and 150 M<sup>-1</sup>cm<sup>-1</sup>, respectively.<sup>21</sup>

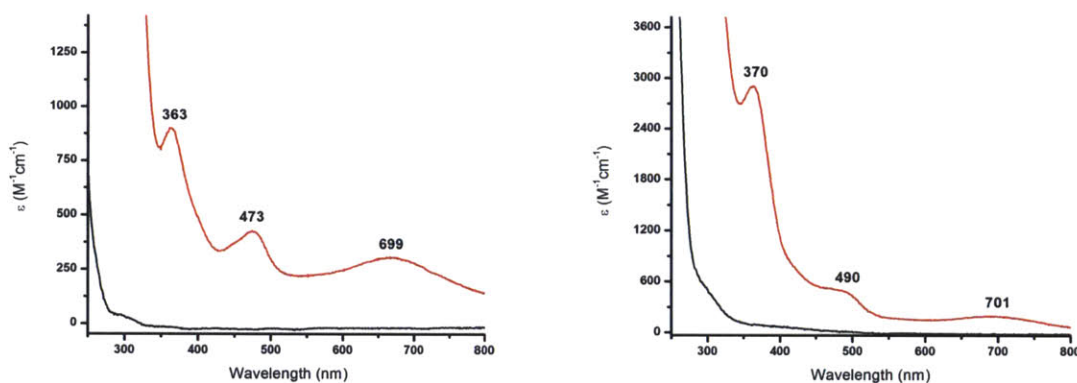


**Figure 2.9.** UV-Vis spectra of **1** (left) and **2** (right) and their NO (g) products. Color scheme: black, starting; red, nitrosylated product.

The formation of these bands allows for **1** to be used as a quantitative and qualitative assay to measure NO (g) release into the reaction headspace. Using complex **1** in this manner was very instrumental in the elucidation of reaction products of SNO<sup>-</sup> with protons and metal centers reported in chapters 3 and 4. A solution of **1** could be prepared and set up to share the headspace of a reaction that may evolve NO (g) and subsequently convert **1** into **5**. This conversion could be qualitatively observed by the formation of a green solution from a colorless starting solution (Figure 2.10). This reaction could be qualitatively observed with less than 2

$\mu\text{mol}$  of NO (g) added. To quantify the conversion, the solution of **1**/**5** could then be transferred to a volumetric flask and appropriately diluted to measure the absorbance. Because **1** does not absorb at 363 nm, 473 nm, or 699 nm, there is no interference with quantification of the formation of **5**.

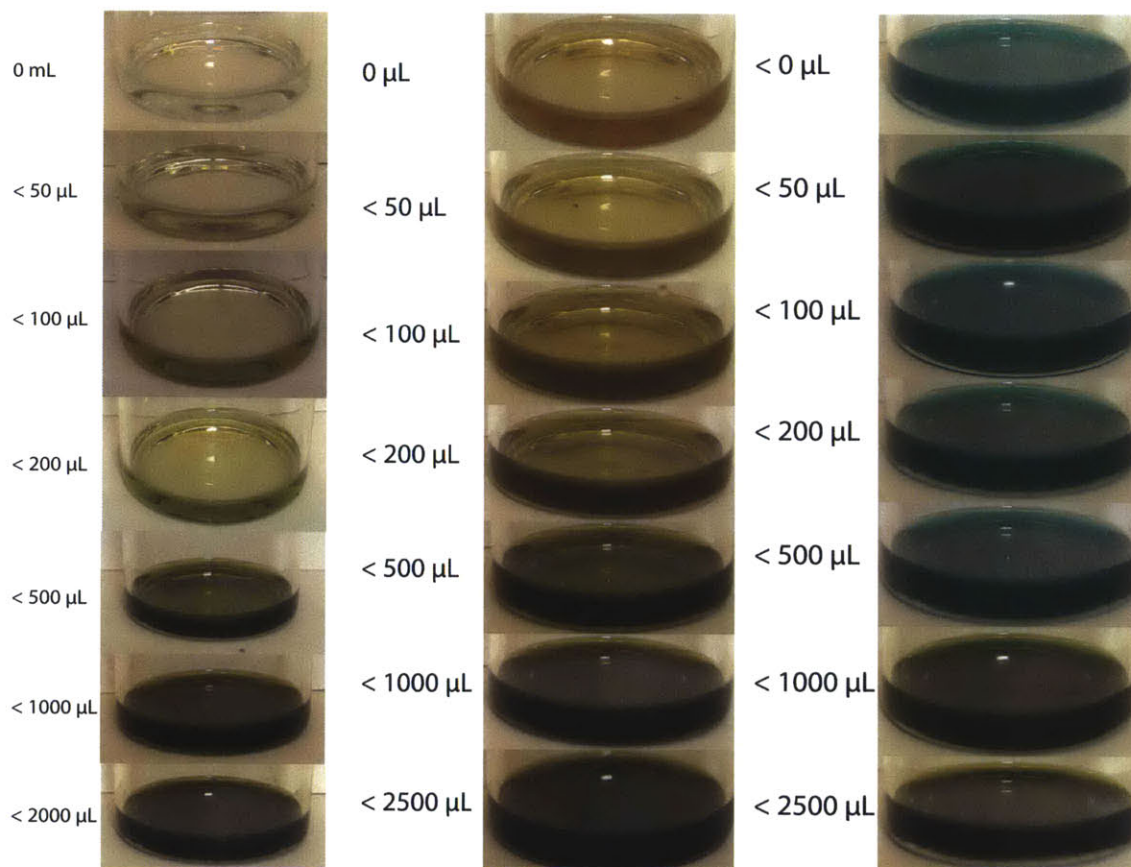


**Figure 2.10.** Solutions of **1** (left; 24 mM), **2** (middle; 32 mM), and **4** (right; 35 mM) in methylene chloride that were exposed to varying amounts of NO (g).

The IR spectrum of **1** shows two bands at  $1709\text{ cm}^{-1}$  and  $1792\text{ cm}^{-1}$  (Figure 2.11) assigned as  $\nu_{\text{NO}}$ . Upon reaction with  $^{15}\text{NO}$  these bands shift to  $1681\text{ cm}^{-1}$  and  $1757\text{ cm}^{-1}$ , which are close to the calculated values of  $1678\text{ cm}^{-1}$  and  $1760\text{ cm}^{-1}$ . The  $\nu_{\text{NO}}$  band at  $1792\text{ cm}^{-1}$  is assigned to  $[\text{Fe}(\text{NO})\text{Cl}_3]^-$  based on literature published values of  $1777\text{ cm}^{-1}$ ,  $1794\text{ cm}^{-1}$ , and  $1806\text{ cm}^{-1}$ .<sup>20,22,23</sup> The  $\nu_{\text{NO}}$  band at  $1709\text{ cm}^{-1}$  is attributed to the complex  $[\text{Fe}(\text{BIPhMe})_2(\text{NO})\text{Cl}]^+$ , which is comparable to the published  $\nu_{\text{NO}}$  value of  $1720\text{ cm}^{-1}$  and  $1690\text{ cm}^{-1}$  for the related

octahedral complexes  $cis\text{-}[\text{Fe}(\text{cyclam})(\text{NO})\text{Cl}]^+$  and  $[\text{Fe}(\text{Me}_3\text{-TACN})(\text{N}_3)_2(\text{NO})]$ , respectively.<sup>24,25</sup>

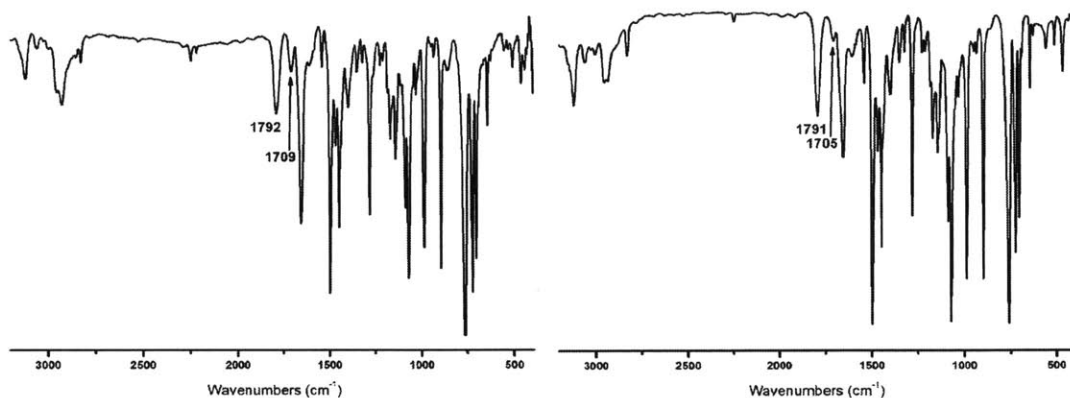


**Figure 2.11.** FT-IR spectra of **5** (left) and **6** (right) with NO.

The positive-mode ESI-MS spectrum of **5** (Figure 2.12) shows peaks that match the isotopic distribution of  $[\text{Fe}(\text{BIPhMe})_2\text{Cl}]^+$  at 655.2 m/z. The negative-mode ESI-MS of **5** has two sets of peaks that correspond to  $[\text{FeCl}_3]^-$  and  $[\text{FeCl}_2]^-$  at 162.6 m/z and 125.8 m/z, respectively. The loss of the nitrosyl ligands was anticipated based on the observed ESI-MS spectra of the  $\{\text{Fe-S-NO}\}$  clusters described in chapter 2, where loss of multiple nitrosyls from the parent complex was observed during the ESI-MS experiment.

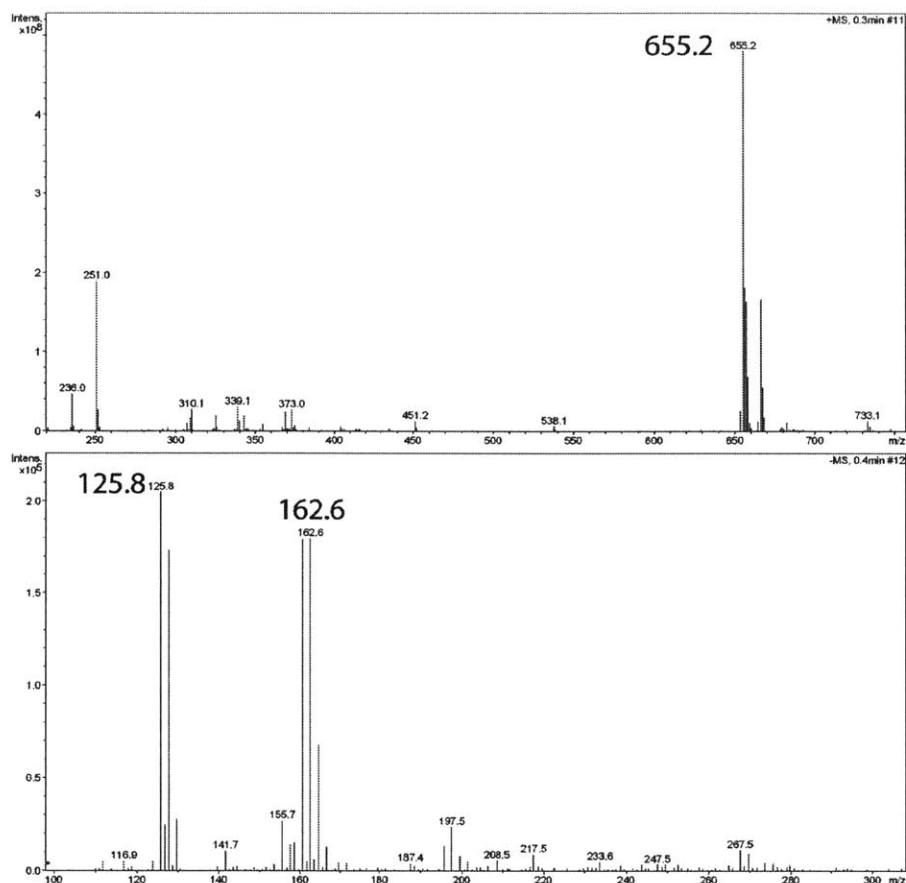


**Figure 2.12.** Positive-mode (top) and negative-mode (bottom) ESI-MS spectra of **5** in acetonitrile. Peak assignments ( $m/z$ ): 655.2 ( $[\text{Fe}(\text{BIPhMe})_2\text{Cl}]^+$ , calc'd 655.2); 162.6 ( $[\text{FeCl}_3]^-$ , calc'd 162.8); 125.8 ( $[\text{FeCl}_2]^-$ , calc'd 125.8).

The reaction of **2** with  $\text{NO}$  (g) forms a similar product,  $[\text{Fe}(\text{BIPhMe})_2(\text{NO})\text{Br}][\text{Fe}(\text{NO})\text{Br}_3]$ , **6**. The UV-Vis spectrum of **6** shows bands at 370 nm, 490 nm, and 701 nm (Figure 2.10). The IR spectrum of **6** (Figure 2.11) shows  $\nu_{\text{NO}}$  bands at  $1705\text{ cm}^{-1}$  and  $1791\text{ cm}^{-1}$ . The ESI-MS spectrum (Figure 2.13) shows isotopic patterns for  $[\text{Fe}(\text{BIPhMe})_2\text{Br}]^+$ ,  $[\text{FeBr}_3]^-$ , and  $[\text{FeBr}_2]^-$  at 701.1  $m/z$ , 296.5  $m/z$ , and 252.6  $m/z$ , respectively.



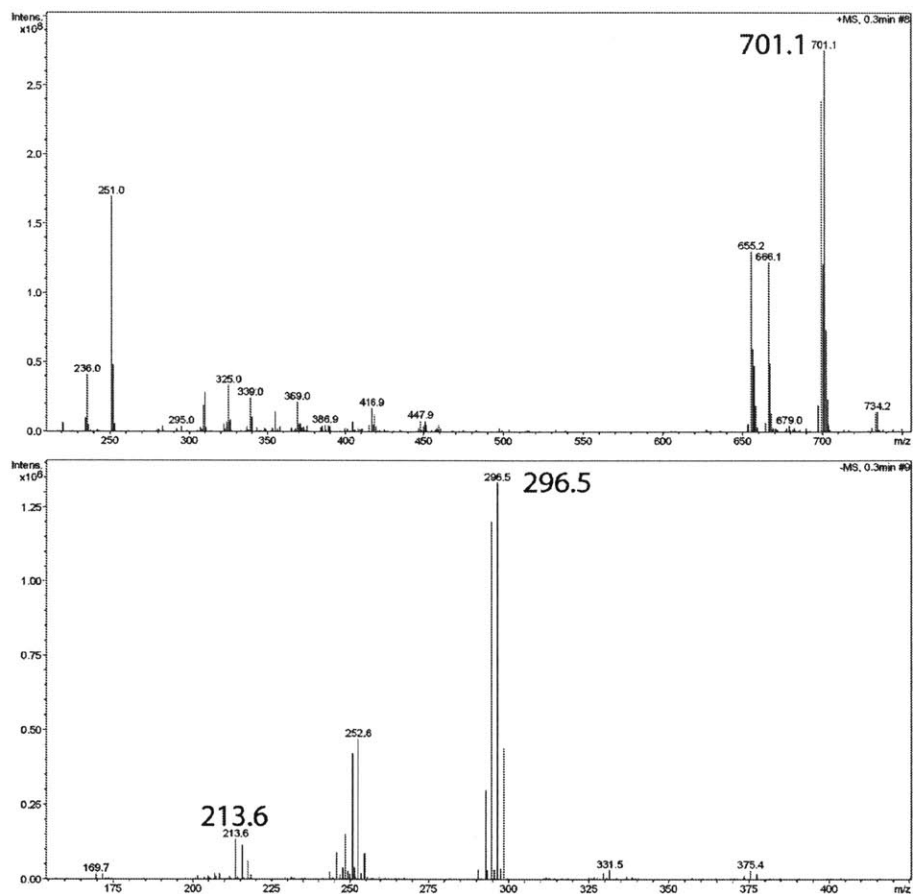


**Figure 2.13.** Positive-mode (top) and negative-mode (bottom) ESI-MS spectra of **6** in acetonitrile. Peak assignments ( $m/z$ ): 701.1 ( $[\text{Fe}(\text{BIPhMe})_2\text{Br}]^+$ , calc'd 701.2); 296.5 ( $[\text{FeBr}_3]^-$ , calc'd 296.7); 213.6 ( $[\text{FeBr}_2]^-$ , calc'd 213.8).

Crystals of **5** were obtained by vapor diffusion of diethyl ether into a methylene chloride solution of the compound over the course of two days. The crystal structure of **5** contains a bent MNIC,  $[\text{Fe}(\text{BIPhMe})_2(\text{NO})\text{Cl}]^+$ , and a linear MNIC,  $[\text{Fe}(\text{NO})\text{Cl}_3]^-$  (Figure 2.14). The Fe–N–O angle of the bent, octahedral complex is  $148.9(3)^\circ$  and the N–O bond distance is  $1.102(3) \text{ \AA}$ . The Fe–N–O angle in the linear, tetrahedral complex is  $170.6(3)^\circ$  and it has an N–O bond distance of  $1.153(3) \text{ \AA}$ . These values match the published values of  $177(1)^\circ$  and  $1.12(2) \text{ \AA}$ .<sup>26</sup> To verify that the anion was actually  $[\text{Fe}(\text{NO})\text{Cl}_3]^-$  instead of  $[\text{FeCl}_4]^-$ , the NO ligand was replaced with chloride during the structure refinement. This substitution resulted in the thermal ellipsoid of the substituted chloride being elongated along the Fe–Cl bond, showing that the electron density of

the appropriate ligand is spread linearly along the bond axis and that a linear NO ligand was the correct assignment. The final structure solution does contain residual electron density 1.1 Å from the Fe(10) atom, trans to the N(11) atom. The geometric parameters of the  $[\text{Fe}(\text{NO})\text{Cl}_3]^-$  complex are similar to the published values confirming our atom assignment and refinement is true (Table 2.4). Crystals of **6** were obtained and refinement of  $[\text{Fe}(\text{BIPhMe})_2(\text{NO})\text{Br}]^+$  proceeded satisfactorily, but the NO moiety is disordered over multiple positions with the  $\text{Br}^-$  ligands on the  $[\text{Fe}(\text{NO})\text{Br}_3]^-$  complex, resulting in an overall unsatisfactory refinement of the structure.

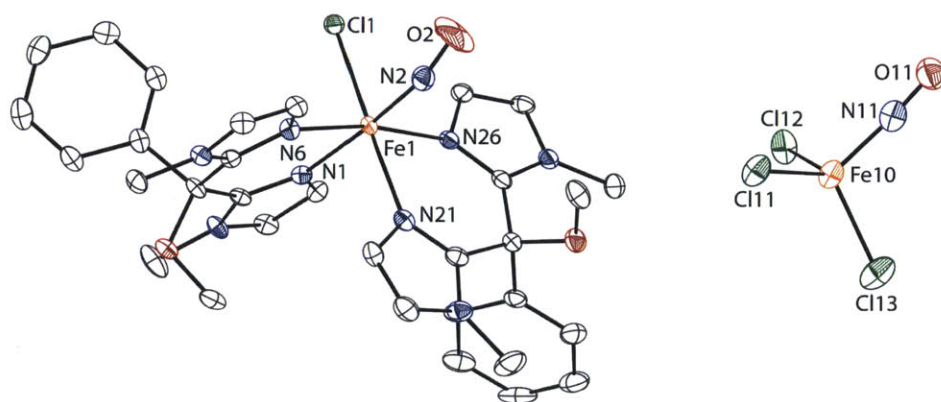


**Figure 2.14.** Drawing of the X-ray crystal structure of **5** with ellipsoids shown at 50% probability. Hydrogen atoms are omitted for clarity. Color scheme: iron, orange; chloride, dark green; nitrogen, blue; oxygen, red; carbon, colorless.

**Table 2.4.** Selected geometric parameters and vibrational stretches of **5** and related compounds.

	$[\text{Fe}(\text{BIPhMe})_2(\text{NO})\text{Cl}]^+$ , <b>5</b>	$[\text{Fe}(\text{Me}_3\text{TACN})(\text{N}_3)_2(\text{NO})]$ , <sup>25</sup>	$[\text{Fe}(\text{NO})\text{Cl}_3]^-$ , <b>5</b>	$[\text{Fe}(\text{NO})\text{Cl}_3]^-$ , <sup>26</sup>
<b>bond length, (Å)</b>				
Fe–N <sub>NO</sub>	1.818(3)	1.738(5)	1.738(3)	1.700(10)
N <sub>NO</sub> –O	1.102(3)	1.142(7)	1.153(3)	1.120(20)
Fe–X <sup>a</sup>	2.4043(8)	2.075(4)	2.2207(11)	2.224(7)
		2.032(4)	2.2320(9)	2.258(7)
			2.2340(9)	2.228(8)
<b>bond angle, (°)</b>				
Fe–N <sub>NO</sub> –O	148.9(3)	155.5(10)	170.6(3)	177.0(1)
X–Fe–N <sub>NO</sub> <sup>a</sup>	87.50(9)	97.2(3)	109.93(10)	109.8(5)
		94.2(3)	109.70(10)	111.0(5)
			104.69(10)	103.3(5)
$\nu_{\text{NO}}$ , (cm <sup>-1</sup> )	1709	1690	1792	1802
				1794 <sup>23</sup>
				1777 <sup>20</sup>

*a.* X = Cl<sup>-</sup> or N<sub>3</sub><sup>-</sup>

**Table 2.5.** X-ray crystallographic data for compounds **5** and **7** at 100K.

compounds	[Fe(BIPhMe) <sub>2</sub> (NO)Cl][FeCl <sub>3</sub> (NO)], <b>5</b>	[Fe(BIPhMe)(NO <sub>3</sub> ) <sub>2</sub> Cl]·0.5CH <sub>2</sub> Cl <sub>2</sub> , <b>7</b>
formula	C <sub>32</sub> H <sub>36</sub> Cl <sub>4</sub> Fe <sub>2</sub> N <sub>10</sub> O <sub>4</sub>	C <sub>16.5</sub> H <sub>19</sub> Cl <sub>2</sub> FeN <sub>6</sub> O <sub>7</sub>
formula weight	878.21	540.13
crystal system	monoclinic	monoclinic
space group	P2 <sub>1</sub> /n	P2 <sub>1</sub> /c
a, Å	17.7234(6)	9.5411(3)
b, Å	12.4526(4)	13.6642(5)
c, Å	20.6292(7)	17.0791(6)
β, deg	110.4730(10)	93.3630(10)
V, Å <sup>3</sup>	4265.3(2)	2222.79(13)
Z	4	4
ρ <sub>calcd</sub> , g/cm <sup>3</sup>	1.368	1.614
μ, mm <sup>-1</sup>	0.976	0.970
θ range, deg	1.31 to 25.73	1.91 to 30.94
completeness to θ, %	100.0	95.0
reflections collected	70218	47637
independent reflections	8151	6682
R(int)	0.0620	0.0219
restraints	0	0
parameters	476	310
Max., min. transmission	0.7453, 0.6664	0.7461, 0.6563
R1(wR2) [I>2σ(I)]	0.0455 (0.1156)	0.0369 (0.1315)
R1(wR2)	0.0622 (0.1213)	0.0399 (0.1338)
GoF(F <sup>2</sup> )	1.232	2.067
max, min peaks, e.Å <sup>-3</sup>	2.518, -0.654	1.048, -1.198

The reaction of **1** with NO<sub>2</sub>(g) results in disproportionation to NO<sub>3</sub><sup>-</sup> and N<sub>2</sub>O, and formation of the yellow seven-coordinate complex [Fe(BIPhMe)(NO<sub>3</sub>)<sub>2</sub>Cl], **7**. The UV-Vis spectrum of **7** (Figure 2.15) has a shoulder at 335 nm with an extinction coefficient of 568 M<sup>-1</sup> cm<sup>-1</sup>. The ESI-MS spectrum shows an isotopic distribution that matches values expected for the complex and an additional bound BIPhMe ligand (Figure 2.17).

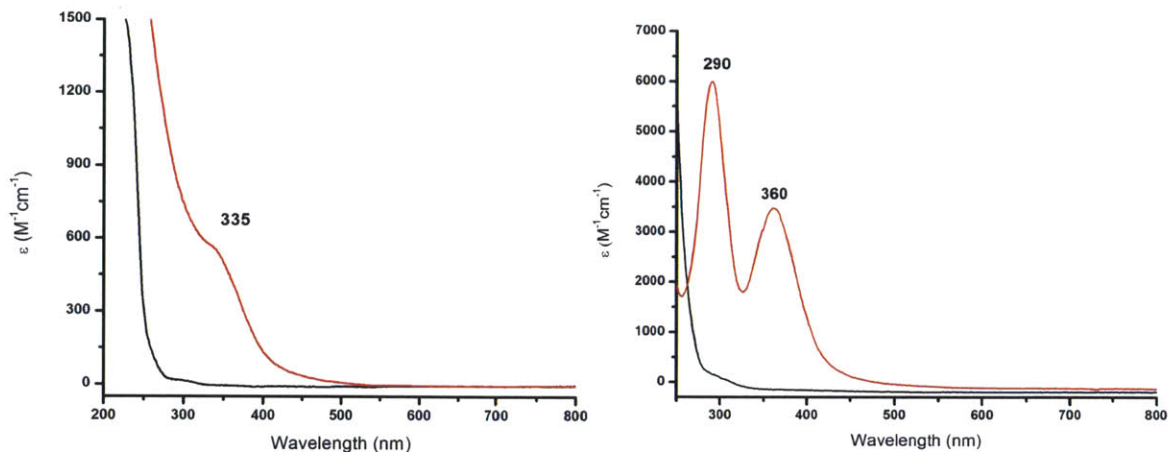


**Figure 2.15.** UV-Vis spectra of **1** (left) and **2** (right) and their  $\text{NO}_2(\text{g})$  products. Color scheme: black, starting; red, reaction product.

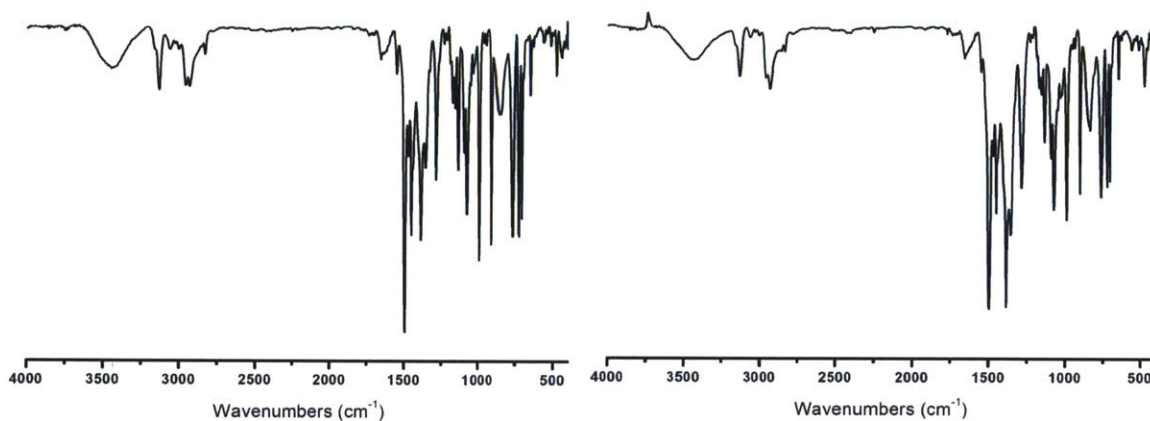


**Figure 2.16.** FT-IR spectra of **7** (left) and **8** (right) with  $\text{NO}_2(\text{g})$ .

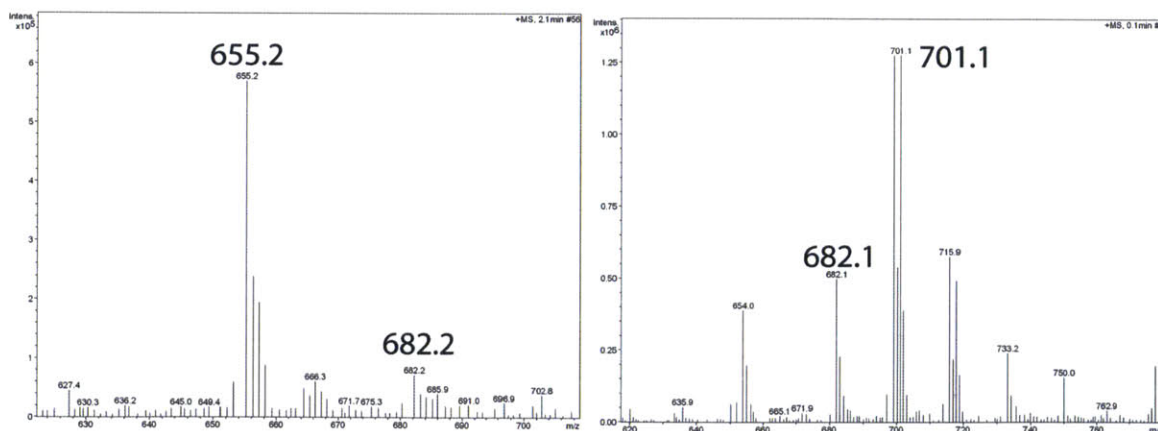


**Figure 2.17.** Positive-mode ESI-MS spectra of **7** (left) and **8** (right) in acetonitrile. Peak assignments ( $m/z$ ): 655.2 ( $[\text{Fe}(\text{BIPhMe})_2\text{Cl}]^+$ , calc'd 655.2); 682.2 ( $[\text{Fe}(\text{BIPhMe})_2(\text{NO}_3)]^+$ , calc'd 682.2); 701.1 ( $[\text{Fe}(\text{BIPhMe})_2\text{Br}]^+$ , calc'd 701.1); 682.1 ( $[\text{Fe}(\text{BIPhMe})_2(\text{NO}_3)]^+$ , calc'd 682.2).

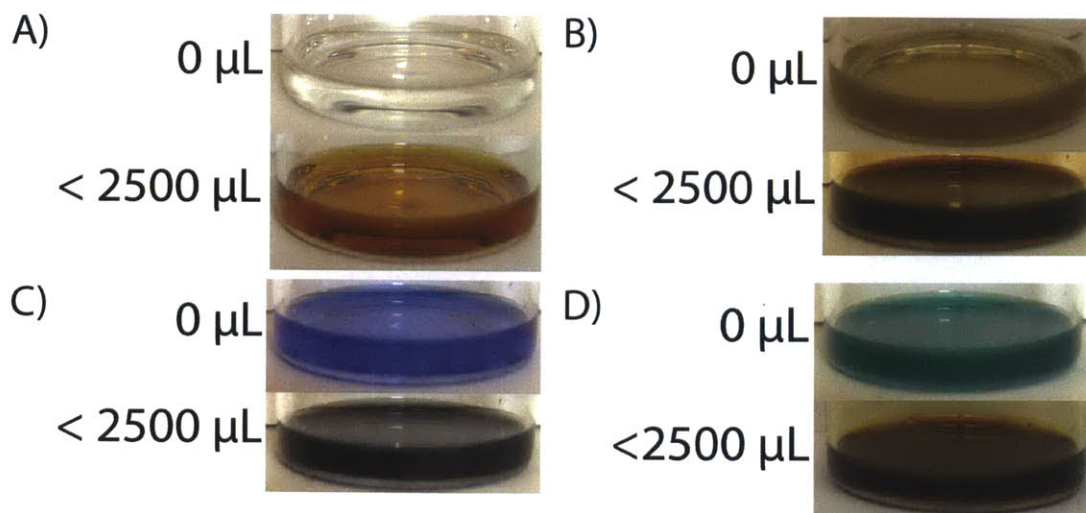


**Figure 2.18.** Solutions of A) **1**, B) **2**, C) **3**, and D) **4** in methylene chloride that were exposed to  $\text{NO}_2(\text{g})$ .

The seven-coordinate iron(III) compound **7** has a pentagonal bipyramid geometry with the oxygen atoms of the nitrate ligands and one of the nitrogen atoms of the BIPhMe ligand in the equatorial plane, while the other nitrogen atoms of the BIPhMe ligand and the chloride atom occupy the apical positions. The Fe–N bond distances involving the BIPhMe ligand are 2.0819(12) Å and 2.0882(12) Å, and the N–Fe–N bond angle is 85.84(5)°. The Fe–O bond distances are 2.1357(11) Å, 2.1439(11) Å, 2.1860(11) Å, and 2.1974(12) Å. The intra O–Fe–O bond angles of the nitrates are 59.43(4)° and 59.54(4)°. The inter O–Fe–O bond angles are 76.26(4)°, 135.56(4)°, 135.69(4)°, and 163.81(4)°. The O–Fe–N<sub>eq</sub> bond angles are 81.75(5)°, 82.41(5)°, 140.71(5)°, and 141.28(5)°. The O–Fe–N<sub>ax</sub> bond angles are 86.23(5)°, 86.24(4)°, 87.68(4)°, and 87.84(5)°. The Fe–Cl bond distance is 2.2651(4) Å. The Cl–Fe–N<sub>ax</sub> bond angle is 178.03(4)°, the Cl–Fe–N<sub>eq</sub> bond angle is 95.53(3)°, and the Cl–Fe–O bond angles are 91.08(3)°, 91.80(3)°, 93.58(3)°, and 95.53(3)°. The iron atom is not planar with the equatorial ligands, but rather puckered towards the chloride ion, as indicated by the X<sub>eq</sub>–Fe–Cl angles being greater than 90°. According to a search of the Cambridge structural database, this is the first compound that has a bidentate *N*-binding ligand, two bidentate nitrates, and a non-oxygen ligand. The

binding motif is similar to the other known seven-coordinate iron(III) nitrates with bidentate *N*-binding ligands:  $\{cis-[Ru(CN-^iBu)_4(CN)_2]Fe(NO_3)_3\}_2$ ,  $[Fe_2(\mu-O)(bpy)_2(NO_3)_4]$ , and  $[Fe_2(\mu-O)(ethyl-(bpy)_2)(NO_3)_4]$ .<sup>27-29</sup> Seven-coordinate iron(III) complexes are relatively rare, comprising only 0.7% of the published iron-containing crystal structures in the Cambridge structural database.<sup>30</sup>

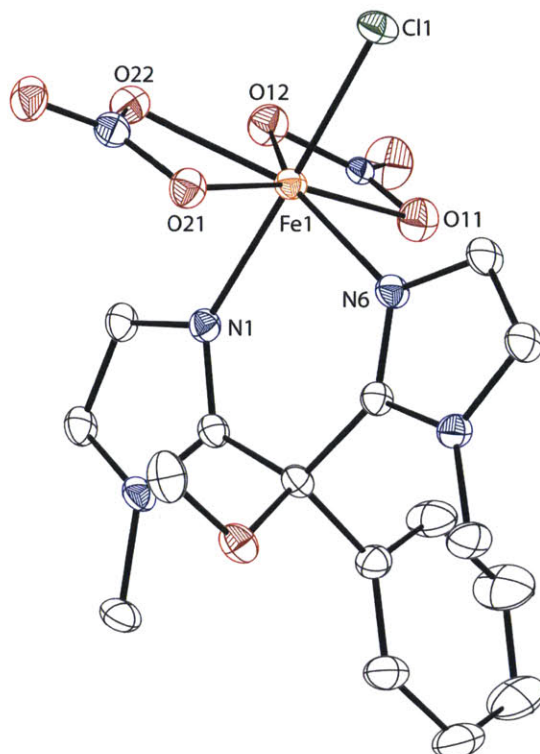


**Figure 2.19.** Drawing of the X-ray crystal structure of **7** with ellipsoids shown at 50% probability. Solvent molecules and hydrogen atoms are omitted for clarity. Color scheme: iron, orange; chloride, dark green; nitrogen, blue; oxygen, red; carbon, colorless.

**Table 2.6.** Selected geometrical parameters of **7** and **9**.

	[Fe(BIPhMe)(NO <sub>3</sub> ) <sub>2</sub> Cl], <b>7</b>		[Co(BIPhMe)(NO <sub>3</sub> ) <sub>2</sub> ], <b>9</b>	
<b>bond length, (Å)</b>				
M–N	Axial:	Equatorial		
	2.0819(12)	2.0882(12)	2.0242(11)	2.0330(11)
M–O	2.1357(11)		2.2136(10)	
	2.1439(11)		2.0903(10)	
	2.1439(11)		2.0766(10)	
	2.1974(12)		2.2398(10)	
M–Cl	2.2651(4)		–	
<b>bond angle, (°)</b>				
O–M–O	Intra:	Inter:	Intra:	Inter:
	59.43(4)	76.26(4)	59.94(4)	91.71(4)
	59.54(4)	135.56(4)	59.80(4)	94.04(4)
		135.69(4)		94.50(4)
		163.81(4)		141.08(4)
N–M–N	85.84(5)		90.95(4)	
N–M–O	Axial:	Equatorial:	110.43(4)	
	86.23(5)	82.41(5)	102.99(4)	
	86.24(4)	81.75(5)	96.32(4)	
	87.68(4)	140.71(5)	104.33(4)	
	87.84(5)	141.28(5)		
N–M–Cl	178.03(4)	95.53(3)	–	
O–M–Cl	93.58(3)		–	
	91.80(3)			
	91.08(3)			
	93.75(3)			

Similar to the formation of **7**, compound **8** forms from the reaction of **2** and NO<sub>2</sub>(g). This reaction can be followed using UV-vis spectroscopy involving by the formation of bands at 290 nm and 360 nm (Figure 2.15). The visible absorption bands of **8** are more intense than the bands observed for **7** (Figure 2.18).

**Reactions of Co(BIPhMe)Cl<sub>2</sub> and Co(BIPhMe)I<sub>2</sub> with NO (g) and NO<sub>2</sub> (g).** No reactivity is observed between **3** and NO (g) by UV-Vis or FT-IR spectroscopy. The reaction of **3** with NO<sub>2</sub> (g) results a color change from deep blue to dark green in methylene chloride. This color change can be followed by UV-Vis (Figure 2.20), where the growth of new bands at 359 nm and 700 nm are observed. A decrease in intensity of the bands at 554 nm and 632 nm is also observed, suggesting that the chloride ligands are retained. This is further corroborated by the ESI-MS spectrum.

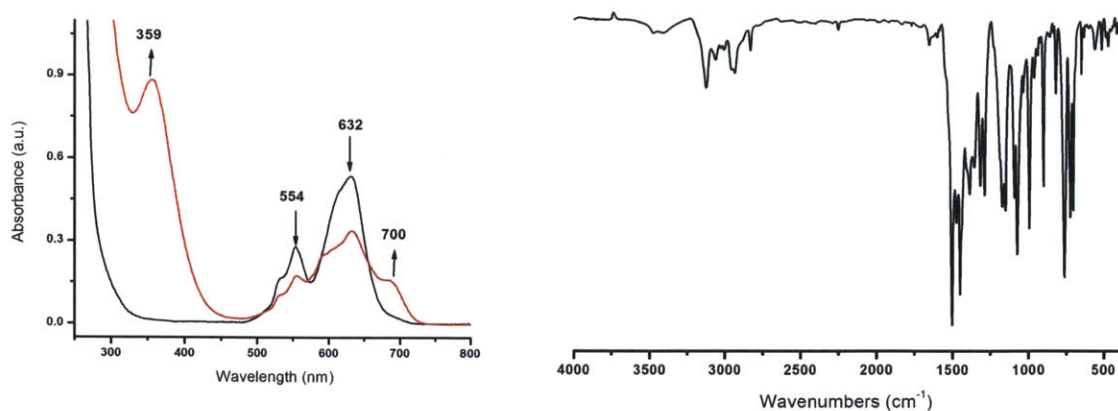


**Figure 2.20.** Spectroscopic characterization of the product generated by the reaction of **3** and  $\text{NO}_2(\text{g})$ . The UV-Vis spectrum (left) was recorded in acetonitrile (1.12 mM) under nitrogen. The FT-IR spectra (right) was recorded as a KBr pellet. Color scheme: black, starting material; red, product.

The reaction of **4** in methylene chloride with  $\text{NO}(\text{g})$  results in a color change from deep green to dark yellow. When this reaction is followed by UV-vis spectroscopy (Figure 2.21), the bands at 244 nm and from 583 – 668 nm are diminished upon addition of excess  $\text{NO}(\text{g})$ . The bands at 310 nm and 373 nm blue shift and increase in intensity to 293 nm and 362 nm. These two bands may be associated with the  $\text{I}_3^-$  ion which has absorption maxima at 297 nm and 350 nm. Cobalt-mediated iodide oxidation may be the reaction route observed, resulting in formation of a new species that cannot be identified by optical spectroscopy from the crude product.

The FT-IR spectrum of the crude nitrosylated product of **4** shows bands at  $1748\text{ cm}^{-1}$ ,  $1784\text{ cm}^{-1}$ ,  $1818\text{ cm}^{-1}$ , and  $1866\text{ cm}^{-1}$ . The shape and separation of the bands suggests the formation of two separate cobalt dinitrosyl species. One of these putative cobalt dinitrosyl species would consist of the bands with  $1748\text{ cm}^{-1}$  and  $1818\text{ cm}^{-1}$ , and the other species would consist of the bands at  $1784\text{ cm}^{-1}$  and  $1866\text{ cm}^{-1}$ .



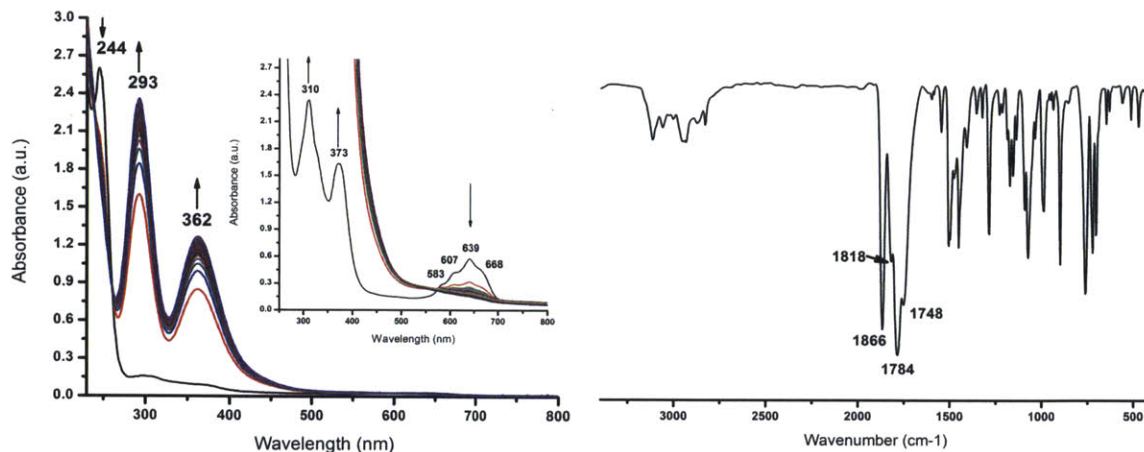


**Figure 2.21.** Spectroscopic characterization of the product generated by the reaction of **4** and NO (g). The UV-Vis spectrum (left) was recorded in acetonitrile (1.02 mM) under nitrogen. The FT-IR spectra (right) was recorded as a KBr pellet.

The positive-mode ESI-MS spectrum (Figure 2.22) shows two sets of peaks with the most abundant ions located at 341.1 m/z and 371.1 m/z. These two peaks correspond well with the potential ions of  $[\text{Co}(\text{BIPhMe})(\text{NO})]^+$ , calculated to have a mass of 371.1 m/z, and  $[\text{Co}(\text{BIPhMe})]^+$ , calculated to have a mass of 341.1 m/z. Both of these ions may form from the synthetically possible  $[\text{Co}(\text{BIPhMe})(\text{NO})_2]$  complex. Evidence for the formation of the complex  $[\text{Co}(\text{BIPhMe})_2(\text{NO})_2]$  is observed in the ESI-MS spectrum by the group of peaks with the most abundant ion located at 668.2 m/z, which matches well with the calculated value of 668.2 m/z for  $[\text{Co}(\text{BIPhMe})_2(\text{NO})_2]$ . The negative-mode ESI-MS shows peaks at 312.6 m/z ( $[\text{CoI}_2]^-$ , calc'd 312.7 m/z), 380.5 m/z ( $\text{I}_3^-$ , calc'd 380.7 m/z), and 439.5 m/z ( $[\text{CoI}_3]^-$ , calc'd 439.6 m/z). Attempts at crystallization, separation, and structural characterization of the two nitrosyl species have proved to be unsuccessful.

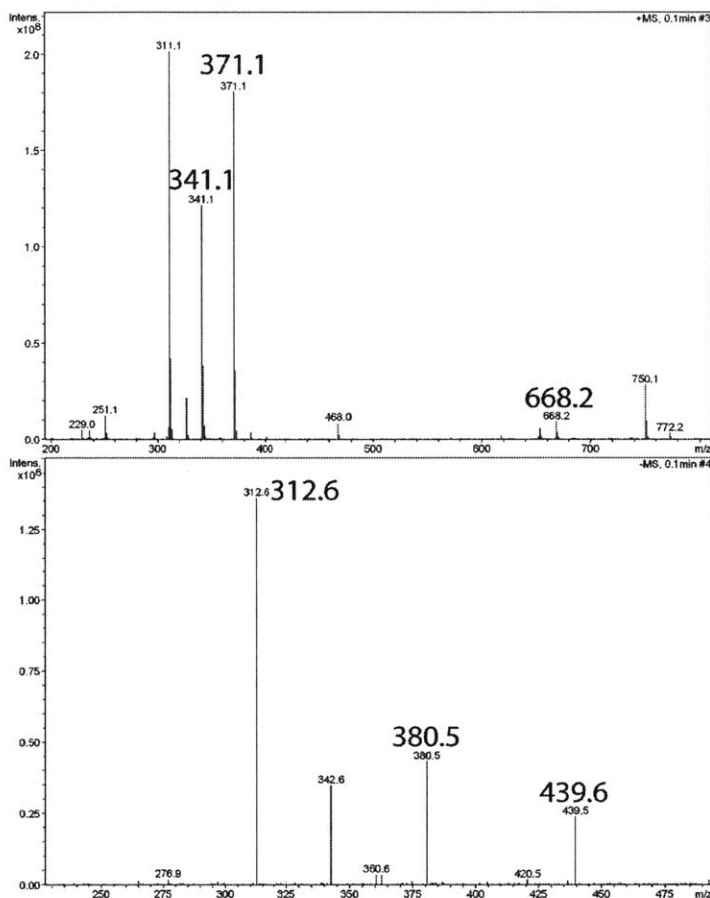


**Figure 2.22.** Positive-mode (top) and negative-mode (bottom) ESI-MS spectra of the product formed in the reaction of **4** and NO (g) in acetonitrile. Peak assignments (m/z): 371.1 ( $[\text{Co}(\text{BIPhMe})(\text{NO})]^+$ , calc'd 371.1); 341.1 ( $[\text{Co}(\text{BIPhMe})]^+$ , calc'd 341.1); 668.2 ( $[\text{Co}(\text{BIPhMe})_2(\text{NO})_2]^+$ , calc'd 668.2); 312.6 ( $[\text{CoI}_2]^-$ , calc'd 312.7); 380.5 ( $\text{I}_3^-$ , calc'd 380.7), 439.5 ( $[\text{CoI}_3]^-$ , calc'd 439.6).

Exposure of **4** in methylene chloride to NO<sub>2</sub> (g) results in a color change from dark green to red-purple, from which the pink complex  $[\text{Co}(\text{BIPhMe})(\text{NO}_3)_2]$ , **9**, was isolated. This qualitative color change (Figure 2.18C) corresponds to loss of the absorption band at 244 nm and the cluster of bands ranging from 583 – 668 nm. A new, broad band grows in at 462 nm along with a shoulder at 270 nm (Figure 2.23). These two spectral features correspond well with the formation of I<sub>2</sub>, which has absorption bands at 288 nm, 350 nm, and 460 nm. The absorption band at 350 nm is obscured by the absorption bands of dissolved NO<sub>2</sub>(g).

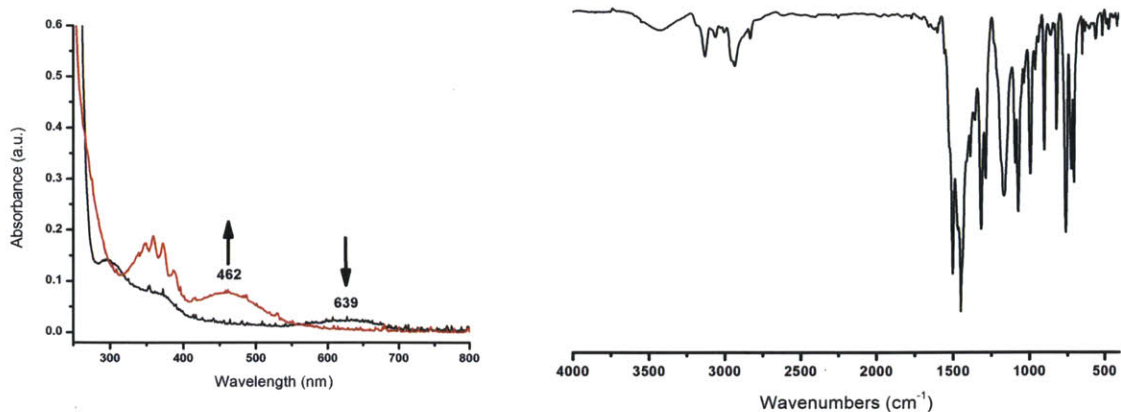


**Figure 2.23.** Spectroscopic characterization of the product generated by the reaction of **4** and  $\text{NO}_2(\text{g})$ . The UV-Vis spectra (left) was recorded in acetonitrile ( $102 \mu\text{M}$ ) under nitrogen. The FT-IR spectra (right) was recorded as a KBr pellet.

Compound **9** crystallizes in  $C2/c$  with a six-coordinate cobalt(II) center (Figure 2.24). The compound has Co–N bond distances of 2.0242(11) and 2.0330(11) and a 90.95(4) N–Co–N bond angle. Both nitrates are bidentate and bound to the cobalt by the oxygen atoms. The Co–O bond distances are 2.0766(10), 2.0903(10), 2.2136(10), and 2.2398(10). The inter O–Co–O bond angles are 59.94(4) and 59.80(4), and intra O–Co–O bond angles of 91.71(4), 94.04(4), 94.50(4), and 141.08(4). The O–Co–N bond angles are 88.00(4), 89.35(4), 96.32(4), 102.99(4), 104.33(4), 110.43(4), 164.18(4), and 169.53(4). The ligands form a propeller-like geometry around the cobalt due to the acute O–Co–O angles.

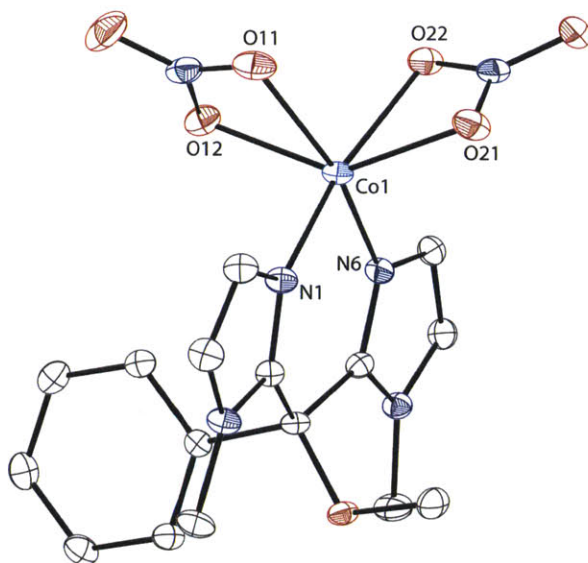


**Figure 2.24.** Drawing of the X-ray crystal structures of **9** with ellipsoids shown at 50% probability. Solvent molecules and hydrogen atoms are omitted for clarity. Color scheme: cobalt, light blue; nitrogen, blue; oxygen, red; carbon, colorless.

**Table 2.7.** X-ray crystallographic data for **9** at 100K.

compound	Co(BIPhMe)(NO <sub>3</sub> ) <sub>2</sub> , <b>9</b>
formula	C <sub>16</sub> H <sub>18</sub> CoN <sub>6</sub> O <sub>7</sub>
formula weight	465.29
crystal system	monoclinic
space group	C2/c
a, Å	15.3271(6)
b, Å	10.6612(4)
c, Å	24.0172(9)
β, deg	101.1750(10) <sup>o</sup>
V, Å <sup>3</sup>	3850.1(3)
Z	8
ρ <sub>calcd</sub> , g/cm <sup>3</sup>	1.605
μ, mm <sup>-1</sup>	0.945
θ range, deg	1.73 to 30.92
completeness to θ, %	94.9
reflections collected	41408
independent reflections	5800
R(int)	0.0366
restraints	0
parameters	274
Max., min. transmission	0.7461, 0.6672
R1(wR2) [I>2σ(I)]	0.0306 (0.0759)
R1(wR2)	0.0418 (0.0808)
GoF(F <sup>2</sup> )	1.344
max, min peaks, e.Å <sup>-3</sup>	0.468, -0.236

**Preparation of NO (g)/NO<sub>2</sub> (g) test strips and syringes.** Experimentalists desire a rapid and easy method to detect chemical changes. Colorimetric test strips are commonly used in synthetic chemistry and biology to quickly evaluate pH changes in aqueous solutions or quantitatively observe H<sub>2</sub>S release, using Pb(OAc)<sub>2</sub> strips, and metals ions, such as Al<sup>3+</sup>, Co<sup>2+</sup>, and Cu<sup>2+</sup>, and are available commercially from scientific vendors.<sup>31</sup>

Compounds **1** – **4** can be loaded on filter paper from a methylene chloride solution (Figure 2.25). Exposure to NO (g) or NO<sub>2</sub> (g) of these loaded paper strips results in qualitative color changes for the strips. This method provides a rapid and low cost method to qualitatively measure NO (g) or NO<sub>2</sub> (g) release from a chemical or biochemical reaction.

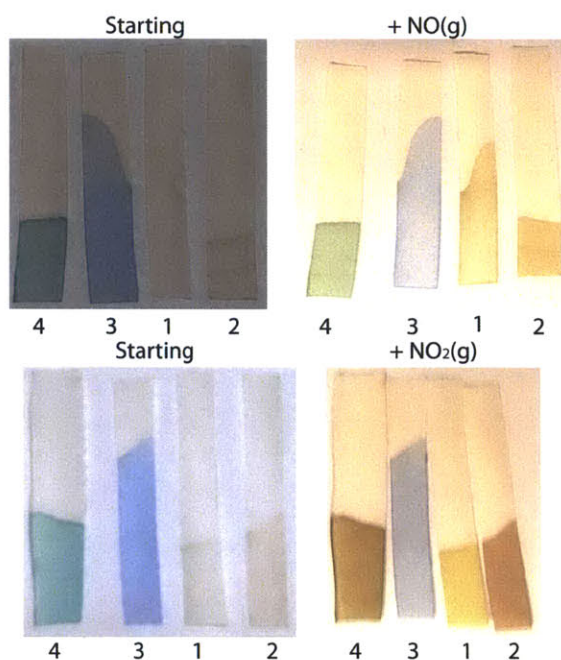


**Figure 2.25.** Filter paper strips loaded with **1** – **4** and exposed to 100 mmol NO (g) (top) and NO<sub>2</sub> (g) (bottom).

These individual strips can be combined into a single test strip by spotting silica TLC plates with multiple solutions of the compounds (Figure 2.26). These silica-based test strips require less space and allow for direct comparison of gas release from multiple compounds to determine whether the color change profile matches what is expected. Silica TLC plates have

been previously developed as test strips by loading with a colorimetric sensor to detect hypochlorite.<sup>32</sup>

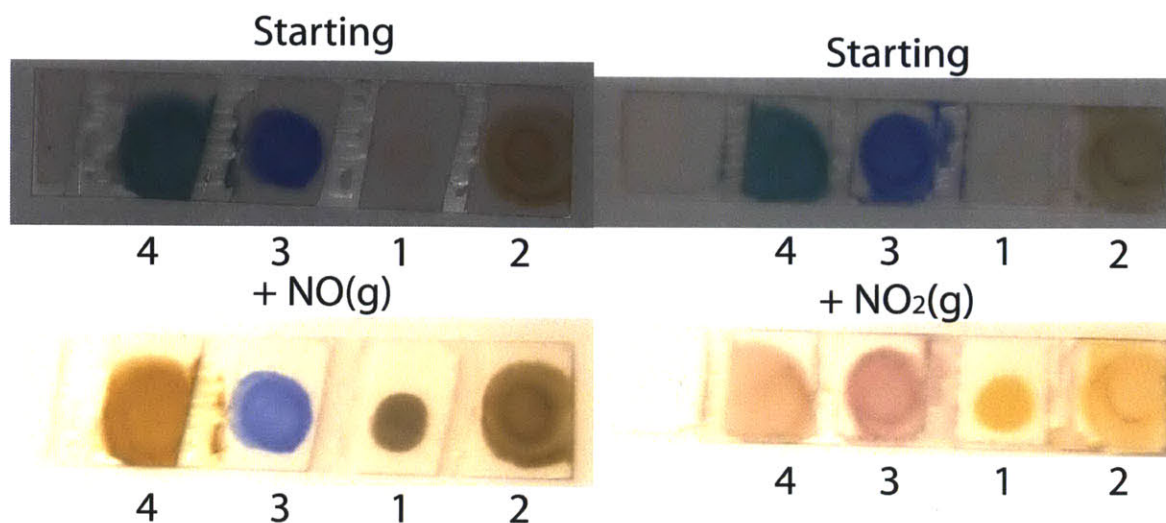


**Figure 2.26.** Silica TLC plates loaded with 1 – 4 and exposed to NO (g) (top) and NO<sub>2</sub>(g) (bottom).

These compounds can be loaded onto silica by dissolving in methylene chloride and evaporating onto silica gel. This silica gel bound sensor can be loaded into syringes equipped with needles (Figures 2.27 and 2.28). By pulling the headspace of a reaction through the syringe, the compound will change color and allow for the observation of NO (g) or NO<sub>2</sub> (g) release into the reaction headspace. An added benefit of using this device is by controlling the amount of compound loaded onto the syringe, we can quantitatively measure the amount of gas released in the reaction by how far along the syringe the color change occurs due to the rapid reaction with the colorimetric sensors. This rapid quantification can serve as an initial experiment for biochemical experiments to determine how much of 1 will be necessary to more accurately measure the amount of gas released by spectroscopic methods.

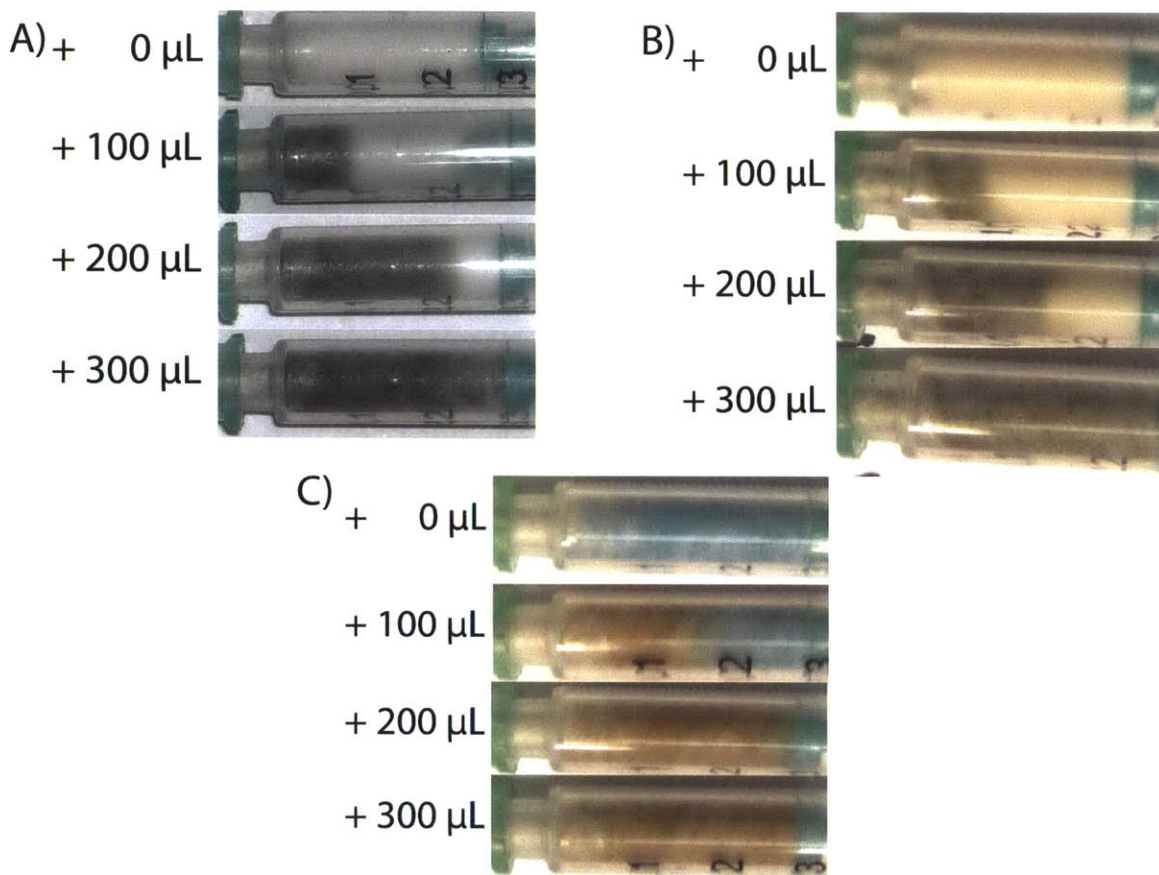


**Figure 2.27.** Syringes filled with A) 1, B) 2, and C) 4 loaded onto silica gel and exposed to varying amounts of NO (g).

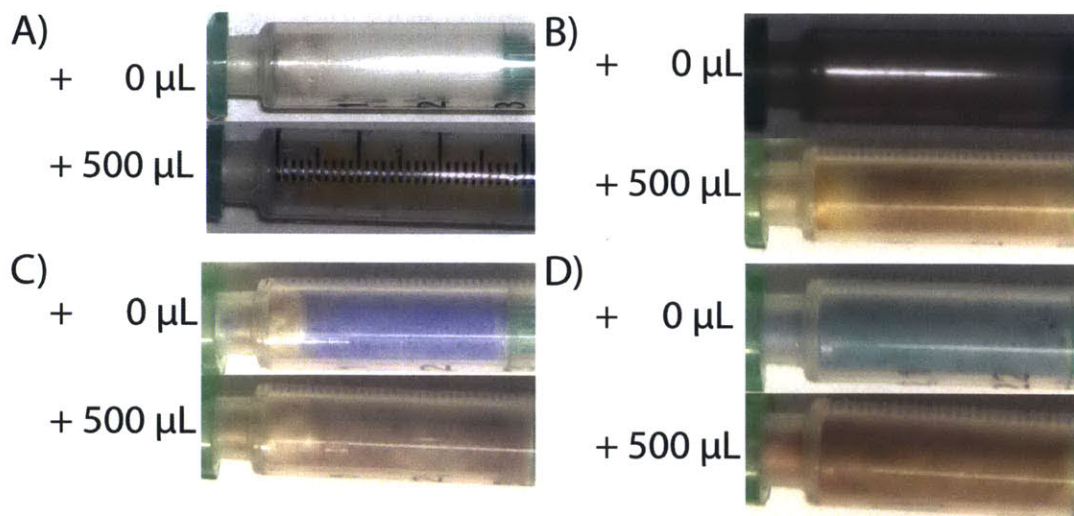


**Figure 2.28.** Syringes filled with A) 1, B) 2, C) 3, and D) 4 loaded onto silica gel and exposed to varying amounts of NO<sub>2</sub>(g).

### 3.4 Summary and Conclusions

New  $\text{Fe}^{2+}$  and  $\text{Co}^{2+}$  complexes using the *bis*-nitrogen donor ligand BIPhMe were prepared. These complexes were crystallographically and spectroscopically characterized. The iron and cobalt complexes are species of the type  $\text{M}(\text{BIPhMe})\text{X}_2$ , where M is  $\text{Fe}^{2+}$  or  $\text{Co}^{2+}$ , and X is  $\text{Cl}^-$ ,  $\text{Br}^-$ , or  $\text{I}^-$ .

The reaction of colorless 1,  $\text{Fe}(\text{BIPhMe})\text{Cl}_2$ , with  $\text{NO}$  (g) forms the dark green complex 5,  $[\text{Fe}(\text{BIPhMe})_2(\text{NO})\text{Cl}][\text{Fe}(\text{NO})\text{Cl}_3]$ , whereas the reaction with  $\text{NO}_2$ (g) forms the yellow complex 7,  $\text{Fe}(\text{BIPhMe})(\text{NO}_3)_2\text{Cl}$ . This complex can serve in a quantitative and qualitative assay to measure the release of  $\text{NO}$  (g) or  $\text{NO}_2$  (g) from reactions. The yellow compound 2,  $\text{Fe}(\text{BIPhMe})\text{Br}_2$ , can be used in a similar manner as it generates similar products.

Compound 3,  $\text{Co}(\text{BIPhMe})\text{Cl}_2$ , shows no reactivity toward  $\text{NO}$  (g), but the related compound 4,  $\text{Co}(\text{BIPhMe})\text{I}_2$ , does react with  $\text{NO}$  (g) to form two dinitrosyl species that we assign as  $[\text{Co}(\text{BIPhMe})(\text{NO})_2]^+$  and  $[\text{Co}(\text{BIPhMe})_2(\text{NO})_2]^+$ , as well as  $\text{I}_3^-$ . Both  $\text{Co}^{2+}$  complexes react with  $\text{NO}_2$  (g) and change color.

Using these metal complexes,  $\text{NO}$  (g) and  $\text{NO}_2$  (g) test strips were prepared using filter paper or silica TLC plates. These test strips could be placed in enclosed containers that share the headspace with reactions that form  $\text{NO}$  (g) and  $\text{NO}_2$  (g) and provide qualitative proof that these gases are generated. To more quantitatively measure gas generation, silica loaded syringes can be used to measure gas amounts.



### 3.5 References

1. Davies, I. R.; Zhang, X., Nitric Oxide Selective Electrodes. In *Methods Enzymol.*, Robert, K. P., Ed. Academic Press: 2008; Vol. Volume 436, pp 63.
2. Skodje, K. M.; Kwon, M.-Y.; Chung, S. W.; Kim, E., *Chem. Sci.* **2014**, DOI: 10.1039/C3SC53319K.
3. Wennmalm, Å.; Lanne, B.; Petersson, A.-S., *Analytical Biochemistry* **1990**, *187*, 359.
4. Abcam, Nitric Oxide Assay Kit (Colorimetric). In [http://www.abcam.com/ps/products/65/ab65328/documents/ab65328 Nitric Oxide Assay Kit Colorimetric \(Website\).pdf](http://www.abcam.com/ps/products/65/ab65328/documents/ab65328%20Nitric%20Oxide%20Assay%20Kit%20Colorimetric%20(Website).pdf), : 2012.
5. Green, L. C.; Wagner, D. A.; Glogowski, J.; Skipper, P. L.; Wishnok, J. S.; Tannenbaum, S. R., *Analytical Biochemistry* **1982**, *126*, 131.
6. Dacres, H.; Narayanaswamy, R., *Sens. Actuators, B* **2005**, *107*, 14.
7. Meng, Q. T.; Zhang, Y. X.; Hou, D. Y.; Xin, G.; Li, T. C.; He, C.; Duan, C. Y., *Tetrahedron* **2013**, *69*, 636.
8. Rathore, R.; Abdelwahed, S. H.; Guzei, I. A., *J. Am. Chem. Soc.* **2004**, *126*, 13582.
9. McQuade, L. E.; Pluth, M. D.; Lippard, S. J., *Inorg. Chem.* **2010**, *49*, 8025.
10. Lim, M. H.; Xu, D.; Lippard, S. J., *Nat. Chem. Biol.* **2006**, *2*, 375.
11. Tolman, W. B.; Liu, S. C.; Bentsen, J. G.; Lippard, S. J., *J. Am. Chem. Soc.* **1991**, *113*, 152.
12. Lorkovic, I. M.; Ford, P. C., *Inorg. Chem.* **2000**, *39*, 632.
13. Pangborn, A. B.; Giardello, M. A.; Grubbs, R. H.; Rosen, R. K.; Timmers, F. J., *Organometallics* **1996**, *15*, 1518.
14. Kent, T. A. *WMOSS v. 2.5: Mössbauer Spectral Analysis Software*, WEB Research Co., WEB Research Co.: Minneapolis, MN, 1998.
15. APEX2 v2009 *APEX2 v2009*, Bruker AXS: Madison, WI, 2009.
16. Sheldrick, G. M. *SADABS: Area-Detector Absorption Correction*, University of Göttingen: Göttingen, Germany, 2008.
17. Sheldrick, G., *Acta Crystallogr., Sect. A: Found. Crystallogr.* **2008**, *64*, 112.
18. Sheldrick, G. M. *SHELXTL97: Program for Refinement of Crystal Structures*, University of Göttingen: Göttingen, Germany, 1997.
19. Dolomanov, O. V.; Bourhis, L. J.; Gildea, R. J.; Howard, J. A. K.; Puschmann, H., *J. Appl. Crystallogr.* **2009**, *42*, 339.
20. Tran, C. T.; Kim, E., *Inorg. Chem.* **2012**, *51*, 10086.
21. Zang, Y.; Que, L., *Inorg. Chem.* **1995**, *34*, 1030.
22. Connelly, N. G.; Gardner, C., *J. Chem. Soc., Dalton Trans.* **1976**, 1525.
23. Kalyvas, H.; Coucouvanis, D., *Polyhedron* **2007**, *26*, 4765.
24. Siri, O.; Tabard, A.; Pullumbi, P.; Guillard, R., *Inorg. Chim. Acta* **2003**, *350*, 633.
25. Pohl, K.; Wieghardt, K.; Nuber, B.; Weiss, J., *J. Chem. Soc., Dalton Trans.* **1987**, 187.
26. Steimann, M.; Nagel, U.; Grenz, R.; Beck, W., *J. Organomet. Chem.* **1983**, *247*, 171.
27. Taft, K. L.; Masschelein, A.; Liu, S.; Lippard, S. J.; Garfinkel-Shweky, D.; Bino, A., *Inorg. Chim. Acta* **1992**, *198–200*, 627.
28. Halbauer, K.; Spielberg, E. T.; Sterzik, A.; Plass, W.; Imhof, W., *Inorg. Chim. Acta* **2010**, *363*, 1013.
29. Seddon, E. J.; Yoo, J.; Folting, K.; Huffman, J. C.; Hendrickson, D. N.; Christou, G., *J. Chem. Soc., Dalton Trans.* **2000**, 3640.

30. Craig, G. A.; Barrios, L. A.; Costa, J. S.; Roubeau, O.; Ruiz, E.; Teat, S. J.; Wilson, C. C.; Thomas, L.; Aromi, G., *Dalton Trans.* **2010**, *39*, 4874.
31. Machery-Nagel QUANTOFIX® test strips. <http://www.mn-net.com/tabid/4928/default.aspx> (accessed 7 April 2014).
32. Goswami, S.; Paul, S.; Manna, A., *Dalton Trans.* **2013**, *42*, 10097.

**CHAPTER 3: REACTIONS OF (PPN)(SNO)  
AND (PPN)(SSNO) WITH HBF<sub>4</sub> AND  
BIOMIMETIC IRON COMPLEXES**

### 3.1 Introduction

Owing to the high reactivity of NO, a majority of the biological functions attributed to NO may actually occur via secondary translocators such as *S*-nitrosothiols and dinitrosyl iron complexes (DNICs).<sup>1-8</sup> In a collaboration with our lab, it was recently discovered that biologically generated H<sub>2</sub>S promotes trans-membrane transfer of NO from *S*-nitrosated albumin in plasma to form *S*-nitrosohemoglobin inside red blood cells (Figure 3.1).<sup>9</sup> This transfer is presumably facilitated by thionitrous acid (HSNO), the smallest *S*-nitrosothiol.

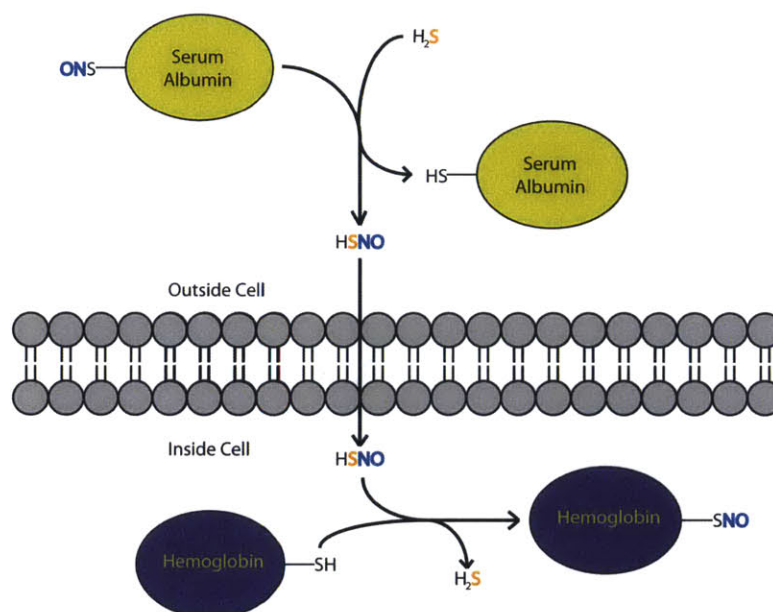


**Figure 3.1.** H<sub>2</sub>S can facilitate the transfer of NO from a *S*-nitrosated albumin across the membrane of white blood cells to an exposed cysteine on hemoglobin. This transfer is proposed to occur by formation of HSNO, the smallest *S*-nitrosothiol.

Preparation of the salts (PPN)(SSNO), **1**, and (PPN)(SNO), **2**, has been reported but no reactivity studies have been published.<sup>10</sup> The recent discovery of HSNO as an NO transfer reagent inspired us to undertake reactivity studies with an organic-soluble acid and known biomimetic iron complexes in organic solvents to make products that may be formed in biological systems. In this chapter, we describe a modified method for preparing **1** and **2**, along with their characterization. Reactivity studies of these *S*-nitrosothiols were performed with the

proton source  $\text{HBF}_4 \cdot \text{Et}_2\text{O}$ , **3**, and the biomimetic iron complexes  $[\text{Fe}^{\text{III}}(\text{TPP})\text{Cl}]$ , **4**,  $[\text{Fe}_2\text{S}_2(\text{SPh})_4]^{2-}$ , **5**,  $[\text{Fe}_2(\text{Et-HPTB})(\text{PHCOO})](\text{BF}_4)_2$ , **6**,  $[\text{Fe}_2(\mu\text{-OH})(\mu\text{-Ph}_4\text{DBA})(\text{TMEDA})_2(\text{OTf})]$ , **7**, and  $[\text{Fe}(\text{BIPhMe})\text{Cl}_2]$ , **8**. The *S*-nitrosothiol and  $\text{NO}(\text{g})$  chemistry of all of the iron compounds is either known or was explored here, and used as a comparison to further understand the chemistry exhibited by the  $\text{SNO}^-$  moiety.

### 3.2 Experimental Methods

**General comments.** All manipulations were performed under an atmosphere of nitrogen gas in an Mbraun glovebox.  $\text{NO}$  (Airgas, 99%) was purified by a literature procedure.<sup>11</sup> The  $\text{NO}$  gas stream was passed through an Ascarite column ( $\text{NaOH}$  fused on silica gel) and a 6 ft coil filled with silica gel that was cooled to  $-78$  °C using a dry ice/acetone bath. Nitric oxide was stored using standard gas storage bulbs and transferred via gastight syringes. Diethyl ether, tetrahydrofuran, pentane, methylene chloride, and acetonitrile were purified by passage through activated alumina then stored over 4-Å molecular sieves prior to use.<sup>12</sup> Acetone was distilled from  $\text{K}_2\text{CO}_3$  under argon and stored over 4-Å molecular sieves prior to use.<sup>13</sup>  $(\text{PPN})(\text{NO}_2)$ ,  $(\text{Bu}_4\text{N})_2[\text{Fe}_2\text{S}_2(\text{SPh})_4]$ ,  $[\text{Fe}_2(\mu\text{-OH})(\mu\text{-Ph}_4\text{DBA})(\text{TMEDA})_2(\text{OTf})]$ ,  $[\text{Fe}_2(\text{Et-HPTB})(\text{PHCOO})](\text{BF}_4)_2$ , and  $\text{Ph}_3\text{CSNO}$  were synthesized per literature procedure.<sup>14-18</sup>  $[\text{Fe}(\text{BIPhMe})\text{Cl}_2]$  was prepared as reported in chapter 2. All organics were purchased from Sigma-Aldrich and used as received. Triphenylphosphine was purchased from Alfa Aesar and purified by recrystallizing from hot hexanes.<sup>13</sup>  $\text{HBF}_4 \cdot \text{Et}_2\text{O}$  was purchased from Alfa Aesar and used as received.  $[\text{Fe}(\text{TPP})\text{Cl}]$  was purchased from Strem Chemicals and used as received after testing its purity by UV-Vis spectroscopy.

**Physical Measurements.** FTIR spectra were recorded on a Thermo Nicolet Avatar 360 spectrometer running the OMNIC software package. Low-resolution mass spectra were obtained with an Agilent 1100 Series LC/MSD mass spectrometer. UV–Vis spectra were recorded on a Cary-50 spectrophotometer in air-tight rubber septum-capped quartz cells at 25.0 °C. X-Band EPR spectra were recorded on a Bruker EMX EPR spectrometer at ambient temperature or at 77K using a quartz finger dewar. Samples for  $^{57}\text{Fe}$  Mössbauer studies were prepared by grinding a solid sample with Apiezon-N grease. These  $^{57}\text{Fe}$  Mössbauer samples were placed in an 80 K cryostat during measurement. A  $^{57}\text{Co/Rh}$  source was moved at a constant acceleration at room temperature against the absorber sample. All isomer shift ( $\delta$ ) and quadrupole splitting ( $\Delta E_Q$ ) values are reported with respect to  $^{57}\text{Fe}$ -enriched meta iron foil that was used for velocity calibration. The displayed spectrum was folded to enhance the signal-to-noise ratio. Fits of the data were calculated by the *WMOSS* plot and fit program, version 2.5.<sup>19</sup>

**Reaction monitoring of (PPN)(SNO) with  $\text{HBF}_4 \cdot \text{Et}_2\text{O}$  by UV–Vis.** A solution of 2 (240  $\mu\text{M}$ ) in acetonitrile was prepared in the glove box and added to a quartz cuvette. An airtight syringe was filled with the appropriate volume to add 10 equiv of 3. The cuvette was removed from the glovebox and placed into a Cary 50 UV–Vis spectrometer. After the initial scan was taken, the filled syringe was injected into the cuvette, which was shaken for 10 – 20 sec and placed back into the spectrometer. Scans were collected every 30 sec for the first 10 min, 1 min for the next 20 min, and every 5 min for the final 90 min.

**Reaction monitoring of (PPN)(SSNO) or (PPN)(SNO) with  $[\text{Fe}^{\text{III}}(\text{TPP})\text{Cl}]$  by UV–Vis.** A solution of 4 (14  $\mu\text{M}$ ) in tetrahydrofuran was prepared in the glove box and added to a quartz cuvette. Solutions of 1 (1.8 mM) and 2 (1.5 mM) in acetonitrile were prepared in the glovebox and an airtight syringe was filled with the appropriate volume to add 1 and 2 equiv. The cuvette

was removed from the glovebox and placed into a Cary 50 UV–Vis spectrometer. After the initial scan was taken, the filled syringe was injected into the cuvette, which was shaken for 10 – 20 sec and placed back into the spectrometer. Scans were collected every 30 sec for the first 10 min, 1 min for the next 20 min, and every 5 min for the final 90 min.

**ReactIR Measurements.** In situ IR spectra were recorded on a ReactIR iC 10 instrument from Mettler Toledo equipped with a 1 in. diameter, 30-reflection silicon ATR (SiComp) probe. In a typical experiment, the instrument was blanked with the solvent and a sample of **4** or **7**, at a concentration of 30 mM. After the first data collection time point, NO(g) was added to the anaerobic sample compartment through a rubber septum with a gas-tight syringe. The data were referenced to the initial scan and imported to *Origin 8.0* as a \*.spc file to generate the figures.

**X-ray Data Collection, and Structure and Solution Refinement.** Crystals of **1**, **2**, **11**·(PPN)(OTf), and **12** suitable for X-ray diffraction were mounted in Paratone N oil and frozen under a nitrogen cold stream maintained by a KRYO-FLEX low-temperature apparatus. Data were collected on a Bruker APEX CCD X-ray diffractometer with Mo K $\alpha$  radiation ( $\lambda$ = 0.71073 Å) controlled by the *APEX2* software package.<sup>20</sup> Empirical absorption corrections were calculated with *SADABS*.<sup>21</sup> The structure was solved by direct methods with refinement by full-matrix least-squares based on  $F^2$  using *SHELXTL-97*.<sup>22-24</sup> All non-hydrogen atoms were located and their positions refined anisotropically. Hydrogen atoms were assigned to idealized positions and given thermal parameters equal to either 1.5 (methyl hydrogen atoms) or 1.2 (non-methyl hydrogen atoms) times the thermal parameters of the atoms to which they were attached. The crystal of **12** exhibited non-merohedral twinning with a twin law of (-1 0 0) (0 -1 0) (0.5 0 1). One of the molecules of diethyl ether was highly disordered and was removed by using the *SQUEEZE* function in *Platon*.<sup>25,26</sup> Space group verification was performed using *Platon*. Figures

were generated using the *Olex 2.1* graphical user interface.<sup>27</sup> See Tables 3.1 and 3.4 below for crystallographic data and refinement details.

**Theoretical calculations.** Quantum mechanical density functional theory (DFT) calculations were performed on the different binding isomers of HSNO. The DFT calculations were carried out in *Gaussian03* using the B3LYP functional and the dgdzvp basis set in the gas phase.<sup>28-33</sup> The atomic coordinates from the crystal structure of **2** were used as the input for geometry optimizations. Frequency calculations were performed to confirm that the geometry converged at an energy minimum on the potential energy surface of the molecule.

**(PPN)(SSNO), 1.**<sup>10</sup> A 250 mL Erlenmeyer flask was charged with (PPN)(NO<sub>2</sub>) (7.36 g, 12.2 mmol) and sulfur (0.798 g, 24.4 mmol). This mixture was dissolved in acetone (210 mL) and stirred for 12 h, after which it had turned dark red with a yellow precipitate. The yellow precipitate was filtered and the dark red filtrate was collected and poured into 16 x 100 mm test tubes. These test tubes were placed into a 1 L jar filled with 400 mL diethyl ether and left standing for one week, after which black, dark red, orange, and yellow crystals formed. The black crystals were mechanically isolated and recrystallized an additional two times in an analogous fashion yielding 1.83 g (2.89 mmol, 23.7 %) of X-ray quality black blocks. The FTIR and UV-Vis spectroscopy matched the previously published spectra.<sup>10</sup> FTIR (KBr, cm<sup>-1</sup>): 3056 (w), 2974 (w), 2924 (w), 2869 (w), 1482 (w), 1437 (s), 1335 (ν<sub>NO</sub>, s), 1305 (s), 1286 (m), 1271 (m), 1181 (w), 1115 (s), 1047 (m), 997 (w), 902 (w), 795 (w), 763 (w), 741 (w), 721 (s), 692 (m), 662 (w), 549 (s), 531 (s), 496 (m). UV-Vis (MeCN, nm, ε, M<sup>-1</sup>cm<sup>-1</sup>): 420 (2720).

**(PPN)(SNO)·(CH<sub>3</sub>)<sub>2</sub>CO, 2.**<sup>10</sup> A 125 mL Erlenmeyer flask was charged with **1** (1.91 g, 3.02 mmol) and PPh<sub>3</sub> (1.58 g, 6.04 mmol). This mixture was dissolved in acetone (100 mL) and stirred for 24 h in the dark, after which the solution turned green. This green solution was filtered



and the filtrate was reduced to 10 mL and poured into 16 x 100 mm test tubes. These test tubes were placed into a 1 L jar filled with 400 mL diethyl ether and left standing for 1 week, after which dark green and orange crystals formed. The dark green crystals were isolated mechanically and recrystallized an additional time in an analogous fashion, yielding 1.163 g (1.765 mmol, 58.5 %) of X-ray quality dark green blocks. The FTIR and UV-Vis spectroscopy matched the previously published spectra.<sup>10</sup> FTIR (KBr,  $\text{cm}^{-1}$ ): 2921 (m), 2876 (w), 1438 (s), 1304 (m), 1264 (s), 1162 (w), 1115 (s), 1046 (m), 1026 (m), 997 (m), 724 (s), 693 (s), 548 (s), 534 (s), 500 (m). UV-Vis (MeCN, nm,  $\epsilon$ ,  $\text{M}^{-1}\text{cm}^{-1}$ ): 332 (2950).

**Reaction of (PPN)(SNO) with  $\text{HBF}_4 \cdot \text{Et}_2\text{O}$ .** In a 20 mL vial, **8** (13.0 mg, 31.8  $\mu\text{mol}$ ) was dissolved in acetonitrile (2 mL), resulting in a colorless solution. In a 5 mL vial, **2** (20.7 mg, 31.4  $\mu\text{mol}$ ) was dissolved in acetonitrile (2 mL), resulting in a dark green solution, and a stir bar was added. The 5 mL vial was placed into the 20 mL vial and the entire system was sealed with a rubber septum. A syringe was filled with **3** (60.4  $\mu\text{mol}$ ) and injected into the solution of **2** while stirring. The solution turned from dark green to orange to colorless within 1 min. The solution of **8** turned green, indicating the release of NO(g) (see chapter 2).

**Reaction of (PPN)(SSNO) with  $[\text{Fe}^{\text{III}}(\text{TPP})\text{Cl}]$ .** A 20 mL vial was charged with **1** (18.0 mg, 28.4  $\mu\text{mol}$ ) and **4** (10.0 mg, 14.2  $\mu\text{mol}$ ). This mixture was dissolved in tetrahydrofuran (10 mL) and stirred for 2 h, after which it was poured into pentanes (100 mL) and stirred for 10 min. A dark purple precipitate formed and was collected by filtration through Celite, followed by tetrahydrofuran extraction. The extracted product was characterized by UV-Vis, IR, and EPR spectroscopy to consist of  $[\text{Fe}^{\text{II}}(\text{TPP})]$ , **9**.<sup>34-36</sup> FTIR (KBr,  $\text{cm}^{-1}$ ): 3105 (w), 3028 (w), 2963 (w), 2923 (w), 2853 (w), 1698 ( $\nu_{\text{NO}}$ , s), 1598 (m), 1440 (m), 1347 (m), 1262 (m), 1203 (w), 1176 (m), 1114(w), 1072 (w), 1003 (s), 803 (m), 753 (m), 720 (m), 703 (m), 665 (w), 548 (w), 534 (m),

464 (w). EPR (X-band, 2Me-THF, RT, g-factor): 2.05 (avg, 3-line). The pentane-containing filtrate was stripped and characterized for  $S^0$  by addition of an excess of  $PPh_3$  (15 mg, 57.2  $\mu\text{mol}$ ), which formed  $Ph_3P=S$  as to contain  $S^0$  as characterized by  $^{31}\text{P}$  NMR spectroscopy.<sup>37</sup>  $^{31}\text{P}$  NMR (300 MHz,  $CDCl_3$ , ppm): 42.85 ( $S=PPh_3$ ), -4.81 ( $PPh_3$ ).

**Reaction of (PPN)(SNO) with  $[Fe^{III}(TPP)Cl]$ .** A 20 mL vial was charged with **2** (18.7 mg, 28.4  $\mu\text{mol}$ ) and **4** (10.0 mg, 14.2  $\mu\text{mol}$ ). This mixture was dissolved tetrahydrofuran (10 mL) and stirred for 2 h, after which it was poured into pentane (100 mL) and stirred for 10 min. A dark purple precipitate formed and was collected by filtration through Celite, followed by tetrahydrofuran extraction. The extracted product was characterized by UV-Vis, IR, and EPR spectroscopies to consist of **9**.<sup>34-36</sup> FTIR (KBr,  $\text{cm}^{-1}$ ): 2966 (w), 2920 (w), 2855 (w), 1697 ( $\nu_{NO}$ , s), 1597 (m), 1486 (w), 1440 (m), 1340 (m), 1263 (w), 1201 (w), 1175 (w), 1071 (m), 1002 (s), 805 (m), 752 (s), 721 (s), 703 (s), 661 (m), 534 (w), 500 (w). EPR (X-band, 2Me-THF, RT, g-factor): 2.05 (avg, 3-line). The pentane-containing filtrate was stripped and characterized by addition of  $PPh_3$  (9.8 mg, 37.4  $\mu\text{mol}$ ) to contain  $S^0$ , as characterized by  $^{31}\text{P}$  NMR spectroscopy.<sup>37</sup>  $^{31}\text{P}$  NMR (300 MHz,  $CDCl_3$ , ppm): 42.88 ( $S=PPh_3$ ), -4.80 ( $PPh_3$ ).

**Reaction of (PPN)(SSNO) with  $(^n\text{Bu}_4\text{N})_2[Fe_2S_2(\text{SPh})_4]$ .** A 20 mL vial was charged with **1** (29.1 mg, 46.0  $\mu\text{mol}$ ) and  $(^n\text{Bu}_4\text{N})_2[Fe_2S_2(\text{SPh})_4]$ , **5**, (10.0 mg, 11.5  $\mu\text{mol}$ ). This mixture was dissolved in tetrahydrofuran (10 mL) and stirred. After 2 h, the solution was poured into pentane (100 mL) and stirred for 10 min. A black precipitate formed and was collected by filtration through Celite, followed by tetrahydrofuran extraction. The extracted product was characterized by IR and EPR spectroscopy to contain the  $[Fe_4S_3(NO)_7]^{2-}$  anion,  $10^{2-}$ , and matched literature values.<sup>38</sup> FTIR (KBr,  $\text{cm}^{-1}$ ): 3052 (w), 2959 (m), 2871 (w), 1739 ( $\nu_{NO}$ , m), 1691 ( $\nu_{NO}$ , s), 1645 ( $\nu_{NO}$ , sh), 1587 (w), 1481 (w), 1437 (s), 1263 (s), 1183 (w), 1115 (s), 1062 (w), 1021 (w), 997 (m), 796 (w), 745

(m), 724 (s), 693 (s), 602 (w), 548 (m), 534 (s), 499 (m). EPR (X-band, 2Me-THF, RT, g-factor): 2.026 (avg, 5-line).

**Reaction of (PPN)(SNO) with  $(^n\text{Bu}_4\text{N})_2[\text{Fe}_2\text{S}_2(\text{SPh})_4]$ .** A 20 mL vial was charged with **2** (30.3 mg, 46.0  $\mu\text{mol}$ ) and **5**, (10.0 mg, 11.5  $\mu\text{mol}$ ). This mixture was dissolved in tetrahydrofuran (10 mL) and stirred. After 2 h, the solution was poured into pentane (100 mL) and stirred for 10 min. A black precipitate formed and was collected by filtration through Celite, followed by tetrahydrofuran extraction. The extracted product was characterized by ESI-MS spectrometry, and IR and EPR spectroscopy to contain  $\mathbf{10}^{2-}$ , and matched literature values.<sup>38</sup> ESI-MS (MeCN, m/z, calc'd): 242.3 ( $(\text{Et}_4\text{N})^+$ , 242.3 m/z), 538.4 ( $(\text{PPN})^+$ , 538.2), 439.5 ( $([\mathbf{10}-3\text{NO}]^-)$ , 439.6). FTIR (KBr,  $\text{cm}^{-1}$ ): 3053 (w), 2960 (m), 2933 (m), 2873 (m), 1741 ( $\nu_{\text{NO}}$ , m), 1691 ( $\nu_{\text{NO}}$ , s), 1659 ( $\nu_{\text{NO}}$ , sh), 1576 (w), 1470 (m), 1438 (m), 1381 (w), 1266 (m), 1183 (w), 1115 (s), 1082 (w), 1071 (w), 1024 (w), 997 (w), 884 (w), 741 (m), 724 (s), 693 (s), 547 (m), 535 (s), 501 (m). EPR (X-band, 2Me-THF, RT, g-factor): 2.026 (avg, 5-line).

**Reaction of (PPN)(SSNO) with  $[\text{Fe}_2(\text{Et}-\text{HPTB})(\text{PHCOO})](\text{BF}_4)_2$ .** A 20 mL vial was charged with **1** (11.5 mg, 18.2  $\mu\text{mol}$ ) and **6** (10.0 mg, 9.10  $\mu\text{mol}$ ). This mixture was dissolved in tetrahydrofuran (10 mL) and stirred for 6 h, after which it was poured into pentane (100 mL) and stirred for 10 min. A brown precipitate formed and was collected by filtration through Celite, followed by tetrahydrofuran extraction. The extracted product was stripped and characterized to be (PPN)[ $\text{FeS}_5(\text{NO})_2$ ], **11** by ESI-MS spectrometry, and FTIR and EPR spectroscopy and matched literature values.<sup>39</sup> ESI-MS (MeCN, m/z, calc'd): 275.6 ( $([\mathbf{11}]^-)$ , 275.8), 215.5 ( $([\mathbf{11}-2\text{NO}]^-)$ , 215.8). FTIR (KBr,  $\text{cm}^{-1}$ ): 3054 (w), 2974 (w), 1738 ( $\nu_{\text{NO}}$ , s), 1693 ( $\nu_{\text{NO}}$ , s), 1628 (s), 1588 (w), 1482 (w), 1438 (w), 1360 (sh), 1115 (s), 1064 (w), 724 (s), 692 (s), 534 (s). EPR

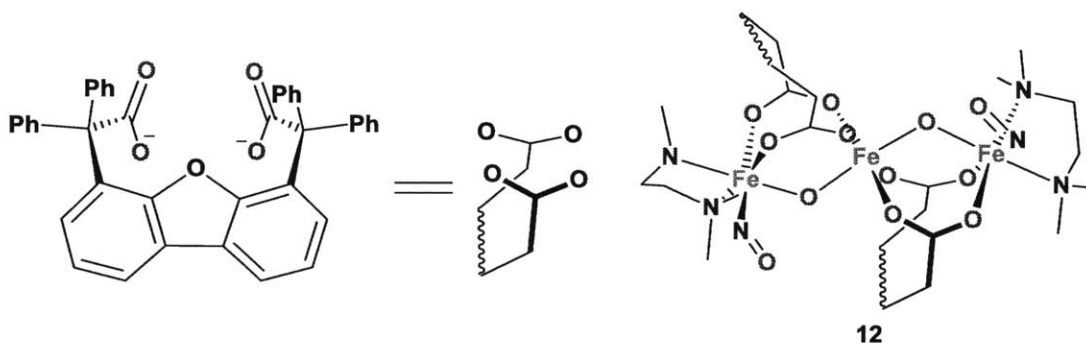
(X-Band, 2Me-THF, RT) g-factor: 2.030. EPR (X-Band, 2Me-THF, 77 K) g-factors: 2.0148, 2.0304, 2.0494.

**Reaction of (PPN)(SNO) with  $[\text{Fe}_2(\text{Et-HPTB})(\text{PHCOO})](\text{BF}_4)_2$ .** A 20 mL vial was charged with **2** (11.5 mg, 18.2  $\mu\text{mol}$ ) and **6** (10.0 mg, 9.10  $\mu\text{mol}$ ). This mixture was dissolved in tetrahydrofuran (10 mL) and stirred for 6 h, after which it was poured into pentane (100 mL) and stirred for 10 min. A black precipitate formed and was collected by filtration through Celite, followed by tetrahydrofuran extraction. The extracted product was characterized by ESI-MS and IR spectroscopy to consist of the  $[\text{Fe}_4\text{S}_3(\text{NO})_7]^-$  anion,  $10^{1-}$ , and matched literature values.<sup>38</sup> ESI-MS (MeCN, m/z, calc'd): 538.2 ((PPN)<sup>+</sup>, 538.2), 529.5 ( $[\text{10}]^-$ , 529.6), 499.4 ( $[\text{10-1NO}]^-$ , 499.6), 469.4 ( $[\text{10-2NO}]^-$ , 469.6), 439.4 ( $[\text{10-3NO}]^-$ , 439.6). FTIR (KBr,  $\text{cm}^{-1}$ ): 3057 (w), 2963 (w), 2923 (w), 1795 ( $\nu_{\text{NO}}$ , w), 1739 ( $\nu_{\text{NO}}$ , s), 1699 ( $\nu_{\text{NO}}$ , m), 1659 (w), 1627 (m), 1483 (w), 1439 (m), 1360 (w), 1268 (s), 1224 (w), 1185 (w), 1149 (w), 1115 (s), 1031 (s), 998 (w), 799 (w), 745 (w), 724 (s), 693 (s), 637 (s), 547 (m), 534 (s), 501 (m).

**Reaction of (PPN)(SSNO) with  $[\text{Fe}_2(\mu\text{-OH})(\mu\text{-Ph}_4\text{DBA})(\text{TMEDA})_2(\text{OTf})]$ .** A 20 mL vial was charged with **1** (11.5 mg, 18.2  $\mu\text{mol}$ ) and **7** (10.0 mg, 9.10  $\mu\text{mol}$ ). This mixture was dissolved in tetrahydrofuran (10 mL) and stirred for 6 h, after which it was poured into pentane (100 mL) and stirred for 10 min. A brown precipitate formed and was collected by filtration through Celite, followed by tetrahydrofuran extraction. The extracted product was stripped and characterized to be (PPN) $[\text{FeS}_5(\text{NO})_2]$ , **11** by ESI-MS spectrometry, and FTIR and EPR spectroscopy, and matched literature values.<sup>39</sup> Dark brown needles were grown by vapor diffusion of diethyl ether into a 2-methyl tetrahydrofuran solution, which were determined to be of **11**·(PPN)(OTf). FTIR (KBr,  $\text{cm}^{-1}$ ): 3054 (w), 2974 (w), 1738 ( $\nu_{\text{NO}}$ , s), 1693 ( $\nu_{\text{NO}}$ , s), 1628 (s),

1588 (w), 1482 (w), 1438 (w), 1360 (sh), 1115 (s), 1064 (w), 724 (s), 692 (s), 534 (s). EPR (X-Band, 2Me-THF, RT) g-factor: 2.030.

**Reaction of (PPN)(SNO) with  $[\text{Fe}_2(\mu\text{-OH})(\mu\text{-Ph}_4\text{DBA})(\text{TMEDA})_2(\text{OTf})]$ .** A 20 mL vial was charged with **2** (11.5 mg, 18.2  $\mu\text{mol}$ ) and **7** (10.0 mg, 9.10  $\mu\text{mol}$ ). This mixture was dissolved in tetrahydrofuran (10 mL) and stirred for 6 h, after which it was poured into pentane (100 mL) and stirred for 10 min. A black precipitate formed and was collected by filtration through Celite, followed by tetrahydrofuran extraction. The extracted product was characterized by ESI-MS and IR spectroscopy to consist of the  $[\text{Fe}_4\text{S}_3(\text{NO})_7]^-$  anion, **10**<sup>1-</sup>, and matched literature values.<sup>38</sup> ESI-MS (MeCN, m/z, calc'd): 538.2 ((PPN)<sup>+</sup>, 538.2), 529.5 ([**10**]<sup>-</sup>, 529.6), 499.4 ([**10**-1NO]<sup>-</sup>, 499.6), 469.4 ([**10**-2NO]<sup>-</sup>, 469.6), 439.4 ([**10**-3NO]<sup>-</sup>, 439.6). FTIR (KBr, cm<sup>-1</sup>): 3057 (w), 2963 (w), 2923 (w), 1795 (w), 1739 ( $\nu_{\text{NO}}$ , s), 1699 ( $\nu_{\text{NO}}$ , m), 1659 (w), 1627 (m), 1483 (w), 1439 (m), 1360 (w), 1268 (s), 1224 (w), 1185 (w), 1149 (w), 1115 (s), 1031 (s), 998 (w), 799 (w), 745 (w), 724 (s), 693 (s), 637 (s), 547 (m), 534 (s), 501 (m).



**$[\text{Fe}_3(\mu\text{-O})_2(\mu\text{-Ph}_4\text{DBA})_2(\text{TMEDA})_2(\text{NO})_2](\text{OTf})$ , **12**. Method a.** In a 50 mL Erlenmeyer flask, **7** (150 mg, 137  $\mu\text{mol}$ ) was dissolved in methylene chloride (15 mL). In a separate 20 mL vial,  $\text{Ph}_3\text{CSNO}$  (83.6 mg, 274  $\mu\text{mol}$ ) was dissolved in methylene chloride (15 mL) and instantly poured into the reaction flask and capped with a rubber septum. Throughout the course of the reaction, a 40 – 60  $\mu\text{L}$  aliquot was taken to monitor the reaction by solution IR between  $\text{CaF}_2$  salt

plates. After no further growth or decay in bands was observed in the 1500 – 1850  $\text{cm}^{-1}$  region (6 h), the reaction mixture was poured into 300 mL pentane and stirred for 10 minutes. The mixture was filtered through Celite and the remaining solid was extracted with 15 mL methylene chloride. The volume of the methylene chloride extract was reduced to 4 mL. Diethyl ether was vapor diffused into the methylene chloride solution to yield 60.5 mg dark green crystals of 11 (33.3  $\mu\text{mol}$ , 24.3 %) of X-ray diffraction quality. Anal. Calc'd for  $\text{C}_{93}\text{H}_{84}\text{F}_3\text{Fe}_3\text{N}_6\text{O}_{17}\text{S}\cdot(\text{CH}_2\text{Cl}_2)_{1.25}$ : C, 58.95; H, 4.54; N, 4.38. Found: C, 58.84; H, 4.37; N, 4.49. ESI-MS (MeCN,  $m/z$ ): 148.7 ( $(\text{OTf})^-$ , 149.0). FTIR ( $\text{CH}_2\text{Cl}_2$ ,  $\text{cm}^{-1}$ ): 1722 ( $\nu_{\text{NO}}$ , m). FTIR (KBr,  $\text{cm}^{-1}$ ): 3057 (w), 2954 (m), 2923 (s), 2852 (m), 1724 ( $\nu_{\text{NO}}$ , m), 1591 (s), 1492 (m), 1468 (s), 1444 (m), 1423 (w), 1375 (s), 1264 (s), 1223 (w), 1186 (m), 1156 (m), 1063 (w), 1030 (s), 951 (w), 860 (w), 801 (w), 767 (m), 741 (m), 725 (m), 700 (m), 680 (w), 638 (s), 575 (w), 517 (w), 492 (w).  $^{57}\text{Mössbauer}$  (mm/s) (80 K,  $\delta$  mm/s,  $\Delta E_{\text{Q}}$  mm/s,  $\Gamma$  mm/s): Site 1 – 0.70(2), 1.02(2), 0.32(2), Site 2 – 0.68(2), 1.47(2), 0.35(2), Site 3 – 0.51(2), 0.95(2), 0.49(2).

**Method b.** In a 20 mL vial, 7 (23.1 mg, 21.1  $\mu\text{mol}$ ) was dissolved in methylene chloride (3 mL) and the vial was sealed with a rubber septum.  $\text{NO}(\text{g})$  (2.5 mL, 102.6  $\mu\text{mol}$ ) was injected using a gas tight syringe into the reaction vial. After 6 h, the reaction mixture was poured into 100 mL pentane and stirred for 10 minutes. The mixture was filtered over and the remaining solid was extracted with 5 mL methylene chloride and stripped to yield 7.8 mg (4.3  $\mu\text{mol}$ , 19%) of a green-brown solid. The sample spectroscopically and crystallographically matched the isolated product from method a.

**Reaction of (PPN)(SSNO) with  $[\text{Fe}(\text{BIPhMe})\text{Cl}_2]$ .** A 20 mL vial was charged with 8 (21.4 mg, 52.3  $\mu\text{mol}$ ) and 1 (65.9 mg, 104  $\mu\text{mol}$ ). This mixture was dissolved in acetonitrile (10 mL) and stirred for 2 h, after which it was poured into diethyl ether (120 mL) and stirred for 10 min. A

light brown precipitate formed and was collected by filtration through Celite. The black filtrate was collected and stripped to leave a 46.9 mg of black solid. The black solid was dissolved in tetrahydrofuran (1.5 mL) and layered with pentanes. Black needle crystals formed over the course of 2 weeks and were collected to yield 27.9 mg of **11** (65 %) as characterized by FTIR and EPR spectroscopy.<sup>39</sup> FTIR (KBr,  $\text{cm}^{-1}$ ): 3054 (w), 2951 (w), 2859 (w), 1739 ( $\nu_{\text{NO}}$ , s), 1693 ( $\nu_{\text{NO}}$ , s), 1587 (w), 1482 (m), 1437 (s), 1281 (s), 1266 (s), 1183 (w), 1114 (s), 1067 (m), 1026 (w), 998 (w), 975 (w), 894 (w), 746 (m), 732 (s), 692 (s), 547 (m), 533 (s), 500 (m). EPR (X-Band, 2Me-THF, RT) g-factor: 2.030.

**Reaction of (PPN)(SNO) with [Fe(BIPhMe)Cl<sub>2</sub>].** A 20 mL vial was charged with **8** (21.7 mg, 53.1  $\mu\text{mol}$ ) and **2** (74.8 mg, 114  $\mu\text{mol}$ ). This mixture was dissolved in acetonitrile (10 mL) and stirred for 2 h, after which it was poured into diethyl ether (120 mL) and stirred for 10 min. A light brown precipitate formed and was collected by filtration through Celite. The black filtrate was collected and stripped to leave a 33.8 mg of black solid. The black solid was dissolved in tetrahydrofuran (1.5 mL) and layered with pentanes. Black needle crystals formed over the course of 2 weeks and were collected to yield 18.4 mg of **11** (43 %) as characterized by FTIR and EPR spectroscopy.<sup>39</sup> FTIR (KBr,  $\text{cm}^{-1}$ ): 3054 (w), 2954 (w), 2929 (w), 2842 (w), 1738 ( $\nu_{\text{NO}}$ , s), 1694 ( $\nu_{\text{NO}}$ , s), 1621 (w), 1587 (w), 1483 (m), 1438 (s), 1281 (s), 1264 (s), 1183 (w), 1115 (s), 1067 (m), 1027 (w), 997 (w), 975 (w), 894 (w), 747 (m), 723 (s), 692 (s), 547 (m), 534 (s), 500 (m). EPR (X-Band, 2Me-THF, RT) g-factor: 2.03 EPR (X-Band, 2Me-THF, 77 K) g-factors: 2.0138, 2.0294, 2.0485.

### 3.3 Results and Discussion

**Preparation and characterization of SSNO<sup>-</sup> and SNO<sup>-</sup>.** The originally reported syntheses of **1** and **2** were performed using only Schlenk techniques.<sup>10</sup> (PPN)(NO<sub>2</sub>) and elemental sulfur are

combined in a Schlenk flask and dissolved in acetone distilled over  $K_2CO_3$ . Over the course of a day, the solution would turn from a pale yellow to orange to a black solution containing the intended product **1** along with a variety of other sulfur, nitrogen, and oxygen containing species. Black crystals of **1** were formed by slow vapor diffusion of diethyl ether into the crude solution and then mechanically separated from the other colorless, yellow, orange, and red crystals. Fractional crystallization was used to prepare pure **1**. This tedious process was repeated multiple times until only black crystals crystallized. The apparatus for crystallization consisted of a specialized Schlenk flask with multiple tubes allowing for the filtration of the crude reaction solution into a tube that had common headspace with another tube containing diethyl ether. This setup allowed for the slow evaporation, deposition, and diffusion of diethyl ether into the solution of **1**.

The preparation of **2** would then follow by sulfur extraction from **1** by  $PPh_3$  in dry acetone. This reaction would yield a green solution. The purification of **2** was described as following a similar method as for **1**, but was described as being even more air-sensitive.

We were able to simplify the preparation of **1** and **2** by switching from Schlenk to glove box techniques. Mixing  $(PPN)(NO_2)$ , elemental sulfur, and acetone in an Erlenmeyer flask gives the color changes that were described in the original synthesis. The reaction mixture was then filtered through a glass frit and the filtrate was poured into test tubes to about a third of the maximum volume. These filled test tubes were placed into a 1 L jar filled with 400 mL diethyl ether and sealed. Over the course of a week, the diethyl ether would diffuse into the test tubes and generate a mixture of black, red, orange, yellow, and colorless crystals. Larger and easier to separate crystals were generated when the reaction was performed on a multi-gram scale rather



than a hundreds-of-milligram scale. To prepare batches of crystals that were only black, this method was employed at least three times.

The character of the black crystals was verified by UV-Vis and IR spectroscopy (Figure 3.2) and by X-ray crystallography (Figure 3.5). The UV-Vis spectrum of **1** (Figure 3.2) shows an absorption band at 420 nm in acetonitrile compared to the published value of 425 nm in methanol and 448 nm in acetone.<sup>10</sup> The  $\nu_{NO}$  band in the IR spectrum of **1** was determined to be  $1335\text{ cm}^{-1}$ , whereas the  $\nu_{NO}$  band shifts to  $1310\text{ cm}^{-1}$  when  $(PPN)(^{15}NO)$  was used. The shift upon isotopic labeling matches the calculated value of  $1311\text{ cm}^{-1}$  using the harmonic oscillator model.

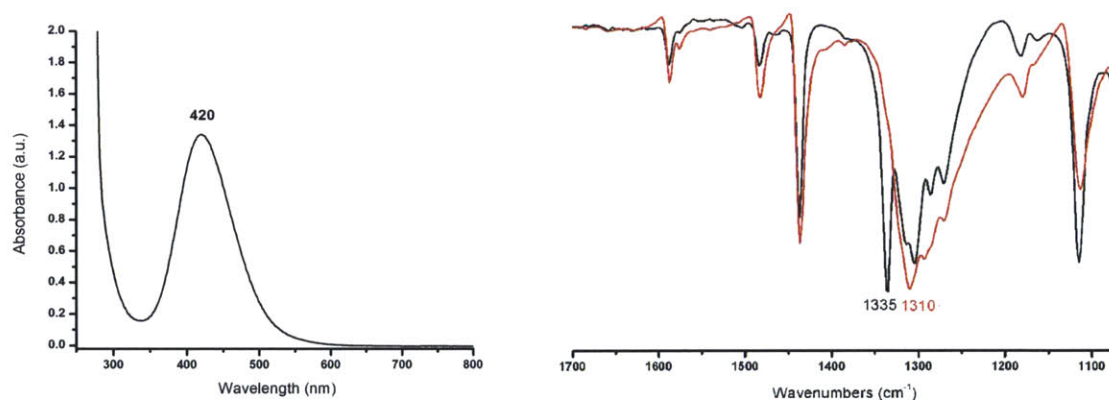


**Figure 3.2.** Spectroscopic characterization of  $(PPN)(SSNO)$ . The UV-Vis spectrum (left) was collected in acetonitrile at  $650\ \mu\text{M}$  at  $25^\circ\text{C}$ . The IR spectra of KBr pellets (right) of  $(PPN)(SSNO)$  (black line) and  $(PPN)(SS^{15}NO)$  (red line).

Compound **2** was prepared in a similar manner by dissolving crystals of **1** in acetone and adding freshly purified  $\text{PPh}_3$ . This reaction results in a deep green solution reminiscent of solutions consisting of  $\text{Ph}_3\text{CSNO}$ . During the first attempt to crystallize **2**, the solution turned orange and resulted in orange crystals, the nature of which is still unknown. However, when the reaction and crystallization were performed in the dark, deep green crystals were obtained that

were characterized as  $2 \cdot (\text{CH}_3)_2\text{CO}$  by X-ray crystallography and by UV-Vis and IR spectroscopy. The photoinstability of **2** should have been expected because other *S*-nitrosothiols degrade when exposed to light.<sup>40,41</sup> The collected crystals were stored in a  $-30^\circ\text{C}$  freezer to minimize exposure to light and to slow down any possible thermal decomposition pathways that may occur at ambient temperature.

In the UV-Vis spectrum (Figure 3.3), **2** has an absorption band at 332 nm in acetonitrile (Figure 3.3) that matches well with the published value of 350 nm in acetone. The spectrum of **2** in acetonitrile was published in the original synthesis paper to compare the absorption spectrum with that of  $(\text{PPN})(\text{NO}_2)$ , but no exact values were given for the absorption wavelength of **2**.<sup>10</sup> The absorption band of  $(\text{PPN})(\text{NO}_2)$  is listed as 352 nm in this report with a 10 – 20 nm blue shift for **2**.

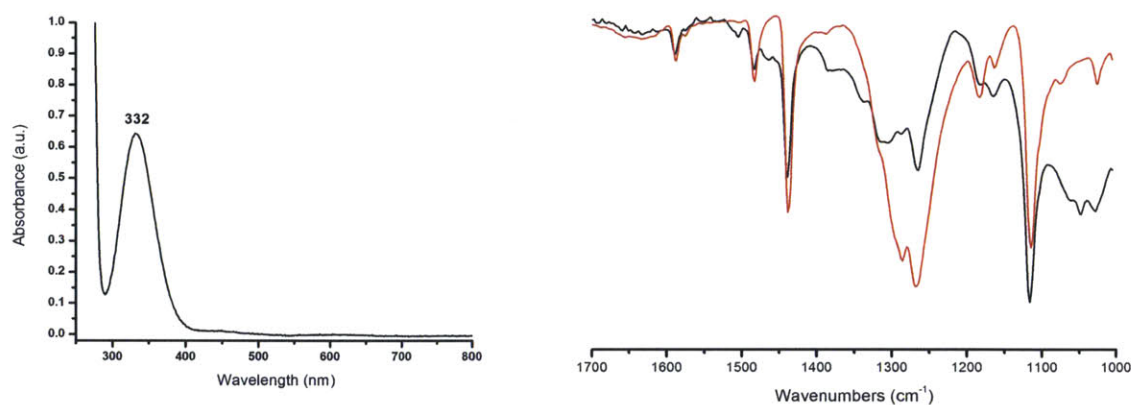


**Figure 3.3.** Spectroscopic characterization of  $(\text{PPN})(\text{SNO})$ . The UV-Vis spectrum (left) was collected in acetonitrile at  $220\ \mu\text{M}$  at  $25^\circ\text{C}$ . The IR spectra of KBr pellets (right) of  $(\text{PPN})(\text{SNO})$  (black line) and  $(\text{PPN})(\text{S}^{15}\text{NO})$  (red line).

*S*-nitrosothiols decompose electrochemically, and sulfur-containing compounds can exist in multiple redox states. The cyclic voltammogram of **2** (Figure 3.4) has an irreversible reduction at  $-2.64\ \text{V}$ , which is much lower than the value of  $-1.36\ \text{V}$  published for  $\text{Ph}_3\text{CSNO}$ .<sup>42</sup> Measurement of the oxidation potential was hindered by the strongly oxidizing ability of **2**

because after a single scan the silver wire pseudo-reference electrode would be covered in a black material and the redox events would be shifted, requiring us to perform all CV measurements with ferrocene present as an internal reference. The reduction potential of **2** is so great that dissolution in methylene chloride results in effervescence and a color change from green to orange.

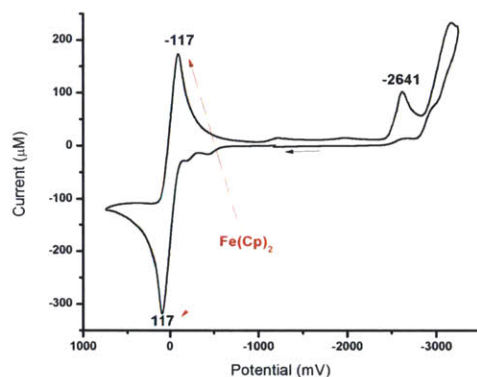


**Figure 3.4.** Cyclic voltammogram of **2** in acetonitrile performed at 100 mV/s. The scan was referenced to the Fc/Fc<sup>+</sup> redox couple at 0.00 V.

The crystal structure of **1** (Figure 3.5) consists of a single PPN<sup>+</sup> cation and a disordered SSNO<sup>-</sup> anion. The SSNO<sup>-</sup> anion has a *syn* conformation with a dihedral angle of 20.34°. The S–N–O bond angle is 117.3(4)°. The N–O bond distance is 1.257(6) Å and the S–N bond distance is 1.689(7) Å. The crystal structure of **2** has a co-crystallized acetone molecule. For **2**, the S–N–O bond angle is 118.30(15)°, and has an N–O bond distance of 1.222(2) Å and a S–N bond distance of 1.707(2) Å. The S–N bonds are shorter and the N–O bonds are longer for **1** and **2** compared to the published crystal structures of three other crystallographically characterized *S*-nitrosothiols Ph<sub>3</sub>CSNO, *S*-nitrosoacetyl-D,L-penicillamine (SNAP), and TrmSNO (Table 3.2, Figure 3.6).<sup>42,43</sup>

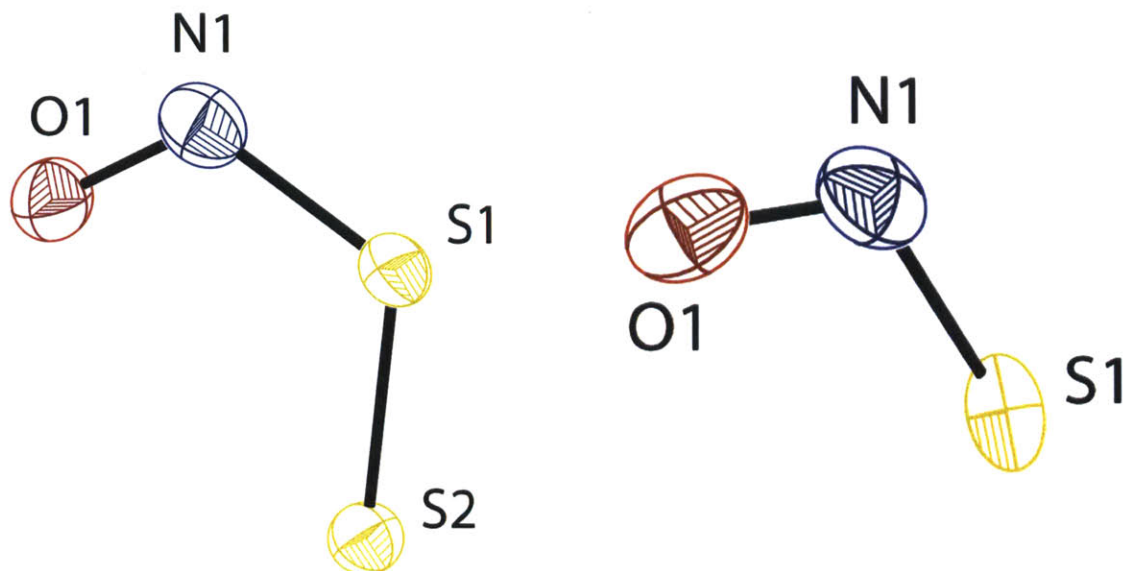


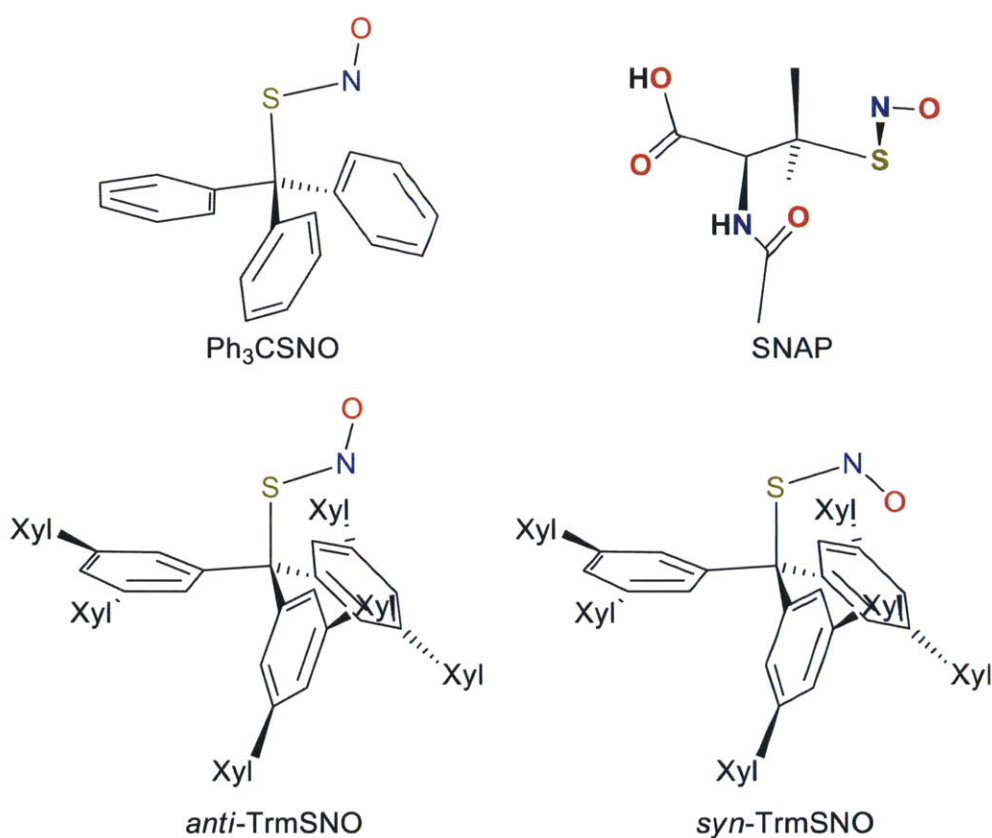
**Figure 3.5.** Drawings of the X-ray crystal structures of  $\text{SSNO}^-$  (left) and  $\text{SNO}^-$  (right). Ellipsoids are drawn at 50% probability. Cations and solvent molecules are omitted for clarity. Color scheme: sulfur, yellow; nitrogen, blue; oxygen, red.

**Table 3.1.** Crystallographic parameters for **1** and **2** at 100K.

compounds	(PPN)(SSNO), <b>1</b>	(PPN)(SNO)·(CH <sub>3</sub> ) <sub>2</sub> O, <b>2</b>
formula	C <sub>36</sub> H <sub>30</sub> N <sub>2</sub> OP <sub>2</sub> S <sub>2</sub>	C <sub>39</sub> H <sub>36</sub> N <sub>2</sub> O <sub>2</sub> P <sub>2</sub> S
formula weight	632.68	658.70
crystal system	orthorhombic	triclinic
space group	Pbcn	P $\bar{1}$
a, Å	11.8640(5)	9.4246(4)
b, Å	16.7022(7)	10.5576(4)
c, Å	15.5266(6)	17.2008(7)
$\alpha$ , deg	90	92.356(1)
$\beta$ , deg	90	95.200(1)
$\gamma$ , deg	90	92.392(1)
V, Å <sup>3</sup>	3076.7(2)	1701.24(12)
Z	4	2
$\rho_{\text{calcd}}$ , g/cm <sup>3</sup>	1.366	1.286
$\mu$ , mm <sup>-1</sup>	0.311	0.227
$\theta$ range, deg	2.11 to 25.13	1.93 to 27.97
completeness to $\theta$ , %	99.8	99.5
reflections collected	45752	33356
independent reflections	2755	8140
R(int)	0.0239	0.0247
restraints	0	0
parameters	213	417
Max., min. transmission	0.7452, 0.6952	0.7456, 0.7018
R1(wR2) [ $I > 2\sigma(I)$ ]	0.0351 (0.1360)	0.0422 (0.1340)
R1(wR2)	0.0380 (0.1384)	0.0484 (0.1381)
GoF( $F^2$ )	2.669	1.877
max, min peaks, e.Å <sup>-3</sup>	0.351, -0.324	1.030, -0.711

**Table 3.2.** Bond lengths and angles of *S*-nitrosothiols.

	(PPN)(SSNO), <b>1</b>	(PPN)(SNO), <b>2</b>	Ph <sub>3</sub> CSNO <sup>42</sup>	SNAP <sup>42</sup>	<i>anti</i> -TrmSNO <sup>43</sup>	<i>syn</i> -TrmSNO <sup>43</sup>
bond lengths, (Å)						
N–O	1.257(6)	1.222(2)	1.177(6)	1.206(3)	1.205(6)	1.189(12)
S–N	1.689(7)	1.707(2)	1.792(5)	1.762(3)	1.781(5)	1.781(5)
S/C–S	1.978(2)	–	1.867(3)	1.842(2)	1.841(4)	1.841(4)
bond angles, (°)						
O–N–S	117.3(4)	118.30(15)	114.0(4)	114.9(2)	111.4(6)	123.6(7)
N–S–S/C	115.7(2)	–	102.1(2)	96.56(8)	104.2(3)	104.2(3)
O–N–S–X	20.34	–	175.7	179.7	179.6	7.3

**Figure 3.6.** Crystallographically characterized small molecule organo-*S*-nitrosothiols.

**HBF<sub>4</sub>·Et<sub>2</sub>O reactivity.** To explore the affect that protons have on SNO<sup>−</sup> and to possibly prepare HSNO in an organic solvent for further reactivity studies, the acid HBF<sub>4</sub>·Et<sub>2</sub>O, **3**, was allowed to react with **2** in acetonitrile. When the reaction was followed by UV-Vis (Figure 3.7), instant bleaching and a loss of the absorption band at 332 nm was observed.

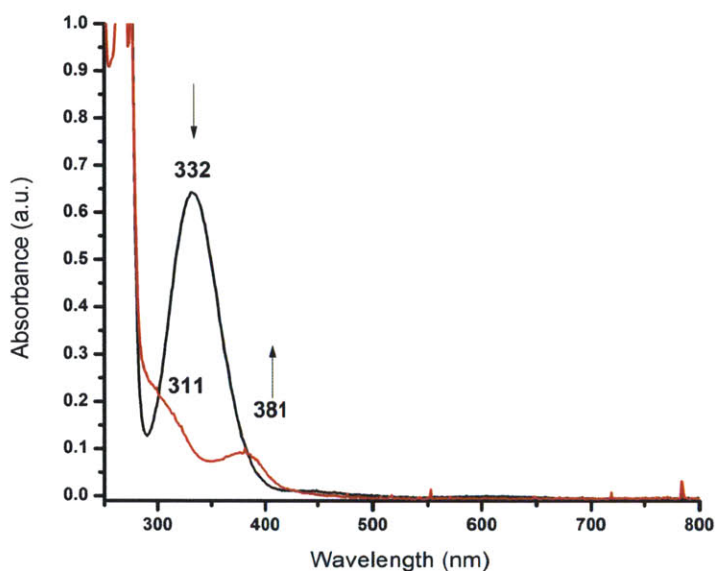


**Figure 3.7.** UV-Vis spectrum of 0.24 mM **2** (black) and **2** + **3** (red) in acetonitrile at 25° C.

To test whether the S–N bond is being homolytically or heterolytically cleaved upon addition of acid, the reaction was repeated in a enclosed environment also containing the colorimetric NO(g) sensor [Fe(BIPhMe)Cl<sub>2</sub>], **8** (Figure 3.8). Addition of **3** to **2** results in a rapid color change from green to orange to colorless, and a color change of the solution of **8** from colorless to dark green, providing evidence that NO(g) is released in an acidic environment. Homolytic cleavage of the S–N bond was previously proposed by calculations to be the more favorable process.<sup>44</sup>



**Figure 3.8.** Left: A 20 mL vial containing a colorless solution of **8** in acetonitrile and a 5 mL vial containing a green solution of **2** in acetonitrile. Right: Addition of **3** to the solution of **2** results in color loss by decomposition of  $\text{SNO}^-$  to form  $\text{NO}(\text{g})$ . The released  $\text{NO}(\text{g})$  reacted with the solution of **8** to turn it green.

This reaction product of  $\text{SNO}^-$  differs from the known reactivity of *S*-nitrosothiols in acidic environments that results in the heterolytic cleavage of the S–N bond to form  $\text{RS}^-$  and  $\text{NO}^+$ , while we observe  $\text{NO}(\text{g})$  release.<sup>45</sup> The fate of the sulfur is currently unknown but the sulfanyl radical ( $\text{HS}^\bullet$ ) could potentially form and subsequently react with itself to form persulfide ( $\text{H}_2\text{S}_2$ ) and further disproportionate to  $\text{H}_2$  and  $\text{S}^0$ .<sup>46</sup> The sulfanyl radical is a known product in thermal decomposition of methyl and ethyl thiolates, or as an intermediate in sulfide dehydrogenation of  $\text{HS}^-$  to  $\text{S}^0$  in sulfur bacteria.<sup>47,48</sup>

The  $\text{SNO}^-$  anion can be protonated at three different sites, the sulfur, the nitrogen, or the oxygen atom. DFT calculations using Gaussian 03 using the B3LYP functional with the dgdzvp basis set allowed us to compare the effects that protonation could have on the  $\text{SNO}^-$  anion (Figure 3.9). Protonation of the sulfur resulted in the structure with the lowest energy. Protonation of the nitrogen to form a  $\text{S}(\text{HN})\text{O}$  molecule results in a free energy that is 12.9 kJ/mol higher, whereas protonation of the oxygen to form  $\text{SNOH}$  has a free energy that is 31.5 kJ/mol higher than  $\text{HSNO}$ . The calculated S–N bond length for  $\text{SNO}^-$  is 1.741 Å, which is

longer than the crystallographically determined value of 1.689(7) Å, however, upon protonation the calculated S–N bond is elongated to 1.889 Å. Previously reported calculations determined the S–N bond bond energy to be 27.76 kcal/mol in HSNO and would therefore have a homolytic dissociation rate constant of  $1.75 \times 10^{-10} \text{ s}^{-1}$  at 298 K. Possible double protonation of the sulfur may induce S–N bond cleavage and result in the observed NO(g) release.

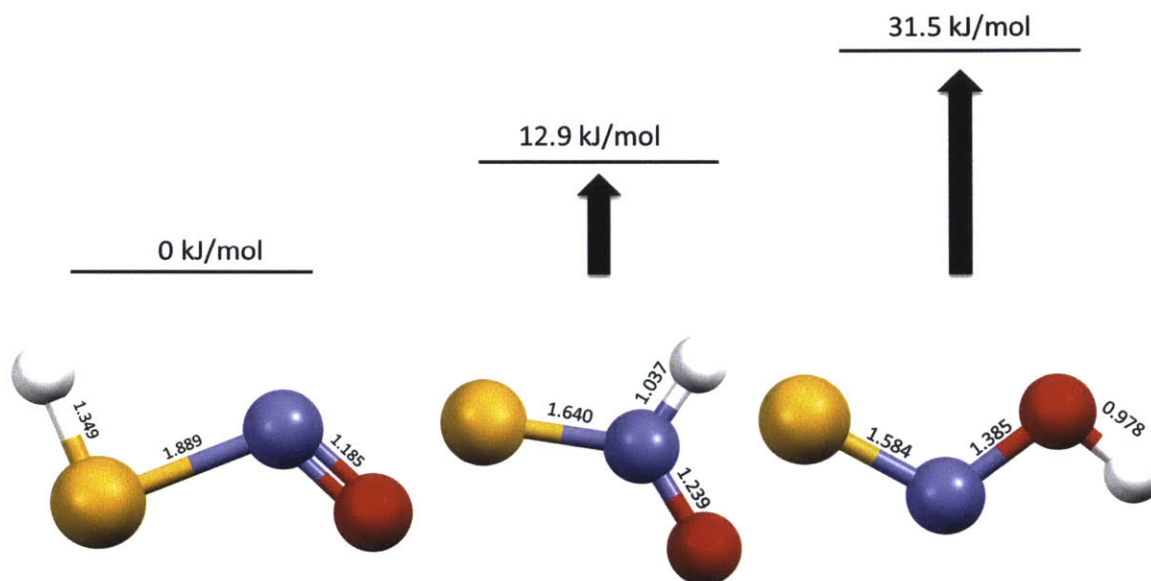


**Figure 3.9.** Calculated Energies and structures of the protonated forms of  $\text{SNO}^-$ . These values were calculated by DFT methods in the gas phase using B3LYP/DGDZVP.

**Iron-porphyrin reactivity.** The reaction of **1** or **2**, with  $[\text{Fe}^{\text{III}}(\text{TPP})\text{Cl}]$ , **4**, forms the products  $[\text{Fe}^{\text{II}}(\text{TPP})(\text{NO})]$ , **9**, a  $\{\text{Fe}(\text{NO})\}^7$  species by the Enemark-Feltham notation, and  $\text{S}^0$ .<sup>49</sup> A 3-line EPR spectrum with  $\langle g \rangle = 2.05$  at ambient temperature provided evidence that **9** was formed and is in agreement with previously published spectra of **9** (Figure 3.10).<sup>36</sup> In the IR spectrum, a  $\nu_{\text{NO}}$  band at  $1698 \text{ cm}^{-1}$  is observed in the IR spectrum. This result matches well with the different published values for the  $\nu_{\text{NO}}$  band of **9**, ranging from  $1670 \text{ cm}^{-1}$  to  $1700 \text{ cm}^{-1}$ .<sup>34,50</sup> The lack of other bands in the  $1650 - 1950 \text{ cm}^{-1}$  region suggested that coordination of a sulfur species did not occur to any of the nitrosated complexes.<sup>50</sup> Attempts to measure the conversion of **4** to **9** by



ReactIR were unsuccessful due to the high concentration of analyte needed that is above the solubility limit of **1** and **2** in CD<sub>3</sub>CN.

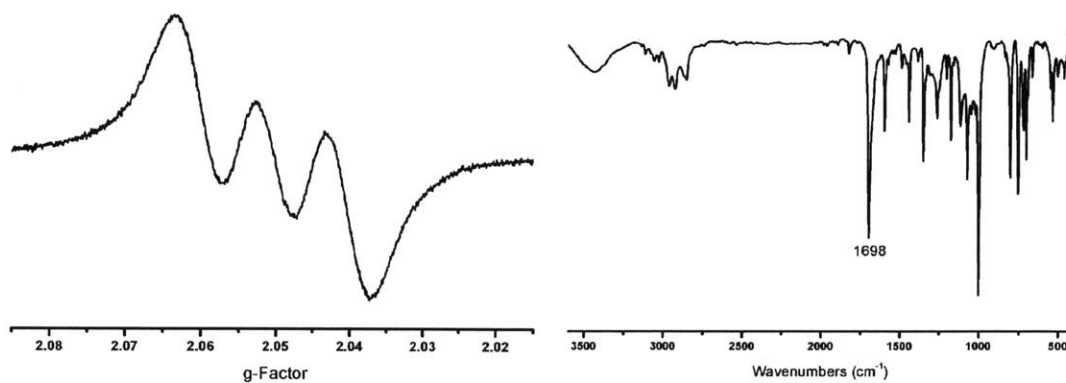


**Figure 3.10.** EPR (left) and FTIR (right) spectroscopic characterization of [Fe<sup>II</sup>(TPP)(NO)] (**9**) from [Fe<sup>III</sup>(TPP)Cl] (**4**) and (PPN)(SNO) (**2**). EPR Conditions: RT; frequency 9.845 GHz, microwave power 2.017 mW, modulation amplitude 2.0 G;  $\langle g \rangle = 2.05$ .

Formation of S<sup>0</sup> was observed by extraction into pentanes and addition of a slight excess of triphenylphosphine to form triphenylphosphine sulfide, S=PPh<sub>3</sub>. The <sup>31</sup>P NMR experiment shows a peak at 42.88 ppm that matches the published value of 42.6 ppm for S=PPh<sub>3</sub>, along with some residual PPh<sub>3</sub> at -4.80 ppm (Figure 3.11).<sup>37</sup> This result suggests that oxidation of the sulfur is what drives the reduction of the iron.

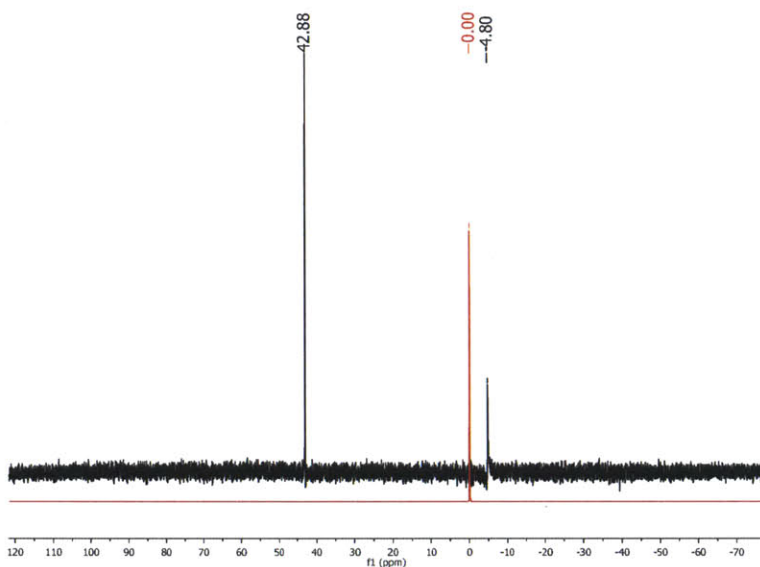


**Figure 3.11.**  $^{31}\text{P}$  NMR spectrum of the pentane extract of the reaction of **4** and **1**, in  $\text{CDCl}_3$  (black line) and the external reference  $\text{H}_3\text{PO}_4$  (red line). The peak at 42.88 ppm is  $\text{S}=\text{PPh}_3$  and the peak at -4.80 ppm is residual  $\text{PPh}_3$ .

Conversion of **4** to **9** can be monitored by UV-Vis spectroscopy (Figure 3.12) by watching the blue shift of the Soret band from 417 nm to 410 nm, along with the loss of the Q-band at 507 nm and formation of new Q-bands at 472 and 546 nm. This reaction is similar to the reductive nitrosylation observed when the DNIC  $[\text{Fe}(\text{NO})_2((2,6\text{-diisopropylphenyl})\text{NC}(\text{Me})_2\text{CH})]$  reacts with **4**, resulting in the formation of **9** and the MNIC  $[\text{Fe}(\text{NO})\text{Cl}((2,6\text{-diisopropylphenyl})\text{NC}(\text{Me})_2\text{CH})]$ .<sup>35</sup> The reaction of the DNIC with **4** goes to completion after 30 min, but the reaction of **1** or **2** with **4** goes to completion within minutes.

Stopped-flow UV-Vis spectroscopy was used to determine some kinetic parameters for the reaction of **1** with **4** (Figure 3.13). The  $k_1$  and  $k_2$  parameters of the reaction were in agreement for all spectral changes, 0.17(1) a.u./sec and 0.0322(7) a.u./sec respectively.

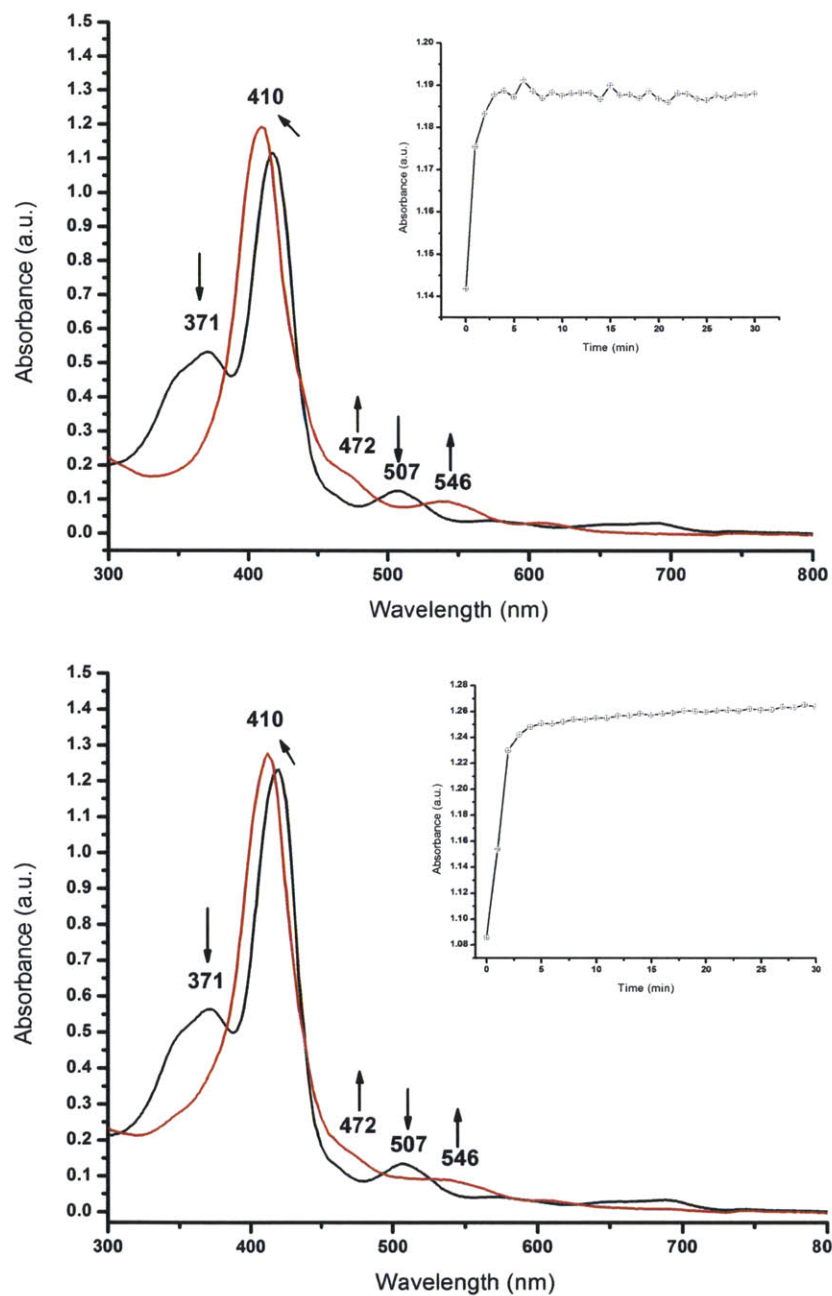


**Figure 3.12.** UV-Vis spectrum of the reaction of **4** ( $14 \mu\text{M}$ ) with 1 equiv **1** (top) and **2** (bottom) to form **9**. Insets are kinetic traces of the Soret band at 410 nm.

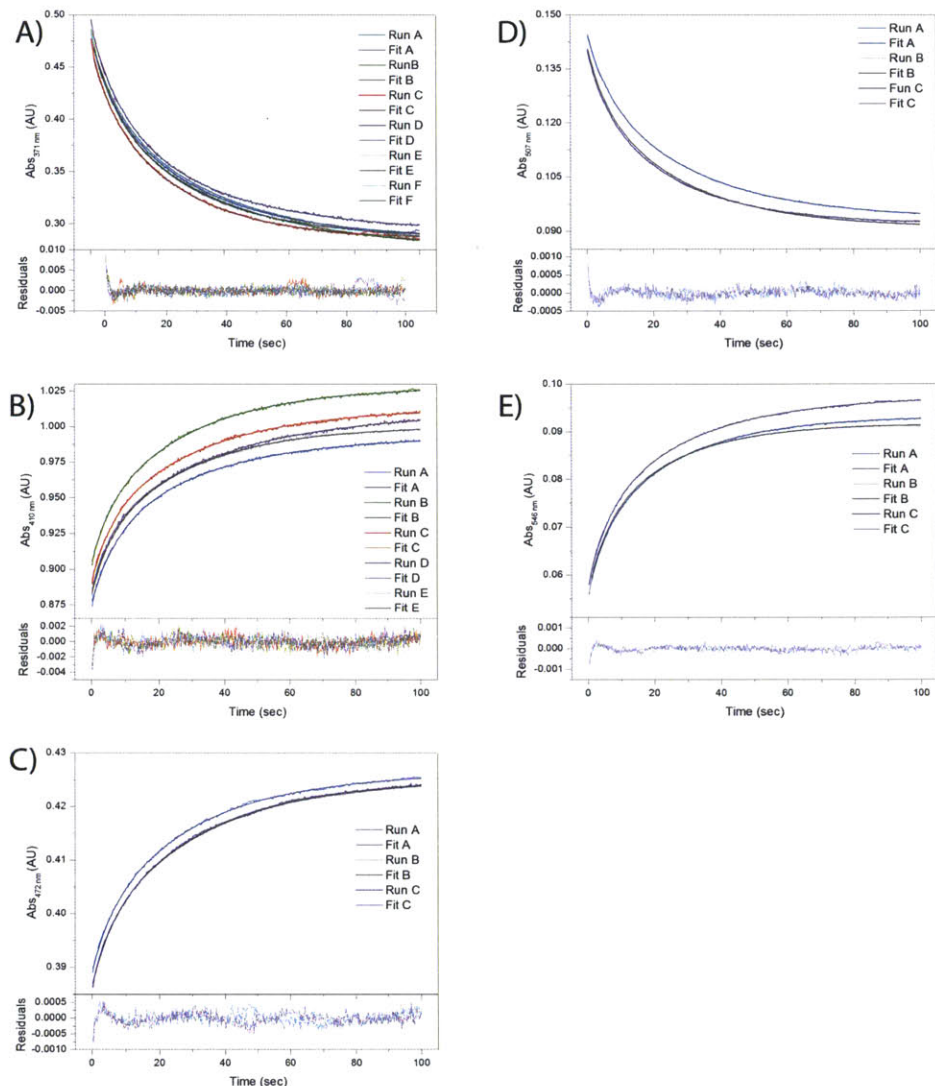
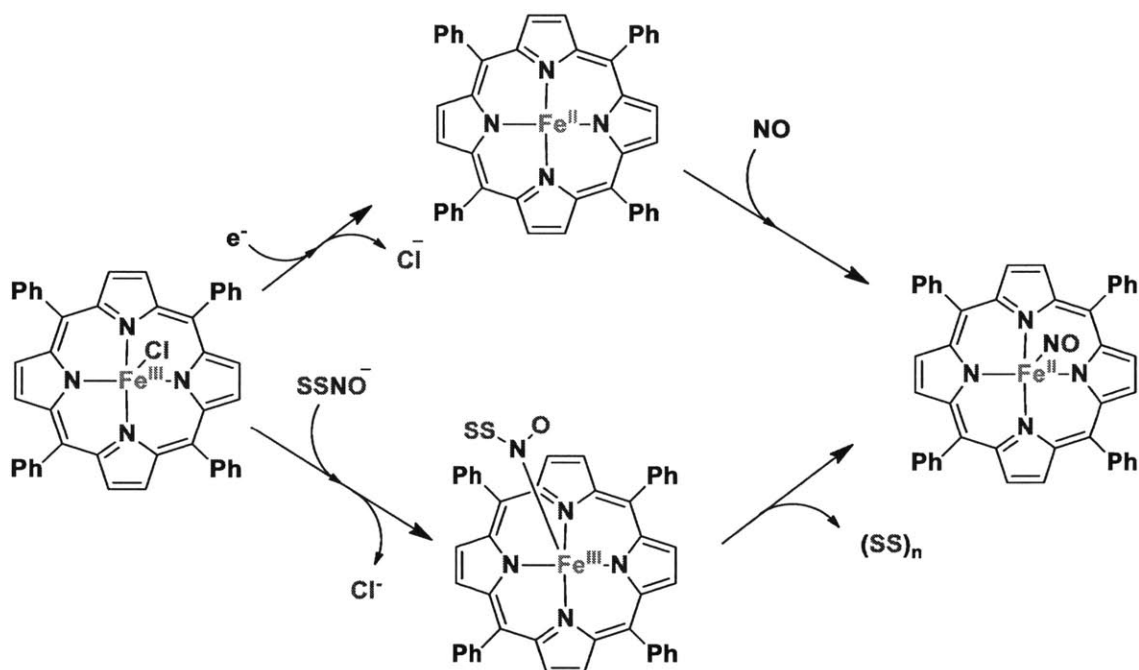


**Figure 3.13.** Stopped-flow kinetic traces and fits of the reaction of 28  $\mu\text{M}$  **1** and 14  $\mu\text{M}$  **4** at different wavelengths in tetrahydrofuran. Residuals of the fits are shown below each kinetic trace. A) 371 nm, B) 410 nm, C) 472 nm, D) 507 nm, and E) 546 nm.

This kinetic data allow for two potential reaction pathways to exist (Scheme 3.1). In one pathway, outer-sphere electron transfer can occur with dissociation of the chloride ligand resulting in  $[\text{Fe}^{\text{II}}(\text{TPP})]$ , which would then react with the release of  $\text{NO}(\text{g})$  to form **9**. The other potential pathway involves ligand metathesis of the chloride with  $\text{SSNO}^-$ . Heterolytic cleavage of the S–N bond would then occur to form **9** and release  $\text{S}_n^0$ . A previous study using a water-soluble iron(II) porphyrin nitrosonium complex,  $[\text{Fe}^{\text{II}}(\text{P})(\text{NO}^+)]$ , and  $\text{HS}^-$  resulted in the

formation of  $[\text{Fe}^{\text{II}}(\text{P})(\text{HSNO})]$ .<sup>51</sup> This result suggests that the second reaction pathway may be the correct route.



**Scheme 3.1.** Suggested pathways in the reaction of **1** and **4**.

In an attempt to compare the reactivity of **4** with  $\text{NO}(\text{g})$  in acetonitrile, the reaction was monitored by ReactIR (Figure 3.14). The result was not a  $\nu_{\text{NO}}$  band in the  $1670 - 1700 \text{ cm}^{-1}$  region, but rather a strong band at  $1883 \text{ cm}^{-1}$ , corresponding to the formation of  $[\text{Fe}^{\text{III}}(\text{TPP})(\text{NO})\text{Cl}]$ .<sup>36</sup> Reductive nitrosylation of ferric porphyrins using  $\text{NO}(\text{g})$  occurs only in protic solvents, such as  $\text{H}_2\text{O}$  and  $\text{MeOH}$ , to form  $[\text{Fe}^{\text{II}}(\text{por})(\text{NO})]$  and  $\text{HNO}_2$ .<sup>36,52</sup> The reaction occurs on a slower time scale, taking longer than an hour to complete. The reaction of **4** with  $\text{Ph}_3\text{CSNO}$  in acetonitrile did not form **9** in any appreciable amount. These results suggest that **1** and **2** have a stronger nitrosating effect on iron(III) porphyrins than typical *S*-nitrosothiols,  $\text{NO}(\text{g})$ , and DNICs.

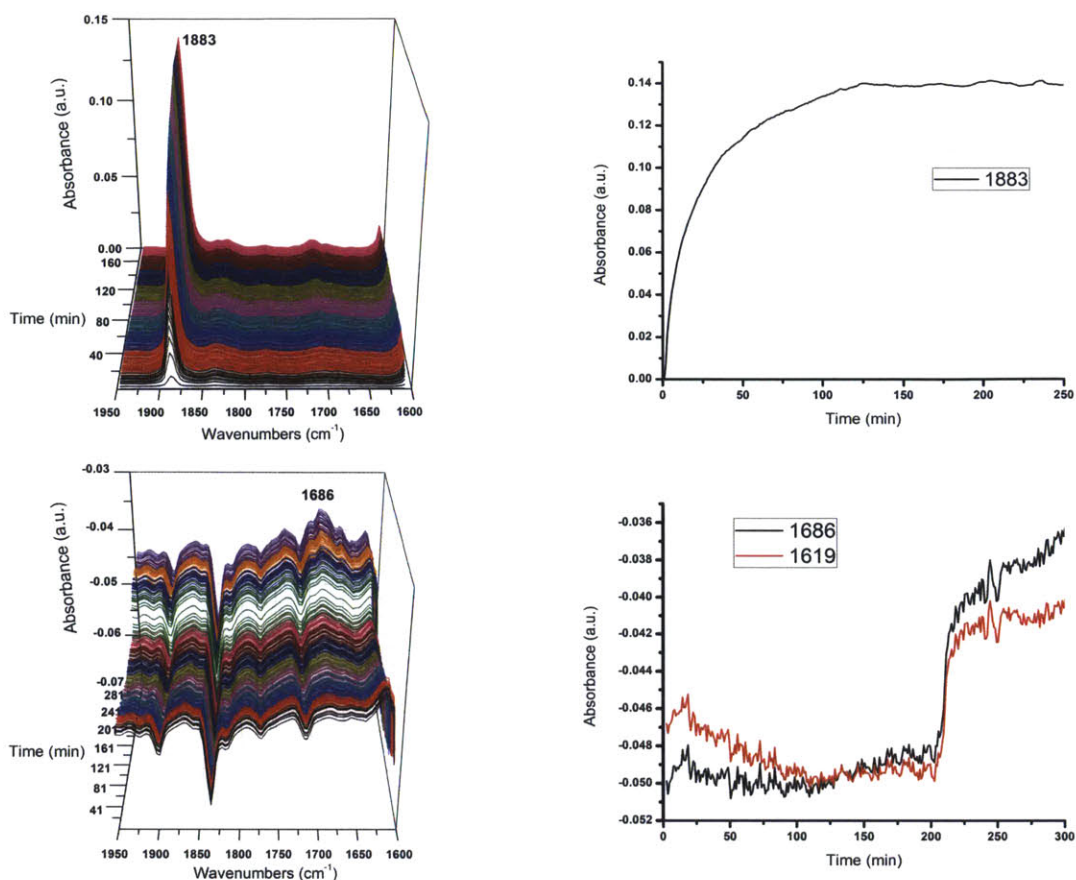


**Figure 3.14.** ReactIR spectra of the reaction of **9** with NO(g) (top) and Ph<sub>3</sub>CSNO (bottom) in CD<sub>3</sub>CN at ambient temperature.

**[Fe<sub>2</sub>S<sub>2</sub>] reactivity.** Reactions of [Fe<sub>2</sub>S<sub>2</sub>(SPh)<sub>4</sub>]<sup>2-</sup>, **5**, with NO(g) or the *S*-nitrosothiol Ph<sub>3</sub>CSNO result in the formation of the DNIC [Fe(SPh)<sub>2</sub>(NO)<sub>2</sub>]<sup>-</sup> and S<sup>0</sup>.<sup>16</sup> Upon standing, S<sup>0</sup> will react with the DNICs to form RBA, [Fe<sub>4</sub>S<sub>3</sub>(NO)<sub>7</sub>]<sup>-</sup>, **10**<sup>1-</sup>, and PhSSPh. When **5** is allowed to react with either **1** or **2** the dianionic form of RBA, [Fe<sub>4</sub>S<sub>3</sub>(NO)<sub>7</sub>]<sup>2-</sup>, **10**<sup>2-</sup>, forms. The FTIR spectrum (Figure 3.15) of **10**<sup>2-</sup> displays  $\nu_{NO}$  bands at 1691 cm<sup>-1</sup> and 1740 cm<sup>-1</sup> and a shoulder at 1651 cm<sup>-1</sup>, which are in agreement with the published spectral values of 1748 cm<sup>-1</sup>, 1689 cm<sup>-1</sup>, and 1660 cm<sup>-1</sup> and differ from the values of 1795 cm<sup>-1</sup>, 1743 cm<sup>-1</sup>, and 1708 cm<sup>-1</sup> for **10**<sup>1-</sup>.<sup>38</sup>

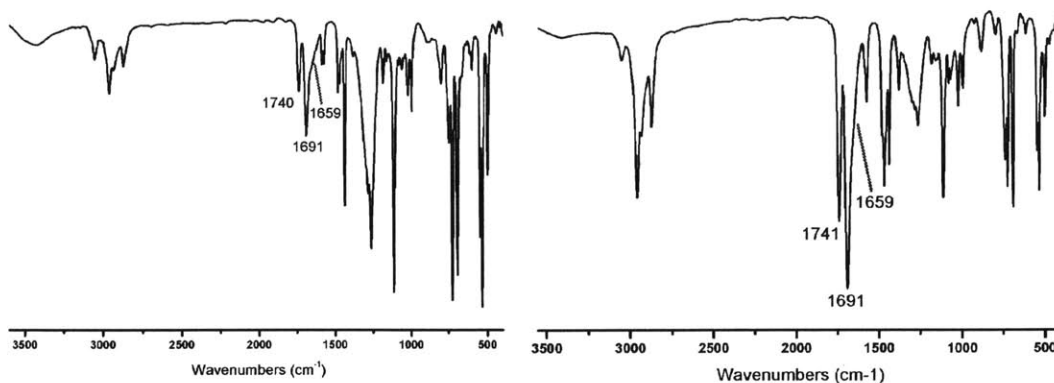


**Figure 3.15.** FTIR spectrum (KBr) of the reaction of **5** with **1** (left) and **2** (right). The nitrosylated product in both cases is  $10^{2-}$ .

Compound  $10^{2-}$  is paramagnetic compared to  $10^{1-}$ , which is diamagnetic. At room temperature, compound  $10^{2-}$  has a 5-line EPR spectrum with a  $\langle g \rangle = 2.026$  that matches the published shape and  $\langle g \rangle$  value of 2.025 (Figure 3.16).<sup>38</sup> The ESI-MS shows peaks corresponding to a mass of 529.5 m/z, which matches closely to the mass of **10** (529.6 m/z).

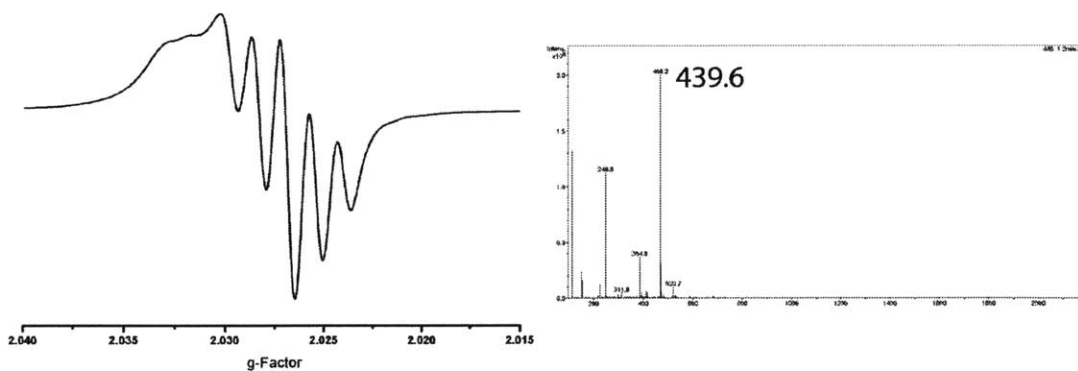
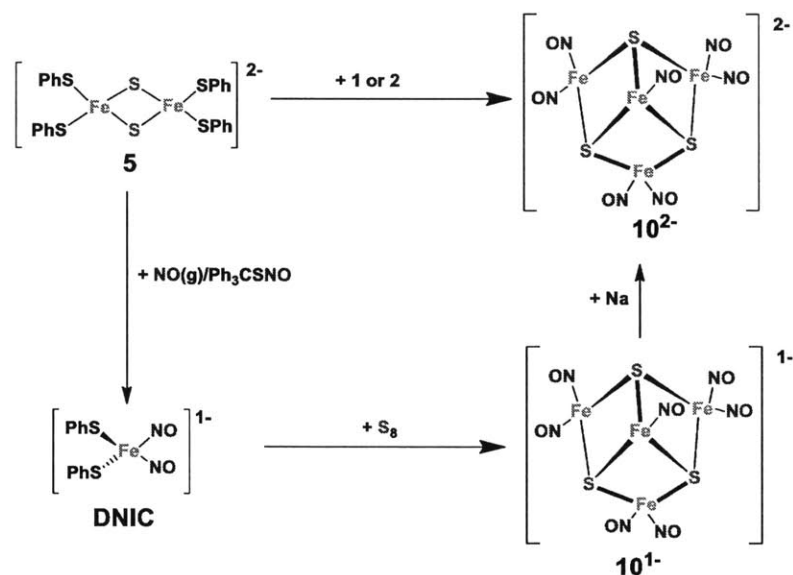


**Figure 3.16.** X-Band EPR spectrum (left) and negative-mode ESI-MS (right) of  $10^{2-}$ . EPR Conditions: RT; frequency 9.850 GHz, microwave power 2.017 mW, modulation amplitude 0.5 G;  $\langle g \rangle = 2.025$ . ESI-MS peak assignments (m/z): 439.5 ( $[10-3NO]^-$ ), 439.6).

The formation of  $10^{2-}$  from a  $[2Fe-2S]^{2-}$  cluster and a single reagent has not been previously reported (Scheme 3.2). We propose that the formation of the sulfanyl radical may promote formation of the reduced form of Roussin's black anion.



**Scheme 3.2.** Reaction pathways of **5** to form iron-sulfur-nitrosyl products.

**Nitrogen rich carboxylate-bridged diiron reactivity.** The reaction of  $[\text{Fe}_2(\text{Et-HPTB})(\text{PHCOO})](\text{BF}_4)_2$ , **6**, with  $\text{NO}(\text{g})$  and  $\text{Ph}_3\text{CSNO}$  has been previously explored and results in the formation of a di-MNIC species,  $[\text{Fe}_2(\text{Et-HPTB})(\text{PhCOO})(\text{NO})_2](\text{BF}_4)_2$ , **6·NO**, with a  $\nu_{\text{NO}}$  band at  $1785 \text{ cm}^{-1}$ .<sup>53,54</sup> Recently our lab reported that oxidation of **7** with  $\text{NOBF}_4$  results in the formation of the first synthetically prepared diiron-mono-MNIC,  $[\text{Fe}_2(\text{Et-HPTB})(\text{OH})(\text{NO})(\text{DMF})_2](\text{BF}_4)_3$ .<sup>54</sup> The known  $\text{NO}$  chemistry of this carboxylate-bridged diiron complex gave us a reference framework to examine and compare the chemistry that **1** and **2** exhibits.

In the reaction of **6** with **2**, the iron dissociates from the original complex to form **10**<sup>1-</sup>. This transformation was observed by the formation of  $\nu_{\text{NO}}$  bands at 1700, 1739, and  $1795 \text{ cm}^{-1}$  in the FTIR spectrum and mass peaks corresponding to **10** in the ESI-MS spectrum (Figure 3.17).<sup>38</sup>



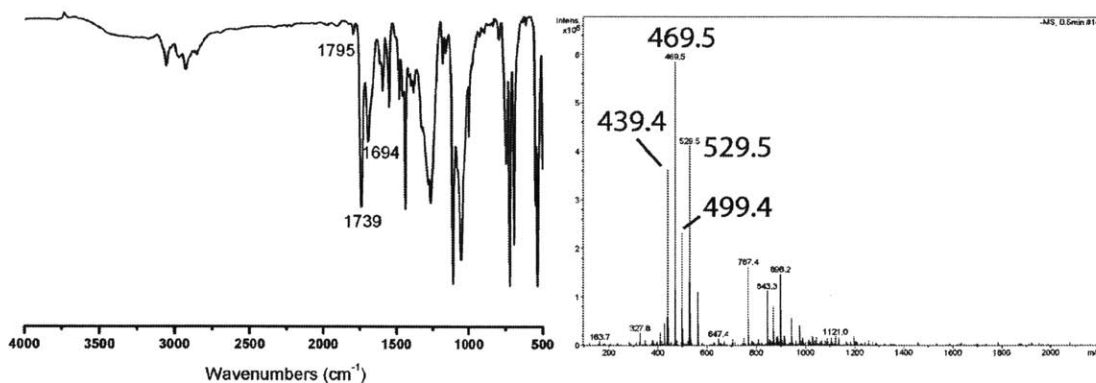


**Figure 3.17.** FTIR (left) and negative-mode ESI-MS (right) spectra of  $10^{1-}$  formed from **6** and **2**. ESI-MS peak assignments (m/z): 529.5 ( $[10]^-$ , 529.6), 499.4 ( $[10-1NO]^-$ , 499.6), 469.4 ( $[10-2NO]^-$ , 469.6), 439.4 ( $[10-3NO]^-$ , 439.6).

The formation of  $(PPN)[FeS_5(NO)_2]$ , **11**, is observed when **6** is allowed to react with 2.5 equivs of **1**. The FTIR spectrum (Figure 3.18) shows two strong  $\nu_{NO}$  bands at 1694 cm<sup>-1</sup> and 1739 cm<sup>-1</sup>, values comparable to the published data of 1695 cm<sup>-1</sup> and 1739 cm<sup>-1</sup>.<sup>39</sup> The characterization of **11** is further corroborated by an X-Band EPR spectrum (Figure 3.19) showing an isotropic signal at room temperature with  $\langle g \rangle = 2.030$  and a rhombic pattern with  $g_1 = 2.0148$ ,  $g_2 = 2.0304$ ,  $g_3 = 2.0494$  as a frozen solution at 77 K. In the ESI-MS experiment peaks similar to **10** are observed which are ascribed to air oxidation from the experimental setup, along with a peak at 275.6 m/z that matches that of **11**.

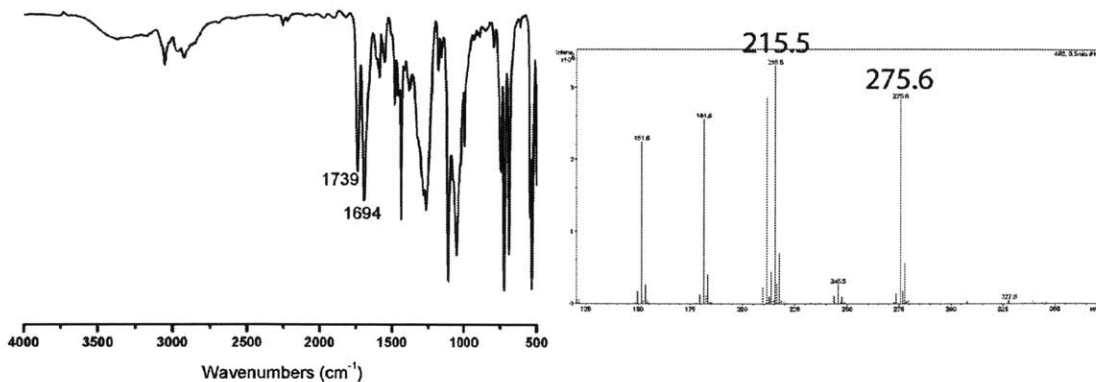


**Figure 3.18.** FTIR (left) and negative-mode ESI-MS (right) spectra of **11** formed from **6** and **1**. ESI-MS peak assignments (m/z): 275.6 ( $[11]^-$ , 275.8), 215.5 ( $[11-2NO]^-$ , 215.8).

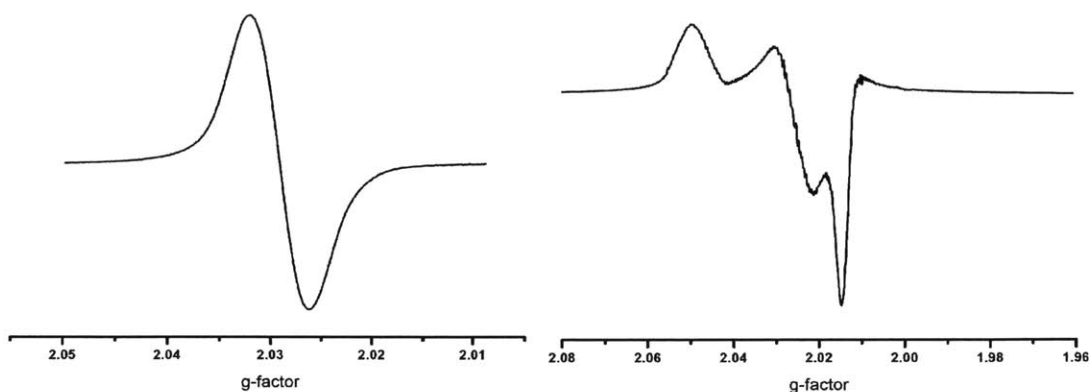


**Figure 3.19.** X-band EPR spectra of **11** at room temperature (left) and 77 K (right). EPR Conditions: RT – frequency 9.846 GHz, microwave power 2.017 mW, modulation amplitude 0.5 G,  $\langle g \rangle = 2.03$ ; 77 K – frequency 9.193 GHz, microwave power 2.012 mW, modulation amplitude 5.0 G,  $g_1 = 2.0148$ ,  $g_2 = 2.0304$ ,  $g_3 = 2.0494$ .

**Oxygen-rich carboxylate-bridged diiron reactivity.** In an attempt to further the understanding in the reactivity of RNOS with carboxylate-bridged diiron complexes, we prepared the known compound  $[\text{Fe}_2(\mu\text{-OH})(\mu\text{-Ph}_4\text{DBA})(\text{TMEDA})_2(\text{OTf})]$ , **7**, which has both 5- and 6-coordinate irons. We wanted to exploit this difference in coordination to form a diiron-mono-MNIC species, however, upon reaction with  $\text{NO}(\text{g})$  or  $\text{Ph}_3\text{CSNO}$  the complex  $[\text{Fe}_3(\mu\text{-O})_2(\text{TMEDA})_2(\text{Ph}_4\text{DBA})_2(\text{NO})_2](\text{OTf})$ , **12**, was formed. This species does not exhibit a signal in the EPR experiment at ambient temperature and 77 K, similar to the results obtained previously using **6** with  $\text{NO}(\text{g})$  or  $\text{NO}^+$ .

Two full molecules of **12**, a methylene chloride, and two molecules of diethyl ether are present in the asymmetric unit of crystals grown by vapor diffusion of diethyl ether into a methylene chloride solution (Figure 3.20). The iron atoms form a linear chain bridged by two carboxylate ligands and an oxygen atom. This linear chain has been observed before when using bridging-carboxylate ligands but never with bound nitrosyls.<sup>55</sup>

The iron atoms were assigned to have a 3+ oxidation state based on the bond valence method.<sup>56</sup> The bridging oxygen atoms were assigned to be  $\text{O}^{2-}$  rather than  $\text{HO}^-$ , for a hydrogen

atom could not be detected near the oxygen atoms. The outer irons are bound to a bent nitrosyl and chelated by a TMEDA ligand. The central iron is bound only to oxygen atoms of the  $\text{Ph}_4\text{DBA}^{2-}$  ligands and the bridging oxygen atoms. The nitrosyls are bent inwards with Fe–N–O bond angles of  $146.0(5)^\circ$ ,  $145.1(5)^\circ$ ,  $142.0(6)^\circ$ , and  $138.7(6)^\circ$ . The nitrosyls have N–O bond distances of  $1.128(7)$  Å,  $1.133(7)$  Å,  $1.132(8)$  Å, and  $1.085(7)$  Å, and Fe–N bond distances of  $1.803(5)$  Å,  $1.778(5)$  Å,  $1.777(5)$  Å, and  $1.864(6)$  Å. The Fe–N–O bond angles of **12** are more acute than those of other published nitrosyl-diiron complexes (table 3.3), suggesting that they could be formally assigned as  $\text{NO}^-$ , which would change the assignment of the bridging oxygen atoms from  $\text{O}^{2-}$  to  $\text{HO}^-$ . The  $\text{Fe}_{\text{out}}\text{--O}_{\text{bridge}}\text{--Fe}_{\text{in}}$  bond angles of **12** are  $121.56(17)^\circ$ ,  $123.73(17)^\circ$ ,  $122.05(18)^\circ$ , and  $124.07(18)^\circ$ , which are greater than the Fe– $\text{O}_{\text{bridge}}\text{--Fe}$  bond angle of  $110.45(11)^\circ$  for **1**. The Fe– $\text{O}_{\text{bridge}}$  bond lengths for **12** are  $1.956(4)$  Å,  $2.026(4)$  Å,  $2.034(4)$  Å, and  $1.955(4)$  Å for the outer iron atoms, and  $1.985(3)$  Å,  $1.977(3)$  Å,  $1.958(4)$  Å, and  $1.961(4)$  Å for the inner iron atom. In the structure of **7** the Fe– $\text{O}_{\text{bridge}}$  bond distances are  $2.020(2)$  Å for the six-coordinate iron and  $1.953(2)$  Å for the five-coordinate iron.

**Table 3.3.** Selected geometrical parameters of **12** and other diiron-nitrosyl species.

	<b>12</b>	<b>6·NO</b> , <sup>53</sup>	$[\text{Fe}_2(\text{Et-HBTP})(\text{DMF})_2(\text{NO})(\text{OH})]^{2+}$ , <sup>54</sup>	$[\text{Fe}_2(\text{BPMP})(\text{O}_2\text{Pr})(\text{NO})_2]^{2+}$ , <sup>57</sup>
<b>bond Length, Å</b>				
Fe–N	1.778(5)	1.777(5)	1.749(8)	1.787(2)
	1.803(5)	1.864(6)	1.750(7)	1.774(2)
N–O	1.128(7)	1.132(8)	1.156(8)	1.796(3)
	1.133(7)	1.085(7)	1.151(8)	1.156(3)
Fe– $\text{O}_{\text{bridge}}$	1.956(4)	2.034(4)	2.017(5)	1.172(3)
	2.026(4)	1.955(4)	2.006(5)	2.0570(19)
				2.044(2)
				2.020(2)
<b>bond angle, °</b>				
Fe–N–O	138.7(6)	145.1(5)	166.6(7)	171.0(3)
	142.0(6)	146.0(5)	168.3(7)	155.4(2)
Fe–O–Fe	121.56(17)	122.05(18)	117.7(2)	144.7(2)
	123.73(17)	124.07(18)		116.71(9)

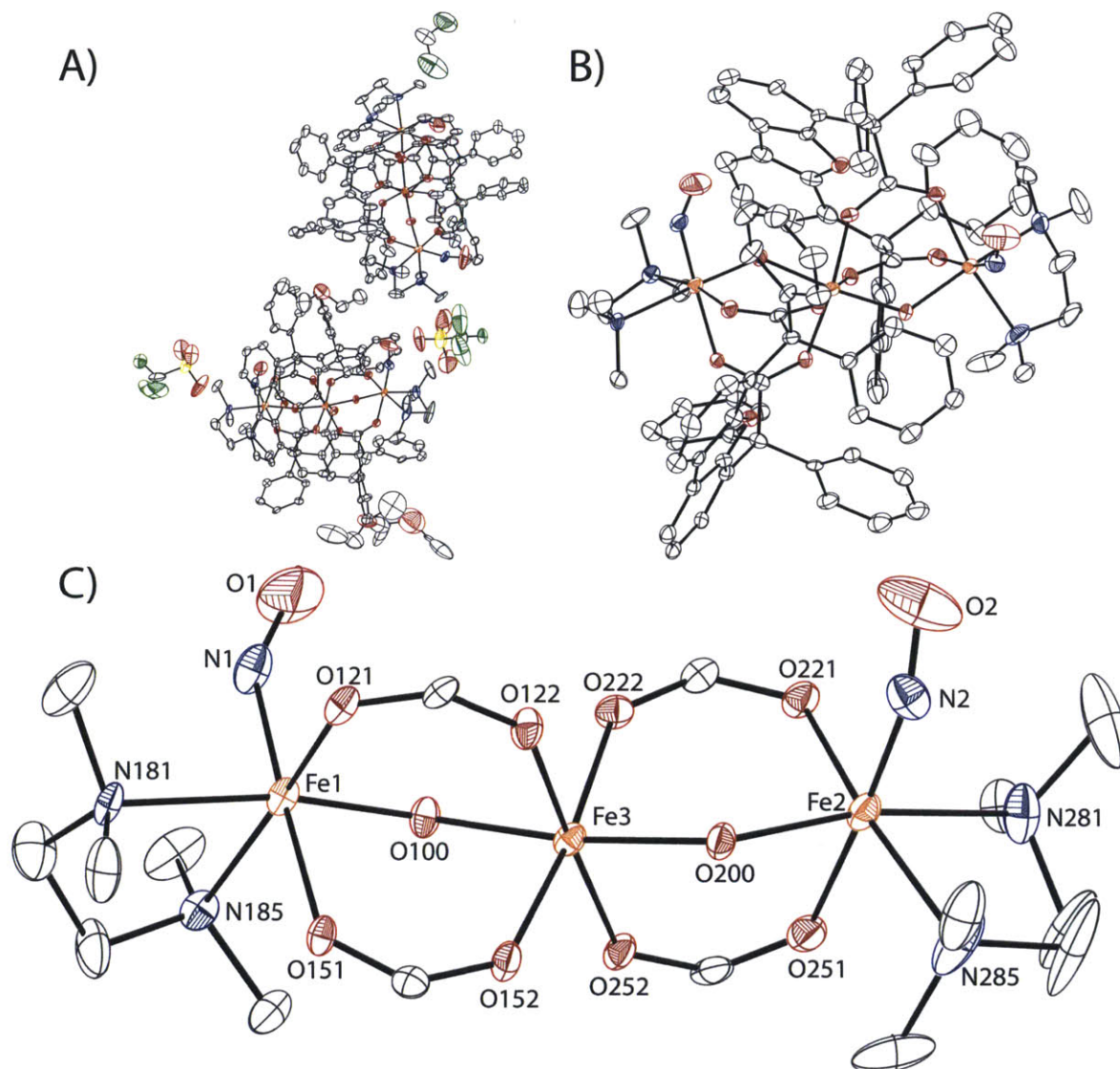


**Figure 3.20.** Drawing of the crystal structure of **12**. A) Complete asymmetric unit prior to applying the *SQUEEZE* function of *Platon* to remove the disordered diethyl ether.<sup>25</sup> B) Single molecule of **12**. C) Coordination environment of the linear iron chain of **12**. Ellipsoids are shown at 50% probability. Hydrogens are omitted for clarity.

**Table 3.4.** X-ray crystallographic data for **11**·(PPN)(OTf) and **12**·2Et<sub>2</sub>O·0.5CH<sub>2</sub>Cl<sub>2</sub> at 100K.

Compounds	(PPN)(Fe(NO) <sub>2</sub> S <sub>5</sub> ], <b>11</b>	[Fe <sub>3</sub> (μ-O) <sub>2</sub> (TMEDA) <sub>2</sub> (Ph <sub>4</sub> DBA) <sub>2</sub> (NO) <sub>2</sub> ](OTf), <b>12</b>
Formula	C <sub>73</sub> H <sub>60</sub> F <sub>3</sub> FeN <sub>4</sub> O <sub>5</sub> P <sub>4</sub> S <sub>6</sub>	C <sub>95.5</sub> H <sub>90</sub> Cl <sub>17.5</sub> Fe <sub>3</sub> N <sub>6</sub> O <sub>17.5</sub> S
formula weight	1502.34	1893.8
crystal system	orthorhombic	monoclinic
space group	P2 <sub>1</sub> 2 <sub>1</sub> 2 <sub>1</sub>	P2 <sub>1</sub> /c
a, Å	15.2542(12)	12.7891(10)
b, Å	30.042(3)	43.864(4)
c, Å	30.062(3)	33.243(3)
β, deg	90	95.5330(10)
V, Å <sup>3</sup>	13776(2)	18562(3)
Z	8	8
ρ <sub>calcd</sub> , g/cm <sup>3</sup>	1.449	1.355
μ, mm <sup>-1</sup>	0.557	0.589
θ range, deg	0.96 to 30.51	0.77 to 25.26
completeness to θ, %	100.0	99.5
reflections collected	400185	292850
independent reflections	42061	33495
R(int)	0.0811	0.0714
restraints	9611	0
parameters	1732	2306
Max., min. transmission	0.9413, 0.8419	0.7452, 0.6091
R1(wR2) [I>2σ(I)]	0.0633 (0.1524)	0.1081 (0.2456)
R1(wR2)	0.0818 (0.1676)	0.1207 (0.2494)
GoF(F <sup>2</sup> )	1.067	2.339
max, min peaks, e.Å <sup>-3</sup>	2.365, -0.848	1.810, -1.486

When the reaction of **4** and NO(g) was followed by UV-Vis (Figure 2) in acetonitrile at 25° C, bands initially grew in at 434 nm and 617 nm along with a shoulder at 341 nm. The spectrum then continued to change, with the shoulder at 341 nm continuing to increase in intensity and the band at 431 nm red-shifts to 452 nm and decreasing in intensity, with a pseudo-isosbestic point at 420 nm. These changes suggest that the reaction is multi-phasic with multiple kinetic parameters. The reaction may proceed through oxidation of the iron atoms, which then leads to disproportionation into **12** and an unknown non-nitrosylated iron species.

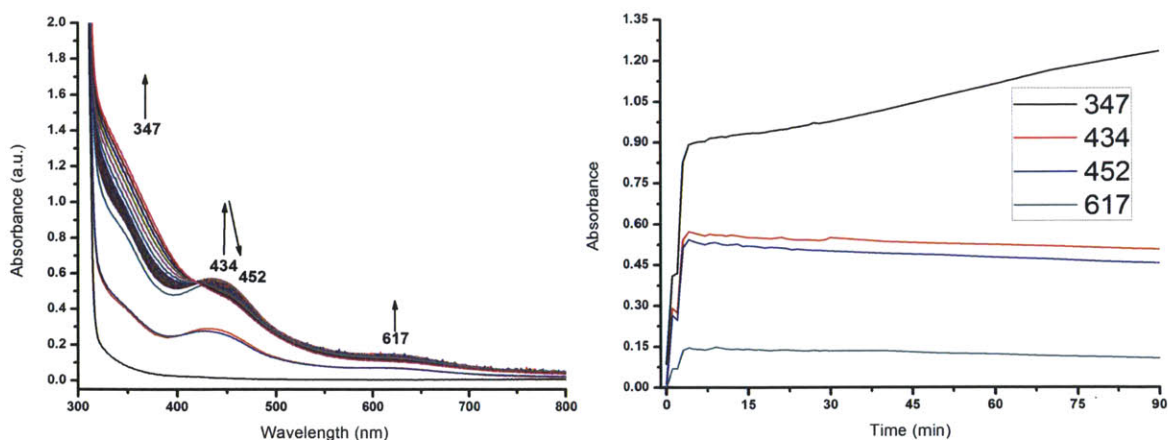


**Figure 3.21.** The UV-Vis spectrum (left) and selected kinetic traces (right) of the reaction of **7** and excess NO(g) in acetonitrile at 25° C. Scans were collected every 30 seconds.

The reaction could also be followed by ReactIR in CH<sub>2</sub>Cl<sub>2</sub> at ambient temperature (Figure 3.22). Four bands were monitored that have different rates of change in intensity. Bands at 1722 cm<sup>-1</sup> and 1602 cm<sup>-1</sup> grow in, while a the initial carboxylate band at 1627 cm<sup>-1</sup> diminishes. A band at 1615 cm<sup>-1</sup> initially forms, but begins to disappear after 4 min. The band at 1722 cm<sup>-1</sup> is the  $\nu_{NO}$  band, while the 1602 cm<sup>-1</sup>, 1615 cm<sup>-1</sup>, and 1627 cm<sup>-1</sup> are the changes of the vibrations from the carboxylate stretch. No intermediate iron-nitrosyl species were observed, even at -77° C. The observed changes of the band intensities suggest that oxidation of the iron atoms and rearrangement of the iron-carboxylate coordination occurs prior to NO binding. The  $\nu_{NO}$  band is 40 – 80 cm<sup>-1</sup> lower in energy than other published synthetic nitrosyl-diiron models, but is closer to the resonance Raman  $\nu_{NO}$  value of 1681 cm<sup>-1</sup> observed for a mononitrosyl-diiron species of the flavodiiron nitric oxide reductases active site (FDP-NO).<sup>53,54,57,58</sup> The FDP-NO species is proposed to have a bent nitrosyl oriented toward the non-nitrosylated iron atom, a geometry that we observe in the crystal structure of **12**.

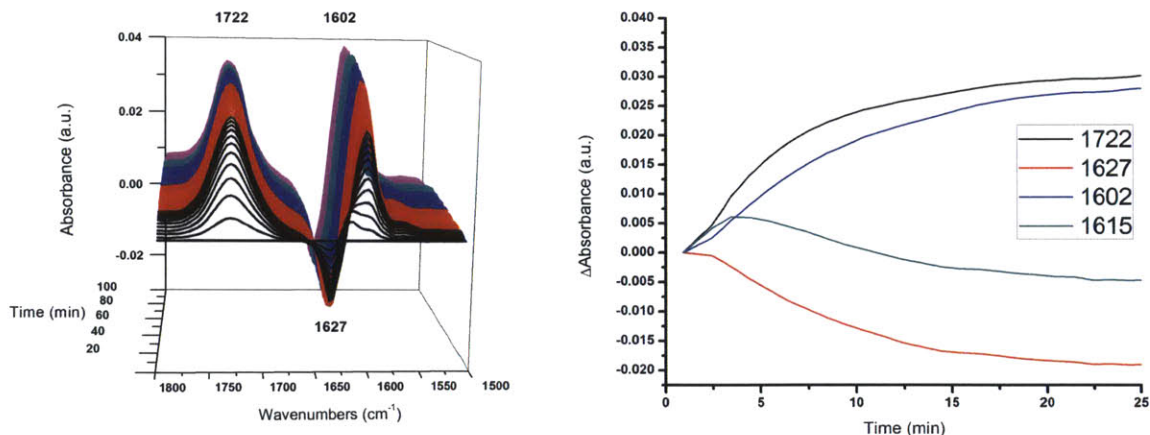


**Figure 3.22.** ReactIR spectrum (left) and selected kinetic traces (right) of the reaction of **7** with NO(g) recorded in CH<sub>2</sub>Cl<sub>2</sub> at ambient temperature. Scans were collected every min and the spectra were referenced to the initial scan.

The <sup>57</sup>Fe Mössbauer spectrum of compound **5** was fit with three sites (Figure 4). The first and second fitted sites have similar isomer shifts, but different quadrupole splitting parameters. The second fitted site compares favorably to the value published for **1** ( $\delta$ , 0.67 mm/z;  $\Delta E_Q$ , 1.44 mm/z). The third fitted site compares favorably to the published values of the iron atoms in the oxygen-rich coordination environment in the complex [Fe<sub>4</sub>( $\mu$ -OH)<sub>6</sub>(PIM)(Ph<sub>3</sub>CCO<sub>2</sub>)<sub>2</sub>] ( $\delta$ , 0.51(2) mm/s;  $\Delta E_Q$ , 1.06(2) mm/s) and similar to the published value of the species formed in the reaction of **7** and O<sub>2</sub> at low temperature ( $\delta$ , 0.53(1) mm/s;  $\Delta E_Q$ , 1.28(3) mm/s), suggesting that this site corresponds to the central iron atom.

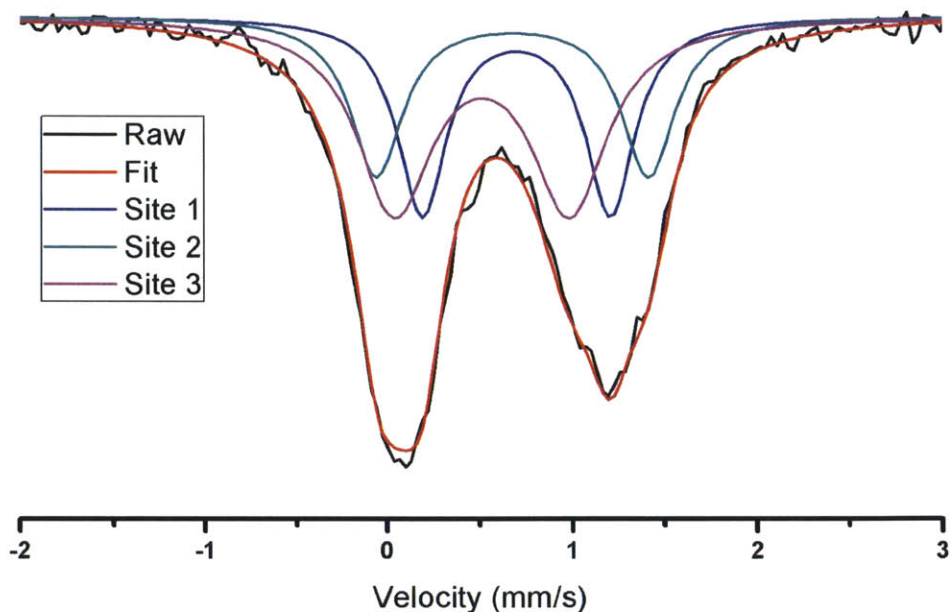


**Figure 3.23.**  $^{57}\text{Fe}$  Mössbauer spectrum of **5** collected at 80 K. Color coding: raw, black; full fit, red; site 1, blue; site 2, green; site 3, pink. Site 1:  $\delta$ , 0.70(2) mm/s;  $\Delta E_Q$ , 1.02(2) mm/s;  $\Gamma$ , 0.32(2) mm/s; Area, 0.30%. Site 2:  $\delta$ , 0.68(2) mm/s;  $\Delta E_Q$ , 1.47(2) mm/s;  $\Gamma$ , 0.35(2) mm/s; Area, 0.26%. Site 3:  $\delta$ , 0.51(2) mm/s;  $\Delta E_Q$ , 0.95(2) mm/s;  $\Gamma$ , 0.49(2) mm/s; Area, 0.44%.

The reaction of **7** with both **1** and **2** yielded similar results as for **6**. Formation of  $10^{1-}$  was observed by the characteristic  $\nu_{NO}$  bands at  $1700\text{ cm}^{-1}$ ,  $1739\text{ cm}^{-1}$ , and  $1795\text{ cm}^{-1}$  in the FTIR spectrum as well as the correct mass isotopic patterns in the ESI-MS spectrum in the reaction with **2**.<sup>38</sup> In the reaction with **1** the formed product was **11**, as characterized by the  $\nu_{NO}$  bands at  $1695\text{ cm}^{-1}$  and  $1739\text{ cm}^{-1}$  in the IR spectrum, the  $\langle g \rangle = 2.030$  in the room temperature X-band EPR spectrum, and the X-ray crystal structure.<sup>39</sup>

Crystals of **11** were formed with (PPN)(OTf) by vapor diffusion of diethyl ether into 2-methyl tetrahydrofuran (Figure 3.24). The crystals appeared as plates with merohedral twinning. The crystals initially appeared to be in a tetragonal space group, but were found to be in the orthogonal crystal system with the space group  $P2_12_12_1$ . Within the asymmetric unit there are two molecules of (PPN)[FeS<sub>5</sub>(NO)<sub>2</sub>] and two molecules of (PPN)(OTf). The FeS<sub>5</sub> ring has a



chair conformation. The N–O bond distances are 1.123(7) Å, 1.159(7) Å, 1.143(6) Å, and 1.170(7) Å, which are a little shorter than the published values of (PPN)[FeS<sub>5</sub>(NO)<sub>2</sub>] of 1.177(3) Å and 1.178(3) Å.<sup>39</sup> The Fe–N–O bond angles are almost linear at 167.2(5)°, 174.8(5)°, 164.9(5)°, and 174.2(5)°, which compare favorably to the published values of 165.9(2)° and 172.8(2)°.

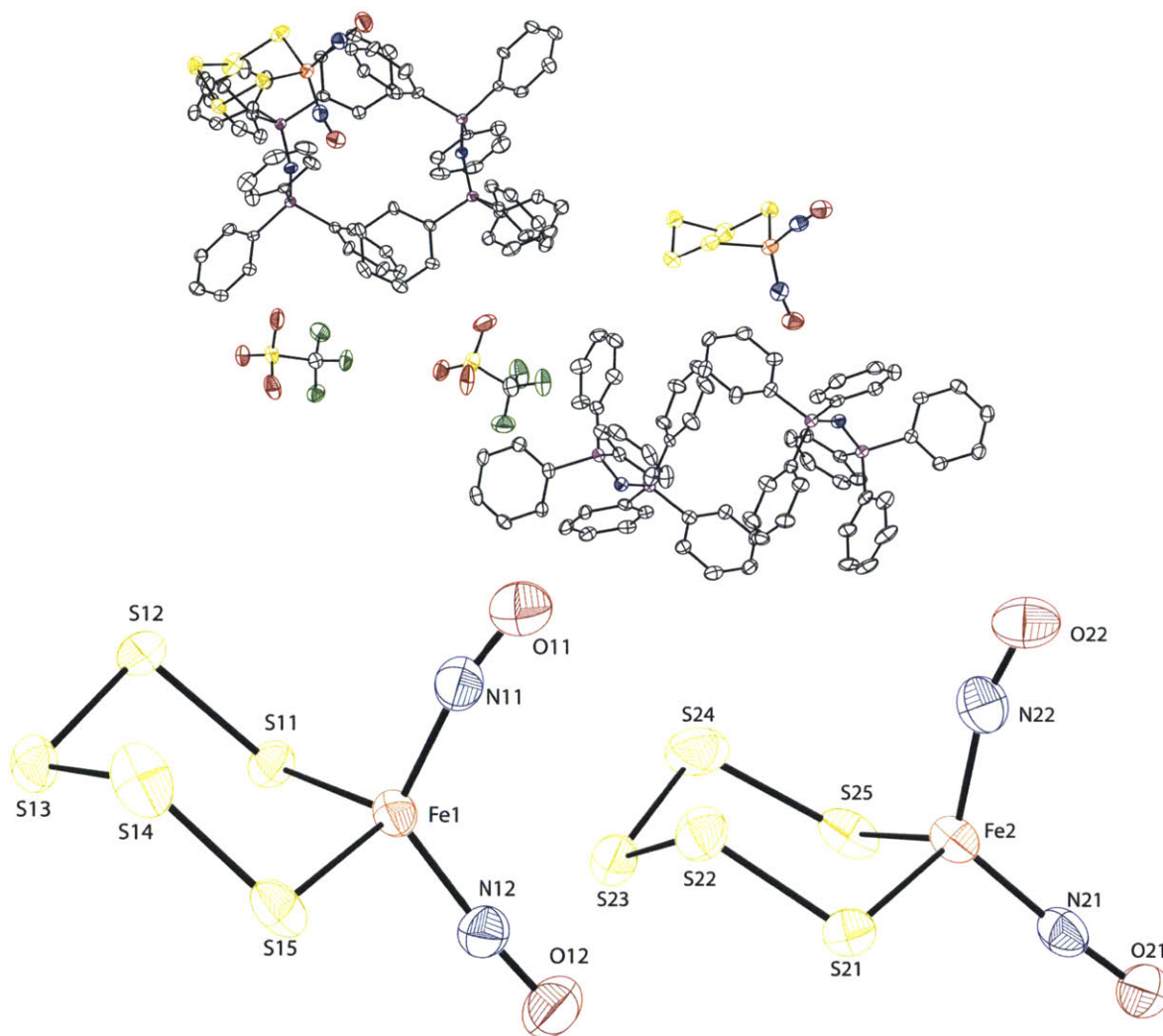
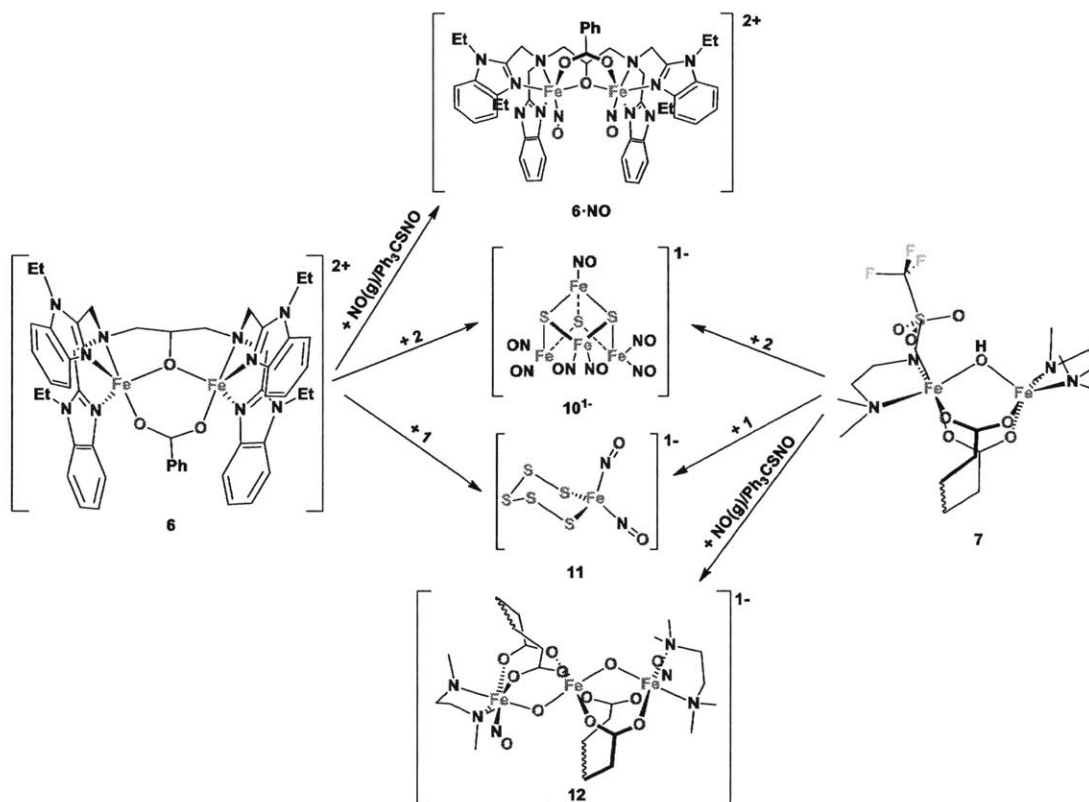


**Figure 3.24.** Drawings of the X-ray crystal structures of the asymmetric unit (top) and the two independent [FeS<sub>5</sub>(NO)<sub>2</sub>]<sup>-</sup>, **11**, molecules (bottom). Ellipsoids are drawn at 50% probability. Hydrogen atoms are omitted for clarity. Color scheme: iron, orange; sulfur, yellow; nitrogen, blue; oxygen, red; phosphorous, magenta; fluorine, green; carbon, colorless.

Complex **11** has been proposed as an intermediate in the formation of  $10^{1-}$ .<sup>59</sup> Oxidation of **11** by  $[\text{Cp}_2\text{Fe}](\text{BF}_4)$  is reported to form  $10^{1-}$  in 65 % yield. The reaction of **6** and **7** with **1** and **2** extrudes the iron atoms from their carboxylate and *N*-donating ligands to form these sulfur and nitrosyl-containing complexes, but it is currently unclear why the reaction with **1** prefers to form the DNIC **11** over  $10^{1-}$ . Current speculation posits that the polysulfide nature of **1** forms the  $\text{S}_5^{2-}$  ligand more readily than the single sulfide released from **2**.



**Scheme 3.3.** Reaction pathways of **6** and **7** with various RNOS species.

**Mononuclear iron complex reactivity.** To test whether the difference in reactivity between **1** and **2** could also be observed with a mononuclear iron complex we used  $[\text{Fe}(\text{BIPhMe})\text{Cl}_2]$ , **8**. The reaction of **8** and **1** also formed **11**, but this result was expected based on the reactivity of **6** and **7**, however, when compound **8** was allowed to react with **2**, compound **11** was the only iron-nitrosyl species that formed. The FTIR spectra (Figure 3.25) of the reactions have two  $\nu_{\text{NO}}$  bands

at  $1694\text{ cm}^{-1}$  and  $1739\text{ cm}^{-1}$ . The 77 K X-band EPR spectrum shows a rhombic signal with  $g_1 = 2.0485$ ,  $g_2 = 2.0294$ , and  $g_3 = 2.0138$ , which compares favorably to the spectrum of **11** obtained from **6**.

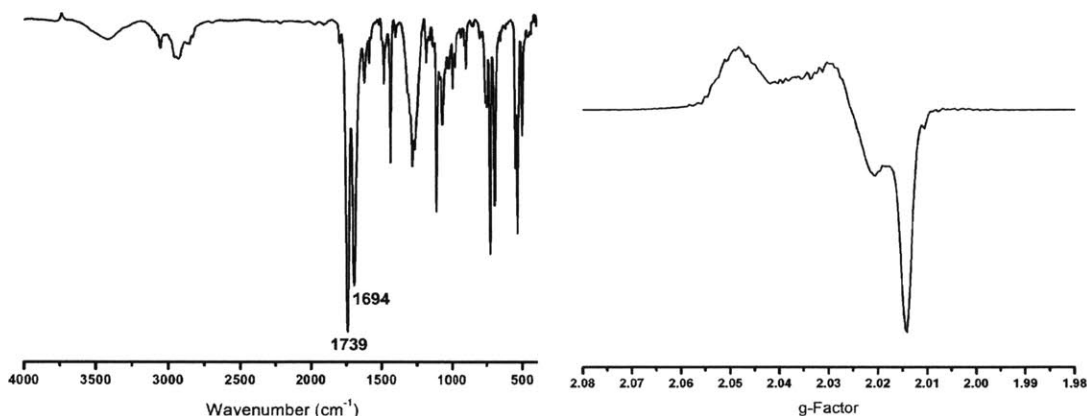


**Figure 3.25.** Spectroscopic characterization of the product in the reaction of **8** and **2**. The FTIR spectrum (left) was collected as a KBr pellet. The X-band EPR spectrum (right) was collected at 77K. EPR Conditions: 77 K – frequency 9.175 GHz, microwave power 0.2017 mW, modulation amplitude 1.0 G,  $g_1 = 2.0485$ ,  $g_2 = 2.0294$ , and  $g_3 = 2.0138$ .

The formation of only **11** from the reaction with **2** was somewhat surprising, formation of  $10^{1-}$  being anticipated. The current hypothesis is that the close proximity of the iron atoms to one another in **6** and **7**, and the single sulfide that is released from **2** may promote self-assembly of an iron-sulfur cluster that is then converted into  $10^{1-}$ . The iron atoms of **8** are farther apart, allowing for the formation of polysulfide ligands from the sulfides.

### 3.4 Summary and Conclusions

The *S*-nitrosothiol salts **1** and **2** were prepared using an altered experimental setup of a previously published synthesis. These salts were characterized by UV-Vis, FTIR, and X-ray crystallography to match the published compounds. Compound **2** was further characterized by cyclic voltammetry to have an irreversible reduction occur at -2.64 V.

These *S*-nitrosothiols readily release NO(g) upon addition of acid. The reaction of **1** and **2** with [Fe<sup>III</sup>(TPP)Cl] resulted in reductive nitrosylation of iron to form [Fe<sup>II</sup>(TPP)(NO)]. In the reaction of a [2Fe–2S] cluster with these *S*-nitrosothiols, dianionic Roussin's black anion, **10**<sup>2-</sup>, forms, a result that has not been previously reported from a single nitrosating reagent. The reaction of **1** or **2** with a mononuclear iron(II) complex resulted in the formation of the DNIC **11**. A difference in reactivity between **1** and **2** was observed with the carboxylate-bridged diiron complexes. In the reactions with **1**, **11** was formed, but in the reaction with **2**, the nitrosated product is Roussin's black anion, **10**<sup>1-</sup>.

This reactivity profile for these *S*-nitrosothiols is very unique but did not produce any new compounds or improve upon known synthetic methods for obtaining the previously reported compounds.

### 3.5 References

1. Bosworth, C. A.; Toledo, J. C., Jr.; Zmijewski, J. W.; Li, Q.; Lancaster, J. R., Jr., *Proc. Natl. Acad. Sci. U.S.A.* **2009**, *106*, 4671.
2. Chen, Y.-J.; Ku, W.-C.; Feng, L.-T.; Tsai, M.-L.; Hsieh, C.-H.; Hsu, W.-H.; Liaw, W.-F.; Hung, C.-H.; Chen, Y.-J., *J. Am. Chem. Soc.* **2008**, *130*, 10929.
3. Cho, D.-H.; Nakamura, T.; Fang, J.; Cieplak, P.; Godzik, A.; Gu, Z.; Lipton, S. A., *Science* **2009**, *324*, 102.
4. Foster, H. W.; Cowan, J. A., *J. Am. Chem. Soc.* **1999**, *121*, 4093.
5. Hickok, J. R.; Vasudevan, D.; Thatcher, G. R.; Thomas, D. D., *Antioxid. Redox Signaling* **2012**, *17*, 962.
6. Lewandowska, H.; Kalinowska, M.; Brzoska, K.; Wojciuk, K.; Wojciuk, G.; Kruszewski, M., *Dalton Trans.* **2011**, *40*, 8273.
7. Tennyson, Andrew G.; Lippard, Stephen J., *Chem. Biol.* **2011**, *18*, 1211.
8. Tonzetich, Z. J.; McQuade, L. E.; Lippard, S. J., *Inorg. Chem.* **2010**, *49*, 6338.
9. Filipovic, M. R.; Miljkovic, J. L.; Nauser, T.; Royzen, M.; Klos, K.; Shubina, T.; Koppenol, W. H.; Lippard, S. J.; Ivanović-Burmazović, I., *J. Am. Chem. Soc.* **2012**, *134*, 12016.
10. Seel, F.; Kuhn, R.; Simon, G.; Wagner, M., *Z. Naturforsch. B* **1985**, *40b*, 1607
11. Lorkovic, I. M.; Ford, P. C., *Inorg. Chem.* **2000**, *39*, 632.
12. Pangborn, A. B.; Giardello, M. A.; Grubbs, R. H.; Rosen, R. K.; Timmers, F. J., *Organometallics* **1996**, *15*, 1518.
13. Armarego, W. L. F.; Chai, C., *Purification of Laboratory Chemicals*. 6 ed.; Butterworth-Heinemann: 2009; p 760.
14. Dong, Y.; Menage, S.; Brennan, B. A.; Elgren, T. E.; Jang, H. G.; Pearce, L. L.; Que, L., *J. Am. Chem. Soc.* **1993**, *115*, 1851.
15. Hagen, K. S.; Reynolds, J. G.; Holm, R. H., *J. Am. Chem. Soc.* **1981**, *103*, 4054.
16. Harrop, T. C.; Tonzetich, Z. J.; Reisner, E.; Lippard, S. J., *J. Am. Chem. Soc.* **2008**, *130*, 15602.
17. Martinsen, A.; Songstad, J., *Acta Chem. Scand.* **1977**, *31A*, 645.
18. Mizoguchi, T. J.; Kuzelka, J.; Spingler, B.; DuBois, J. L.; Davydov, R. M.; Hedman, B.; Hodgson, K. O.; Lippard, S. J., *Inorg. Chem.* **2001**, *40*, 4662.
19. Kent, T. A. *WMOSS v. 2.5: Mössbauer Spectral Analysis Software*, WEB Research Co., WEB Research Co.: Minneapolis, MN, 1998.
20. APEX2 v2009 APEX2 v2009, Bruker AXS: Madison, WI, 2009.
21. Sheldrick, G. M. *SADABS: Area-Detector Absorption Correction*, University of Göttingen: Göttingen, Germany, 2008.
22. Sheldrick, G., *Acta Crystallogr., Sect. A: Found. Crystallogr.* **2008**, *64*, 112.
23. Sheldrick, G. M. *SHELXTL97: Program for Refinement of Crystal Structures*, University of Göttingen: Göttingen, Germany, 1997.
24. SHELXTL v. 6.10: *Program Library for Structure Solution and Molecular Graphics*, Bruker AXS, Madison, WI, 2001.
25. Spek, A. L. *PLATON, A Multipurpose Crystallographic Tool*, Utrecht University, Utrecht, The Netherlands, 2000.
26. Spek, A. L., *J. Appl. Crystallogr.* **2003**, *36*, 7.
27. Dolomanov, O. V.; Bourhis, L. J.; Gildea, R. J.; Howard, J. A. K.; Puschmann, H., *J. Appl. Crystallogr.* **2009**, *42*, 339.

28. Frisch, M. J.; Trucks, G. W.; Schlegel, H. B.; Scuseria, G. E.; Robb, M. A.; Cheesman, J. R.; Montgomery, J. A. J.; Vreven, T.; Kudin, K. N.; Burant, J. C.; Millam, J. M.; Iyengar, S. S.; Tomasi, J.; Barone, V.; Mennucci, B.; Cossi, M.; Scalmani, G.; Rega, N.; Petersson, G. A.; Nakatsuji, H.; Hada, M.; Ehara, M.; Toyota, K.; Fukuda, R.; Hasegawa, J.; Ishida, M.; Nakajima, T.; Honda, Y.; Kitao, O.; Nakai, H.; Klene, M.; Li, X.; Know, J. E.; Hratchian, H. P.; Cross, J. B.; Adamo, C.; Jaramillo, J.; Gomperts, R.; Stratmann, R. E.; Yazyev, O.; Austin, A. J.; Cammi, R.; Pomelli, C.; Ochterski, J. W.; Ayala, P. Y.; Morokuma, K.; Voth, G. A.; Salvador, P.; Dannenberg, J. J.; Zakrzewski, V. G.; Dapprich, S.; Daniels, A. D.; Strain, M. C.; Farkas, O.; Malick, D. K.; Rabuck, A. D.; Raghavachari, K.; Foresman, J. B.; Ortiz, J. V.; Cui, Q.; Baboul, A. G.; Clifford, S.; Cioslowski, J.; Stefanov, B. B.; Liu, G.; Liashenko, A.; Piskorz, P.; Komaromi, I.; Martin, R. L.; Fox, D. J.; Keith, T.; Al-Laham, M. A.; Peng, C. Y.; Nanayakkara, A.; Challacombe, M.; Gill, P. M. W.; Johnson, B.; Chen, W.; Wong, M. W.; Gonzalez, C.; Pople, J. A. *Gaussian 03*, Pittsburgh, PA, 2003.
29. Becke, A. D., *J. Chem. Phys.* **1993**, *98*, 5648.
30. Lee, C.; Yang, W.; Parr, R. G., *Phys. Rev. B* **1988**, *37*, 785.
31. Vosko, S. H.; Wilk, L.; Nusair, M., *Can. J. Phys.* **1980**, *58*, 1200.
32. Stephens, P. J.; Devlin, F. J.; Chabalowski, C. F.; Frisch, M. J., *J. Phys. Chem.* **1994**, *98*, 11623.
33. Godbout, N.; Salahub, D. R.; Andzelm, J.; Wimmer, E., *Can. J. Chem.* **1992**, *70*, 560.
34. Kurtikyan, T. S.; Martirosyan, G. G.; Lorkovic, I. M.; Ford, P. C., *J. Am. Chem. Soc.* **2002**, *124*, 10124.
35. Tonzetich, Z. J.; Héroguel, F.; Do, L. H.; Lippard, S. J., *Inorg. Chem.* **2011**, *50*, 1570.
36. Wayland, B. B.; Olson, L. W., *J. Am. Chem. Soc.* **1974**, *96*, 6037.
37. Moedritzer, K.; Maier, L.; Groenweghe, L. C. D., *J. Chem. Eng. Data* **1962**, *7*, 307.
38. D'Addario, S.; Demartin, F.; Grossi, L.; Iapalucci, M. C.; Laschi, F.; Longoni, G.; Zanello, P., *Inorg. Chem.* **1993**, *32*, 1153.
39. Tsai, M.-L.; Chen, C.-C.; Hsu, I.-J.; Ke, S.-C.; Hsieh, C.-H.; Chiang, K.-A.; Lee, G.-H.; Wang, Y.; Chen, J.-M.; Lee, J.-F.; Liaw, W.-F., *Inorg. Chem.* **2004**, *43*, 5159.
40. Veleparampil, M. M.; Aravind, U. K.; Aravindakumar, C. T., *Adv. Phys. Chem.* **2009**, *2009*.
41. Wang Peng, G.; Xian, M.; Tang, X.; Wu, X.; Wen, Z.; Cai, T.; Janczuk, A. J., *Chem. Rev.* **2002**, *102*, 1091.
42. Arulsamy, N.; Bohle, D. S.; Butt, J. A.; Irvine, G. J.; Jordan, P. A.; Sagan, E., *J. Am. Chem. Soc.* **1999**, *121*, 7115.
43. Goto, K.; Hino, Y.; Kawashima, T.; Kaminaga, M.; Yano, E.; Yamamoto, G.; Takagi, N.; Nagase, S., *Tetrahedron Lett.* **2000**, *41*, 8479.
44. Fazaeli, R.; Solimannejad, M.; Seif, A., *J. Chem. Sci.* **2013**, *125*, 913.
45. Barnett, D. J.; Rios, A.; Williams, D. L. H., *J. Chem. Soc., Perkin Trans. 2* **1995**, 1279.
46. Tjee, J. J.; Wampler, F. B.; Oldenborg, R. C.; Rice, W. W., *Chem. Phys. Lett.* **1981**, *82*, 80.
47. Schon, A. H.; deB. Darwent, B., *J. Am. Chem. Soc.* **1954**, *76*, 4806.
48. Sorokin, D. Y.; de Jong, G. A. H.; Robertson, L. A.; Kuenen, G. J., *FEBS Lett.* **1998**, *427*, 11.
49. Enemark, J. H.; Feltham, R. D., *Coord. Chem. Rev.* **1974**, *13*, 339.
50. Mu, X. H.; Kadish, K. M., *Inorg. Chem.* **1988**, *27*, 4720.

51. Miljkovic, J. L.; Kenkel, I.; Ivanović-Burmazović, I.; Filipovic, M. R., *Angew. Chem. Int. Ed.* **2013**, *52*, 12061.
52. Fernandez, B. O.; Lorkovic, I. M.; Ford, P. C., *Inorg. Chem.* **2004**, *43*, 5393.
53. Feig, A. L.; Bautista, M. T.; Lippard, S. J., *Inorg. Chem.* **1996**, *35*, 6892.
54. Majumdar, A.; Lippard, S. J., *Inorg. Chem.* **2013**, *52*, 13292.
55. Rardin, R. L.; Bino, A.; Poganiuch, P.; Tolman, W. B.; Liu, S.; Lippard, S. J., *Angew. Chem. Int. Ed.* **1990**, *29*, 812.
56. Brown, I. D., *Chem. Rev.* **2009**, *109*, 6858.
57. Zheng, S.; Berto, T. C.; Dahl, E. W.; Hoffman, M. B.; Speelman, A. L.; Lehnert, N., *J. Am. Chem. Soc.* **2013**, *135*, 4902.
58. Hayashi, T.; Caranto, J. D.; Matsumura, H.; Kurtz, D. M.; Moënné-Loccoz, P., *J. Am. Chem. Soc.* **2012**, *134*, 6878.
59. Chen, T.-N.; Lo, F.-C.; Tsai, M.-L.; Shih, K.-N.; Chiang, M.-H.; Lee, G.-H.; Liaw, W.-F., *Inorg. Chim. Acta* **2006**, *359*, 2525.

# **CHAPTER 4: REACTIONS OF NITROGEN OXIDE SPECIES WITH A MONOFUNCTIONAL PLATINUM COMPLEX**



## 4.1 Introduction

In the previous chapter, we explored the reactivity of  $\text{SNO}^-$  with iron complexes, but we were unable to obtain a stable, crystalline metal-bound  $\text{SNO}$  complex for structural characterization. The related anion thionylimide,  $\text{NSO}^-$ , has been stabilized as metal salts, as a silyl reagent, and as the acid.<sup>1-3</sup> The binding of  $\text{NSO}^-$  to Ti, Hf, Zr, Ru, Os, Co, Rh, Ir, Pd, and Pt compounds (Figure 4.1) has been studied by X-ray crystallography and by NMR and FTIR spectroscopy.<sup>3-5</sup>

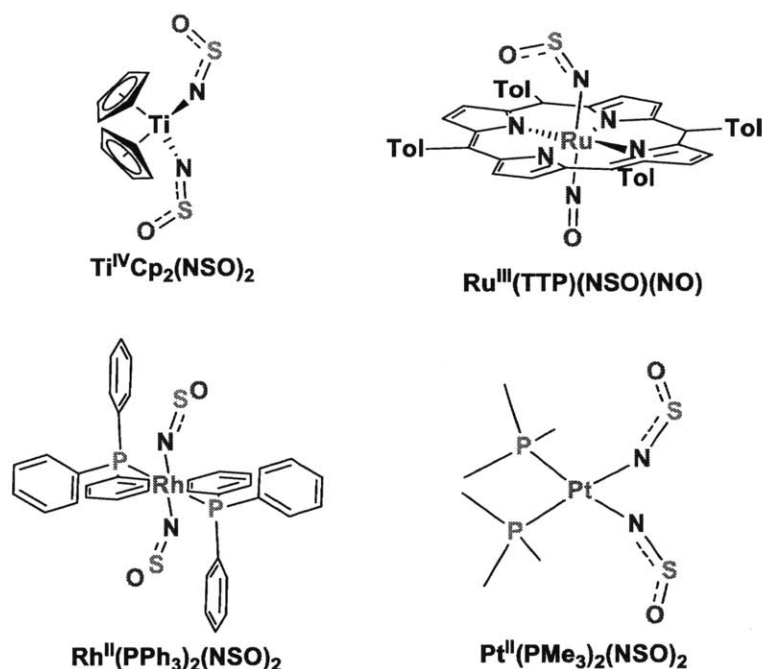


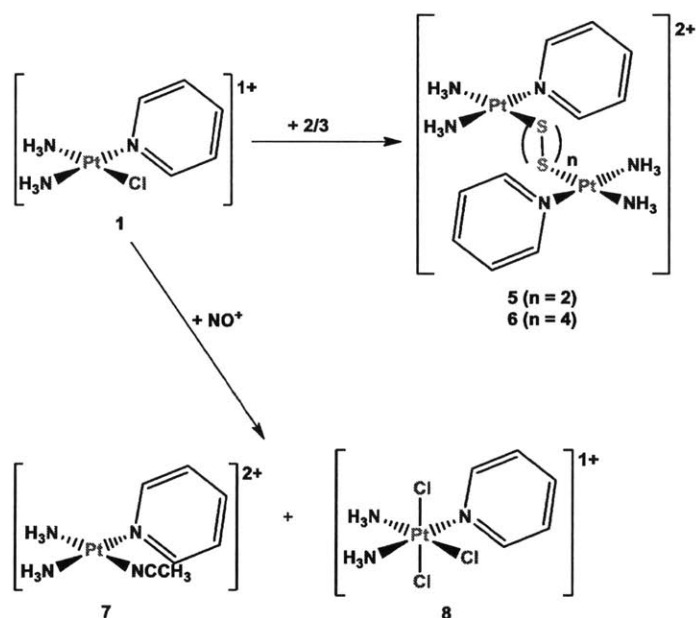
**Figure 4.1** Known metal complexes containing the  $\text{NSO}^-$  ligand.

The most common source of  $\text{NSO}^-$  in these reactions is the alkali metal salt. These alkalimetalthionylimides are prepared in tetrahydrofuran from alkali *t*-butoxides and trimethylsilylthionylimide,  $(\text{CH}_3)_3\text{SiNSO}$ , which is synthesized from tris(trimethylsilyl) amine,  $((\text{CH}_3)_3\text{Si})_3\text{N}$ , and thionyl chloride,  $\text{SOCl}_2$ .<sup>1,2</sup> The  $\text{M}(\text{NSO})$  salts can then be used for ligand metathesis to replace a halide ion of a metal complex to form the intended  $\text{M-NSO}$  species as

well as to precipitate the alkali halide salt.<sup>4-6</sup> Other sources used in direct ligand metathesis reactions are HOSN, S(NSO)<sub>2</sub>, and Hg(NSO)<sub>2</sub>.<sup>7-11</sup>

M–NSO complexes can also be prepared by oxygen atom transfer to a thionitrosyl, NS<sup>–</sup> ligand. This reaction can occur by addition of NO<sub>2</sub><sup>–</sup>, as is the case for Ru(TTP)(NO)(NSO), by running a solution of the compound through a SiO<sub>2</sub> column, as with Cp<sub>2</sub>Ti(NSO)<sub>2</sub>, or by using molecular oxygen, such as for Co(NSO)Cl<sub>2</sub>(P(OPh)<sub>3</sub>)<sub>2</sub>.<sup>4,12,13</sup> Sulfur insertion into the N–O bond of Os(NO)X<sub>2</sub>(PPh<sub>3</sub>)<sub>2</sub>, where X = Cl<sup>–</sup> or Br<sup>–</sup>, results in the formation of Os(NSO)X<sub>2</sub>(PPh<sub>3</sub>)<sub>2</sub>.<sup>7</sup>

Most of the metals used to form complexes are either second- or third-row transition elements, that are typically considered to be under thermodynamic control compared to first-row transition metals. We were hoping to exploit this characteristic to prepare an SNO<sup>–</sup>- or SSNO<sup>–</sup>-bound complex to pyriplatin, *cis*-[Pt(NH<sub>3</sub>)<sub>2</sub>(py)Cl](OTf), **1**, and to compare the physical properties to known NSO<sup>–</sup> complexes, however, this goal was not achieved. We studied the reaction of **1** with NO<sup>+</sup> to compare the reactivity and, in the process, obtained Pt(II) and Pt(IV) complexes (Scheme 4.1).



**Scheme 4.1.** Reactions of *cis*-[Pt(NH<sub>3</sub>)<sub>2</sub>(py)Cl]<sup>+</sup> with SNO<sup>–</sup>, SSNO<sup>–</sup>, and NO<sup>+</sup>.

## 4.2 Experimental Methods

**General.** All manipulations were performed under an atmosphere of nitrogen gas using standard Schlenk techniques or in an MBraun glovebox under an atmosphere of purified nitrogen. Diethyl ether, pentane, methylene chloride, and acetonitrile were purified using a Glass Contour solvent system.<sup>14</sup> Deuterated solvents and Na<sup>15</sup>NO<sub>2</sub> were purchased from Cambridge Isotope Labs Inc. (Tewksbury, MA). *cis*-[Pt(NH<sub>3</sub>)<sub>2</sub>(py)Cl](OTf), **1**, was prepared according to a literature procedure.<sup>15</sup> (PPN)(SS<sup>14/15</sup>NO), **2**, and (PPN)(S<sup>14/15</sup>NO), **3**, were synthesized according to the procedure in chapter 4. [Fe(BIPhMe)Cl<sub>2</sub>], **4**, was synthesized according to the procedure in chapter 2. NOBF<sub>4</sub> was purchased from Sigma-Aldrich, used as received, and stored in a -30° C freezer.

**Physical Measurements.** NMR spectra were recorded on a Varian spectrometer operating at 500 MHz at ambient temperature and referenced to residual signals in the deuterated solvent. Low-resolution ESI mass spectra were obtained with an Agilent 1100 Series LC/MSD mass spectrometer using degassed acetonitrile as the carrier solvent. FTIR spectra were recorded on a Thermo Nicolet Avatar 360 spectrometer running the OMNIC software package; solid samples were pressed into KBr disks.

**X-ray Data Collection and Structure Solution Refinement.** Crystals of **7** and **8** suitable for X-ray diffraction were mounted in Paratone N oil and frozen under a nitrogen cold stream maintained at 100 K by a KRYO-FLEX low-temperature apparatus. Data were collected on a Bruker APEX CCD X-ray diffractometer with Mo K $\alpha$  radiation ( $\lambda = 0.71073 \text{ \AA}$ ) controlled by the *APEX2* software package.<sup>16</sup> Empirical absorption corrections were calculated with *SADABS*.<sup>17</sup> The structures were solved by direct methods with refinement by full-matrix least-squares based

on F<sup>2</sup> using *SHELXTL-97*.<sup>18-20</sup> All non-hydrogen atoms were located and refined anisotropically. Hydrogen atoms were assigned to idealized positions and given thermal parameters equal to either 1.5 (methyl hydrogen atoms) or 1.2 (non-methyl hydrogen atoms) times the thermal parameters of the atoms to which they were attached. Figures were generated using the *Olex2.1* Graphical User Interface.<sup>21</sup> See Tables 2.1, 2.3, and 2.4 below for crystallographic data and refinement details.

**Theoretical calculations.** Quantum mechanical density functional theory (DFT) calculations were performed on the different binding isomers of *cis*-[Pt(NH<sub>3</sub>)<sub>2</sub>(py)(SNO)]<sup>+</sup> and *cis*-[Pt(NH<sub>3</sub>)<sub>2</sub>(py)(SSNO)]<sup>+</sup>, and for the two sulfide-bridged species *cis*-[Pt<sub>2</sub>(NH<sub>3</sub>)<sub>4</sub>(py)<sub>2</sub>(μ-S<sub>2</sub>)]<sup>2+</sup> and *cis*-[Pt<sub>2</sub>(NH<sub>3</sub>)<sub>4</sub>(py)<sub>2</sub>(μ-S<sub>4</sub>)]<sup>2+</sup>. The DFT calculations were carried out in *Gaussian03* using the RPBE1PBE functional and the 31++g(d,p) basis set for non-platinum atoms and the LANL2DZ effective core potential for the platinum atom.<sup>22,23</sup> The atomic coordinates from the crystal structures of **2** and **3** reported in chapter 4, and the crystal structure of **7** were used as the input geometry optimizations for the platinum centers and the SNO and SSNO ligands. Frequency calculations were performed to confirm that each converged upon geometry was at an energy minimum on the potential energy surface of the molecule.

**Reaction of *cis*-[Pt(NH<sub>3</sub>)<sub>2</sub>(py)Cl](OTf), **1**, with (PPN)(SSNO), **2**.** A 20 mL vial was charged with **1** (19.8 mg, 40.6 μmol) and **2** (26.6 mg, 40.7 μmol). The solid mixture was dissolved in acetonitrile (5 mL) and allowed to stir for 2 hrs. Over the course of the reaction, the solution formed a red-orange precipitate. The precipitate, **5**, was filtered off and washed with acetonitrile (3 x 2 mL) and diethyl ether (3 x 2 mL). The filtrate was collected, stripped, and analyzed by <sup>1</sup>H, <sup>19</sup>F, and <sup>31</sup>P NMR spectroscopy, and by ESI-MS to consist of (PPN)(OTf). The red-orange solid **5** (16.2 mg, 35 % total starting weight) was collected and analyzed by FTIR, <sup>1</sup>H, <sup>19</sup>F, <sup>31</sup>P, and

$^{195}\text{Pt}$  NMR.  $^1\text{H}$  NMR (DMF- $d_7$ ,  $\delta$  ppm): 4.83 (3H, br), 5.34 (3H, br), 7.61 (2H, t), 8.09 (1H, t), 8.93 (2H, d).  $^{195}\text{Pt}$  NMR (DMF- $d_7$ ,  $\delta$  ppm): 2311.65 (s). FTIR (KBr,  $\text{cm}^{-1}$ ): 3287 (m), 3242 (s), 3110 (s), 3067 (s), 2963 (m), 2920 (m), 2850 (m), 1658 (sh), 1609 (s), 1571 (m), 1488 (w), 1452 (s), 1370 (w), 1340 (s), 1242 (w), 1212 (w), 1153 (w), 1113 (w), 1075 (m), 1020 (w), 762 (s), 691 (s), 534 (w).

**Reaction of *cis*-[Pt(NH<sub>3</sub>)<sub>2</sub>(py)Cl](OTf), 1, with (PPN)(SS<sup>15</sup>NO), <sup>15</sup>2.** Experimental conditions were similar to reaction with 2 and by  $^1\text{H}$  NMR and FTIR was found to consist of 5. FTIR (KBr,  $\text{cm}^{-1}$ ): 3287 (m), 3244 (s), 3110 (s), 3066 (s), 2924 (m), 2849 (m), 1654 (w), 1609 (s), 1570 (m), 1488 (w), 1452 (s), 1370 (w), 1340 (s), 1242 (w), 1213 (w), 1153 (w), 1075 (m), 1020 (w), 762 (s), 691 (s), 533 (w).

**Reaction of *cis*-[Pt(NH<sub>3</sub>)<sub>2</sub>(py)Cl](OTf), 1, with (PPN)(SNO), 3.** A 5 mL vial was charged with 1 (12.3 mg, 25.0  $\mu\text{mol}$ ) and 3 (15.3 mg, 25.5  $\mu\text{mol}$ ). The vial was placed into a larger 20 mL vial containing a solution of 4 in MeCN (20  $\mu\text{M}$ ). The solid mixture was dissolved in acetonitrile (2 mL) and allowed to stir for 2 hrs. Over the course of the reaction, the reaction solution formed a yellow precipitate and the 4-containing solution turned dark green and was determined by FTIR to consist of [Fe(BIPhMe)<sub>2</sub>(NO)Cl][Fe(NO)Cl<sub>3</sub>], 4•NO. The precipitate, 6, was filtered off and washed with acetonitrile (3 x 2 mL) and diethyl ether (3 x 2 mL). The filtrate was collected, stripped, and analyzed by  $^1\text{H}$ ,  $^{19}\text{F}$ , and  $^{31}\text{P}$  NMR, and by ESI-MS to consist of (PPN)(OTf). The yellow solid 6 (9.4 mg, 34 % total starting weight) was collected.  $^1\text{H}$  NMR (DMF- $d_7$ ,  $\delta$  ppm): 4.76 (3H, br), 5.23 (3H, br), 7.61 (2H, t), 8.10 (1H, t), 8.91 (1H, d). FTIR (KBr,  $\text{cm}^{-1}$ ): 3287 (m), 3239 (s), 3105 (s), 3092 (s), 3067 (s), 2924 (w), 1609 (s), 1570 (m), 1488 (w), 1452 (s), 1370 (m), 1340 (s), 1242 (w), 1213 (w), 1154 (m), 1075 (w), 1020 (w), 762 (s), 691 (s), 465 (w).

**Reaction of *cis*-[Pt(NH<sub>3</sub>)<sub>2</sub>(py)Cl](OTf), 1, with (PPN)(S<sup>15</sup>NO), <sup>15</sup>3.** Experimental conditions were similar to those used with reaction with 3 and by <sup>1</sup>H NMR and IR spectroscopy was concluded to consist of 6. The presence of 4·<sup>15</sup>NO was detected by IR spectroscopy. FTIR (KBr, cm<sup>-1</sup>): 3283 (m), 3244 (s), 3135 (s), 3109 (s), 3097 (s), 3067 (s), 1675 (w), 1610 (s), 1571 (m), 1489 (w), 1452 (s), 1370 (m), 1340 (s), 1242 (w), 1208 (w), 1154 (m), 1075 (w), 1020 (w), 762 (s), 691 (s), 452 (w).

**Reaction of *cis*-[Pt(NH<sub>3</sub>)<sub>2</sub>(py)Cl](OTf), 1, with NOBF<sub>4</sub> to form *cis*-[Pt(NH<sub>3</sub>)<sub>2</sub>(py)(CH<sub>3</sub>CN)](BF<sub>4</sub>), 7, and *cis-mer*-[Pt(NH<sub>3</sub>)<sub>2</sub>(py)Cl<sub>3</sub>]Cl, 8.** A 20 mL vial was charged with 1 (21.4 mg, 43.4 μmol) and dissolved in acetonitrile (4 mL). A portion of NOBF<sub>4</sub> (10.2 mg, 87.3 μmol) was dissolved in acetonitrile (4 mL) and added dropwise over the course of 1 min. The solution turned blue initially but, over the course of 3 h, turned pale yellow. The solution was stripped and redissolved in acetonitrile (0.5 mL). Colorless and yellow block crystals were grown by vapor diffusion of diethyl ether into the acetonitrile solution. The crystals were too small to separate mechanically, but individual crystals could be selected for X-ray and elemental analysis. The elemental analysis produces no useable information, but was still close to the expected values based on the X-ray diffraction study. We suspect that the presence of different anions within the selected crystals may be the reason. The crystal mixture was collected, washed with diethyl ether (3 x 2 mL), and dried to yield a total collected product of 9.5 mg (30 % of expected weight). **Characterization of 7:** Anal. Calc'd for C<sub>7</sub>H<sub>14</sub>B<sub>2</sub>F<sub>8</sub>N<sub>4</sub>Pt: C, 16.08; H, 2.70; N, 10.71. Found: C, 15.77; H, 1.78; N, 9.12. <sup>1</sup>H NMR (CD<sub>3</sub>CN, δ ppm): 3.82 (3H, br), 3.98 (3H, br), 7.62 (2H, t), 8.10 (1H, t), 8.65 (2H, d). **Characterization of 8:** Anal. Calc'd for C<sub>5</sub>H<sub>11</sub>Cl<sub>4</sub>N<sub>3</sub>Pt: C, 13.34; H, 2.46; N, 9.34. Found: C, 13.65; H, 1.88; N, 9.15. <sup>1</sup>H NMR

(CD<sub>3</sub>CN,  $\delta$  ppm): 5.20 (3H, tt,  $J_{H-Pt}$  22.9 Hz,  $J_{H-N}$  63.9 Hz), 5.32 (3H, tt,  $J_{H-Pt}$  24.5 Hz,  $J_{H-N}$  53.8 Hz), 7.71 (2H, dd), 8.24 (1H, tt), 8.91 (2H, dt).

### 4.3 Results and Discussion

**Reaction of *cis*-[Pt(NH<sub>3</sub>)<sub>2</sub>(py)Cl](OTf) with (PPN)(SSNO) and (PPN)(SNO).** In an attempt to form a stable SNO<sup>-</sup> or SSNO<sup>-</sup> complex, [Pt(NH<sub>3</sub>)<sub>2</sub>(py)Cl](OTf), **1**, was used. Both (PPN)(SSNO), **2**, and (PPN)(SNO), **3**, react to form a Pt-containing species **5** and **6** that are highly insoluble in all solvents except for *N,N'*-DMF and DMSO. Attempts were made to grow crystals of *N,N'*-DMF solutions of **5** and **6**, but all were unsuccessful and only resulted in non-crystalline precipitates.

These two reactions form two slightly different species, **5** and **6**, based on their colors, red-orange and yellow, respectively, and their <sup>1</sup>H and <sup>195</sup>Pt spectra (Figure 4.2). The <sup>1</sup>H NMR spectra consist solely of peaks assigned to Pt-bound amines and pyridine that are shifted downfield from the starting material. This result suggests that the Cl<sup>-</sup> ligand may be replaced with a more electron-withdrawing ligand. The PPN<sup>+</sup> cation and OTf<sup>-</sup> anion are removed and only present in the worked up filtrate, based on ESI-MS, and on <sup>19</sup>F, and <sup>31</sup>P NMR spectroscopy.

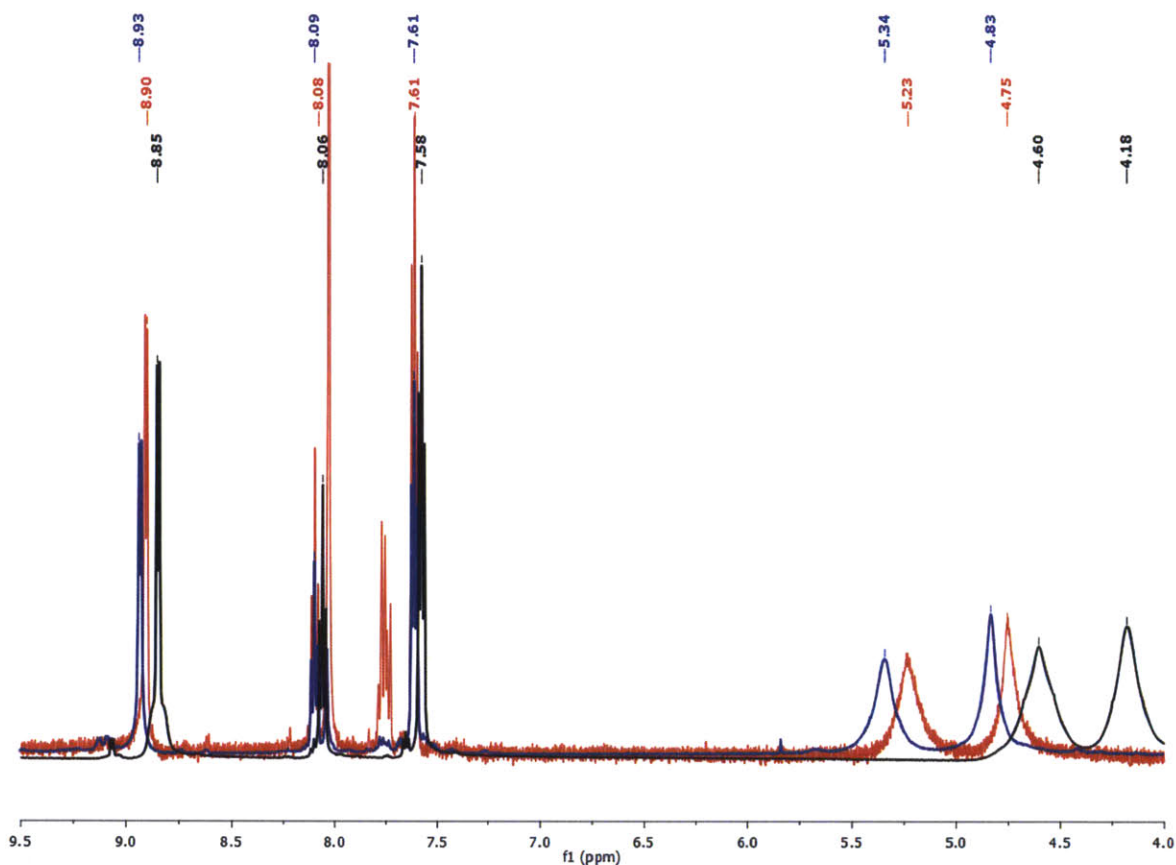


**Figure 4.2.**  $^1\text{H}$  NMR spectra of **1** (black), **1 + 2** (blue), and **1 + 3** (red) in  $\text{DMF-}d_7$ .

Compounds **5** and **6** contain  $\text{Cl}^-$ , as determined by the instant formation of a precipitate upon addition of  $\text{Ag}^+$  and  $\text{Tl}^+$  salts. It was initially thought based on these data and the mass balance of the reaction that the precipitated species **5** and **6** were *cis*- $[\text{Pt}(\text{NH}_3)_2(\text{py})(\text{SSNO})]\text{Cl}$  and *cis*- $[\text{Pt}(\text{NH}_3)_2(\text{py})(\text{SNO})]\text{Cl}$ , respectively. This result was shown to not be the case after preparing **5** and **6** with the use of  $^{15}\text{N}$ -isotopically labeled **2** and **3** and measuring their FTIR spectra (Figure 4.3). The isotopically labeled spectra overlay directly on the natural abundance ones, indicating that the labeled nitrogen of **2** and **3** is not incorporated into the final product.



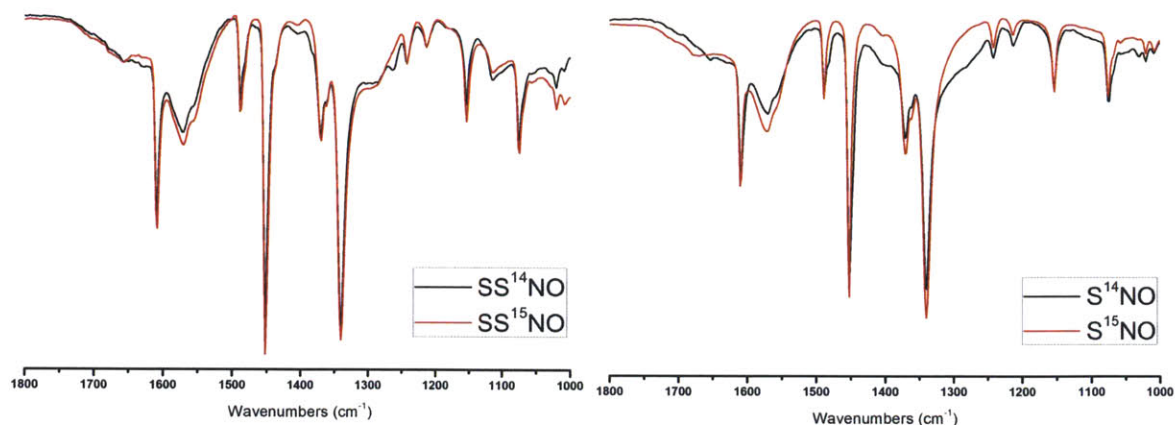


**Figure 4.3.** FTIR spectra (KBr) of natural abundance (black) and  $^{15}\text{N}$  labeled (red) **5** (left) and **6** (right).

To ascertain the fate of the nitrogen atom, the preparation of **6** was repeated while sharing the headspace with a 20  $\mu\text{M}$  solution of **4** in acetonitrile in a closed vessel. After a 2 hour reaction period, the **4**-solution turned green, signaling the presence of  $\text{NO}(\text{g})$  (Figure 4.4) by observing the FTIR spectrum of the green solution. This result shows that **1** homolytically cleaves the S–N bond of **3**.



**Figure 4.4.** Vials following the formation of **6** and release of  $\text{NO}(\text{g})$  to convert **1** into its nitrosylated product. Initial (left) and after 2 hrs (right).

Our current hypothesis is that the Pt-species contains a polysulfide ligand and successful crystallization conditions remain elusive. Because **5** and **6** have different colors and their  $^1\text{H}$  NMR spectra do not overlay, we believe that the difference between these two compounds may

reflect the length of the polysulfide ligand. To investigate the structure of the product more thoroughly, additional spectroscopic characterization using resonance Raman or XAS spectroscopy would be required.

**DFT calculations of polysulfide-bridged Pt-species.** Since we determined that the final species did not contain an NO-containing ligand, we proceeded to calculate the vibrational spectrum of two *cis*-[Pt(NH<sub>3</sub>)<sub>2</sub>(py)]<sup>2+</sup> units bridged by di- and tetrasulfides (Figure 4.5). We optimized the geometry of both molecules, which resulted in the two Pt-centers of each molecule to be equivalent. For both molecules, the Pt–N distances were lengthened by ~0.04 – 0.11 Å compared to the published distances of 1. Between the two calculated structures the only major difference in geometrical parameters is the Pt–S··S–Pt dihedral angle (Table 4.1). For the S<sub>4</sub>-bridged molecule, the dihedral angle is ~180°, whereas for the S<sub>2</sub>-bridged molecule the dihedral angle is ~117°. This difference can be attributed to hydrogen bonding between an amine proton and the secondary sulfur in both structures. The additional sulfur atoms of the S<sub>4</sub>-bridged molecule allow for the Pt–S··S–Pt dihedral angle to adjust itself to ~180°.

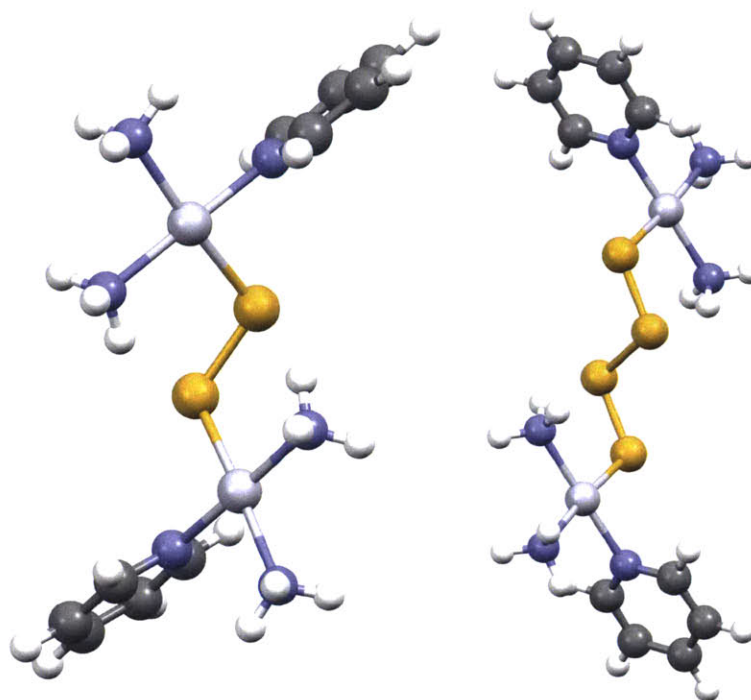


**Figure 4.5.** Calculated structures of  $cis-[Pt_2(NH_3)_4(py)_2(\mu-S_2)]^{2+}$  (left) and  $cis-[Pt_2(NH_3)_4(py)_2(\mu-S_4)]^{2+}$  (right). Color scheme: platinum, light grey; nitrogen, blue; sulfur, yellow; carbon, dark grey; hydrogen, white.

**Table 4.1.** Selected calculated geometrical parameters for **5** and **6**.

	$cis-[Pt_2(NH_3)_4(py)_2(\mu-S_2)]^{2+}$	$cis-[Pt_2(NH_3)_4(py)_2(\mu-S_4)]^{2+}$
<u>bond length, Å</u>		
Pt-N <sub>amine</sub>	2.07311	2.07352
	2.15760	2.15900
Pt-N <sub>pyridine</sub>	2.04351	2.04231
Pt-S	2.32167	2.31776
S-S	2.08500	2.03685
		2.20005
H <sub>amine</sub> -S	2.23192	2.28634
<u>Bond angles, °</u>		
N <sub>amine</sub> -Pt-N <sub>amine</sub>	92.06751	92.10097
N <sub>amine</sub> -Pt-N <sub>pyridine</sub>	89.08125	89.28411
	178.44292	178.59457
N <sub>amine</sub> -Pt-S	92.75949	93.11209
	174.29179	174.77240
N <sub>pyridine</sub> -Pt-S	86.03822	85.50129
Pt-S-S	109.85713	110.17700
S-S-S	–	103.41323
<u>Dihedral angles, °</u>		
Pt-S...S-Pt	116.86187	179.99814
S-S-S-S	–	179.99582

The FTIR spectrum of **5** and **6** match fairly well with only a few features that are shifted by a few wavenumbers, and the same is true of the vibrational spectra of the two calculated

molecules (Figure 4.6). The vibrational spectrum of the two calculated structures were corrected by fitting the calculated values of selected peaks with experimental peaks that looked to be appropriate (Table 4.2). After fitting, the calculated and experimental spectra have fairly similar bands. Any variations in wavenumbers may be attributed to hydrogen bonding interactions that may occur in the solid state and were not calculated. There is a band in both of the calculated structures,  $865\text{ cm}^{-1}$  and  $883\text{ cm}^{-1}$ , that does not have a corresponding experiment peak. These bands are bending modes of the amine protons that do not effect a change in the dipole moment of the molecule, suggesting that these may be IR-silent vibrations. These calculated results provide further data that **5** and **6** have similar structures but with different length polysulfide linkers.

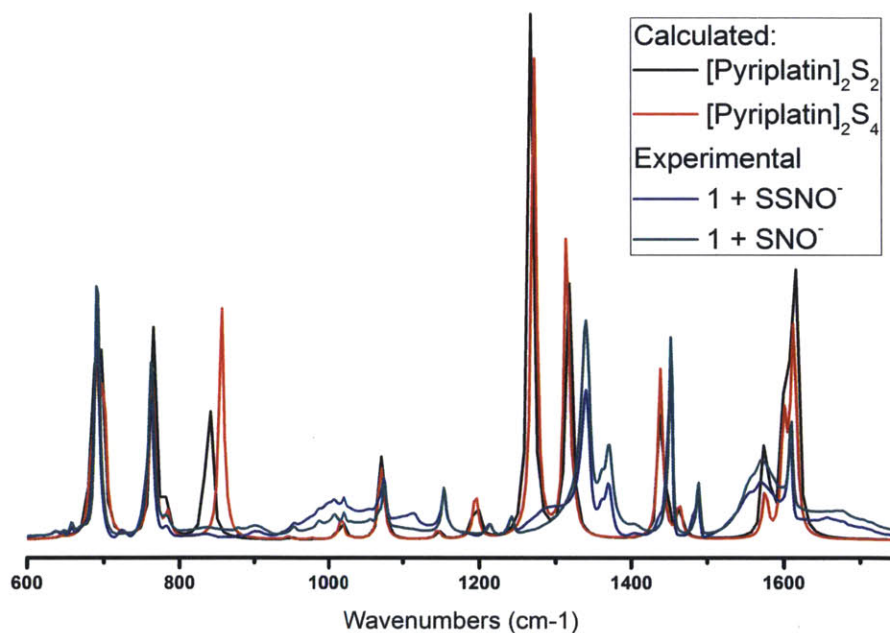


**Figure 4.6.** Calculated spectra of  $cis\text{-}[\text{Pt}_2(\text{NH}_3)_4(\text{py})_2(\mu\text{-S}_2)]^{2+}$  (black) and  $cis\text{-}[\text{Pt}_2(\text{NH}_3)_4(\text{py})_2(\mu\text{-S}_4)]^{2+}$  (red) overlaid on spectra of **5** (blue) and **6** (green). The calculated spectra were corrected by fitting selected peaks to experimental data.

**Table 4.2. Vibrational energies used to prepare fitting equation for calculated spectra.**

Experimental: <b>5</b>	Calculated: <i>cis</i> -[Pt <sub>2</sub> (NH <sub>3</sub> ) <sub>4</sub> (py) <sub>2</sub> (μ-S <sub>4</sub> )] <sup>2+</sup>	Experimental: <b>6</b>	Calculated: <i>cis</i> -[Pt <sub>2</sub> (NH <sub>3</sub> ) <sub>4</sub> (py) <sub>2</sub> (μ-S <sub>2</sub> )] <sup>2+</sup>
691 cm <sup>-1</sup>	708 cm <sup>-1</sup>	691 cm <sup>-1</sup>	707 cm <sup>-1</sup>
761 cm <sup>-1</sup>	786 cm <sup>-1</sup>	761 cm <sup>-1</sup>	787 cm <sup>-1</sup>
1451 cm <sup>-1</sup>	1499 cm <sup>-1</sup>	1451 cm <sup>-1</sup>	1501 cm <sup>-1</sup>
1570 cm <sup>-1</sup>	1644 cm <sup>-1</sup>	1570 cm <sup>-1</sup>	1645 cm <sup>-1</sup>
1609 cm <sup>-1</sup>	1683 cm <sup>-1</sup>	1609 cm <sup>-1</sup>	1684 cm <sup>-1</sup>
Fit equation: R <sup>2</sup> : 0.9997	0.9463x + 20.258 cm <sup>-1</sup>	Fit equation: R <sup>2</sup> : 0.9998	0.9449x + 21.253 cm <sup>-1</sup>

**DFT calculations of *cis*-[Pt(NH<sub>3</sub>)<sub>2</sub>(py)(SNO)]<sup>+</sup> and *cis*-[Pt(NH<sub>3</sub>)<sub>2</sub>(py)(SSNO)]<sup>+</sup>.** We performed DFT calculations using the RPBE1PBE functional in Gaussian 03 to determine how the energy of the N–O vibration changes among the different binding modes possible for *cis*-[Pt(NH<sub>3</sub>)<sub>2</sub>(py)(SNO)]<sup>+</sup>, 1•SNO, and *cis*-[Pt(NH<sub>3</sub>)<sub>2</sub>(py)(SSNO)]<sup>+</sup>, 1•SSNO. In both situations, the binding of the terminal sulfur to the platinum center was the most energetically favorable.

Platinum binding to the nitrogen in 1•SNO has a free energy that is higher by 29.5 kJ/mol, whereas the oxygen-bound species is less favorable by 77.9 kJ/mol compared to the sulfur-bound species. The S–N bond in sulfur-bound 1•SNO is elongated by 0.159 Å to 1.848 Å compared to the anion, but is 0.041 Å shorter than the calculated HSNO structure. The Pt–S bond is calculated to be 2.299 Å.

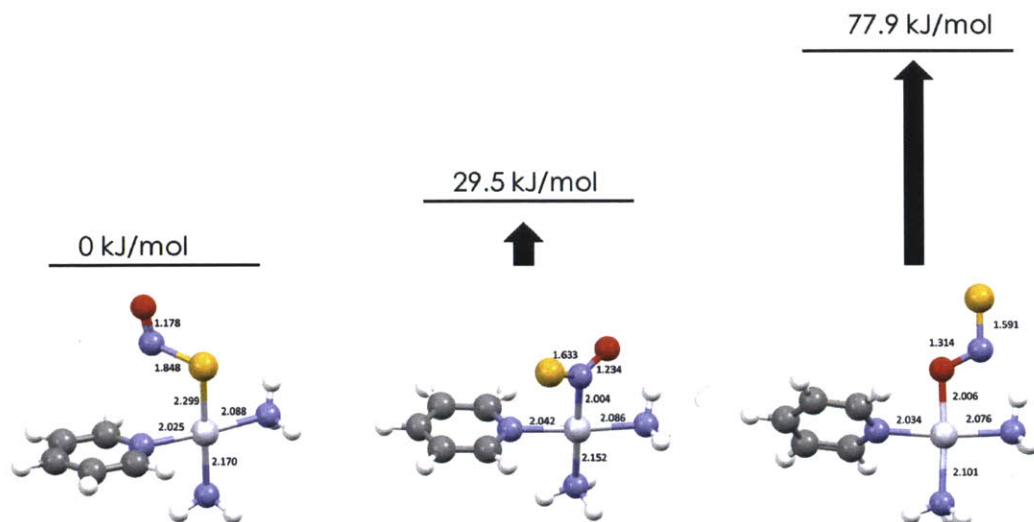


**Figure 4.7.** Energies and structures of  $1\cdot\text{SNO}$  calculated by DFT.

The  $\nu_{\text{NO}}$  stretching frequency of  $1\cdot\text{SNO}$  varies significantly between the different calculated structures. For the energetically favorable sulfur-bound structure the frequency is  $1742\text{ cm}^{-1}$ . The  $\nu_{\text{NO}}$  stretch decreases as the binding site moves to the nitrogen and oxygen, resulting in values of  $1483\text{ cm}^{-1}$  and  $1134\text{ cm}^{-1}$ , respectively.

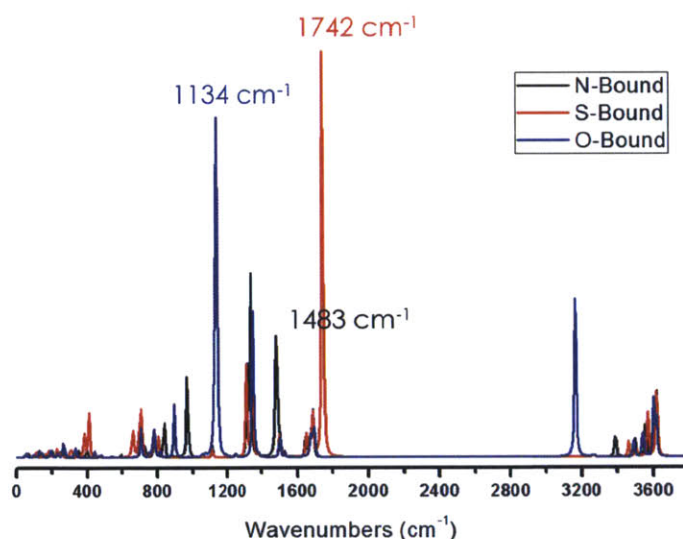


**Figure 4.8.** Vibrational spectra of  $1\cdot\text{SNO}$  calculated by DFT using the RPBE1PBE basis set.

In the calculated structure of  $1\cdot\text{SSNO}$ , binding to the secondary sulfur results in a free energy that is unfavorable by  $52.2\text{ kJ/mol}$ . Nitrogen-binding to the platinum is less favorable by  $90.5\text{ kJ/mol}$  and oxygen-binding is even less favorable, by  $98.4\text{ kJ/mol}$ . When we attempted to

calculate the S- and O-chelated structure of **1·SSNO**, the oxygen atom moved away from the platinum and the SSNO-moiety rotated until it was in the same position as was calculated for the terminal, sulfur-bound species. For the calculated structure of **1·SSNO**, the S–N bond elongated to 1.789 Å with a Pt–S bond of 2.318 Å.

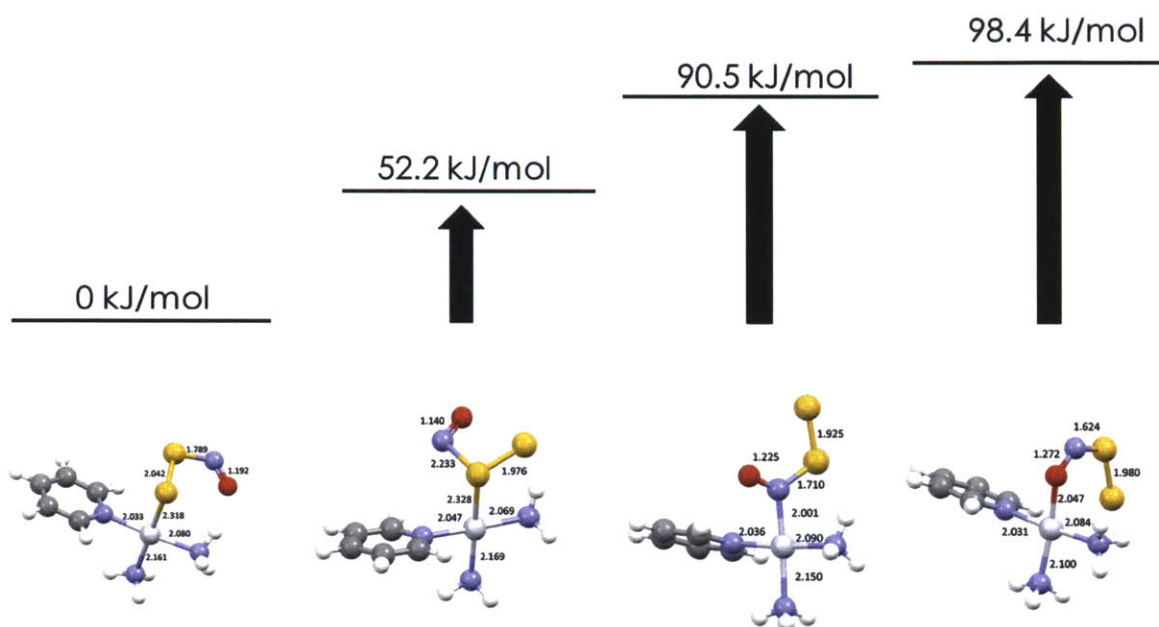


**Figure 4.9.** Energies and structures of **1·SSNO** calculated by DFT.

The calculated  $\nu_{NO}$  stretch of **1·SSNO** spans a wider range than those calculated for **1·SNO**. The energetically favorable terminal sulfur-bound species has a  $\nu_{NO}$  stretch that is calculated to occur at  $1686\text{ cm}^{-1}$ , but this stretch increases in energy for the secondary sulfur-bound case to  $1962\text{ cm}^{-1}$ . The nitrogen-bound species has a calculated  $\nu_{NO}$  stretch at  $1506\text{ cm}^{-1}$ , which is higher than for the N-bound **1·SNO** case. The oxygen-bound species is calculated to occur at  $1287\text{ cm}^{-1}$ .

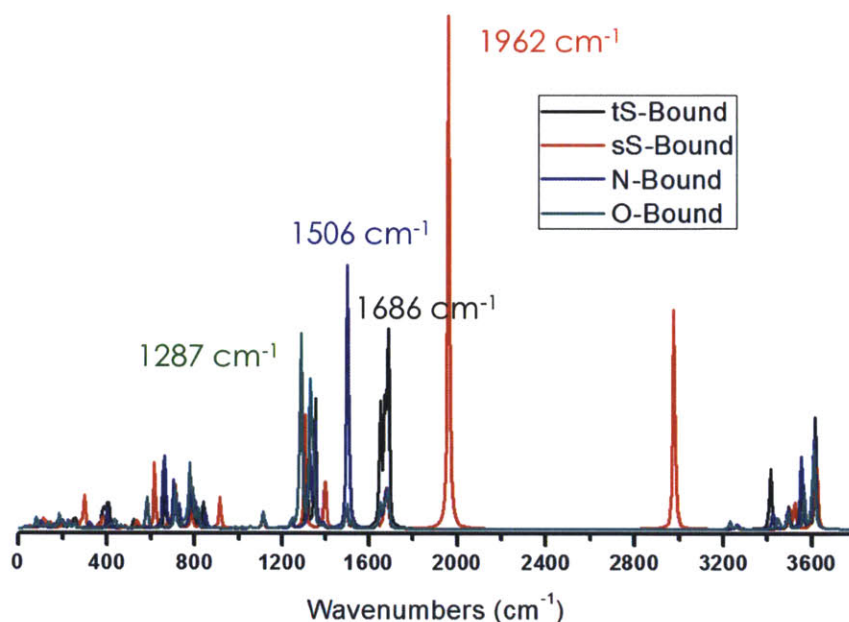


**Figure 4.10.** Vibrational spectra of **1**·SSNO calculated by DFT using the RPBE1PBE basis set.

**Reaction of *cis*-[Pt(NH<sub>3</sub>)<sub>2</sub>(py)Cl](OTf) with NOBF<sub>4</sub>.** To understand whether **1** is susceptible to oxidation by NO<sup>+</sup>, we performed a reaction with the reagent NOBF<sub>4</sub>. Because **2** and **3** can theoretically be perceived as consisting of S<sub>n</sub><sup>2-</sup> and NO<sup>+</sup>, we wanted to compare the reaction products obtained from exposure to NO<sup>+</sup>. Published reaction products of Pt(II) compounds with NO<sup>+</sup> include five-coordinate square pyramidal complexes having NO<sup>+</sup> in the axial position and the counterion of the nitrosonium salt.<sup>24,25</sup>

The reaction initially formed a pale blue solution, proposed to be a platinum-platinum dimer, but turns pale yellow over the course of three hours. The solution contained the Pt(II) species *cis*-[Pt(NH<sub>3</sub>)<sub>2</sub>(py)(CH<sub>3</sub>CN)]<sup>2+</sup>, **7**, and the Pt(IV) species *cis-mer*-[Pt(NH<sub>3</sub>)<sub>2</sub>(py)Cl<sub>3</sub>]<sup>+</sup>, **8**, by X-ray crystallography and by <sup>1</sup>H NMR spectroscopy. Pt(IV) compounds prefer to have an octahedral geometry and therefore require two axial ligands to bind upon oxidation, which is accomplished by removing the chlorides of two equivalents of **1** to form **8**. The now open coordination sites of **1** can be occupied by acetonitrile to form the {PtN<sub>4</sub>} complex **7**.



Both **7** and **8** were crystallized by diffusion of diethyl ether into a crude acetonitrile solution of the reaction. Crystals of **7** are colorless and have two  $\text{BF}_4^-$  molecules as counter ions. The complex is square planar with adjacent bond angles that are  $90^\circ \pm 1^\circ$ . The Pt–N<sub>amine</sub> bond distances are 2.029(3) Å and 2.049(3) Å for the amines *cis* and *trans* to the pyridine ring, respectively, which are shortened compared to the values of 2.0379(18) Å and 2.0404(18) Å published for the structure of **1**. The Pt–N<sub>pyridine</sub> bond distance is 2.024(3) Å, which is comparable to the published value of 2.0222(18) Å for **1**. The Pt–N<sub>acetonitrile</sub> bond distance is 1.975(3) Å and is much shorter than the Pt–Cl bond distance of 2.3047(5) Å in the structure of **1**.

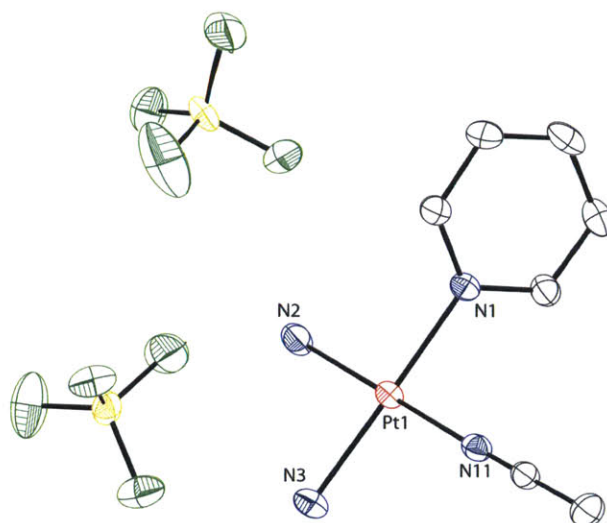


**Figure 4.11.** Representation of the X-ray crystal structure of **7** with ellipsoids shown at 50% probability. Hydrogen atoms are omitted for clarity. Color scheme: platinum, red; nitrogen, blue; fluorine, green; boron, yellow; carbon, colorless.

Yellow crystals of **8** were collected from the same crystallization setup as **7**. These crystals have two molecules of **8**, which have slightly different bond lengths and angles, and two chloride counter ions present in the asymmetric unit. The Pt–N<sub>amine</sub> bond lengths are 2.032(4) and 2.038(4) for one molecule and 2.029(4) and 2.055(4) for the other molecule. The Pt–N<sub>pyridine</sub> bond distances are 2.067(3) and 2.057(3). The three Pt–Cl distances for the two molecules in the crystal structure are more similar to each other than the Pt–N distances with 2.3207(11),

2.3078(10), and 2.3210(10) for one molecule of **8** and 2.3229(11), 2.3007(10), and 2.3167(10) for the other. The two molecules have an octahedral geometry around the platinum atom with the second molecule having bond angles that deviate more from the perfect 90° angles expected.

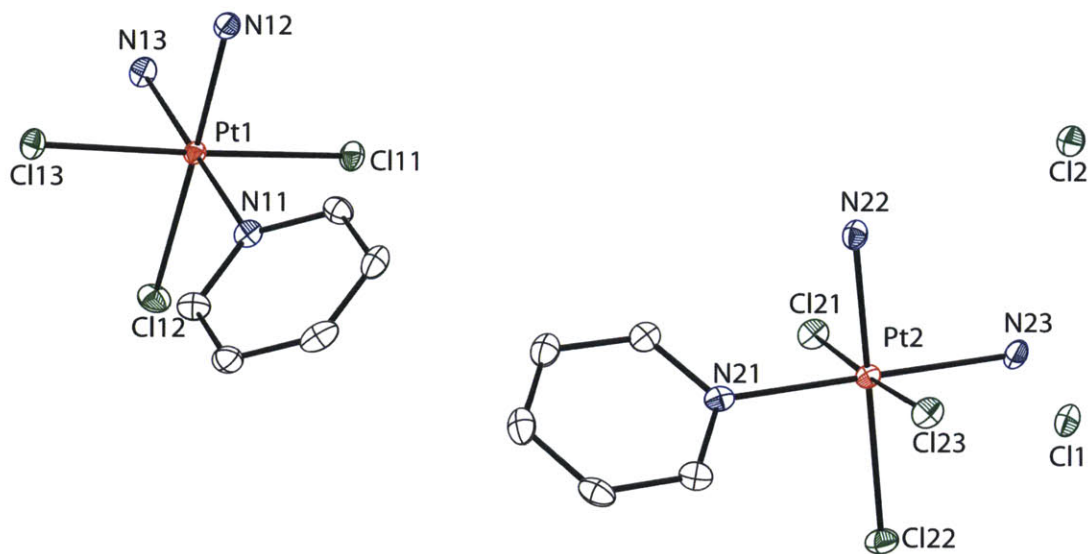


**Figure 4.12.** Graphical representation of the X-ray crystal structure of **8** with ellipsoids shown at 50% probability. Hydrogen atoms are omitted for clarity. Color scheme: platinum, red; nitrogen, blue; chlorine, green; carbon, colorless.

**Table 4.3. Geometrical parameters of pyriplatin and related complexes.**

	<i>cis</i> -[Pt(NH <sub>3</sub> ) <sub>2</sub> (py)Cl](OTf), 1 <sup>15</sup>	<i>cis</i> -[Pt(NH <sub>3</sub> ) <sub>2</sub> (py)(CH <sub>3</sub> CN)](BF <sub>4</sub> ) <sub>2</sub> , 7	<i>cis-mer</i> -[Pt(NH <sub>3</sub> ) <sub>2</sub> (py)Cl <sub>3</sub> ]Cl, 8	
<b>bond length, Å</b>				
Pt–N <sub>amine</sub>	2.0379(18) 2.0404(18)	2.029(3) 2.049(3)	2.032(4); 2.038(4);	2.029(4) 2.055(4)
Pt–N <sub>pyridine</sub>	2.0222(18)	2.024(3)	2.067(3);	2.057(3)
Pt–X <sup>a</sup>	2.3047(5)	1.975(3)	2.3207(11); 2.3078(10); 2.3210(10);	2.3229(11) 2.3007(10) 2.3167(10)
<b>Bond angles, °</b>				
N <sub>amine</sub> –Pt–N <sub>amine</sub>	90.12(7)	89.01(13)	90.27(17);	91.77(16)
N <sub>amine</sub> –Pt–N <sub>pyridine</sub>	89.08(7)	89.89(13)	89.32(16);	88.59(15)
	178.54(7)	178.87(13)	179.46(15);	179.37(15)
N <sub>amine</sub> –Pt–X <sup>a</sup>	89.97(5) 179.61(6)	90.72(13) 178.15(14)	91.76(12); 178.64(12); 87.39(12); 89.15(12);	91.68(12) 178.01(12) 86.24(12) 90.34(12)
			89.64(13); 88.76(12);	89.18(12) 88.11(12)
N <sub>pyridine</sub> –Pt–X <sup>a</sup>	90.84(5)	90.39(12)	90.52(10); 90.78(10); 91.57(10);	89.14(10) 90.47(10) 92.43(10)
Cl–Pt–Cl	–	–	89.60(4); 177.73(4); 91.25(4);	90.06(4) 177.37(4) 92.04(4)

<sup>a</sup> X = Cl<sup>–</sup> or NCCH<sub>3</sub>**Table 4.4. X-ray crystallographic data for 7 and 8 at 100K.**

compounds	<i>cis</i> -[Pt(NH <sub>3</sub> ) <sub>2</sub> (py)(CH <sub>3</sub> CN)](BF <sub>4</sub> ) <sub>2</sub> , 7	<i>cis-mer</i> -[Pt(NH <sub>3</sub> ) <sub>2</sub> (py)Cl <sub>3</sub> ]Cl, 8
formula	C <sub>7</sub> H <sub>14</sub> B <sub>2</sub> F <sub>8</sub> N <sub>4</sub> Pt	C <sub>3</sub> H <sub>11</sub> C <sub>14</sub> N <sub>3</sub> Pt
formula weight	522.93	450.06
crystal system	100(2)	Triclinic
space group	P2 <sub>1</sub> /c	P $\bar{1}$
a, Å	12.4331(7)	7.9480(8)
b, Å	9.8021(6)	11.8530(12)
c, Å	12.4418(7)	14.0649(14)
α, deg	90	67.621(2)
β, deg	90.735(1)	88.870(2)
γ, deg	90	72.3450(10)
V, Å <sup>3</sup>	1516.16(15)	1160.8(2)
Z	4	4
ρ <sub>calcd</sub> , g/cm <sup>3</sup>	2.291	2.575
μ, mm <sup>–1</sup>	9.337	12.969
θ range, deg	1.64 to 30.76	1.58 to 26.46
completeness to θ, %	95.0	99.7
reflections collected	30129	20603
independent reflections	4483	4770
R(int)	0.0363	0.0376
restraints	30	0
parameters	224	283
Max., min. transmission	0.7455, 0.4348	0.7454, 0.6168
R1(wR2) [I>2σ(I)]	0.0272 (0.0661)	0.0216 (0.0426)
R1(wR2)	0.0370 (0.0688)	0.0297 (0.0452)
GoF(F <sup>2</sup> )	1.791	1.044
max, min peaks, e.Å <sup>–3</sup>	3.877, -1.691	1.269, -0.889

Because both **7** and **8** were obtained from crystallization and could not be separated, we collected a  $^1\text{H}$  NMR spectrum of the mixture in  $\text{CD}_3\text{CN}$ . Two sets of peaks that correspond to **7** and **8** could be identified from the obtained spectrum in a ratio of 2:1. The three peaks corresponding to the pyridine protons of **7** occur at 7.62, 8.10, and 8.65 ppm, whereas the pyridine protons of **8** occur downfield at 7.71, 8.24, and 8.91 ppm. The ammine protons of **8** occur in the range of 5.11 – 5.40 ppm and can be distinguished as a triplet of triplets with  $J_{\text{H-Pt}}$  coupling constants of 22.9 and 24.5 Hz and  $J_{\text{H-N}}$  coupling constants of 53.79 and 63.94 Hz. The ammine protons of **7** are further upfield at 3.82 – 3.98 ppm and are less resolved, owing to interactions of the  $^{195}\text{Pt}$  nucleus on the  $^{14}\text{N}$  nucleus of the amines. The peak at 2.42 ppm was assigned as the coordinated acetonitrile in **7** and we attribute the low integration value of this peak to substitution with the solvent  $\text{CD}_3\text{CN}$ . The  $^1\text{H}$  NMR spectra of **7** and **8** do not match the spectra obtained for either **5** or **6**. This result informs us that **2** and **3** are not serving as  $\text{NO}^+$  donors to platinum centers.

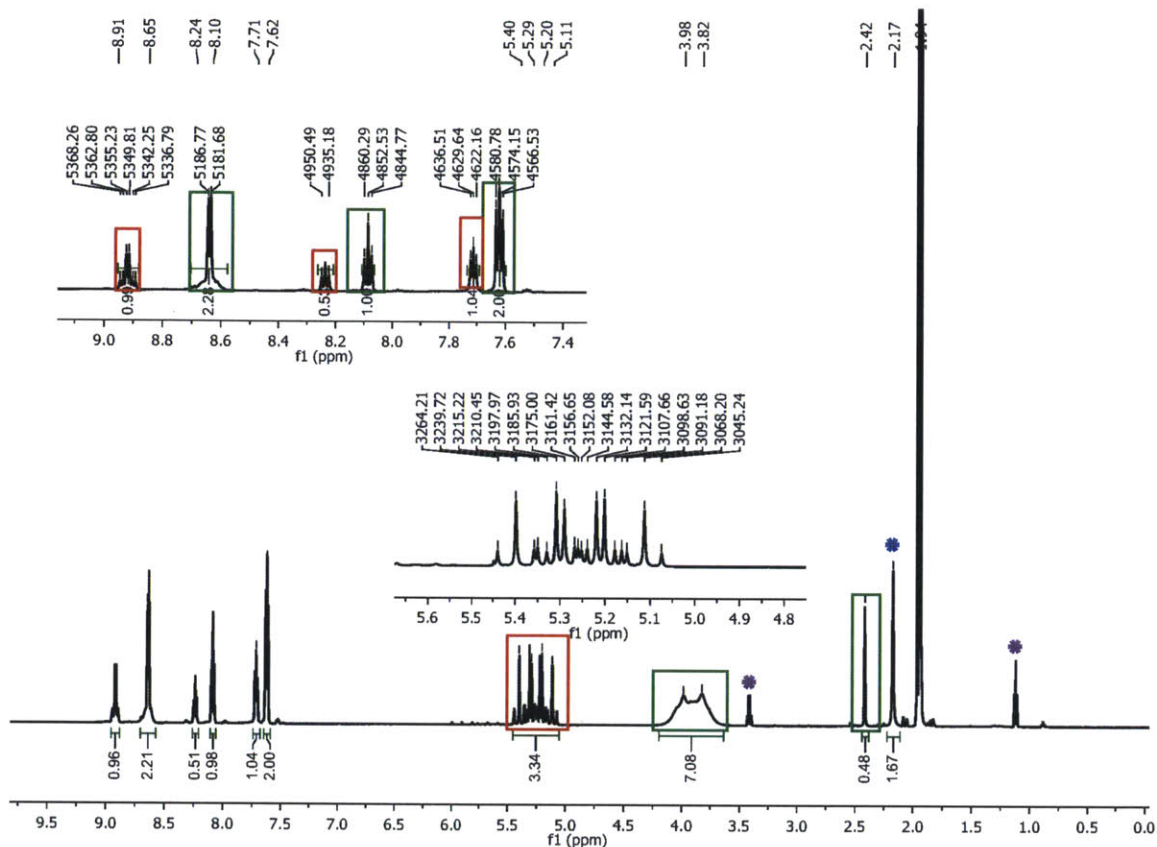


**Figure 4.13.** <sup>1</sup>H NMR spectrum of a mixture of crystalline **7** and **8** collected in CD<sub>3</sub>CN at 500 MHz. Peaks corresponding to **7** are enclosed in green boxes. Peaks corresponding to **8** are enclosed in red boxes. The purple-labeled impurity is Et<sub>2</sub>O. The blue-labeled impurity is H<sub>2</sub>O.

#### 4.4 Summary and Conclusions

We studied reactions of *cis*-[Pt(NH<sub>3</sub>)<sub>2</sub>(py)Cl](OTf), **1**, with (PPN)(S<sub>x</sub>NO), where x = 1 or 2, in an attempt to form a structurally characterizable metal–S<sub>x</sub>NO complexes, but this goal was not achieved. We formed new complexes that do not contain the S<sub>x</sub>NO ligand, but maintain binding of two amines and a pyridine to the platinum center. The physical properties of these complexes differ from those of the starting material and from one another. The exact structures of the products are currently unknown, but we proved that chloride is still present product and that NO(g) is released during the reaction. Calculated results provide data that the products may have polysulfide linkers between two platinum centers, which may account for the difference in color and <sup>1</sup>H NMR spectra of the two species.

We also prepared a Pt(II) and a Pt(IV) derivative of the starting material using NO<sup>+</sup>. The complexes *cis*-[Pt(NH<sub>3</sub>)<sub>2</sub>(py)(CH<sub>3</sub>CN)](BF<sub>4</sub>)<sub>2</sub> and *cis-mer*-[Pt(NH<sub>3</sub>)<sub>2</sub>(py)Cl<sub>3</sub>]Cl were crystallographically characterized and a <sup>1</sup>H NMR spectrum was collected of a mixture containing both compounds. Both species were spectroscopically different from the products obtained in the reaction of **1** with (PPN)(S<sub>x</sub>NO), implying that this reaction does not involve NO<sup>+</sup>.

## 4.5 References

1. Armitage, D. A.; Brand, J. C., *J. Chem. Soc., Chem. Commun.* **1979**, 1078.
2. Mann, S.; Jansen, M., *Z. Anorg. Allg. Chem.* **1995**, 621, 153.
3. Pandey, K. K., Coordination Chemistry of Thionitrosyl (NS), Thiazate (NSO<sup>-</sup>), Disulfidothionitrate (S<sub>3</sub>N<sup>-</sup>), Sulfur Monoxide (SO), and Disulfur Monoxide (S<sub>2</sub>O) Ligands. In *Prog. Inorg. Chem.*, John Wiley & Sons, Inc.: 1992; pp 445.
4. Bohle, D. S.; Hung, C.-H.; Powell, A. K.; Smith, B. D.; Wocadlo, S., *Inorg. Chem.* **1997**, 36, 1992.
5. Bohle, D. S.; Hung, C.-H.; Smith, B. D., *Can. J. Chem.* **2005**, 83, 2021.
6. Plenio, H.; Roesky, H. W.; Edelman, F. T.; Noltemeyer, M., *J. Chem. Soc., Dalton Trans.* **1989**, 1815.
7. Pandey, K. K.; Nehete, D. T.; Tewari, S. K.; Rewari, S.; Bhardwaj, R., *Polyhedron* **1988**, 7, 709.
8. Parkin, I. P.; Slawin, A. M. Z.; Williams, D. J.; Woollins, J. D., *Polyhedron* **1989**, 8, 835.
9. Roesky, H. W.; Panday, K. K.; Krebs, B.; Dartmann, M., *J. Chem. Soc., Dalton Trans.* **1984**, 2271.
10. Parkin, I. P.; Slawin, A. M. Z.; Williams, D. J.; Woollins, J. D., *J. Chem. Soc., Chem. Commun.* **1989**, 1060.
11. Short, R.; Hursthouse, M. B.; Purcell, T. G.; Woollins, J. D., *J. Chem. Soc., Chem. Commun.* **1987**, 407.
12. Tiwari, R. D.; Pandey, K. K.; Agarwala, U. C., *Inorg. Chem.* **1982**, 21, 845.
13. Herberhold, M.; Neumann, F.; Suess-Fink, G.; Thewalt, U., *Inorg. Chem.* **1987**, 26, 3612.
14. Pangborn, A. B.; Giardello, M. A.; Grubbs, R. H.; Rosen, R. K.; Timmers, F. J., *Organometallics* **1996**, 15, 1518.
15. Johnstone, T. C.; Lippard, S. J., *J. Am. Chem. Soc.* **2014**, 136, 2126.
16. APEX2 v2009 APEX2 v2009, Bruker AXS: Madison, WI, 2009.
17. Sheldrick, G. M. *SADABS: Area-Detector Absorption Correction*, University of Göttingen: Göttingen, Germany, 2008.
18. Sheldrick, G., *Acta Crystallogr., Sect. A: Found. Crystallogr.* **2008**, 64, 112.
19. Sheldrick, G. M. *SHELXL97: Program for Refinement of Crystal Structures*, University of Göttingen: Göttingen, Germany, 1997.
20. SHELXTL v. 6.10: *Program Library for Structure Solution and Molecular Graphics*, Bruker AXS, Madison, WI, 2001.
21. Dolomanov, O. V.; Bourhis, L. J.; Gildea, R. J.; Howard, J. A. K.; Puschmann, H., *J. Appl. Crystallogr.* **2009**, 42, 339.
22. Frisch, M. J.; Trucks, G. W.; Schlegel, H. B.; Scuseria, G. E.; Robb, M. A.; Cheesman, J. R.; Montgomery, J. A. J.; Vreven, T.; Kudin, K. N.; Burant, J. C.; Millam, J. M.; Iyengar, S. S.; Tomasi, J.; Barone, V.; Mennucci, B.; Cossi, M.; Scalmani, G.; Rega, N.; Petersson, G. A.; Nakatsuji, H.; Hada, M.; Ehara, M.; Toyota, K.; Fukuda, R.; Hasegawa, J.; Ishida, M.; Nakajima, T.; Honda, Y.; Kitao, O.; Nakai, H.; Klene, M.; Li, X.; Know, J. E.; Hratchian, H. P.; Cross, J. B.; Adamo, C.; Jaramillo, J.; Gomperts, R.; Stratmann, R. E.; Yazyev, O.; Austin, A. J.; Cammi, R.; Pomelli, C.; Ochterski, J. W.; Ayala, P. Y.; Morokuma, K.; Voth, G. A.; Salvador, P.; Dannenberg, J. J.; Zakrzewski, V. G.; Dapprich, S.; Daniels, A. D.; Strain, M. C.; Farkas, O.; Malick, D. K.; Rabuck, A. D.; Raghavachari, K.; Foresman, J. B.; Ortiz, J. V.; Cui, Q.; Baboul, A. G.; Clifford, S.;

Cioslowski, J.; Stefanov, B. B.; Liu, G.; Liashenko, A.; Piskorz, P.; Komaromi, I.; Martin, R. L.; Fox, D. J.; Keith, T.; Al-Laham, M. A.; Peng, C. Y.; Nanayakkara, A.; Challacombe, M.; Gill, P. M. W.; Johnson, B.; Chen, W.; Wong, M. W.; Gonzalez, C.; Pople, J. A. *Gaussian 03*, Pittsburgh, PA, 2003.

23. Hay, P. J.; Wadt, W. R., *J. Chem. Phys.* **1985**, *82*, 299.
24. Uson, R.; Fornies, J.; Tomas, M.; Menjon, B.; Bau, R.; Suenkel, K.; Kuwabara, E., *Organometallics* **1986**, *5*, 1576.
25. Ara, I.; Forniés, J.; García-Monforte, M. A.; Menjón, B.; Sanz-Carrillo, R. M.; Tomás, M.; Tsipis, A. C.; Tsipis, C. A., *Chem. Eur. J.* **2003**, *9*, 4094.



# **CHAPTER 5: SYNTHESIS OF [3:1] SITE-DIFFERENTIATED [4Fe-4S] CLUSTERS AND THEIR REACTIVITY TOWARD NO(g) AND Ph<sub>3</sub>CSNO**

*Portions of this chapter have appeared in print:*

Victor, E; Lippard, S. J. *Inorg. Chem.* **2014**, 52, 5311.

**5.1 Introduction** The reaction pathway between NO and iron-sulfur clusters has not been fully elucidated, particularly within biological settings.<sup>1-3</sup> Initially, dinitrosyl iron complexes (DNIC) were considered to be the major product formed during nitrosation of protein-bound [4Fe-4S] clusters based on EPR spectra that matched those of known DNIC species.<sup>4,5</sup> This technique is limited, however, for it can only detect paramagnetic species and does not provide unambiguous structural information. Work from our laboratory and others has demonstrated that the action of NO on protein-bound iron-sulfur clusters also generates EPR-silent species, which may, in some cases, be the major nitrosated product.<sup>1,6-8</sup> In one study using recombinant *Pyrococcus furiosus* ferredoxin (D14C mutant), the EPR-silent Roussin's black anion (RBA),  $[\text{Fe}_4\text{S}_3(\text{NO})_7]^-$  (Figure 5.1), was detected as the major product by nuclear resonance vibrational spectroscopy.<sup>8</sup>

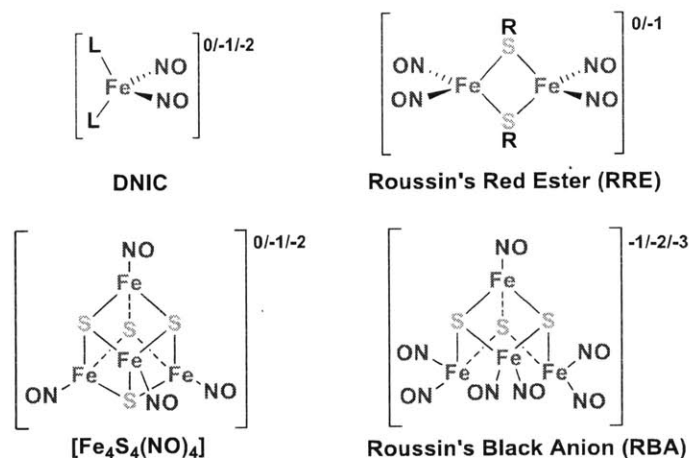
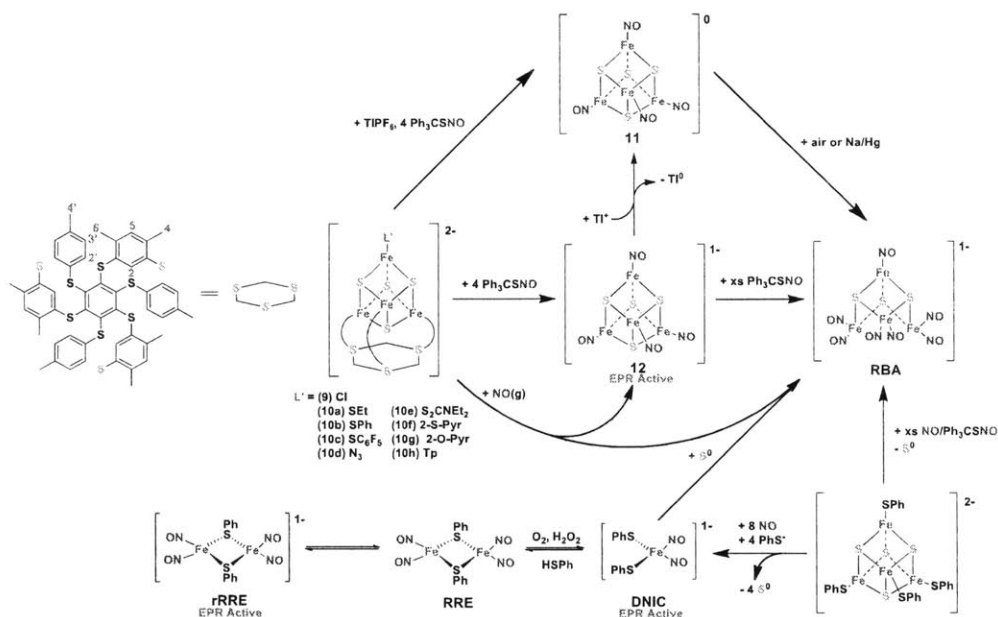


**Figure 5.1.** Iron<sup>-</sup>sulfur nitrosyl compounds.

The reactivity of NO towards aconitase, Wbl, FNR, and other [4Fe-4S] clusters has been studied by EPR, NMR, Mössbauer, and electronic absorption spectroscopies.<sup>5,8-11</sup> The goal of the project described in this chapter was to isolate and characterize potential intermediate species that may form upon nitrosylation of [4Fe-4S] clusters prior to the formation of the known extruded species.

To gain further insight into the nature of the reactions of NO and other RNOS with iron-sulfur clusters, we investigated this chemistry using small-molecule analogs of the metalloproteins.<sup>2,8</sup> Direct reaction of  $[\text{Fe}_4\text{S}_4(\text{SPh})_4]^{2-}$  with NO(g) or  $\text{Ph}_3\text{CSNO}$  results in the formation of RBA and, in the presence of additional thiolates, DNICs (Scheme 5.1).<sup>2,3,12</sup> In the present study, we extend these investigations to previously reported, site-differentiated  $[\text{Fe}_4\text{S}_4(\text{LS}_3)\text{L}']^{2-}$  ( $\text{LS}_3 = 1,3,5\text{-tris}(4,6\text{-dimethyl-3-mercaptophenylthio})\text{-}2,4,6\text{-tris}(p\text{-tolylthio})\text{benzene}$ ;  $\text{L}' = \text{Cl, SEt, SPh, SC}_6\text{F}_5, \text{N}_3, \text{S}_2\text{CNEt}_2, 2\text{-SPyr, 2-OPyr, Tp}$ ) clusters.<sup>13</sup> These clusters were chosen based on the proclivity of the apical ligand ( $\text{L}'$ ) to exchange its ligands preferentially and the ability of the  $\text{LS}_3$  ligand to stabilize a  $[\text{3Fe-4S}]$  cluster after extrusion of the apical iron, a property we wished to explore in order to mimic the observed NO reactivity of mitochondrial aconitase.<sup>14-19</sup> Altering  $\text{L}'$  affects the denticity on the apical iron and further differentiates it from the remainder of the iron atoms in the cluster.



**Scheme 5.1.** Reactivity pathways of synthetic  $[\text{4Fe-4S}]$  clusters with NO(g) and  $\text{Ph}_3\text{CSNO}$ .

## 5.2 Experimental Methods

**General.** All manipulations were performed under an atmosphere of nitrogen gas using standard Schlenk techniques or in an MBraun glovebox under an atmosphere of purified nitrogen. NO (Airgas, 99%) was purified by a literature procedure.<sup>20</sup> The NO gas stream was passed through an Ascarite column (NaOH fused on silica gel) and a 6 ft coil filled with silica gel that was cooled to  $-78$  °C using a dry ice/acetone bath. Nitric oxide was stored using standard gas storage bulbs and transferred via gastight syringes. Diethyl ether, pentane, methylene chloride, and acetonitrile were purified using a Glass Contour solvent system using activated alumina to purify.<sup>21</sup> Deuterated solvents were purchased from Cambridge Isotope Labs Inc. (Tewksbury, MA).  $(\text{Ph}_4\text{P})_2[\text{Fe}_4\text{S}_4(\text{SEt})_4]$  and  $\text{Ph}_3\text{CSNO}$  were synthesized according to literature procedures.<sup>2,22</sup> All organic chemicals were purchased from Sigma-Aldrich and used as received. Metal salts were purchased from Strem Chemicals and used as received.

**Physical Measurements.** NMR spectra were recorded on a Bruker Avance spectrometer operating at 600 MHz at ambient temperature and referenced to residual signals in the deuterated solvent. MALDI-TOF mass spectra were obtained on a Bruker Omnix MALDI-TOF with a Reflectron attachment. Low-resolution ESI mass spectra were obtained with an Agilent 1100 Series LC/MSD mass spectrometer using degassed acetonitrile as the carrier solvent. FT-IR spectra were recorded on a Thermo Nicolet Avatar 360 spectrometer running the OMNIC software package; solid samples were pressed into KBr disks and solution samples were prepared in an air tight Graseby-Specac solution cell with  $\text{CaF}_2$  windows and 0.1 mm spacers. X-Band EPR spectra were recorded on a Bruker EMX EPR spectrometer at ambient or liquid nitrogen temperature using a quartz finger dewar. Electrochemical measurements were performed at ambient temperature in a glovebox on a VersaSTAT3 Princeton Applied Research

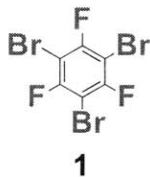
potentiostat running the V3-Studio electrochemical analysis software. A 3-electrode set-up was employed comprising a glassy carbon working electrode, platinum wire auxiliary electrode, and a Ag(s)/Ag<sup>+</sup>(s) silver wire pseudo-reference electrode. Triply recrystallized (Bu<sub>4</sub>N)PF<sub>6</sub> was used as the supporting electrolyte. All electrochemical data were referenced internally to the Fc/Fc<sup>+</sup> couple at 0.00 V.

**ReactIR Measurements.** In situ IR spectra were recorded on a ReactIR iC 10 instrument from Mettler Toledo equipped with a 1 in. diameter, 30-reflection silicon ATR (SiComp) probe. In a typical experiment, the instrument was blanked with CH<sub>2</sub>Cl<sub>2</sub> and the sample, at concentrations ranging from 15 to 30 mM. After the first data collection time point was completed, NO(g) or a 30 mM CH<sub>2</sub>Cl<sub>2</sub> solution of Ph<sub>3</sub>CSNO was added to the anaerobic sample compartment through a rubber septum with a gas-tight syringe. The data was referenced to the initial scan and imported to *Origin 8.0* as a \*.spc file to generate the figures.

**Mössbauer Measurements.** Samples for <sup>57</sup>Fe Mössbauer studies were prepared by grinding a solid sample with Apiezon-N grease. These <sup>57</sup>Fe Mössbauer samples were placed in an 80 K cryostat during measurement. A <sup>57</sup>Co/Rh source was moved at a constant acceleration at room temperature against the absorber sample. All isomer shift (δ) and quadrupole splitting (ΔE<sub>Q</sub>) values are reported with respect to <sup>57</sup>Fe-enriched metallic iron foil that was used for velocity calibration. The displayed spectrum was folded to enhance the signal-to-noise ratio. Fits of the data were calculated by the *WMOSS* plot and fit program, version 2.5.<sup>23</sup> See Table 5.2 below for experimentally determined parameters of **9**, **10a**, **10b**, **10c**, **10e**, **10g**, and **12**.

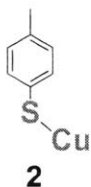
**X-ray Data Collection and Structure Solution Refinement.** Crystals of LS<sub>2</sub>(SCH<sub>2</sub>OCH<sub>3</sub>), 7·(CH<sub>3</sub>)<sub>2</sub>CO, **10d**·4MeCN·Et<sub>2</sub>O·0.5H<sub>2</sub>O, **10e**·2.5Et<sub>2</sub>O, (Ph<sub>3</sub>CS)<sub>2</sub>, and [Cp\*<sub>2</sub>Fe]**12** suitable for X-ray diffraction were mounted in Paratone N oil and frozen under a nitrogen cold stream

maintained at 100 K by a KRYO-FLEX low-temperature apparatus. Data were collected on a Bruker APEX CCD X-ray diffractometer with Mo K $\alpha$  radiation ( $\lambda = 0.71073 \text{ \AA}$ ) controlled by the APEX2 software package.<sup>24</sup> Empirical absorption corrections were calculated with SADABS.<sup>25</sup> The structures were solved by direct methods with refinement by full-matrix least-squares based on  $F^2$  using SHELXTL-97.<sup>26,27</sup> All non-hydrogen atoms were located and refined anisotropically. Hydrogen atoms were assigned to idealized positions and given thermal parameters equal to either 1.5 (methyl hydrogen atoms) or 1.2 (non-methyl hydrogen atoms) times the thermal parameters of the atoms to which they were attached. Figures were generated using the Olex2.1 Graphical User Interface.<sup>28</sup> See Tables 5.1, 5.3, and 5.4 below for crystallographic data and refinement details.

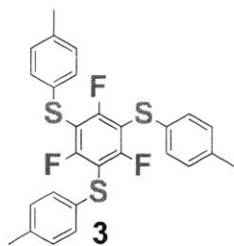


**C<sub>6</sub>Br<sub>3</sub>F<sub>3</sub>, 1.**<sup>29</sup> A solid addition funnel was filled with Al flakes (1.6 g, 70 mmol) and was attached to a 25 mL 3-necked round bottom flask filled with Br<sub>2</sub> (97 mL, 1.9 mol). A condenser was attached to the 3-neck reaction flask and the third opening was covered with a rubber septum. The condenser was connected a reflux condenser attached to a Na<sub>2</sub>S<sub>2</sub>O<sub>3</sub>(aq) trap. The reaction setup was flushed and placed under a constant N<sub>2</sub> stream. Al was added to Br<sub>2</sub> at a rate of 2 flakes per 5 min to minimize the burning of the Al in the reaction vessel. C<sub>6</sub>F<sub>3</sub>H<sub>3</sub> (35 g, 265 mmol) was added at a rate of 4 drops/min via syringe. The reaction flask was then placed into a 60 °C water bath and stirred for 90 min. The reaction flask was then removed from the water bath and allowed to cool to RT. The solution was poured into a 1000 mL separatory funnel filled with H<sub>2</sub>O (450 mL) and an orange aqueous layer formed above the Br<sub>2</sub> layer. To the separatory funnel, 150 mL Et<sub>2</sub>O (400 mL) was added and the funnel was shaken. The aqueous layer was

removed and the organic layer was collected and the Et<sub>2</sub>O removed on a rotary evaporator. A pale orange solid was collected and dissolved in 300 mL hexanes. The solution was ran through a silica plug and the solvent removed on a rotary evaporator. The remaining white solid was collected to yield 82.97 g (85%); mp = 98 °C (Lit. mp = 98 °C). The <sup>19</sup>F NMR spectrum matched that previously published. <sup>19</sup>F NMR (282 MHz, CDCl<sub>3</sub>, ref. CF<sub>3</sub>COOH δ = -78.5 ppm): δ -95.82 ppm. EI-MS (m/z): 368 ([M]<sup>+</sup>, calc'd: 368).

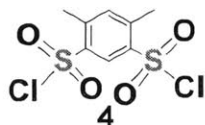


**CuSC<sub>6</sub>H<sub>4</sub>CH<sub>3</sub>, 2.**<sup>30</sup> To a 250 mL Schlenk tube 200 mL anhydrous EtOH was added and sparged with N<sub>2</sub> for 1 hour. To a 500 mL round bottom Schlenk flask 20.1 g of *p*-tolyl mercaptan (HSC<sub>6</sub>H<sub>4</sub>(CH<sub>3</sub>)) and a stir bar was added. The flask was evacuated and filled with N<sub>2(g)</sub> 3 times. The anhydrous EtOH was transferred to the round bottom Schlenk flask via canula transfer and the solution was stirred until the HSC<sub>6</sub>H<sub>4</sub>(CH<sub>3</sub>) was completely dissolved. Under heavy N<sub>2</sub> flow, 14.1 g Cu<sub>2</sub>O was added to the solution. The reaction flask was capped with an N<sub>2</sub> purged reflux condenser. The reaction flask was placed into a 120 °C oil bath and stirred for three days under an N<sub>2</sub> atmosphere, after which time a pale yellow precipitate forms. The reaction solution was then allowed to cool to RT and filtered in air through a Büchner funnel. The remaining pale yellow solid was washed with 600 mL EtOH and 600 mL Acetone. The solid was dried under vacuum and collected to provide a yield of 28.7 g (94.0%) of a pale yellow powder; dp = 254 °C (Lit. dp = 260 °C).

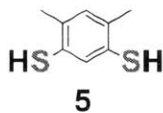


$\text{C}_6\text{F}_3(\text{SC}_6\text{H}_4(\text{CH}_3))_3$ , **3**.<sup>16</sup> To a 500 mL round bottom Schlenk flask 7.9681 g of **1**, 14.932 g of **2**, and a stir bar was added and placed under an inert atmosphere. 250 mL anhydrous N,N'-dimethylformamide (DMF) was transferred via canula from a Sure/Seal™ bottle to the reaction flask. To the reaction flask a  $\text{N}_2$  purged reflux condenser was attached. The reaction flask was placed into a 145 °C silicone oil bath and the slurry was stirred. After 12 h, the slurry turns red-brown and after 36 hours the reaction was complete. The reaction flask is removed from the oil bath and was allowed to cool to RT. The red-brown slurry is poured into a 1 L Erlenmeyer flask filled with 600 mL ice and 80 mL conc. HCl at which point a grey precipitate forms. To the mixture 200 mL  $\text{Et}_2\text{O}$  is added and is stirred vigorously. The precipitate is removed by vacuum filtration and the blue-green aqueous layer is removed from the filtrate in a separatory funnel. The yellow organic layer is washed twice with 500 mL 10% w/v  $\text{K}_2\text{CO}_3(\text{aq})$  and once with Brine. The organic layer was collected and  $\text{Et}_2\text{O}$  was removed by rotary evaporation after which a pale yellow solid remained. The solid was recrystallized from a hot 10% v/v  $\text{CHCl}_3$  in hexanes in a -8 °C freezer. Gray fluffy solid was collected from a brown solution. The solid was dissolved in Toluene and passed through a Silica gel plug. The Toluene was removed by rotary evaporation to yield 5.1 g (47%) of a white fluffy solid; mp = 125.5 -127 °C (Lit. mp = 125.5 - 127 °C). The  $^1\text{H}$  and  $^{19}\text{F}$  NMR spectrum matched that previously published.  $^1\text{H}$  NMR (300 MHz,  $\text{CDCl}_3$ ):  $\delta$  2.31 (s, 3H, Me), 7.06 (d, 2H, Ph), 7.20 (d, 2H, Ph).  $^{19}\text{F}$  NMR (282 MHz,  $\text{CDCl}_3$ , ref.  $\text{CF}_3\text{COOH}$   $\delta$  = -78.5 ppm):  $\delta$  -91.6.



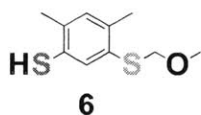


**C<sub>6</sub>H<sub>2</sub>(CH<sub>3</sub>)<sub>2</sub>(SO<sub>2</sub>Cl)<sub>2</sub>, 4.**<sup>31,32</sup> To a 250 mL round bottom flask 100 mL Chlorosulfonic acid (HOSO<sub>2</sub>Cl) and a stir bar was added and was capped with a claisen adapter connected to a NaHCO<sub>3</sub>(aq) acid trap and a septum. The septum is pierced with a 20 mL plastic syringe filled with 15 mL anhydrous *m*-xylenes. The *m*-xylenes is added to the HOSO<sub>2</sub>Cl at a rate of 1 mL/min. Over the course of the addition the color of the solution will transition from colorless to light brown, to pink, and end with purple. The reaction flask is capped with a reflux condenser connected to a NaHCO<sub>3</sub>(aq) acid trap and placed into a 160 °C silicon oil bath. The solution is stirred for 2 hours and subsequently removed from the oil bath and allowed to cool to RT. The solution is poured into an ice filled 4 L Erlenmeyer flask and the product is allowed to precipitate overnight. The beige precipitate is collected by vacuum filtration from a Büchner funnel and washed with methylene chloride. The filtrate is collected and the organic layer is separated from the aqueous layer and collected. The methylene chloride is removed by rotary evaporation and a pale red solid is collected. The final product is recrystallized from hot acetone in a -8 °C freezer and yields 20.1 g (54%) white needles; dp = 124 °C (Lit. dp = 124 °C). The <sup>1</sup>H NMR spectrum matched that previously published. <sup>1</sup>H NMR (300 MHz, CDCl<sub>3</sub>): δ 2.87 (s, 6H, Me), 7.52 (s, 1H, Ph), 8.72 (s, 1H, Ph). EI-MS (m/z): 302 ([M]<sup>+</sup>, calc'd: 302).



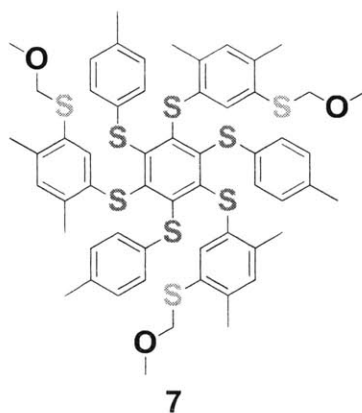
**C<sub>6</sub>H<sub>2</sub>(CH<sub>3</sub>)<sub>2</sub>(SH)<sub>2</sub>, 5.**<sup>33</sup> To a 2 L round bottom flask 800 mL conc. HCl and a large oval-shaped stir bar was added. Under heavy magnetic stirring 260 g Tin was added and the flask was capped with a reflux condenser connected to a NaHCO<sub>3</sub>(aq) acid trap. Bubble formation occurred instantly. The reaction flask was placed into a heating mantle and heated to reflux. The reaction

vessel was allowed to react until all Tin was consumed, which usually occurred within 6 hours. If any solid remained, the solution was gravity filtered. To the colorless solution 32.8 g **4** was added and placed under reflux for 2 hours. The solution was removed from the heat and was allowed to cool to RT. Steam distillation was performed on the solution and 8.4 g (40%) of white crystalline flakes were collected; mp = 118 - 121 °C. The <sup>1</sup>H NMR spectrum matched that previously published. <sup>1</sup>H NMR (400 MHz, CDCl<sub>3</sub>): δ 2.25 (s, 6H, Me), 3.21 (s, 2H, SH), 6.96 (s, 1H, Ph), 7.23 (s, 1H, Ph). EI-MS (m/z): 170 ([M]<sup>+</sup>, calc'd: 170).



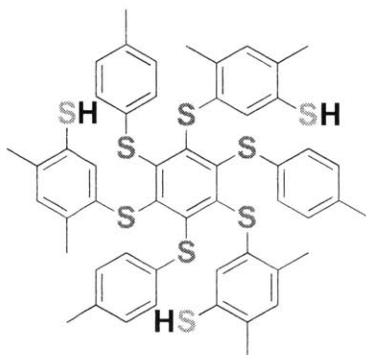
**C<sub>6</sub>H<sub>2</sub>(CH<sub>3</sub>)<sub>2</sub>(SH)(SCH<sub>2</sub>OCH<sub>3</sub>), 6.**<sup>16</sup> To a 100 mL Schlenk flask 3.9132 g of **5** was added. To a 500 mL Schlenk flask 1.9358 g sodium hydride (NaH, 60% oil suspension) and a stir bar was added. Both flasks were evacuated and filled with N<sub>2</sub> 3 times. 80 mL and 100 mL of anhydrous DMF from a Sure/Seal™ bottle was transferred via canula to **5** and NaH respectively. The solution of **5** was transferred to the NaH suspension via canula and bubble formation occurred. The solution was stirred at RT for 3 hours at which time the bubble formation subsided and the solution was red-orange. Under heavy N<sub>2</sub> flow 4x 917μL chloromethyl methyl ether (MOMCl) was added to the solution using a VWR micropipette and the flask was capped. The solution was stirred for 6 hours and turned white with a white precipitate. Under heavy N<sub>2</sub> flow 1.9309 g sodium ethyl thiolate (NaSET) was added and the solution turned beige. The reaction flask was capped and was placed in a 90 °C oil bath. The solution was stirred for 3 hours. The DMF was removed *in vacuo* and a pale orange solid remained. The solid was dissolved in 200 mL Et<sub>2</sub>O and poured into a 500 mL separatory funnel. To the separatory funnel 250 mL 5% w/v NaOH(aq) was added and the product was extracted. The aqueous layer was collected in a 500 mL Erlenmeyer flask and 200 mL 2M Acetic acid (HOAc) was added. A white precipitate forms that

is extracted with 400 mL Et<sub>2</sub>O. The Et<sub>2</sub>O is removed by rotary evaporation and a pale yellow solid remains. The product is obtained by performing silica gel flash chromatography using a 5% v/v Et<sub>2</sub>O in hexanes elutant. Fractions were analyzed by silica gel TLC in Toluene. All fractions containing a single spot at *r<sub>f</sub>* = 0.68 were combined and others that contained additional spots were further purified by flash chromatography using similar conditions. The solvent in the combined fractions was removed by rotary evaporation to yield 2.52 g (52.2%) of a clear and colorless oil. The <sup>1</sup>H NMR spectrum matched that previously published. <sup>1</sup>H NMR (400 MHz, CDCl<sub>3</sub>): δ 2.27 (s, 3H, <sup>Ph</sup>Me), 2.32 (s, 3H, <sup>Ph</sup>Me), 3.27 (s, 1H, SH), 3.43 (s, 3H, OCH<sub>3</sub>), 4.91 (s, 2H, SCH<sub>2</sub>O), 6.98 (s, 1H, Ph), 7.46 (s, 1H, Ph). EI-MS (*m/z*): 214 ([M]<sup>+</sup>, calc'd: 214).



**L(SCH<sub>2</sub>OCH<sub>3</sub>)<sub>3</sub>, 7.**<sup>15</sup> To a 50 mL Schlenk flask 2.34 g of **6** was added and dissolved in 30 mL Tetrahydrofuran (THF) under N<sub>2</sub>. In a 100 mL Schlenk flask 0.2754 g dry NaH was suspended in 15 mL THF with a stir bar. The solution of **6** was transferred via canula to the NaH suspension and was stirred at RT for 3 hours. The THF was removed *in vacuo* and a gray, sticky solid remained. Under heavy N<sub>2</sub> flow 1.2116 g of **3** was added to the reaction flask. 30 mL of anhydrous 1,3-dimethyl-2-imidazolidinone (DMEU) was transferred to the reaction flask via canula transfer. In a 20 mL vial, 5 mL of Milli-Q purified H<sub>2</sub>O was sparged with N<sub>2</sub>. To the reaction vessel 300 μL of the H<sub>2</sub>O was transferred with an air-tight glass syringe. The solution is stirred at RT for 2 days followed by stirring in a 40 °C water bath for 3 days. The reaction

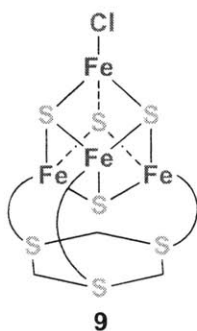
mixture becomes an orange slurry. The mixture is poured into 150 mL of 2M HOAc which is then poured into a 500 mL separatory funnel. The product is extracted from the aqueous solution with 150 mL Et<sub>2</sub>O and washed with 250 mL of 5% w/v NaOH(aq) four times and Brine once. The Et<sub>2</sub>O was removed by rotary evaporation and a bright yellow viscous oil remained. The oil was recrystallized with hot acetone in a -8 °C freezer and yielded 1.4746 g (56.1%) of bright yellow block crystals; mp = 115 - 118 °C (Lit. mp = 115 - 118 °C). The <sup>1</sup>H NMR spectrum matched that previously published. <sup>1</sup>H NMR (400 MHz, CDCl<sub>3</sub>): δ 2.13 (s, 3H, <sup>Ph</sup>Me), 2.23 (s, 3H, <sup>Ph</sup>Me), 2.27 (s, 3H, <sup>Ph</sup>Me), 3.33 (s, 3H, OMe), 4.72 (s, 2H, SCH<sub>2</sub>O), 6.83 (s, 1H, Ph), 6.84 (d, 1H, Ph), 6.87 (s, 1H, Ph), 6.89 (d, 1H, Ph). <sup>13</sup>C NMR (100 MHz, CDCl<sub>3</sub>): δ 20.0, 20.3, 21.2, 56.3, 78.2, 128.4, 129.5, 131.5, 132.1, 132.6, 134.3, 134.8, 135.6, 135.7, 136.9, (central ring) 147.4, 148.5. MALDI-TOF MS (Anthracene, m/z): 1079.8 ([M]<sup>+</sup>, calc'd: 1080.2).



**8**

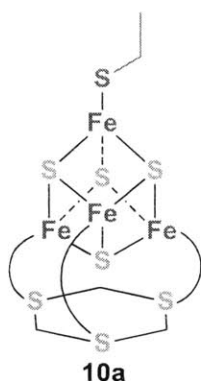
**L(SH)<sub>3</sub>, 8.**<sup>16</sup> In a 50 mL Schlenk tube, 15 mL CHCl<sub>3</sub> and 0.75 mL EtOH was sparged with N<sub>2</sub> for 45 min. Under heavy N<sub>2</sub> flow, 0.3000 g of **7** and 0.2916 g of Hg(OAc)<sub>2</sub> was added to the tube and was covered in aluminum foil. The solution was stirred for 12 h after which time a yellow precipitate formed. H<sub>2</sub>S was bubbled through the solution at a rate of one bubble/sec for 20 minutes. Over the course of the bubbling the solution turns from orange to brown to black. The tube and solution was then purged with N<sub>2</sub> for 45 minutes. A Schlenk frit was filled with 3 cm of Celite, connected to a 500 mL round bottom Schlenk flask, and placed under a N<sub>2</sub> atmosphere.

The solution was transferred to the Schlenk frit via canula transfer. The celite was washed with N<sub>2</sub> sparged CHCl<sub>3</sub> until the filtrate became colorless. The CHCl<sub>3</sub> was removed *in vacuo* and a bright yellow solid remained. The solid was washed with Hot MeCN until the washings were colorless. A yield of 0.2180 g (82.9%) of an air-sensitive, bright yellow solid was collected. The <sup>1</sup>H NMR spectrum matched that previously published. <sup>1</sup>H NMR (400 MHz, CDCl<sub>3</sub>): δ 2.17 (s, 3H, <sup>Ph</sup>Me), 2.17 (s, 3H, <sup>Ph</sup>Me), 2.27 (s, 3H, <sup>Ph</sup>Me), 3.07 (s, 1H, SH), 6.44 (s, 1H, Ph), 6.83 (s, 1H, Ph), 6.85 (d, 2H, Ph), 6.96 (d, 2H, Ph). <sup>13</sup>C NMR (100 MHz, CDCl<sub>3</sub>): δ 20.1, 20.7, 21.3, 128.2, 128.7, 129.8, 130.9, 132.4, 134.3, 134.9, 135.1, 135.1, 136.2, (central ring) 149.4, 149.9. MALDI-TOF MS (Anthracene, m/z): 947.8 ([M]<sup>+</sup>, calc'd: 948.1).



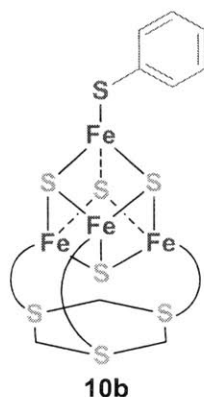
**(Ph<sub>4</sub>P)<sub>2</sub>[Fe<sub>4</sub>S<sub>4</sub>(LS<sub>3</sub>)Cl], 9.**<sup>16</sup> In a 250 mL Schlenk flask, (Ph<sub>4</sub>P)<sub>2</sub>[Fe<sub>4</sub>S<sub>4</sub>(SEt)<sub>4</sub>] (2.2069 g, 1.731 mmol) and L(SH)<sub>3</sub> (1.6436 g, 1.731 mmol) were combined and dissolved in 1:9 DMF/CH<sub>2</sub>Cl<sub>2</sub> (134 mL) and stirred at ambient temperature. After 30 min, the reaction was subjected to dynamic vacuum for three h, after which all volatiles were removed *in vacuo*. The solid was redissolved in DMF (14 mL) and pivaloyl chloride (235 μL, 1.91 mmol) was added to the solution. Aliquots of the solution were taken every 30 min to determine completeness of conversion by <sup>1</sup>H NMR in DMF-*d*<sub>7</sub>, by monitoring the disappearance of the peak at δ = 3.81 ppm. The solution was filtered through a piece of glass microfiber filter paper into a 125 mL Erlenmeyer flask. The solution was layered with 120 mL MeCN and placed into a -30° freezer overnight during to afford a precipitate. The precipitate was collected by filtration and washed

with cold MeCN (3 x 5 mL) and Et<sub>2</sub>O (3 x 5 mL) to yield 2.8393 g (1.411 mmol, 81.5%) of a black microcrystalline material. Crystals suitable for X-ray diffraction studies were grown by vapor diffusion of Et<sub>2</sub>O into a DMF solution of the collected material. The <sup>1</sup>H NMR spectrum matched that previously published. <sup>1</sup>H NMR (600 MHz, CD<sub>3</sub>CN, δ ppm): 8.25 (5-H), 7.13 (2'-H), 6.83 (3'-H), 5.05 (br, 2-H), 3.90 (4-Me), 3.87 (6-Me), 2.24 (4'-Me). ESI-MS (MeCN, m/z): 339.2 ([Ph<sub>4</sub>P]<sup>+</sup>, 339.1), 1672.5 ([M-Ph<sub>4</sub>P]<sup>-</sup>, 1672.8), 666.5 ([M-2(Ph<sub>4</sub>P)]<sup>2-</sup>, 666.9). UV-vis (MeCN, λ<sub>max</sub>, nm, ε M<sup>-1</sup>cm<sup>-1</sup>): 300 (38000), 460 (sh, 10300). FT-IR (KBr, cm<sup>-1</sup>): 2909 (w), 1657 (w), 1585 (w), 1489 (w), 1436 (s), 1378 (w), 1260 (w), 1186 (w), 1107 (s), 1080 (s), 1015 (w), 996 (w), 801 (w), 753 (w), 723 (s), 689 (s), 527 (s).

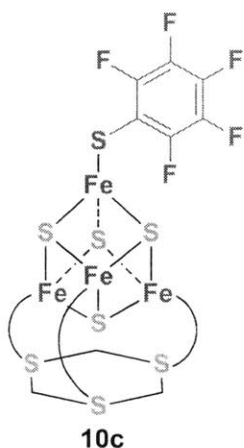


(Ph<sub>4</sub>P)<sub>2</sub>[Fe<sub>4</sub>S<sub>4</sub>(LS<sub>3</sub>)(SEt)], **10a**.<sup>14</sup> In a 25 mL Erlenmeyer flask, **9** (206.5 mg, 102.6 μmol) and NaSEt (10.0 mg, 119 μmol) were combined. The solid mixture was dissolved in MeCN (10 mL) and stirred. After 2 hours the crude reaction solution was filtered through a piece of glass filter paper in a Pasteur pipette into a 125 mL Erlenmeyer flask. The filtrate was stripped to dryness and redissolved in MeCN (3 mL). The solution was layered with Et<sub>2</sub>O (120 mL) and placed in a -30° freezer overnight to afford a precipitate, which was collected on an F-grade frit and washed with Et<sub>2</sub>O (3 x 10 mL) to yield 196.7 mg (96.5 μmol, 97.4 %) of black microcrystalline material. The <sup>1</sup>H NMR spectrum matched that previously published. <sup>1</sup>H NMR (600 MHz, CD<sub>3</sub>CN, δ ppm): 13.16 (SEt-CH<sub>2</sub>), 8.14 (5-H), 7.14 (2'-H), 6.84 (3'-H), 5.18 (br, 2-H), 3.81 (6-Me), 3.69 (4-Me),

2.40 (SEt-CH<sub>3</sub>), 2.24 (4'-Me). ESI-MS (MeCN, m/z): 339.4 ([Ph<sub>4</sub>P]<sup>+</sup>, 339.1), 1701.7 ([M-Ph<sub>4</sub>P]<sup>-</sup>, 1701.9).

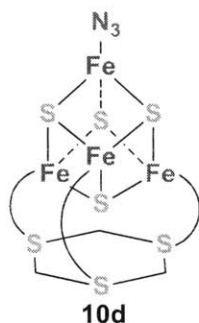


**(Ph<sub>4</sub>P)<sub>2</sub>[Fe<sub>4</sub>S<sub>4</sub>(LS<sub>3</sub>)(SPh)], 10b.**<sup>14</sup> In a 25 mL Erlenmeyer flask, **9** (400 mg, 198 μmol) and NaSPh (26.4 mg, 200 μmol) were combined. The solid mixture was dissolved in MeCN (10 mL) and stirred. After 2 hours the crude reaction solution was filtered through a piece of glass filter paper in a Pasteur pipette into a 125 mL Erlenmeyer flask. The filtrate was stripped to dryness and redissolved in MeCN (3 mL). The solution was layered with Et<sub>2</sub>O (120 mL) and placed in a -30° freezer overnight to afford a precipitate, which was collected on an F-grade frit and washed with Et<sub>2</sub>O (3 x 10 mL) to yield 276.1 mg (132.4 μmol, 66.7%) of brown microcrystalline material. The <sup>1</sup>H NMR spectrum matched that previously published. <sup>1</sup>H NMR (600 MHz, CD<sub>3</sub>CN, δ ppm): 8.16 (SPh-H<sub>m</sub>), 8.16 (5-H), 7.11 (2'-H), 6.84 (3'-H), 6.01 (br, SPh-H<sub>o</sub>), 5.37 (SPh-H<sub>p</sub>), 5.15 (br, 2-H), 3.83 (6-Me), 3.76 (4-Me), 2.23 (4'-Me). ESI-MS (MeCN, m/z) : 339.2 ([Ph<sub>4</sub>P]<sup>+</sup>, 339.1), 1745.5 ([M-Ph<sub>4</sub>P]<sup>-</sup>, 1745.9). FT-IR (KBr, cm<sup>-1</sup>): 2908 (w), 1585 (w), 1575 (w), 1489 (w), 1470 (w), 1436 (s), 1378 (w), 1261 (w), 1187 (w), 1107 (s), 1081 (s), 1015 (w), 996 (w), 955 (w), 801 (w), 751 (w), 723 (s), 688 (s), 527 (s).

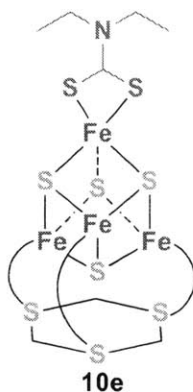


**(Ph<sub>4</sub>P)<sub>2</sub>[Fe<sub>4</sub>S<sub>4</sub>(LS<sub>3</sub>)(SC<sub>6</sub>F<sub>5</sub>)], 10c.** In a 25 mL Erlenmeyer flask, **9** (200 mg, 198 μmol) and NaSC<sub>6</sub>F<sub>5</sub> (44.4 mg, 200 μmol) were combined. The solid mixture was dissolved in 10 mL MeCN and stirred. After 2 hours the crude reaction solution was filtered through a piece of glass filter paper in a Pasteur pipette into a 125 mL Erlenmeyer flask. The filtrate was stripped to dryness and redissolved in MeCN (3 mL). The solution was layered with Et<sub>2</sub>O (120 mL) and placed in a -30° freezer overnight afford a precipitate, which was collected on an F-grade frit and washed with Et<sub>2</sub>O (3 x 10 mL) to yield 186.2 mg (85.6 μmol, 43.2 %) of brown microcrystalline material. <sup>1</sup>H NMR (600 MHz, CD<sub>3</sub>CN, δ ppm): 8.18 (5-H), 7.07 (2'-H), 6.83 (3'-H), 5.15 (br, 2-H), 3.84 (4-Me), 3.82 (6-Me), 2.22 (4'-Me). ESI-MS (MeCN, m/z): 339.3 ([Ph<sub>4</sub>P]<sup>+</sup>, 339.1), 1837.6 ([M-Ph<sub>4</sub>P]<sup>-</sup>, 1837.8). FT-IR (KBr, cm<sup>-1</sup>): 2909 (w), 1586 (w), 1502 (s), 1474 (s), 1437 (s), 1378 (w), 1260 (w), 1187 (w), 1108 (s), 1079 (s), 1015 (w), 997 (w), 970 (w), 856 (w), 802 (w), 751 (w), 723 (s), 689 (s), 507 (s).

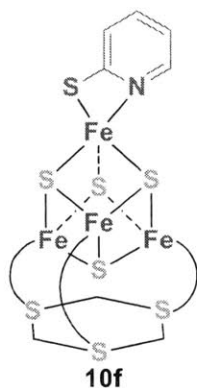




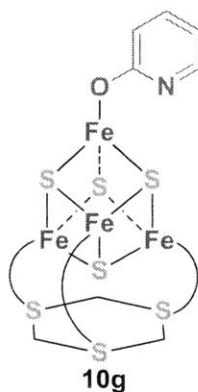
**(Ph<sub>4</sub>P)<sub>2</sub>[Fe<sub>4</sub>S<sub>4</sub>(LS<sub>3</sub>)N<sub>3</sub>], 10d.** In a 25 mL Erlenmeyer flask, **9** (47.2 mg, 23.5 μmol) and NaN<sub>3</sub> (7.2 mg, 111 μmol) were combined, the mixture was dissolved in acetonitrile (14 mL) and then stirred at ambient temperature. After 18 h, the crude reaction solution was filtered through glass microfiber filter paper into a 125 mL Erlenmeyer flask. The filtrate was stripped to dryness and the resulting solid dissolved in acetonitrile (3 mL). The solution was layered with diethyl ether (45 mL) and placed in a -30° C freezer overnight to afford a precipitate, which was collected on an F-grade frit and washed with diethyl ether (3 x 10 mL) to yield 29.3 mg (14.5 μmol, 58.2 %) of blue-black microcrystalline material. Crystals suitable for X-ray diffraction studies were grown by vapor diffusion of diethyl ether into an acetonitrile solution of **10d**. The <sup>1</sup>H NMR spectrum matched that previously published.<sup>18</sup> <sup>1</sup>H NMR (600 MHz, CD<sub>3</sub>CN, δ ppm): 8.25 (5-H), 7.13 (2'-H), 6.83 (3'-H), 5.05 (br, 2-H), 3.90 (4-Me), 3.87 (6-Me), 2.24 (4'-Me). Anal. Calcd for C<sub>99</sub>H<sub>87</sub>Fe<sub>4</sub>N<sub>3</sub>P<sub>2</sub>S<sub>13</sub>O: C, 58.37; H, 4.31; N, 2.06. Found: C, 58.34; H, 4.47; N, 1.82. ESI-MS (MeCN, m/z): 339.2 ([Ph<sub>4</sub>P]<sup>+</sup>, calc'd 339.1), 1678.7 ([M-Ph<sub>4</sub>P]<sup>-</sup>, calc'd 1678.9), 669.6 ([M-2(Ph<sub>4</sub>P)]<sup>2-</sup>, calc'd 669.4). FT-IR (KBr, cm<sup>-1</sup>): 2906 (w), 2055 (s, ν<sub>N3</sub>), 1585 (w), 1488 (w), 1435 (s), 1377 (w), 1336 (w), 1258 (w), 1185 (w), 1107 (s), 1079 (s), 1028 (w), 996 (w), 954 (w), 872 (w), 801 (w), 751 (w), 722 (s), 688 (s), 526 (s).



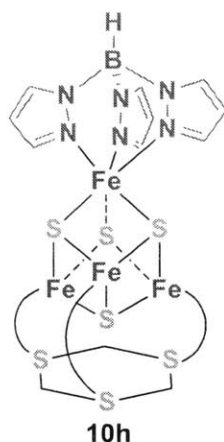
**(Ph<sub>4</sub>P)<sub>2</sub>[Fe<sub>4</sub>S<sub>4</sub>(LS<sub>3</sub>)(S<sub>2</sub>CNEt<sub>2</sub>)], 10e.** In a 25 mL Erlenmeyer flask, **9** (104.6 mg, 52 μmol) and NaS<sub>2</sub>CNEt<sub>2</sub> (10.0mg, 58.4 μmol) were combined. The solid mixture was dissolved in acetonitrile (8 mL) and stirred. After 4 h, the crude reaction solution was filtered through glass microfiber filter paper into a 125 mL Erlenmeyer flask. The filtrate was stripped to dryness and redissolved in acetonitrile (3 mL). The solution was layered with diethyl ether (120 mL) and placed in a -30° C freezer overnight afford a precipitate, which was collected on an F-grade frit and washed with diethyl ether (3 x 10 mL) to yield 83.8 mg (38.9 μmol, 74.8 %) of black microcrystalline material. Crystals suitable for X-ray diffraction studies were grown by vapor diffusion of diethyl ether into a *N,N*-dimethylformamide solution of **10e**. The <sup>1</sup>H NMR spectrum matched that previously published.<sup>19</sup> <sup>1</sup>H NMR (600 MHz, CD<sub>3</sub>CN, δ ppm): 8.26 (5-H), 7.20 (2'-H), 7.01 (CH<sub>2</sub>), 6.74 (3'-H), 4.89 (br, 2-H), 3.88 (6-Me), 3.64 (4-Me), 2.27 (4'-Me), 1.27 (CH<sub>3</sub>). Anal. Calcd for C<sub>104</sub>H<sub>95</sub>Fe<sub>4</sub>NP<sub>2</sub>S<sub>15</sub>·2Et<sub>2</sub>O: C, 559.17; H, 5.10; N, 0.62. Found: C, 59.42; H, 5.15; N, 0.53. ESI-MS (MeCN, m/z): 339.4 ([Ph<sub>4</sub>P]<sup>+</sup>, calc'd 339.1), 1446.0 ([M-2(Ph<sub>4</sub>P)]<sup>-</sup>, calc'd 1445.8). FT-IR (KBr, cm<sup>-1</sup>): 2908 (w), 1585 (w), 1524 (w), 1483 (s), 1435 (s), 1375 (w), 1354 (w), 1266 (w), 1210 (w), 1139 (w), 1107 (s), 1078 (s), 1014 (w), 996 (w), 955 (w), 800 (w), 752 (w), 722 (s), 688 (s), 506 (s).



**(Ph<sub>4</sub>P)<sub>2</sub>[Fe<sub>4</sub>S<sub>4</sub>(LS<sub>3</sub>)(S-2-Pyr)], 10f.**<sup>14</sup> In a 25 mL Erlenmeyer flask, **9** (134.0 mg, 67 μmol) and NaSC<sub>5</sub>H<sub>4</sub>N (10.4mg, 80 μmol) were combined. The solid mixture was dissolved in MeCN (10 mL) and stirred. After 18 hours the crude reaction solution was filtered through a piece of glass filter paper in a Pasteur pipette into a 125 mL Erlenmeyer flask. The filtrate was stripped to dryness and redissolved in MeCN (3 mL). The solution was layered with Et<sub>2</sub>O (120 mL) and placed in a -30° freezer overnight afford a precipitate, which was collected on an F-grade frit and washed with Et<sub>2</sub>O (3 x 10 mL) to yield 103.8 mg (49.7 μmol, 74 %) of brown microcrystalline material. The <sup>1</sup>H NMR spectrum matched that previously published. <sup>1</sup>H NMR (600 MHz, CD<sub>3</sub>CN, δ ppm): 12.32 (Pyr-H<sub>3</sub>), 10.99 (br, Pyr-H<sub>5</sub>), 10.05 (Pyr-H<sub>4</sub>), 8.25 (5-H), 7.20 (2'-H), 6.77 (3'-H), 6.48 (Pyr-H<sub>6</sub>), 5.02 (br, 2-H), 3.89 (6-Me), 3.72 (4-Me), 2.26 (4'-Me). ESI-MS (MeCN, m/z): 339.4 ([Ph<sub>4</sub>P]<sup>+</sup>, 339.1), 1751.2 ([M-Ph<sub>4</sub>P]<sup>-</sup>, 1750.9). FT-IR (KBr, cm<sup>-1</sup>): 2911 (w), 1585 (w), 1570 (w), 1537 (w), 1489 (w), 1437 (s), 1410 (w), 1378 (w), 1259 (w), 1186 (w), 1108 (s), 1080 (s), 1015 (w), 966 (w), 955 (w), 874 (w), 801 (w), 753 (w), 723 (s), 689 (s), 507 (s).



**(Ph<sub>4</sub>P)<sub>2</sub>[Fe<sub>4</sub>S<sub>4</sub>(LS<sub>3</sub>)(O-2-Pyr)], 10g.** In a 25 mL Erlenmeyer flask, **9** (134.0 mg, 67 μmol) and NaSC<sub>5</sub>H<sub>4</sub>N (10.4mg, 80 μmol) were combined. The solid mixture was dissolved in MeCN (10 mL) and stirred. After 18 hours the crude reaction solution was filtered through a piece of glass filter paper in a Pasteur pipette into a 125 mL Erlenmeyer flask. The filtrate was stripped to dryness and redissolved in MeCN (3 mL). The solution was layered with Et<sub>2</sub>O (120 mL) and placed in a -30° freezer overnight afford a precipitate, which was collected on an F-grade frit and washed with Et<sub>2</sub>O (3 x 10 mL) to yield 103.8 mg (49.7 μmol, 74 %) of brown microcrystalline material. <sup>1</sup>H NMR (600 MHz, CD<sub>3</sub>CN, δ ppm): 9.55 (br, Pyr-H<sub>3</sub>), 8.83 (br, Pyr-H<sub>5</sub>), 8.25 (5-H), 7.20 (Pyr-H<sub>4</sub>), 7.17 (2'-H), 6.81 (3'-H), 6.78 (Pyr-H<sub>6</sub>), 4.97 (br, 2-H), 3.87 (6-Me), 3.82 (4-Me), 2.23 (4'-Me). ESI-MS (MeCN, m/z): 339.3 ([Ph<sub>4</sub>P]<sup>+</sup>, 339.1), 1729.6 ([M-Ph<sub>4</sub>P]<sup>-</sup>, 1729.9). FT-IR (KBr, cm<sup>-1</sup>): 2908 (w), 1585 (w), 1489 (w), 1462 (s), 1436 (s), 1421 (s), 1378 (w), 1324 (w), 1280 (w), 1186 (w), 1108 (s), 1080 (s), 1015 (w), 966 (w), 955 (w), 876 (w), 801 (w), 752 (w), 723 (s), 689 (s), 507 (s).

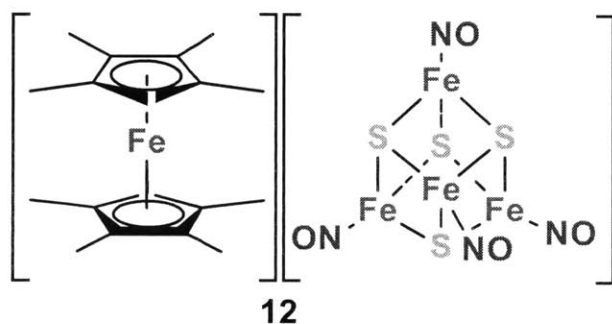


**(Ph<sub>4</sub>P)<sub>2</sub>[Fe<sub>4</sub>S<sub>4</sub>(LS<sub>3</sub>)(Tp)], 10h.**<sup>14</sup> In a 5 mL vial, **9** (100.0 mg, 50 μmol) was dissolved in 10:1 MeCN/DMF (2 mL). In a separate 5 mL vial K(Tp) (13.8 mg, 55 μmol) was dissolved in 10:1 MeCN/DMF (1 mL). The K(Tp) solution was transferred to the solution containing **1·Cl** and the reaction was stirred for 3 hours. The crude mixture was filtered through a piece of glass filter paper in a Pasteur pipette into a 125 mL Erlenmeyer flask and evaporated to dryness. The remaining solid was redissolved in DMF (2 mL), layered with Et<sub>2</sub>O, and placed in a -30° freezer overnight afford a precipitate, which was collected on an F-grade frit and washed with Et<sub>2</sub>O (3 x 10 mL) to yield 60.2 mg (27.5 μmol, 55 %) of brown microcrystalline material. The <sup>1</sup>H NMR spectrum matched that previously published. <sup>1</sup>H NMR (600 MHz, CD<sub>3</sub>CN, δ ppm): 11.61 (pz-H<sub>4</sub>), 10.84 (pz-H<sub>3</sub>), 8.73 (5-H), 7.09 (2'-H), 6.59 (3'-H), 4.45 (6-Me), 4.03 (4-Me), 2.27 (4'-Me). FT-IR (KBr, cm<sup>-1</sup>): 2911 (w), 2448 (w), 1656 (w), 1586 (w), 1489 (w), 1437 (s), 1400 (w), 1304 (w), 1261 (w), 1210 (w), 1109 (s), 1081 (s), 1041 (s), 1015 (w), 997 (w), 877 (w), 801 (w), 754 (w), 721 (s), 689 (s), 527 (s).

**NO(g) reactions.** In a 20 mL vial, **9** or **10a-h** (20.8 μmol) was dissolved in methylene chloride (6 mL) and the vial was sealed with a rubber septum. An equivalent of NO(g) (500 μL, 16.35 μmol) was then injected via a gas-tight syringe into the reaction vial. The reaction was stirred for 2 h and subsequently poured into pentane (120 mL) and stirred for 10 min. The mixture was

filtered through Celite, and the residual solid was extracted with methylene chloride (50 mL). After solvent removal, the remaining solid was characterized by ESI-MS and CH<sub>2</sub>Cl<sub>2</sub> solution FT-IR. Formation of [Fe<sub>4</sub>S<sub>4</sub>(NO)<sub>4</sub>]<sup>-</sup>, **12**, and [Fe<sub>4</sub>S<sub>3</sub>(NO)<sub>7</sub>]<sup>-</sup>, RBA, was observed.

**Ph<sub>3</sub>CSNO reactions.** In a 20 mL vial, **9** or **10a-h** (16.35 μmol) was dissolved in methylene chloride (6 mL) and the vial was sealed with a rubber septum. In a 5 mL vial 1, 2, 4, or 8 equivalents of Ph<sub>3</sub>CSNO (16.35, 32.7, 65.4, and 130.8 μmol, respectively) was dissolved in methylene chloride (5 mL) and instantly injected via syringe into the reaction vial. Throughout the course of the reaction, 40 – 60 μL aliquots were taken to monitor the reaction by solution IR. After no further growth of the bands in the region between 1600 and 1850 cm<sup>-1</sup> was observed (2 – 6 h), the reaction mixture was poured into pentane (120 mL) and stirred for 10 min. The mixture was filtered through Celite. The filtrate was analyzed by GC-MS to reveal the formation of (Ph<sub>3</sub>CS)<sub>2</sub> and by <sup>1</sup>H NMR spectroscopy in CD<sub>3</sub>CN to show the presence of the LS<sub>3</sub> ligand. The solid remaining on the Celite was extracted with methylene chloride (50 mL). After solvent removal the remaining solid was characterized by ESI-MS, Mössbauer, CH<sub>2</sub>Cl<sub>2</sub> solution FT-IR, and KBr solid-state FT-IR. If up to four equivalents of Ph<sub>3</sub>CSNO were used, the isolated nitrosated product was **12**. When eight equivalents of Ph<sub>3</sub>CSNO were used, the isolated product was RBA.



[(C<sub>5</sub>Me<sub>5</sub>)<sub>2</sub>Fe][Fe<sub>4</sub>S<sub>4</sub>(NO)<sub>4</sub>], [Cp<sup>\*</sup><sub>2</sub>Fe]**12**. In a 20 mL vial, **9** (32.9 mg, 16.4 μmol) and TIPF<sub>6</sub> (28.4 mg, 81.3 μmol) were dissolved in methylene chloride (6 mL). The reaction vial was sealed

with a septum. In a 5 mL vial Ph<sub>3</sub>CSNO (20.0 mg, 65.4 μmol) was dissolved in methylene chloride (5 mL) and instantly injected via syringe into the reaction vial. After 2 h, the reaction mixture was poured into pentane (120 mL) and stirred for 10 min. The mixture was filtered through Celite, and the filtrate was stripped to yield 30.4 mg of a yellow-brown solid. Characterization of the mixture using ESI-MS, CH<sub>2</sub>Cl<sub>2</sub> solution FT-IR spectroscopy, and cyclic voltammetry confirmed the presence of **11**. This solid mixture was dissolved in methylene chloride (2 mL) and (C<sub>5</sub>Me<sub>5</sub>)<sub>2</sub>Fe (22.3 mg) was added. The reaction was stirred for 30 min and subsequently poured into pentane (100 mL) affording a black precipitate. The precipitate was collected via filtration through Celite and extracted with methylene chloride (10 mL). The methylene chloride solution was stripped to yield 8.3 mg (10.0 μmol, 61.0 %) of a black powder. Crystals suitable for X-ray diffraction studies were grown by vapor diffusion of diethyl ether into a methylene chloride solution of [Cp<sup>\*</sup><sub>2</sub>Fe]**12**. ESI-MS (MeCN, m/z): 326.2 ([Cp<sup>\*</sup><sub>2</sub>Fe]<sup>+</sup>, 326.3), 471.6 ([**12**]<sup>-</sup>, 471.6), 441.5 ([**12**-NO]<sup>-</sup>, 441.6), 411.5 ([**12**-2NO]<sup>-</sup>, 411.6), 381.5 ([**12**-3NO]<sup>-</sup>, 381.6), 351.5 ([**12**-4NO]<sup>-</sup>, 351.6). FT-IR (CH<sub>2</sub>Cl<sub>2</sub>, cm<sup>-1</sup>): 1725 (s, ν<sub>NO</sub>). Anal. Calcd for C<sub>20</sub>H<sub>30</sub>Fe<sub>5</sub>S<sub>4</sub>N<sub>4</sub>O<sub>4</sub>: C, 30.10; H, 3.79; N, 7.02. Found: C, 30.04; H, 3.41; N, 6.80.

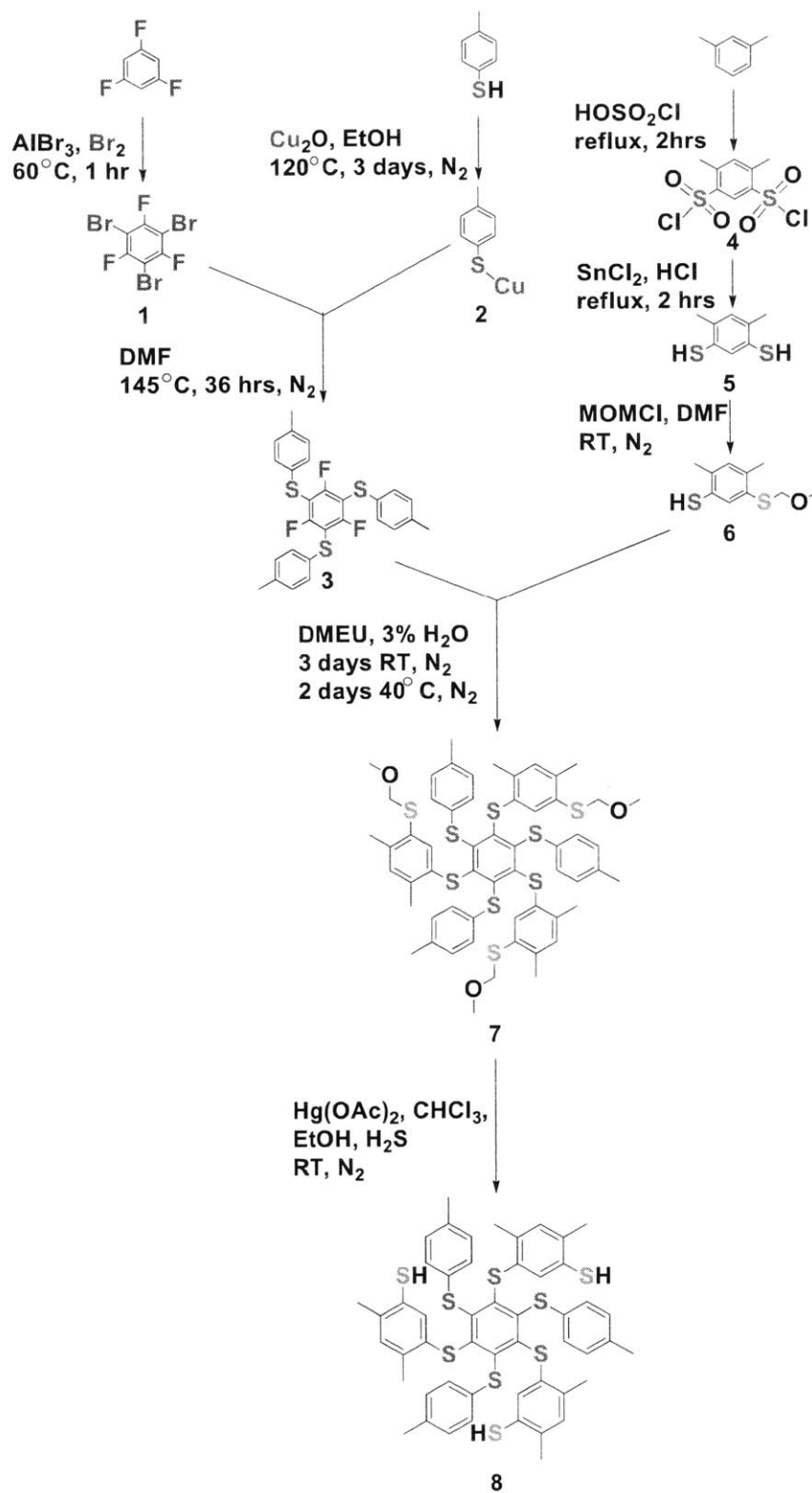
### 5.3 Results and Discussion

**Synthesis of the [3:1] Site-differentiated Cluster.** Synthesis of the [3:1] site-differentiated ligand, previously developed by Stack and Holm, involves an 8-step reaction pathway that exploits the differences in reactivity between aryl fluorides and aryl bromides to build a ligand with an *ababab* configuration (Scheme 5.2).<sup>16</sup> The initial step in the synthesis involves formation of 1,3,5-tribromo-2,4,6-trifluorobenzene, **1**, by AlBr<sub>3</sub>-catalyzed bromination of 1,3,5-trifluorobenzene. Purification of **1** was modified to substitute the recrystallization using hot

ethanol, by dissolution of the crude product in hexanes and running through a silica plug to remove any residual Br<sub>2</sub>. This alternate purification improved the yield of the final product from 40% to 83% in our hands.

The alternating bromines and fluorines allow correct positioning of the “arms” and “legs” of the final ligand scaffold without the need to separate various isomers that could arise during the copper-mediated aryl-thiol coupling. The coupling agent is the pale yellow copper salt *p*-tolylthiocuprate, **2**, which is prepared by reaction of copper(I) oxide and *p*-tolyl mercaptan over the course of three days in near-refluxing ethanol. The Ullman coupling reaction produces 1,3,5-trifluoro-2,4,6-tris(*p*-tolylthio)benzene, **3**. The purification of **3** was modified from the published procedure to include silica gel chromatography with toluene as elutant. This step was deemed necessary because residual copper salts were promoting deprotection of the “arms” during the synthesis of the final protected ligand L(SCH<sub>2</sub>OCH<sub>3</sub>)<sub>3</sub>, **7**, leading to side-product formation and decreased yields.





**Scheme 5.2.** Synthesis of the [3:1] site-differentiated ligand  $\text{L}(\text{SH})_3$ , **8**.

The synthesis of the “arms” of the ligand begins with sulfonation of *m*-xylenes with chlorosulfonic acid to produce 4,6-dimethyl-1,3-disulfonyl dichloride, **4**. The synthesis described in the thesis of Tard reported, no further purification beyond washing with water.<sup>34</sup> An alternative method of purification is described in Stack’s thesis involving dissolution of the product in methylene chloride and separation of water and a red oil.<sup>15</sup> Removal of methylene chloride is followed by recrystallization from hot acetone. This additional purification step proved to be necessary for reduction of **4** to the sulfide with tin(II) chloride. Otherwise, formation of a yellow-brown, insoluble polymer reduced the yield of 1,3-dimercapto-4,6-dimethylbenzene, **5**.

Initially, monoprotection of **5** was attempted with chloromethyl ethyl ether (EOMCl), which is a more widely available and less expensive reagent than the published protecting reagent, chloromethyl methyl ether (MOMCl). Unfortunately, the EOMCl protecting group was too bulky to allow for complete substitution of the aryl fluoride during the synthesis of **7**, resulting in the coupling of only two arms to the backbone (Figure 5.2).

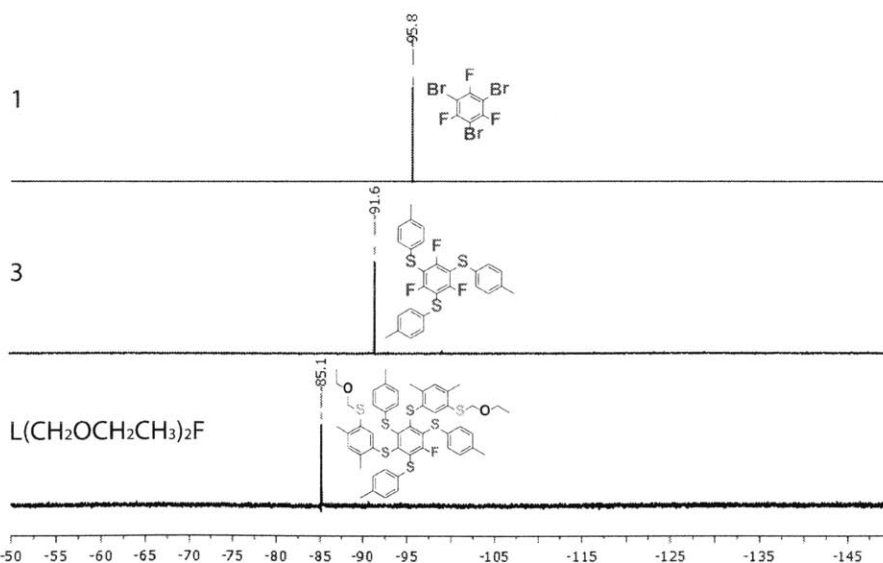


**Figure 5.2.** <sup>19</sup>F NMR of **1**, **3**, and L(SCH<sub>2</sub>OCH<sub>2</sub>CH<sub>3</sub>)<sub>2</sub>F. The coupling of **6-EOM** with **3** was incomplete and resulted an undesired product.

We also attempted to monoprotect **5** directly rather than to diprotect the thiols. In this protection, triethylamine replaced sodium hydride as the deprotonation agent. This method was used by Gebbink and coworkers to selectively protect the sulfide on the thioindole of Tris(SH)<sub>3</sub> by exploiting differences in pKa between the –SH and the –NH functional groups.<sup>17,35</sup> In our case the reaction was not successful and led to production of mono- and diprotected product along with starting material (Figure 5.3), which hindered easy purification of 4,6-dimethyl-3-((methoxymethyl)thio)benzenethiol, **6**.

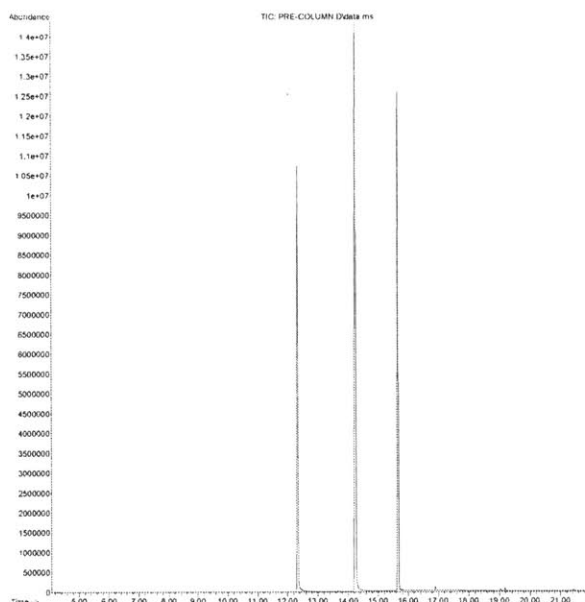


**Figure 5.3.** Gas Chromatogram of crude product obtained when attempting to protect **5** using Et<sub>3</sub>N as the base. The three peaks correspond to **5** (12.5 min), **6** (14 min), and [6-H+CH<sub>2</sub>OCH<sub>3</sub>] (16 min).

The best yields of **6** were obtained when the published synthetic procedure was followed with the only alteration being that the mono-deprotection occurred at 90° C rather than 120° C. Decomposition of the protecting groups was observed at the higher temperature when we performed the synthesis on a gram rather than the published dozen-gram scale.

The aryl-fluoride substitution to synthesize **7** proved to be one of the more trying synthetic steps. It requires multiple days to complete and is not properly described in the original published procedure. Initial attempts resulted in unrecoverable yields of **7** due to the multitude of products formed. The published purification for **7** by silica gel flash column chromatography resulted in decomposition of the product into unknown species. This decomposition could be monitored by loss of the signal assigned to the methylene peak of the methoxymethyl protecting group and formation of new peaks in the 4.5 - 5.0 ppm region. One of the side products was determined to be an intramolecular disulfide by X-ray crystallography from a crystal that was serendipitously obtained upon evaporation of a column fraction (Figure 5.4). An investigation of Stack's thesis yielded an altered synthesis that limited heating of the reaction to 40 °C and addition of water.<sup>15</sup> The modified purification involved an acid-wash step using acetic acid and recrystallization from hot acetone, rather than purification by column chromatography. These changes proved successful and led to the multi-gram synthesis of the protected ligand.

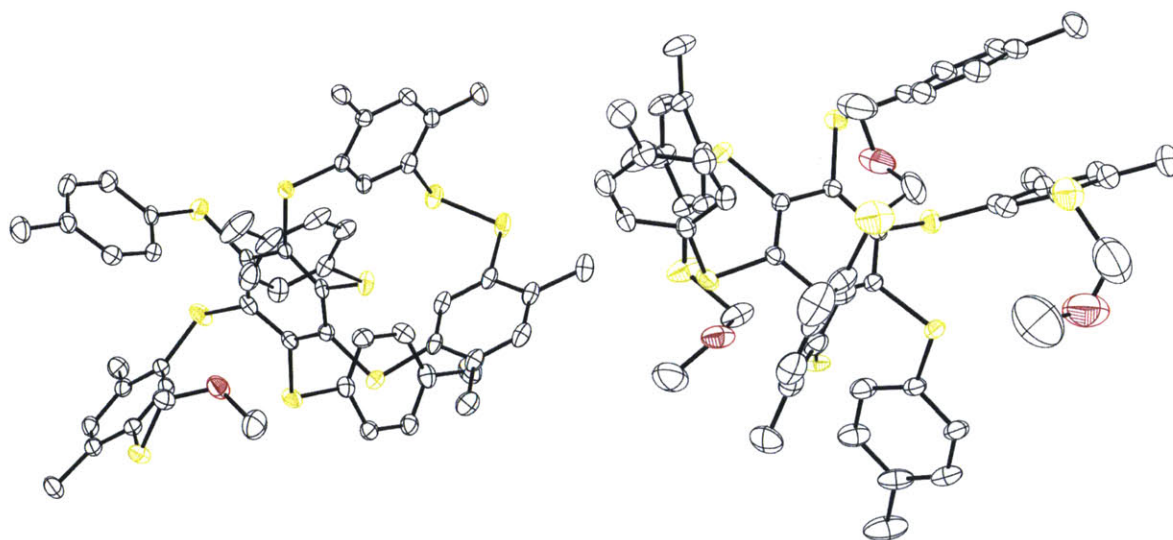


**Figure 5.4.** Drawings of the X-ray crystal structures of  $LS_2(SCH_2OCH_2CH_3)$  (left) and  $L(SCH_2OCH_2CH_3)_3 \cdot (CH_3)_2CO$ , **7**, (right) with ellipsoids shown at 50% probability. Solvent molecules and hydrogen atoms are omitted for clarity. Color scheme: sulfur, yellow; oxygen, red; carbon, colorless.

**Table 5.1.** X-ray crystallographic data for  $\text{LS}_2(\text{SCH}_2\text{OCH}_2\text{CH}_3)$  and  $7 \cdot (\text{CH}_3)_2\text{CO}$  at 100K.

compounds	$\text{LS}_2(\text{SCH}_2\text{OCH}_2\text{CH}_3)$	$7 \cdot (\text{CH}_3)_2\text{CO}$
formula	$\text{C}_{53}\text{H}_{50}\text{OS}_9$	$\text{C}_{60}\text{H}_{66}\text{O}_4\text{S}_9$
formula weight	991.47	1139.67
crystal system	monoclinic	triclinic
space group	$\text{P}2_1/\text{n}$	$\text{P}\bar{1}$
a, Å	9.2558(9)	12.5412(7)
b, Å	23.454(2)	14.1338(8)
c, Å	22.517(2)	18.4442(10)
$\alpha$ , deg	90	88.0090(10)
$\beta$ , deg	100.684(2)	85.1100(10)
$\gamma$ , deg	90	64.3000(10)
V, Å <sup>3</sup>	4803.5(8)	2935.2(3)
Z	4	2
$\rho_{\text{calcd}}$ , g/cm <sup>3</sup>	1.371	1.290
$\mu$ , mm <sup>-1</sup>	0.455	0.385
$\theta$ range, deg	1.27 to 26.28	1.11 to 31.00
completeness to $\theta$ , %	99.6	91.6
reflections collected	82271	64717
independent reflections	9699	17126
R(int)	0.0497	0.0230
restraints	0	0
parameters	578	672
Max., min. transmission	0.7454, 0.6804	0.7462, 0.6917
R1(wR2) [ $I > 2\sigma(I)$ ]	0.04665 (0.1142)	0.0652 (0.2321)
R1(wR2)	0.0612 (0.1218)	0.0783 (0.2449)
GoF(F <sup>2</sup> )	1.446	1.708
max, min peaks, e.Å <sup>-3</sup>	0.979, -0.470	2.145, -1.352

Deprotection of **7** to form the final tridentate ligand  $\text{L}(\text{SH})_3$ , **8**, was effected by use of  $\text{Hg}(\text{OAc})_2$  and protonation by  $\text{H}_2\text{S}(\text{g})$ , as shown by  $^1\text{H}$  NMR spectroscopy (Figure 5.5). Because **8** has a tendency to form intramolecular disulfides when exposed to air, becoming useless as a tridentate cluster scaffold, the final product was kept under nitrogen in the glove box.

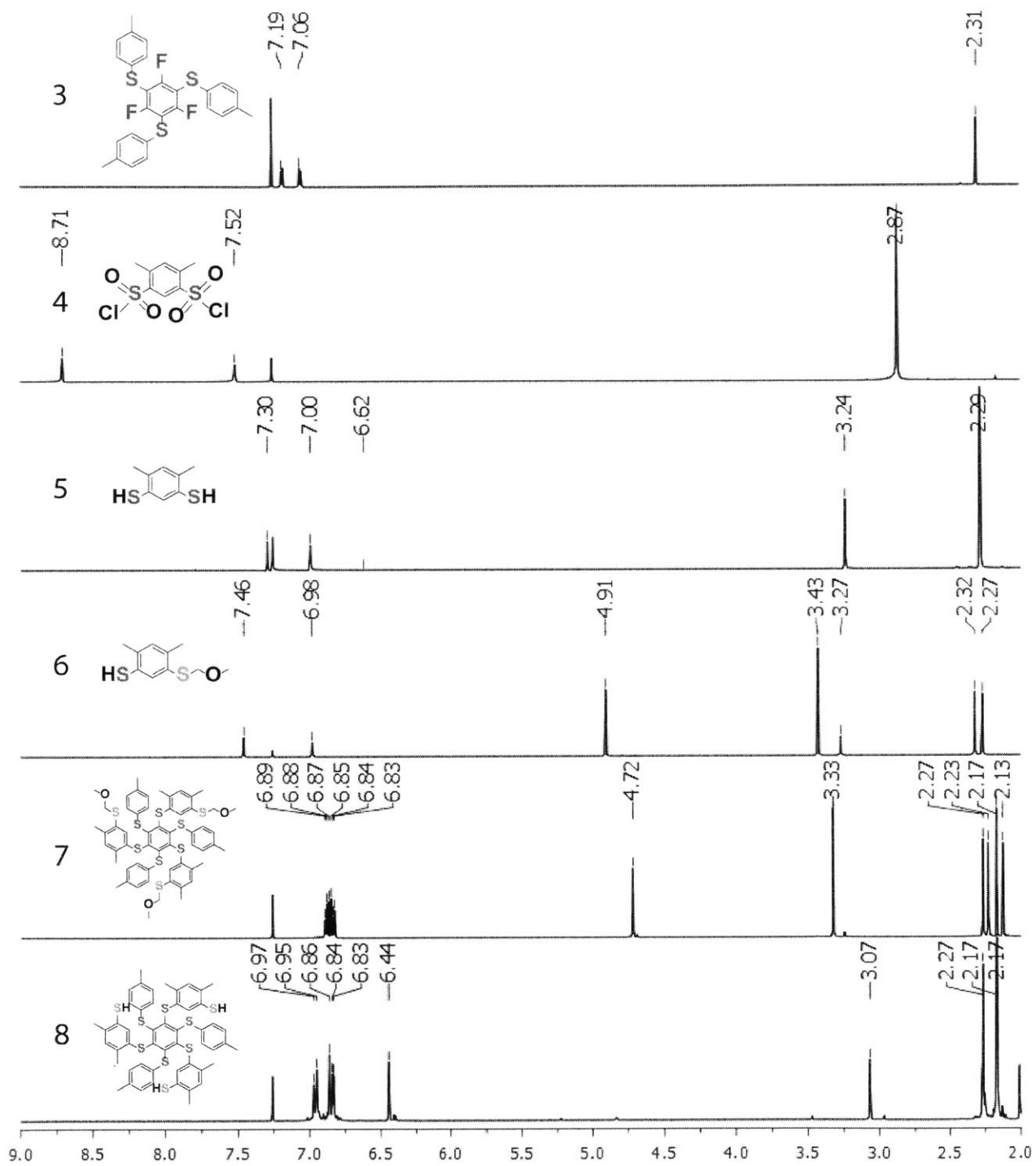
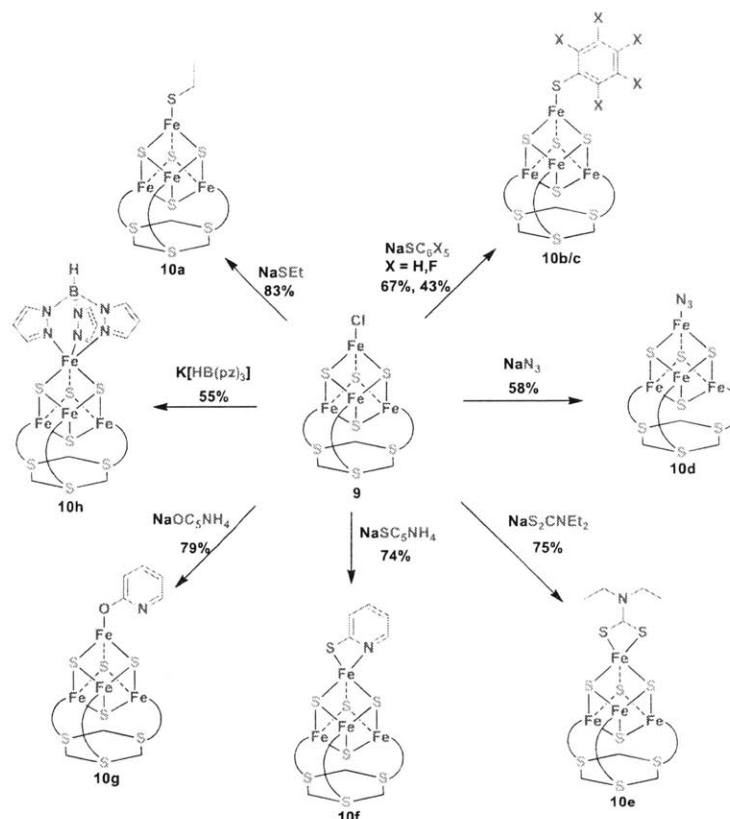


**Figure 5.5.**  $^1\text{H}$  NMR spectra of compounds 3-8 in  $\text{CDCl}_3$ .

**Synthesis and Characterization of Clusters.** Over the course of two decades numerous ligand substitutions were carried out on the site-differentiated, apical iron atom of  $[\text{Fe}_4\text{S}_4(\text{LS}_3)\text{L}']^{2-}$ .<sup>36</sup> Cluster incorporation to the ligand is achieved by stirring  $\text{L}(\text{SH})_3$  with  $(\text{Ph}_4\text{P})_2[\text{Fe}_4\text{S}_4(\text{SEt})_4]$  while under dynamic vacuum to remove ethyl mercaptan and push the equilibrium to form  $(\text{Ph}_4\text{P})_2[\text{Fe}_4\text{S}_4(\text{SEt})_4]$ . Addition of pivaloyl chloride forms **9** and  $(\text{CH}_3)_3\text{COSEt}$ , which are separated by crystallization from DMF and acetonitrile.

Formation of compounds **10a-h** begins with **9** and is performed using alkali metal salts of the ligands in organic solvents (Scheme 5.3). The use of alkali metals to precipitate  $\text{MCl}$  (where  $\text{M}$  is  $\text{Na}^+$  or  $\text{K}^+$ ) drives the reaction toward completion by replacing the ligand on the apical iron atom to afford the ligand-substituted product as microcrystalline material in 50 to 90 % yield and an insoluble alkali-halide salt.



**Scheme 5.3.** Preparation of **10a-h** from **9** using different alkali metal salts.

The synthesized complexes were chosen based on a few factors. The thiolate complexes were chosen as they mimic the coordination sphere of a majority of biological [4Fe-4S] clusters. The published and experimentally determined Mössbauer parameters of **10a-c** (Table 5.2) suggest that the apical iron in these complexes are not differentiated electronically from the remaining [Fe-S] core (Figure 5.6).<sup>14</sup>

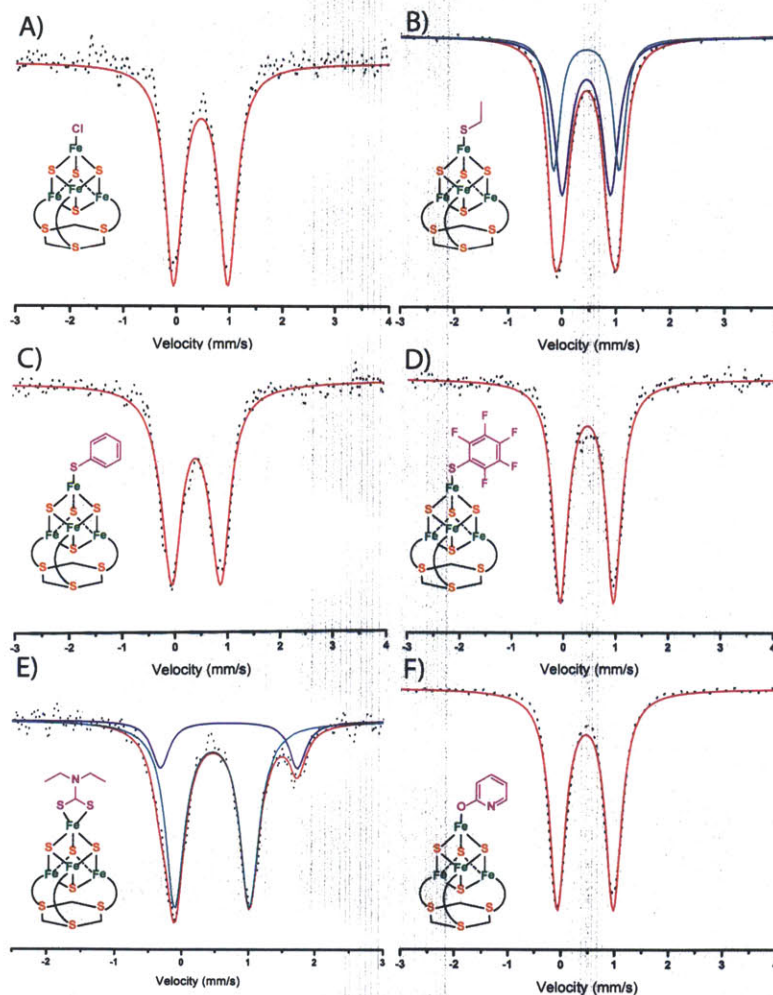


**Figure 5.6.** <sup>57</sup>Fe Mössbauer spectra of A) **9**, B) **10a**, C) **10b**, D) **10c**, E) **10e**, and F) **10g**. All spectra were recorded at 80 K. Color scheme: black dots, raw data; red line, full fit; blue line, site one; green line, site two. <sup>57</sup>Fe Mössbauer parameters for each spectrum are given in Table 5.2.



**Table 5.2.** Mössbauer parameters of relevant iron-sulfur complexes.

Complex	Temperature (K)	Isomer Shift ( $\delta$ , mm/s)	Quadrupole splitting ( $\Delta_{EQ}$ , mm/s)	Line width ( $\Gamma$ , mm/s)	Area (%)	Ref.
(Ph <sub>4</sub> P) <sub>2</sub> [Fe <sub>4</sub> S <sub>4</sub> (LS <sub>3</sub> )Cl], <b>9</b>	80	0.46(2)	1.03(2)	0.39(2)	100	<i>a</i>
(Ph <sub>4</sub> P) <sub>2</sub> [Fe <sub>4</sub> S <sub>4</sub> (LS <sub>3</sub> )(SET)], <b>10a</b>	80	0.44(2)	0.90(2)	0.36(2)	60	<i>a</i>
		0.44(2)	1.21(2)	0.27(2)	40	
(Ph <sub>4</sub> P) <sub>2</sub> [Fe <sub>4</sub> S <sub>4</sub> (LS <sub>3</sub> )(SPh)], <b>10b</b>	80	0.41(2)	0.93(2)	0.46(2)	100	<i>a</i>
(Ph <sub>4</sub> P) <sub>2</sub> [Fe <sub>4</sub> S <sub>4</sub> (LS <sub>3</sub> )(SC <sub>6</sub> F <sub>5</sub> )], <b>10c</b>	80	0.45(2)	1.02(2)	0.36(2)	100	<i>a</i>
(Ph <sub>4</sub> P) <sub>2</sub> [Fe <sub>4</sub> S <sub>4</sub> (LS <sub>3</sub> )(S <sub>2</sub> CNEt <sub>2</sub> )], <b>10e</b>	80	0.71(2)	2.06(2)	0.31(2)	20	<i>a</i>
		0.46(2)	1.12(2)	0.34(2)	80	
(Ph <sub>4</sub> P) <sub>2</sub> [Fe <sub>4</sub> S <sub>4</sub> (LS <sub>3</sub> )(S-2-Pyr)], <b>10f</b>	4.2	0.52	1.70	0.56	25	<sup>14</sup>
		0.34	0.94	0.30	39	
		0.34	1.26	0.29	36	
(Ph <sub>4</sub> P) <sub>2</sub> [Fe <sub>4</sub> S <sub>4</sub> (LS <sub>3</sub> )(O-2-Pyr)], <b>10g</b>	80	0.41(2)	0.93(2)	0.46(2)	100	<i>a</i>
(Ph <sub>4</sub> P) <sub>2</sub> [Fe <sub>4</sub> S <sub>4</sub> (LS <sub>3</sub> )(Tp)], <b>10h</b>	4.2	0.79	2.03	0.38	25	<sup>14</sup>
		0.31	0.84	0.30	34	
		0.34	1.23	0.33	41	
<b>12</b>	80	0.25(2)	0.90(2)	0.42(2)	100	<i>a</i>
<b>9 + 12</b>	80	0.25(2)	0.90(2)	0.38(2)	48	<i>a</i>
		0.46(2)	1.03(2)	0.36(2)	52	
[K(2,2,2-crypt)] <b>12</b>	300	0.156	0.935	N/A	100	<sup>37</sup>
[Fe <sub>4</sub> S <sub>4</sub> (NO) <sub>4</sub> ], <b>11</b>	78	0.150	1.473	0.334	100	<sup>38</sup>
(Et <sub>4</sub> N)[Fe <sub>4</sub> S <sub>3</sub> (NO) <sub>7</sub> ], RBA	90	0.15(2)	0.97(2)	0.32(2)	100	<sup>8</sup>
(Et <sub>4</sub> N)[Fe(SPh) <sub>2</sub> (NO) <sub>2</sub> ]	90	0.17(2)	0.68(2)	0.26(2)	100	<sup>8</sup>
Fe(NO)(S <sub>2</sub> CNEt <sub>2</sub> ) <sub>2</sub>	300	0.51(1)	0.80(1)	N/A	100	<sup>39</sup>

<sup>a</sup>This work

The potential ability of those apical ligands to disassociate more readily than LS<sub>3</sub> was intended to lend itself in the study of the mechanism by which most [4Fe-4S] clusters are degraded by reactive nitrogen oxide species. Compound **10d** was synthesized to possibly serve as a precursor in the synthesis of a cluster-bound nitrogen oxide via formation of an intermediate iron-nitrido complex, however, photoirradiation of the cluster did not result in a nitride species. Compounds **10e**, **10f**, and **10h** were chosen due to their ability to electronically differentiate irons in the cluster based on published Mössbauer parameters (Table 5.2).<sup>14</sup> These clusters also provide the unique opportunity of having an additional coordination site occupied on the apical iron to potentially allow the abstraction of that iron by NO and leave an intact [3Fe-4S] core. This would provide a similar environment to that seen biologically where additional coordinating ligands can be in close proximity to the reaction site in the form of amino acid residues or

unbound thiolates and histidines. Compound **10g** was originally proposed to be bidentate but the Mössbauer spectrum (Figure 5.7) suggests that the apical ligand coordinates only through the oxygen.

Characterization of these clusters by  $^1\text{H}$  NMR spectroscopy was possible owing to the  $S = 0$  ground state of their  $[\text{Fe}_4\text{S}_4]^{2+}$  cores. The chemical shifts of the protons appear downfield from those of the free ligand, and their line widths are broadened from what would be expected of a diamagnetic complex, suggesting that thermal excitation produces a weakly paramagnetic state (Figure 5.8). Electronic effects imparted by varying the apical ligand are manifested in different chemical shifts, especially of protons closest in proximity to the cluster. As a result, distinct  $^1\text{H}$  NMR spectra can be obtained for almost every compound.

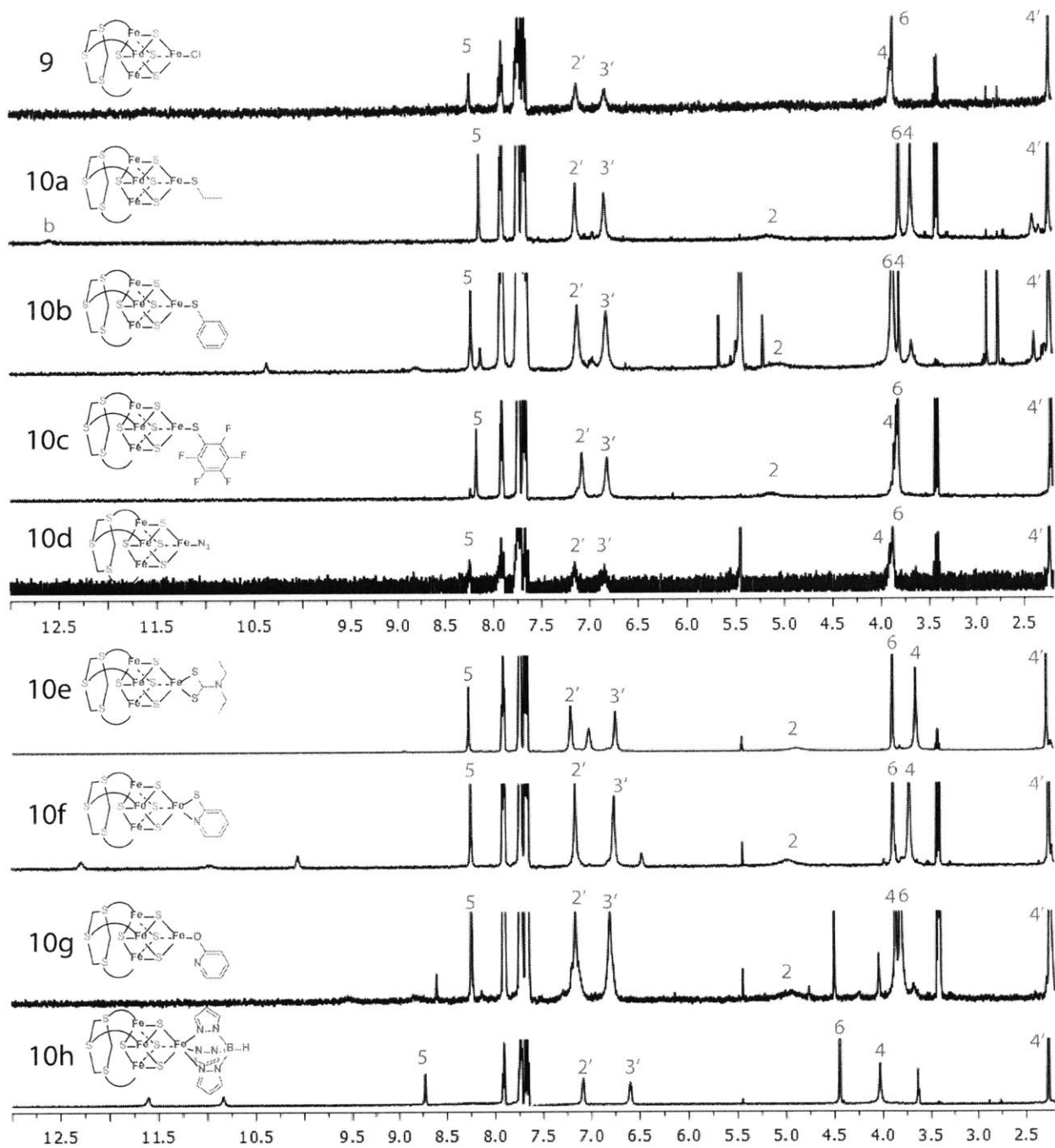


**Figure 5.7.**  $^1\text{H}$  NMR of **9** and **10a-h** in  $\text{CD}_3\text{CN}$ . Assignments of protons on the  $\text{LS}_3$  ligand are associated with the numbering order shown in Scheme 5.1.

These complexes were also identified by ESI-MS, with mass peaks corresponding to  $[\text{M}-\text{Ph}_4\text{P}]^-$  being common, and additional peaks arising from the presence of  $[\text{M}-2\text{Ph}_4\text{P}]^{2-}$ . Infrared spectroscopy is useful in identifying the formation of **10d** by the  $\nu_{\text{azide}}$  stretch at 2055

cm<sup>-1</sup> but does not provide information about the extent of substitution. Shifts in the IR bands of the derivatives of **1** are minimal and not useful in assessing conversion.

The synthesis of **10d** has been previously reported using Me<sub>3</sub>SiN<sub>3</sub> as the azide source.<sup>18</sup> We report the formation of **10d** using excess NaN<sub>3</sub> over the course of 18 h. This synthesis is more convenient than the previously published route. Sodium azide is readily available and is not as dangerous as the silane. The <sup>1</sup>H NMR spectrum of **10d** is identical to that in starting complex **9**, preventing us from monitoring reaction completion by this technique as was the case for other [Fe<sub>4</sub>S<sub>4</sub>(LS<sub>3</sub>)L']<sup>2-</sup> products. Conversion of the apical ligand from Cl<sup>-</sup> to N<sub>3</sub><sup>-</sup> can, however, be followed using ESI-MS, observing the decrease of a peak at 1672.6 m/z and formation of one at 1678.7 m/z (Figure 5.8).

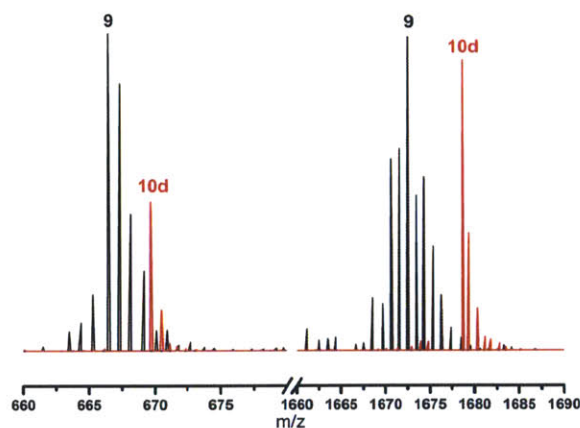


**Figure 5.8.** ESI-MS of **9** (black) and **10d** (red) using acetonitrile as the carrier solvent.

The X-ray crystal structure of **10d** (Figure 5.9) reveals an almost linear azide ion (N–N–N = 177.2(9)°) with a bent coordination geometry at the apical iron atom (Fe–N–N = 132.4(6)°). The three *p*-tolyl groups of the LS<sub>3</sub> ligand are oriented away from the cluster, a result that differs from the published structure of **9**, but most likely arises owing to packing of co-crystallized molecules of acetonitrile occupying the voids created by these aryl groups in the crystal lattice.<sup>16</sup>

The presence of co-crystallized H<sub>2</sub>O in the lattice may be arise from adventitious water in the acetonitrile.

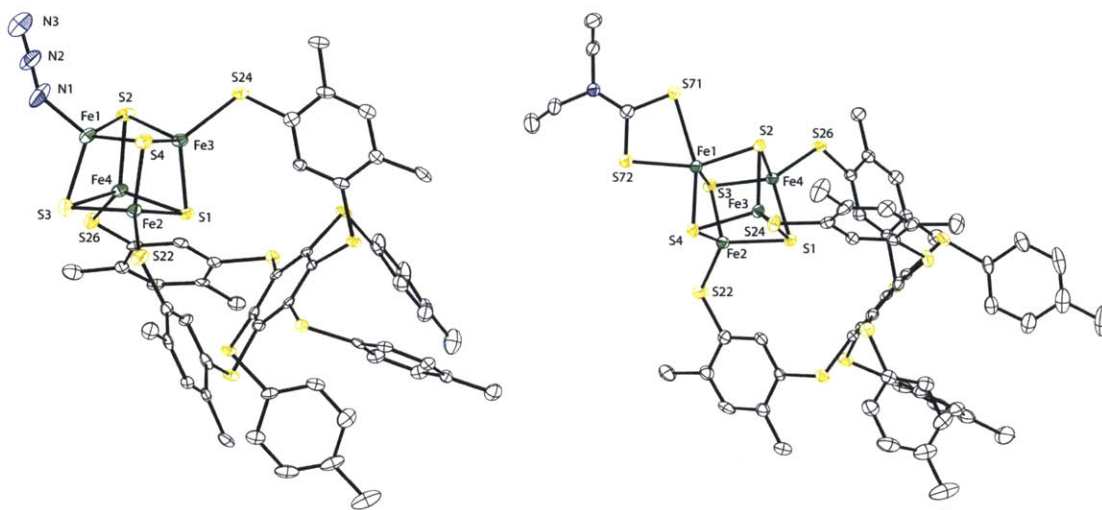


**Figure 5.9.** Drawings of the X-ray crystal structures of  $[\text{Fe}_4\text{S}_4(\text{LS}_3)(\text{N}_3)]^{2-}$ , **10d**, (left) and  $[\text{Fe}_4\text{S}_4(\text{LS}_3)(\text{S}_2\text{CNET}_2)]^{2-}$ , **10e**, (right) with ellipsoids shown at 50% probability. Cations, solvent molecules, and hydrogen atoms are omitted for clarity. Color scheme: iron, green; sulfur, yellow; nitrogen, blue; carbon, colorless.

**Table 5.3.** X-ray crystallographic data for **10d**·4MeCN·Et<sub>2</sub>O·0.5H<sub>2</sub>O and **10e**·2.5Et<sub>2</sub>O at 100K.

compounds	<b>10d</b> ·4MeCN·Et <sub>2</sub> O·0.5H <sub>2</sub> O	<b>10e</b> ·2.5Et <sub>2</sub> O
formula	C <sub>113</sub> H <sub>110</sub> Fe <sub>4</sub> N <sub>8</sub> O <sub>1.50</sub> P <sub>2</sub> S <sub>13</sub>	C <sub>114</sub> H <sub>120</sub> Fe <sub>4</sub> NO <sub>2.5</sub> P <sub>2</sub> S <sub>15</sub>
formula weight	2306.21	2310.35
crystal system	Triclinic	Triclinic
space group	P $\bar{1}$	P $\bar{1}$
a, Å	15.1180(12)	14.2454(10)
b, Å	16.8098(13)	16.7845(11)
c, Å	22.7156(18)	26.5044(18)
$\alpha$ , deg	96.5660(10)	87.4210(10)
$\beta$ , deg	105.1310(10)	76.7280(10)
$\gamma$ , deg	91.6890(1)	69.4440(10)
V, Å <sup>3</sup>	5525.4(8)	5770.3(7)
Z	2	2
$\rho_{\text{calcd}}$ , g/cm <sup>3</sup>	1.386	1.330
$\mu$ , mm <sup>-1</sup>	0.842	0.840
$\theta$ range, deg	1.80 to 25.31	1.49 to 27.33
completeness to $\theta$ , %	99.2	99.4
reflections collected	89482	108120
independent reflections	19989	25908
R(int)	0.1308	0.0505
restraints	24	30
parameters	1295	1281
Max., min. transmission	0.7452, 0.6104	0.7455, 0.6570
R1(wR2) [ $I > 2\sigma(I)$ ]	0.0690 (0.1319)	0.0537 (0.1485)
R1(wR2)	0.1344 (0.1554)	0.0808 (0.1643)
GoF(F <sup>2</sup> )	1.016	1.264
max, min peaks, e.Å <sup>-3</sup>	0.940, -0.663	2.322, -0.741

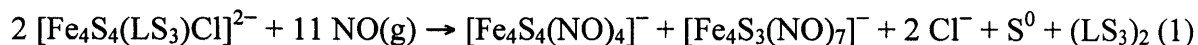
The formation of **10e** was previously observed by <sup>1</sup>H NMR spectroscopy and cyclic voltammetry, but it was never isolated and characterized. The synthesis of the (Ph<sub>4</sub>P)<sub>2</sub>[Fe<sub>4</sub>S<sub>4</sub>(LS<sub>3</sub>)(S<sub>2</sub>CNMe<sub>2</sub>)] analog was published but an X-ray crystal structure was never obtained, resulting in some ambiguity as to whether the apical iron atom is four- or five-coordinate. We have isolated **10e** in high yield and were able to obtain X-ray diffraction quality crystals (Figure 5.10).

The apical iron is five-coordinate with asymmetric thiocarbamate sulfur atoms, S(71) and S(72) at distances from the apical iron of 2.3918(10)Å and 2.6063(10)Å, respectively. As in **10d**, the *p*-tolyl groups of the LS<sub>3</sub> ligand in **10e** are oriented away from the cluster, but with the aryl

rings of the  $(\text{Ph}_4\text{P})^+$  cation partially occupying the voids. The refined structure has high residual electron density ( $2.322 \text{ e. \AA}^{-3}$ ) near an oxygen atom of one of the  $\text{Et}_2\text{O}$  molecules at a site of positional disorder that could not be refined satisfactorily.

The Mössbauer spectrum of **10e** (Figure 5.6E) shows that the apical iron atom is electronically differentiated from the remainder of the cluster. This differentiation is typically observed when the iron is multiply bound to the apical ligand (as in the case of **10f** and **10h**).<sup>14</sup>

**Reactions with NO(g).** In the reaction of clusters **9** and **10a-h** with one equivalent of  $\text{NO(g)}$ , two nitrosyliron species (eq 1) are observed by IR spectroscopy and ESI mass spectrometry (Figure 5.10). The first species is RBA as evidenced by  $\nu_{\text{NO}}$  bands at 1797, 1742, 1705  $\text{cm}^{-1}$  ( $\text{CH}_2\text{Cl}_2$ ) and observed masses for  $[\text{Fe}_4\text{S}_3(\text{NO})_x]^-$ , where  $x$  ranges from 1 to 7.<sup>40</sup> The formation of RBA was anticipated because it has been identified as the dominant nitrosyliron product in the reaction of  $\text{NO(g)}$  and  $\text{Ph}_3\text{CSNO}$  with  $[\text{Fe}_4\text{S}_4(\text{SPh})_4]^{2-}$  and other synthetic iron-sulfur clusters.<sup>2</sup> The second nitrosyliron species was identified as **12**, based on a  $\nu_{\text{NO}}$  band at 1725  $\text{cm}^{-1}$  ( $\text{CH}_2\text{Cl}_2$ ) and observed masses for  $[\text{Fe}_4\text{S}_4(\text{NO})_y]^-$ , where  $y$  ranges from 0 to 4 (Figure 5.10).<sup>37</sup> In situ monitoring of the reaction by ReactIR showed concomitant formation of both species (Figure B.1). Upon addition of eight equivalents of  $\text{NO(g)}$ , the sole nitrosyliron product is RBA.



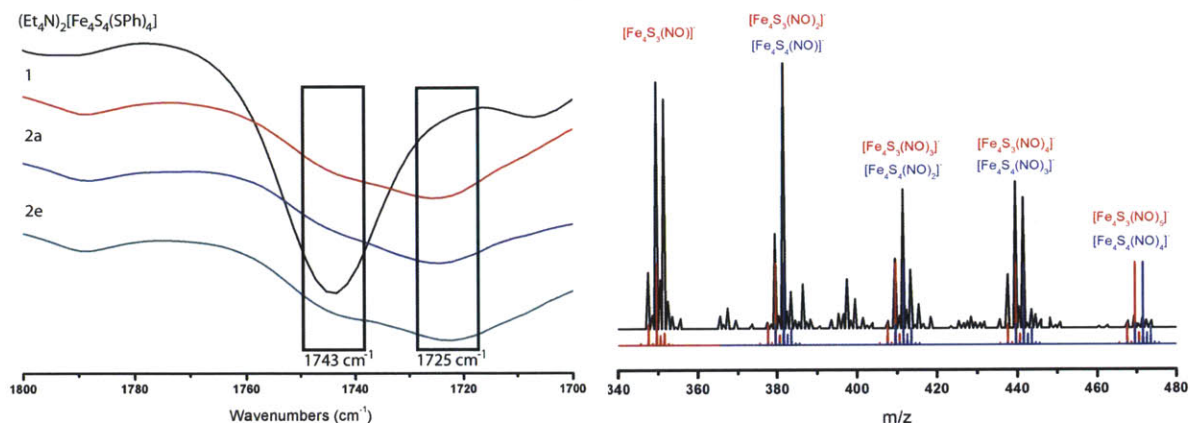


**Figure 5.10.** Characterization of the products formed between clusters and NO(g). Left: CH<sub>2</sub>Cl<sub>2</sub> solution IR spectra. Right: ESI-MS negative mode spectrum from the reaction of **10b** (Black, experimental; Red, simulated [Fe<sub>4</sub>S<sub>3</sub>(NO)<sub>x</sub>]<sup>-</sup>; Blue; simulated [Fe<sub>4</sub>S<sub>4</sub>(NO)<sub>x</sub>]<sup>-</sup>).

This result differs from that in previously published work, which reported the formation of only RBA from synthetic, undifferentiated [4Fe–4S] clusters even in the presence of only one equivalent of NO(g).<sup>2</sup> Our results suggest that the tridentate character of the LS<sub>3</sub> ligand may slow the reaction kinetics of these clusters with NO(g) by inhibiting access of NO to the less exposed iron sites of the cluster.

**Reactions with Ph<sub>3</sub>CSNO.** In an attempt to control the release of NO and isolate possible intermediate species, the *S*-nitrosothiol Ph<sub>3</sub>CSNO was allowed to react with clusters **9** and **10a-h**. When monitoring the cluster reaction with 1-4 equivalents of Ph<sub>3</sub>CSNO by solution FTIR (Figure B.14 – B.20) and ReactIR spectroscopy, the sole nitrosyliron product observed was **12** (eq 2), which is in contrast to the reaction of (Et<sub>4</sub>N)<sub>2</sub>[Fe<sub>4</sub>S<sub>4</sub>(SPh)<sub>4</sub>] with one equivalent of Ph<sub>3</sub>CSNO forming RBA (Figure 5.11). After addition of two equivalents of Ph<sub>3</sub>CSNO, the unreacted cluster was still observed by ESI-MS and Mössbauer spectroscopy. Upon addition of four equivalents of Ph<sub>3</sub>CSNO, only **12** is observed in the mass spectrum and the <sup>57</sup>Fe Mössbauer spectrum (Figure 5.12). Further addition to a combined total of eight equivalents of Ph<sub>3</sub>CSNO results in the conversion of **12** into RBA (eq 3). This conversion was previously observed while



trying to obtain X-ray quality crystals of  $[\text{AsPh}_4]\mathbf{12}$ , but only  $[\text{AsPh}_4]\text{RBA}$  was isolated, formed presumably by an unknown decomposition pathway.<sup>41</sup> Formation of RBA has not been reported to occur during nitrosation of  $[\text{Fe}_4\text{S}_4(\text{SR})_4]^{2-}$  clusters. Formation of RBA from  $\mathbf{12}$  has also been observed by the 1-electron oxidation of  $\mathbf{12}$  to  $\mathbf{11}$  followed by air exposure.<sup>42</sup> This known reaction pathway suggests that  $\mathbf{12}$  may form in biology at low NO concentrations from  $[\text{4Fe-4S}]$  clusters but then converts readily to RBA in the presence of cellular oxidants and oxygen.

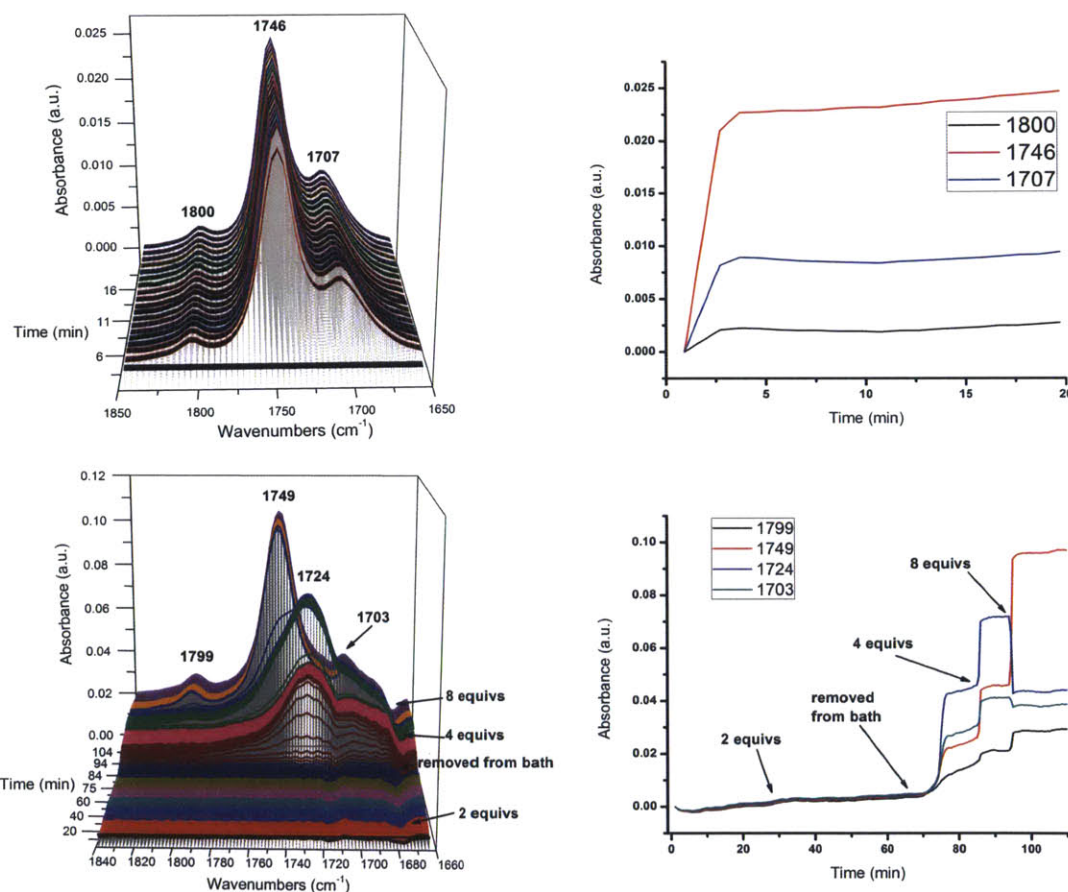


**Figure 5.11.** ReactIR spectra of  $(\text{Et}_4\text{N})_2[\text{Fe}_4\text{S}_4(\text{SPh})_4]$  and one equivalent of  $\text{Ph}_3\text{CSNO}$  in  $\text{CH}_2\text{Cl}_2$  at ambient temperature in  $\text{CH}_2\text{Cl}_2$  (top),  $\mathbf{10b}$  and varying equivalents of  $\text{Ph}_3\text{CSNO}$  in  $\text{CH}_2\text{Cl}_2$  (bottom). The time-dependent absorbances at different wavenumbers were monitored to observe the formation of  $\mathbf{12}$  en route to RBA, which did not occur in the  $[\text{Fe}_4\text{S}_4(\text{SPh})_4]^{2-}$  reaction but did in the reaction of  $\mathbf{10b}$ . The  $\mathbf{10b}$  solution was initially maintained in a dry ice/acetone bath, but after no detectable product formed after one hour, the reaction was removed from the bath and allowed to warm to room temperature.

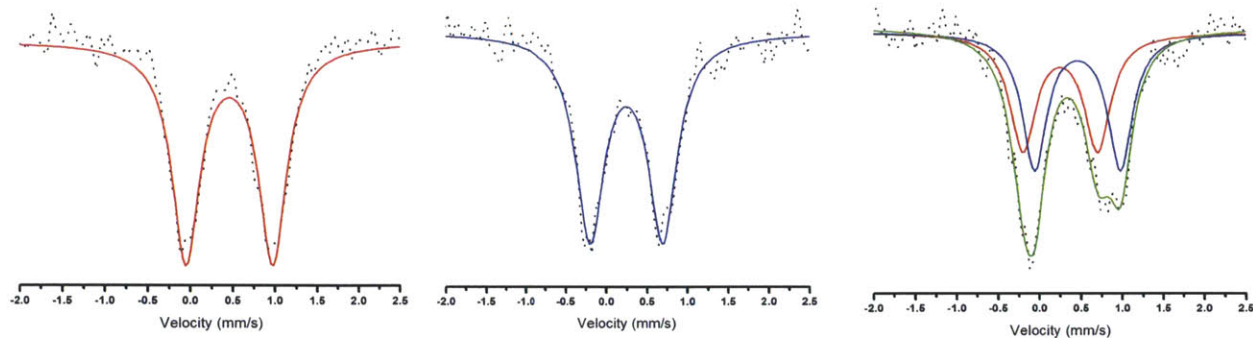


**Figure 5.12.** 80 K  $^{57}\text{Fe}$  Mössbauer spectrum of **9** (left; raw data, black dots; fitted spectrum, red line), **12** (middle; raw data, black dots; fitted spectrum, blue line), and **9** and **12** via the reaction with two equivalents of  $\text{Ph}_3\text{CSNO}$  (right; raw data, black dots; fitted spectrum, green line; **9**, red line; **12**, blue line).  $^{57}\text{Fe}$  Mössbauer parameters for each spectrum are given in Table 5.2.

The reactions were worked up by pouring the mixture into a 10-fold greater volume of pentanes, filtering through Celite, and extracting the remaining solid with methylene chloride. Solvent was removed under vacuum from the filtrate and the methylene chloride extract to afford masses of 26.4 mg and 17.2 mg, respectively. These masses correspond to the  $\text{LS}_3$  ligand and  $(\text{Ph}_3\text{CS})_2$  in the filtrate and  $(\text{Ph}_4\text{P})\text{Cl}$  and **12** in the methylene chloride. The expected masses were 33.5 mg for the filtrate and 19.4 mg for the methylene chloride extract. The presence of the  $\text{LS}_3$  ligand and  $(\text{Ph}_3\text{CS})_2$  in the filtrate was confirmed by  $^1\text{H}$  NMR spectroscopy. The formation of  $(\text{Ph}_3\text{CS})_2$  was further evidenced by GC-MS and X-ray crystallography (Figure 5.13 and 5.14). Separation of **12** and  $(\text{Ph}_4\text{P})\text{Cl}$  from the methylene chloride extract was not achieved, but spectroscopic characterization of **12** was not affected by this impurity.



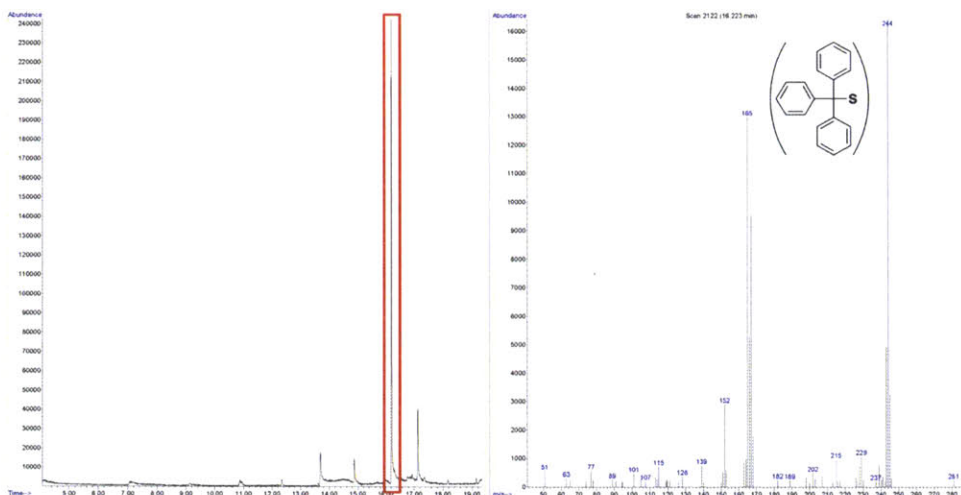


**Figure 5.13.** Gas chromatogram and EI-MS spectrum of pentane extract of the reaction of **1** with one equivalent of  $\text{Ph}_3\text{CSNO}$ .

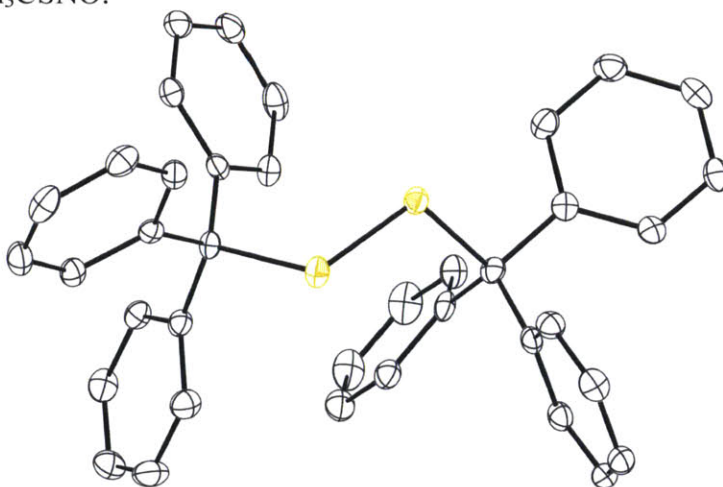


**Figure 5.14.** Drawing of the crystal structure of  $(\text{Ph}_3\text{CS})_2$ , ellipsoids are shown at 50% probability. Hydrogen atoms are removed for clarity. Color scheme: sulfur, yellow; carbon, colorless.

**Table 5.4.** X-ray crystallographic data for (Ph<sub>3</sub>CS)<sub>2</sub> and [Cp\*<sub>2</sub>Fe]**12** at 100K.

compounds	(Ph <sub>3</sub> CS) <sub>2</sub>	[Cp* <sub>2</sub> Fe] <b>12</b>
formula	C <sub>38</sub> H <sub>30</sub> S <sub>2</sub>	C <sub>20</sub> H <sub>30</sub> Fe <sub>5</sub> N <sub>4</sub> O <sub>4</sub> S <sub>4</sub>
formula weight	550.74	797.7
crystal system	monoclinic	triclinic
space group	P2 <sub>1</sub> /c	P $\bar{1}$
a, Å	13.8744(15)	11.8500(9)
b, Å	12.0428(19)	14.8878(11)
c, Å	17.2348(19)	17.1595(13)
$\alpha$ , deg	90	90.1420(10)
$\beta$ , deg	103.484(2)	105.8060(10)
$\gamma$ , deg	90	92.2720(10)
V, Å <sup>3</sup>	2800.3(5)	2910.3(4)
Z	4	4
$\rho_{\text{calcd}}$ , g/cm <sup>3</sup>	1.306	1.821
$\mu$ , mm <sup>-1</sup>	0.217	2.754
$\theta$ range, deg	1.51 to 25.03	1.37 to 25.03
completeness to $\theta$ , %	99.9	100.0
reflections collected	43518	45631
independent reflections	4956	10269
R(int)	0.0957	0.0741
restraints	0	0
parameters	361	690
max., min. transmission	0.7452, 0.6251	0.7452, 0.6438
R1(wR2) [ $I > 2\sigma(I)$ ]	0.0427 (0.0862)	0.0419 (0.0631)
R1(wR2)	0.0708 (0.0959)	0.0829 (0.0722)
GoF(F <sup>2</sup> )	1.204	1.008
max, min peaks, e.Å <sup>-3</sup>	0.434, -0.266	0.550, -0.442

The 80 K <sup>57</sup>Fe Mössbauer spectrum of the methylene chloride extract shows a doublet with an isomer shift of 0.25 mm/s (Figure 5.13). This value varies from the published one of [K(2,2,2-crypt)]**12** at 300 K (0.156 mm/s), but is close to the temperature-corrected value at 4.2 K (0.27 mm/s) (Table 5.2). The observed quadruple splitting of **12** at 80 K is 0.90 mm/s, in agreement with the previously reported value of 0.935 mm/s at 300 K of [K(2,2,2-crypt)]**12**.<sup>37,43</sup> The slight variations in isomer shifts may be due to temperature differences, but they are nonetheless distinct from values of other known iron-nitrosyl species and the starting materials used in this work (Table 2).<sup>38</sup> The Mössbauer spectrum of **12** also appears, in a 1:1 ratio with the starting material, in a methylene chloride extract from the reaction of **9** with two equivalents of

Ph<sub>3</sub>CSNO, providing further evidence that at substoichiometric amounts of Ph<sub>3</sub>CSNO the only observable product is **12**.

An X-band EPR spectrum of the sample recorded at ambient temperature gave an isotropic signal with  $g_{avg} = 2.030$ , and at 77 K a rhombic signal appeared with  $g_1 = 2.014$ ,  $g_2 = 2.026$ , and  $g_3 = 2.049$  (Figure 5.15). These spectra have features similar to those in published EPR spectra of biological DNICs, suggesting that previously reported experiments describing the formation of DNICs were in fact observations of **12**.<sup>4,10,44</sup> This conclusion may apply particularly when products of [4Fe–4S] cluster nitrosation were assigned by their EPR spectra as non-protein bound DNICs. In a previous study using NRVS using recombinant *P. furiosus* ferredoxin (D14C mutant), RBA was identified as the major nitrosated product upon exposure to propylamine propylamine NONOate.<sup>8</sup> A minor EPR-active byproduct having  $\langle g \rangle = 2.03$  was assigned as a protein-bound DNIC. Our current findings suggest that this and other results may merit reconsideration. Further investigation of low-molecular weight products of protein nitrosations using mass spectrometry, IR, NRVS, and Mössbauer spectroscopy are required to improve our understanding of the nitrosated products.<sup>45</sup>

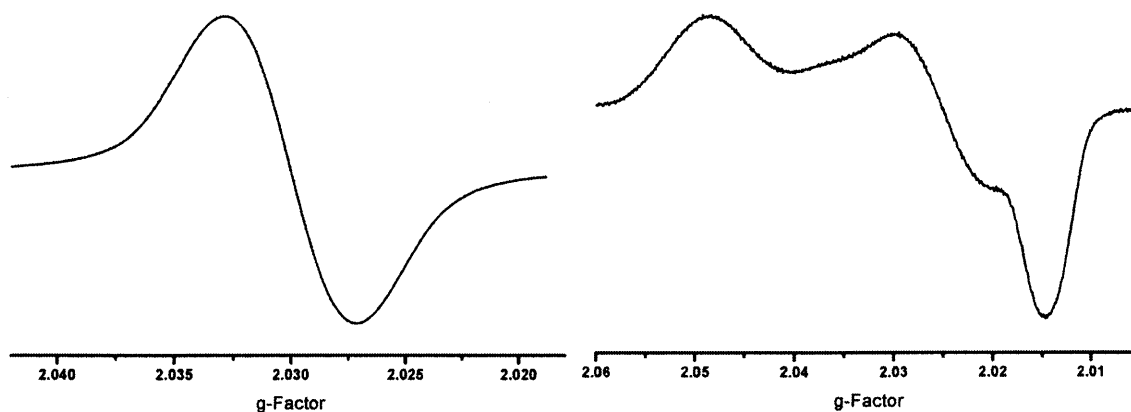


**Figure 5.15.** X-Band EPR spectra of **12** at room temperature (left) and 77 K (right). Conditions: RT – frequency 9.847 GHz, microwave power 2.017 mW, modulation amplitude 10.0 G; 77K – frequency 9.208 GHz, microwave power 1.992 mW, modulation amplitude 10.0 G. The RT spectra is an isotropic  $S = \frac{1}{2}$  signal with a  $\langle g \rangle = 2.030$ . The 77 K spectra is a rhombic  $S = \frac{1}{2}$  signal with  $g_1 = 2.014$ ,  $g_2 = 2.026$ , and  $g_3 = 2.049$ . The shape and  $g$ -values of both spectra are typically associated with DNICs in the literature.

Diamagnetic nitrosated products have been identified in stopped-flow kinetic studies of two proteins of the Wbl family.<sup>1,6</sup> This study reported evidence that the final product was generated via the formation of mono-, di-, and tetra-nitrosated intermediates. The absence of additional vibrational bands in the ReactIR traces during the present investigation, even at low temperature, suggests that isolation and characterization of a mono- or dinitrosated iron-sulfur cubane cluster is a difficult task. The instability of these thiol-bound, partially nitrosated cubane clusters may lead to complete extrusion of the cluster from the  $LS_3$  ligand, as has been previously reported when attempting salt metathesis of **9** using  $NaS^tBu$ .<sup>16</sup>

**Reactions with NO(g)/Ph<sub>3</sub>CSNO in the presence of TlPF<sub>6</sub>** Attempts to isolate a mono-nitrosated cubane were unsuccessful. When attempts were made to identify a  $[Fe_4S_4(LS_3)(NO)]^{x-}$  species from the reaction of **9** and Ph<sub>3</sub>CSNO in the presence of a 5-fold excess of TlPF<sub>6</sub>, a  $\nu_{NO}$  band at  $1790\text{ cm}^{-1}$  ( $CH_2Cl_2$ ) was observed in the IR spectrum (Figure 5.16). This species was subsequently identified as  $Fe_4S_4(NO)_4$ , **11**, by cyclic voltammetry (Figure 5.17) and ESI mass

spectrometry (Figure 5.18). The CV shows two reversible reductions centered at -314 mV and -1097 mV, which match the literature values of -370 mV and -1150 mV.<sup>37</sup> The reaction of **9** and NO(g) in the presence of TlPF<sub>6</sub> yields **11** and RBA (eq 4, Figure 5.16). Compound **11** can also be obtained by addition of a 5-fold excess of TlPF<sub>6</sub> after formation of **12** from **9** (eq 5) or **10a/b**.

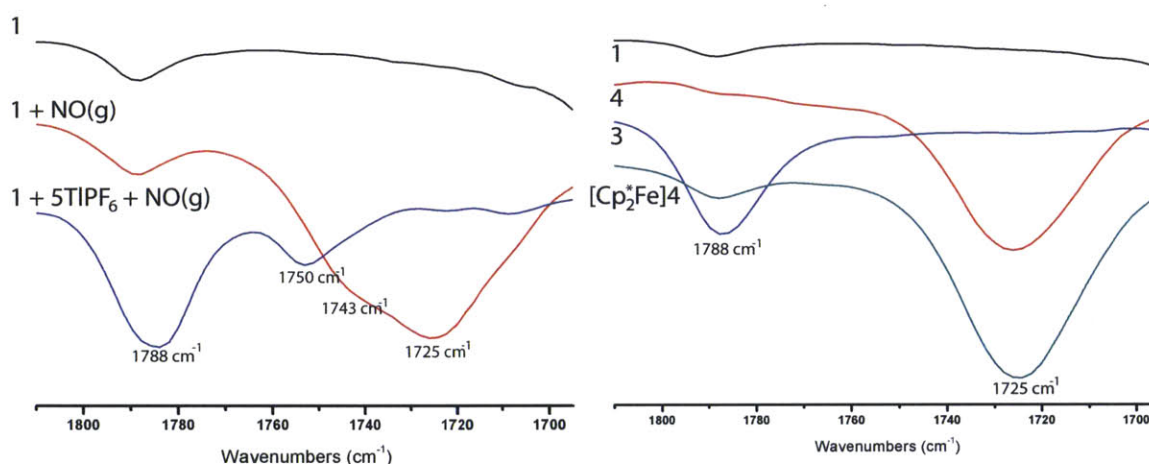
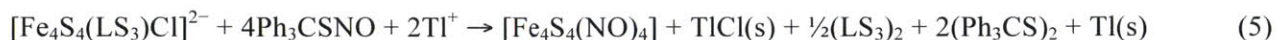
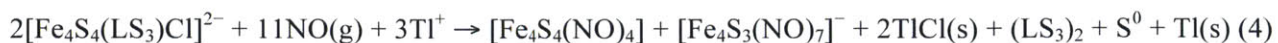


**Figure 5.16.** CH<sub>2</sub>Cl<sub>2</sub> solution FTIR of the reaction of **1** in the presence of excess TlPF<sub>6</sub> and one equivalent of NO(g) (left) and Ph<sub>3</sub>CSNO (right).

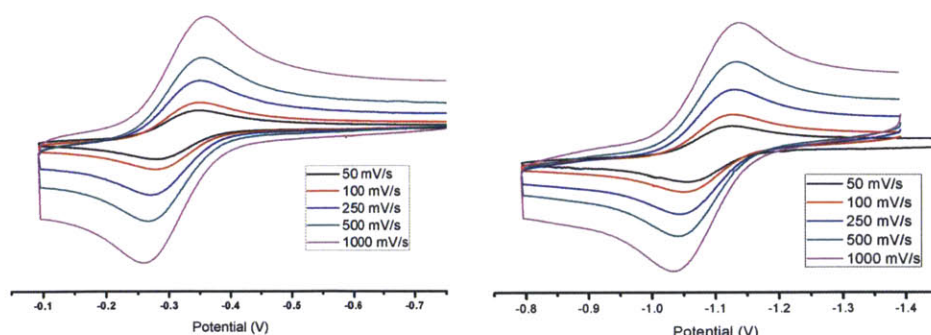


**Figure 5.17.** Cyclic voltammogram of **11** at ambient temperature at scan speeds from 50 – 1000 mV/s. The **11/12** couple appears at -314 mV and **12/12<sup>-</sup>** couple at -1097 mV, both vs. Fc/Fc<sup>+</sup>. All electrochemical data were referenced internally to the ferrocene/ferrocenium couple at 0.00 V.

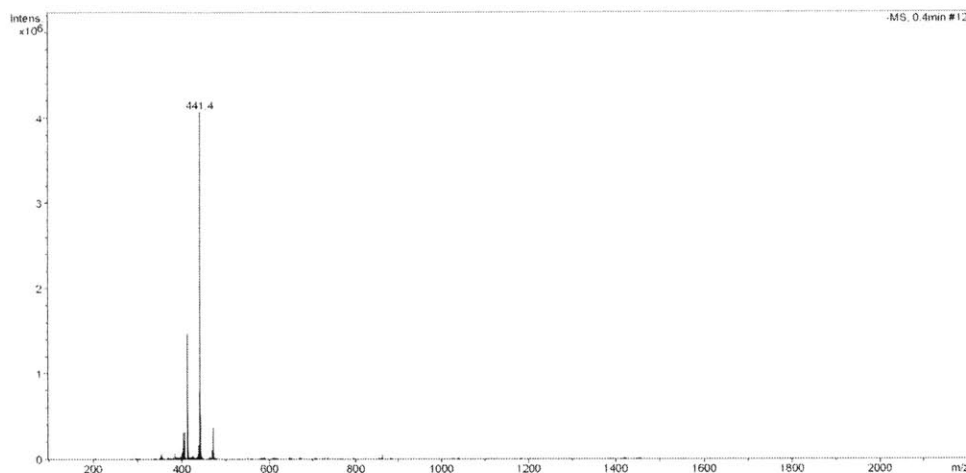


**Figure 5.18.** Negative-mode ESI-MS spectrum of **11** in acetonitrile. Only peaks corresponding to  $[\text{Fe}_4\text{S}_4(\text{NO})_x]^-$ , where  $x$  is 0 – 4, were observed.

The one electron reduction of **11** using  $(\text{C}_5\text{Me}_5)_2\text{Fe}$  resulted in formation of  $[(\text{C}_5\text{Me}_5)_2\text{Fe}][\text{Fe}_4\text{S}_4(\text{NO})_4]$ ,  $[\text{Cp}^*_2\text{Fe}]\mathbf{12}$  (Figure 5.19). This complex was crystallized from  $\text{CH}_2\text{Cl}_2/\text{Et}_2\text{O}$  with two crystallographically independent molecules in the asymmetric unit. The bond lengths and angles of the cluster are comparable to those published for  $[\text{K}(2,2,2\text{-crypt})]\mathbf{12}$  and other mono-nitrosyl capped iron-sulfur clusters (Table 5.5).<sup>37</sup> The observed isotopic patterns in the mass spectrum and the  $\nu_{\text{NO}}$  band in the IR match published values and those observed in direct reactions of **9** with  $\text{Ph}_3\text{CSNO}$ , providing further proof that the major isolatable product of stoichiometric nitrosation of  $[\text{Fe}_4\text{S}_4(\text{LS}_3)\text{L}']^{2-}$  is **12**.



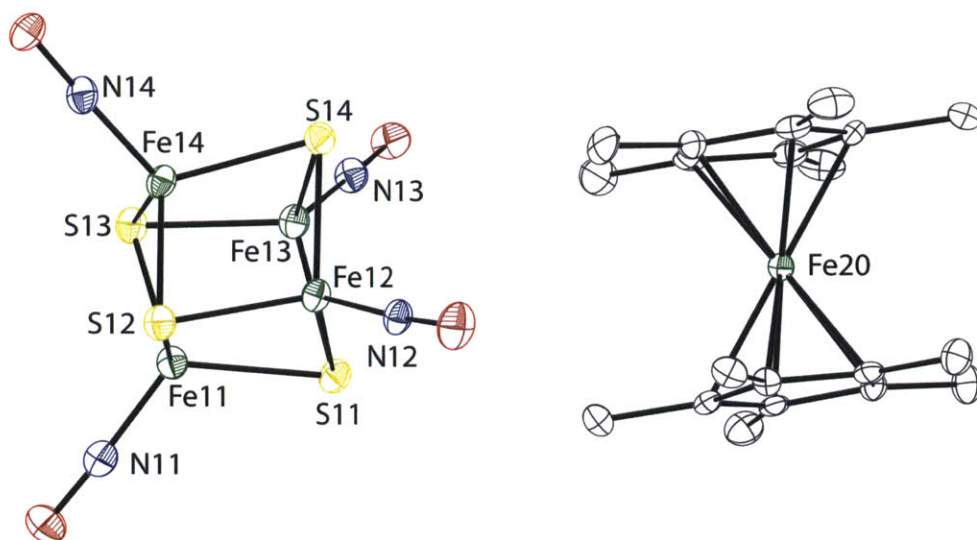


**Figure 5.19.** Drawing of  $[\text{Cp}^*_2\text{Fe}]12$  with thermal ellipsoids drawn at 50%. The other complex in the asymmetric unit and hydrogen atoms are omitted for clarity. Color scheme: iron, green; sulfur, yellow; nitrogen, blue, oxygen, red; carbon, colorless.

**Table 5.5.** Selected geometric parameters of iron-sulfur clusters capped with mono-nitrosyls.

	$(\text{Cp}^*_2\text{Fe})[12]$	$[\text{K}(2,2,2\text{-crypt})][12]^{37}$	$11^{37}$	$(\text{Me}_4\text{N})_2[\text{Fe}_4\text{S}_4(\text{NO})_4]^3$	$(\text{PPN})_2[\text{Fe}_8\text{S}_6(\text{NO})_8]^{46}$	
bond length, Å						
Fe–N	1.654(4);	1.655(5)	1.661(5)	1.665(6)	1.673(3)	
	1.655(4)	1.659(5)	1.662(6)	1.665(7)	1.674(2)	
	1.658(4);	1.660(5)	1.663(5)		1.676(2)	
	1.664(4)	1.663(5)	1.666(6)		1.676(2)	
	1.660(4);					
	1.664(4)					
	1.665(4);					
	1.665(4)					
	N–O	1.176(4);	1.162(6)	1.143(6)	1.181(9)	1.177(2)
		1.175(4)	1.166(6)	1.148(7)	1.193(9)	1.179(3)
1.183(4);		1.167(6)	1.157(6)		1.179(4)	
1.179(4)		1.178(6)	1.171(6)		1.184(3)	
1.185(4);						
1.180(4)						
1.192(4);						
1.189(4)						
bond angle, °						
Fe–N–O	175.8(3);	176.8(5)	176.9(5)	176.4(6)	174.6(2)	
	175.8(3)	176.9(5)	177.3(5)	176.7(6)	176.7(2)	
	176.7(3);	177.4(4)	177.6(5)		178.1(2)	
	176.8(3)	178.9(6)	178.8(5)		178.8(2)	
	178.1(4);					
	177.9(3)					
	179.1(3);					
	179.1(3)					

## 5.4 Summary and Conclusions

Synthesis of ligand **8** was successfully accomplished and modified to improve overall yields. Cluster incorporation was achieved to form **9** which served as a starting material to form other clusters of the type  $[\text{Fe}_4\text{S}_4(\text{LS}_3)\text{L}']^{2-}$ , **10a-h**.

The reactions of the site-differentiated clusters **9** and **10a-h** with either NO(g) or Ph<sub>3</sub>CSNO produce the S = ½ nitrosated cluster **12** en route to the formation of the diamagnetic RBA. The transformation of **12** into RBA by addition of an oxidant has been observed previously, but the present study is the first to demonstrate that nitrosation reaction of [4Fe–4S] clusters proceed through **12** en route to the RBA.<sup>41</sup> The tetranitrosated cluster has a similar EPR spectrum to that typically associated with DNICs, but only a single  $\nu_{\text{NO}}$  band in the IR spectrum as well as different Mössbauer parameters. The detection and isolation of EPR-active **12** via the direct reaction of [4Fe–4S] clusters suggests that some nitrosyliron products previously reported in the literature may have been mischaracterized as DNICs. This result is of particular interest when the most of the nitrosated products are EPR-silent, suggesting formation of RBA as the end product. Further investigations of low molecular weight nitrosyliron products by methods other than EPR are necessary to determine conclusively whether **12** or a DNIC is generated in a biological setting.

The isolation of a partially nitrosated cluster was not achieved. Even in the presence of thallium, added to remove the apical chloride ion, the cluster was oxidized by Tl<sup>+</sup> to form **11**, which was then used to form  $[\text{Cp}^*_2\text{Fe}]\text{12}$  for crystallographic verification of the formation of **12**.

## 5.5 References

1. Crack, J. C.; Smith, L. J.; Stapleton, M. R.; Peck, J.; Watmough, N. J.; Buttner, M. J.; Buxton, R. S.; Green, J.; Oganessian, V. S.; Thomson, A. J.; Le Brun, N. E., *J. Am. Chem. Soc.* **2010**, *133*, 1112.
2. Harrop, T. C.; Tonzetich, Z. J.; Reisner, E.; Lippard, S. J., *J. Am. Chem. Soc.* **2008**, *130*, 15602.
3. Tsou, C.-C.; Lin, Z.-S.; Lu, T.-T.; Liaw, W.-F., *J. Am. Chem. Soc.* **2008**, *130*, 17154.
4. Drapier, J. C.; Pellat, C.; Henry, Y., *J. Biol. Chem.* **1991**, *266*, 10162.
5. Kennedy, M. C.; Antholine, W. E.; Beinert, H., *J. Biol. Chem.* **1997**, *272*, 20340.
6. Crack, J. C.; Stapleton, M. R.; Green, J.; Thomson, A. J.; Le Brun, N. E., *J. Biol. Chem.* **2013**, *288*, 11492.
7. Tinberg, C. E.; Tonzetich, Z. J.; Wang, H.; Do, L. H.; Yoda, Y.; Cramer, S. P.; Lippard, S. J., *J. Am. Chem. Soc.* **2010**, 18168.
8. Tonzetich, Z. J.; Wang, H.; Mitra, D.; Tinberg, C. E.; Do, L. H.; Jenney, F. E.; Adams, M. W. W.; Cramer, S. P.; Lippard, S. J., *J. Am. Chem. Soc.* **2010**, *132*, 6914.
9. Cruz-Ramos, H.; Crack, J.; Wu, G. G.; Hughes, M. N.; Scott, C.; Thomson, A. J.; Green, J.; Poole, R. K., *EMBO J.* **2002**, *21*, 3235.
10. Foster, M. W.; Cowan, J. A., *J. Am. Chem. Soc.* **1999**, *121*, 4093.
11. Emptage, M. H.; Kent, T. A.; Kennedy, M. C.; Beinert, H.; Munck, E., *Proc. Natl. Acad. Sci. U.S.A.* **1983**, *80*, 4674.
12. Chen, T.-N.; Lo, F.-C.; Tsai, M.-L.; Shih, K.-N.; Chiang, M.-H.; Lee, G.-H.; Liaw, W.-F., *Inorg. Chim. Acta* **2006**, *359*, 2525.
13. Stack, T. D. P.; Holm, R. H., *J. Am. Chem. Soc.* **1987**, *109*, 2546.
14. Ciurli, S.; Carrie, M.; Weigel, J. A.; Carney, M. J.; Stack, T. D. P.; Papaefthymiou, G. C.; Holm, R. H., *J. Am. Chem. Soc.* **1990**, *112*, 2654.
15. Stack, T. D. P. Subsite differentiated analogues of biological Fe<sub>4</sub>S<sub>4</sub><sup>2+</sup> clusters: Steps towards and detours from. Harvard University, Cambridge, MA, 1988.
16. Stack, T. D. P.; Holm, R. H., *J. Am. Chem. Soc.* **1988**, *110*, 2484.
17. van der Geer, E. P. L.; van den Brom, C. R.; Arfaoui, I.; Houssiau, L.; Rudolf, P.; van Koten, G.; Klein Gebbink, R. J. M.; Hessen, B., *J. Phys. Chem. C* **2008**, *112*, 17225.
18. Weigel, J. A.; Holm, R. H., *J. Am. Chem. Soc.* **1991**, *113*, 4184.
19. Zhou, C.; Holm, R. H., *Inorg. Chem.* **1997**, *36*, 4066.
20. Lorkovic, I. M.; Ford, P. C., *Inorg. Chem.* **2000**, *39*, 632.
21. Pangborn, A. B.; Giardello, M. A.; Grubbs, R. H.; Rosen, R. K.; Timmers, F. J., *Organometallics* **1996**, *15*, 1518.
22. Christou, G.; Garner, C. D., *J. Chem. Soc., Dalton Trans.* **1979**, 1093.
23. Kent, T. A. *WMOSS v. 2.5: Mössbauer Spectral Analysis Software*, WEB Research Co., WEB Research Co.: Minneapolis, MN, 1998.
24. APEX2 v2009 *APEX2 v2009*, Bruker AXS: Madison, WI, 2009.
25. Sheldrick, G. M. *SADABS: Area-Detector Absorption Correction*, University of Göttingen: Göttingen, Germany, 2008.
26. Sheldrick, G., *Acta Crystallogr., Sect. A: Found. Crystallogr.* **2008**, *64*, 112.
27. Sheldrick, G. M. *SHELXTL97: Program for Refinement of Crystal Structures*, University of Göttingen: Göttingen, Germany, 1997.
28. Dolomanov, O. V.; Bourhis, L. J.; Gildea, R. J.; Howard, J. A. K.; Puschmann, H., *J. Appl. Crystallogr.* **2009**, *42*, 339.

29. Bolton, R.; Sandall, J. P. B., *Journal of the Chemical Society, Perkin Transactions 2* **1978**, 137.
30. Hardy, A. D. U.; Macnicol, D. D.; Wilson, D. R., *Journal of the Chemical Society, Perkin Transactions 2* **1979**, 1011.
31. Pollak, J.; Meissner, F. v., *Monatsh. Chem.* **1928**, 50, 237.
32. Pollak, J.; Rudich, Z., *Monatsh. Chem.* **1922**, 43, 209
33. Morgenstern, J.; Mayer, R., *Z. Chem.* **1968**, 8, 106.
34. Tard, C. CHEMISTRY RELATED TO THE [Fe]-HYDROGENASES. University of East Anglia, Norwich, 2005.
35. Walsdorff, C.; Saak, W.; Pohl, S., *J. Chem. Soc., Dalton Trans.* **1997**, 1857.
36. Rao, P. V.; Holm, R. H., *Chem. Rev.* **2004**, 104, 527.
37. Chu, C. T.-W.; Lo, F. Y.-K. W.; Dahl, L. F., *J. Am. Chem. Soc.* **1982**, 104, 3409.
38. Sedney, D.; Reiff, W. M., *Inorg. Chim. Acta* **1979**, 34, 231.
39. Sarte, B.; Stanford, J.; LaPrice, W. J.; Uhrich, D. L.; Lockhart, T. E.; Gelerinter, E.; Duffy, N. V., *Inorg. Chem.* **1978**, 17, 3361.
40. D'Addario, S.; Demartin, F.; Grossi, L.; Iapalucci, M. C.; Laschi, F.; Longoni, G.; Zanello, P., *Inorg. Chem.* **1993**, 32, 1153.
41. Chu, C. T. W.; Dahl, L. F., *Inorg. Chem.* **1977**, 16, 3245.
42. Butler, A. R.; Glidewell, C.; Li, M., *Adv. Inorg. Chem.* **1988**, 32, 335.
43. Hopmann, K. H.; Ghosh, A.; Noodleman, L., *Inorg. Chem.* **2009**, 48, 9155.
44. Duan, X.; Yang, J.; Ren, B.; Tan, G.; Ding, H., *Biochem. J.* **2009**, 417, 783.
45. Tonzetich, Z. J.; McQuade, L. E.; Lippard, S. J., *Inorg. Chem.* **2010**, 49, 6338.
46. Kalyvas, H.; Coucouvanis, D., *Inorg. Chem.* **2006**, 45, 8462.

# **APPENDIX A: M(BIPhMe) COMPLEXES AND THEIR REACTIONS WITH RNOS**

## A.1 Introduction

While exploring starting materials using the BIPhMe ligand, new iron, copper, and zinc complexes were prepared. Some reactivity with nitrogen oxide species was explored for these new complexes, but no studies were performed.

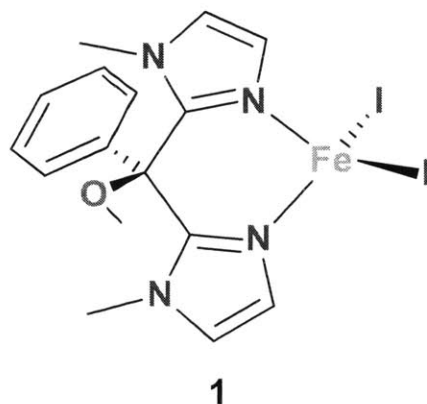
## A.2 Experimental Methods

**General.** All manipulations were performed under an atmosphere of nitrogen gas using standard Schlenk techniques or in an MBraun glovebox under an atmosphere of purified nitrogen. NO (Airgas, 99%) was purified by a literature procedure.<sup>1</sup> The NO gas stream was passed through an Ascarite column (NaOH fused on silica gel) and a 6 ft. coil filled with silica gel that was cooled to  $-78\text{ }^{\circ}\text{C}$  using a dry ice/acetone bath. Nitric oxide was stored using standard gas storage bulbs and transferred by gastight syringes. Diethyl ether, pentane, methylene chloride, and acetonitrile were purified using a Glass Contour solvent system.<sup>2</sup> Deuterated solvents were purchased from Cambridge Isotope Labs.  $[\text{Fe}(\text{BIPhMe})\text{Cl}_2]$  was prepared as described in chapter 2. (PPN)(SNO) and (PPN)(SSNO) were prepared as described in chapter 3. All organic chemicals were purchased from Sigma-Aldrich and used as received. Metal salts were purchased from Strem Chemicals and used as received.

**Physical Measurements.** NMR spectra were recorded on a Bruker Avance spectrometer operating at 400 MHz at ambient temperature and referenced to residual signals in the deuterated solvent. Low-resolution ESI mass spectra were obtained with an Agilent 1100 Series LC/MSD mass spectrometer using degassed acetonitrile as the carrier solvent. FTIR spectra were recorded on a Thermo Nicolet Avatar 360 spectrometer running the *OMNIC* software package; solid samples were pressed into KBr disks and solution samples were prepared in an air-tight Graseby-Specac solution cell with  $\text{CaF}_2$  windows and 0.1 mm spacers.

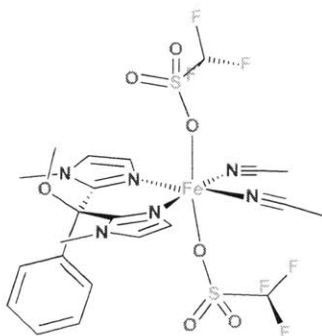
**Mössbauer Measurements.** Samples for  $^{57}\text{Fe}$  Mössbauer studies were prepared by grinding a solid sample with Apiezon-N grease. These  $^{57}\text{Fe}$  Mössbauer samples were placed in an 80 K cryostat during measurement. A  $^{57}\text{Co/Rh}$  source was moved at a constant acceleration at room temperature against the absorber sample. All isomer shift ( $\delta$ ) and quadrupole splitting ( $\Delta E_Q$ ) values are reported with respect to  $^{57}\text{Fe}$ -enriched metallic iron foil that was used for velocity calibration. The displayed spectrum was folded to enhance the signal-to-noise ratio. Fits of the data were calculated by the *WMOSS* plot-and-fit program, version 2.5.<sup>3</sup>

**X-ray Data Collection, and Structure and Solution Refinement.** Crystals of suitable for X-ray diffraction were mounted in Paratone N oil and frozen under a nitrogen cold stream maintained at 100 K by a KRYO-FLEX low-temperature apparatus. Data were collected on a Bruker APEX CCD X-ray diffractometer with Mo  $K\alpha$  radiation ( $\lambda = 0.71073 \text{ \AA}$ ) controlled by the *APEX2* software package.<sup>4</sup> Empirical absorption corrections were calculated with *SADABS*.<sup>5</sup> The structures were solved by direct methods with refinement by full-matrix least-squares based on  $F^2$  using *SHELXTL-97*.<sup>6-8</sup> All non-hydrogen atoms were located and refined anisotropically. Hydrogen atoms were assigned to idealized positions and given thermal parameters equal to either 1.5 (methyl hydrogen atoms) or 1.2 (non-methyl hydrogen atoms) times the thermal parameters of the atoms to which they were attached. Figures were generated using the *Olex2.1* Graphical User Interface.<sup>9</sup> See Tables A.1 – A.4 below for crystallographic data and refinement details, and geometrical parameters.



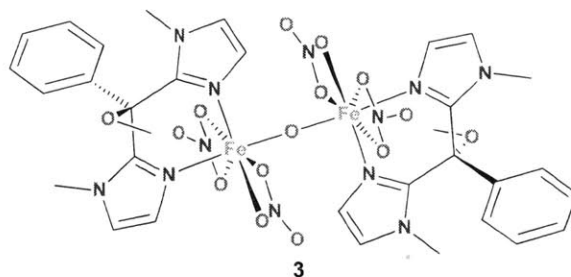
**Fe(BIPhMe)I<sub>2</sub>, 1.** A 50 mL Erlenmeyer flask was charged with FeI<sub>2</sub> (290 mg, 0.937 mmol) and BIPhMe (261 mg, 0.922 mmol). Tetrahydrofuran (20 mL) and acetonitrile (10 mL) were added to the flask and the solution was stirred for 30 min. The solvent was evaporated in vacuo and the remaining brown solid was redissolved in methylene chloride (4 mL), then filtered through a glass filter paper in a Pasteur pipette. The crystals were collected by filtration and washed with diethyl ether (3x 10 mL) to afford 220.9 mg (0.373 mmol, 44%) of **1**. X-ray quality crystals of **1** were grown by vapor diffusion of diethyl ether into the methylene chloride solution. Anal. Calc'd for C<sub>16</sub>H<sub>18</sub>FeI<sub>2</sub>N<sub>4</sub>O: C, 32.46; H, 3.06; N, 9.46. Found: C, 32.60; H, 2.69; N, 9.32. ESI-MS (MeCN, m/z): 747.1 (calc'd [M+BIPhMe-I]<sup>+</sup>: 747.1), 465.0 (calc'd [M-I]<sup>+</sup>: 465.0), 339.1 (calc'd [M+H-I<sub>2</sub>]<sup>+</sup>: 339.1), 283.1 (calc'd [BIPhMe+H]<sup>+</sup>: 283.2), 251.1 (calc'd [BIPhMe-OMe]<sup>+</sup>: 251.1). <sup>1</sup>H NMR (400 MHz, CDCl<sub>3</sub>, ppm): 10.88 (s), 11.55 (s), 12.00(br), 12.99 (s), 20.37 (br), 29.06 (br), 32.83 (br). FTIR (KBr, cm<sup>-1</sup>): 3148 (w), 3108 (m), 3057 (w), 2933 (w), 2956 (w), 2924 (w), 2829 (w), 1977 (w), 1921 (w), 1839 (w), 1787 (w), 1636 (w), 1608 (w), 1540 (m), 1496 (s), 1467 (m), 1448 (s), 1399 (w), 1350 (w), 1324 (w), 1282 (s), 1255 (w), 1210 (w), 1171 (m), 1153 (m), 1138 (m), 1089 (m), 1072 (s), 984 (s), 897 (s), 762 (s), 723 (s), 701 (m), 645 (m), 628 (w), 664 (w), 511 (w), 467 (w). <sup>57</sup>Mössbauer (mm/s) (80 K, δ mm/s, ΔE<sub>Q</sub> mm/s, Γ mm/s): 0.872(2), 3.100(2), 0.308(2).



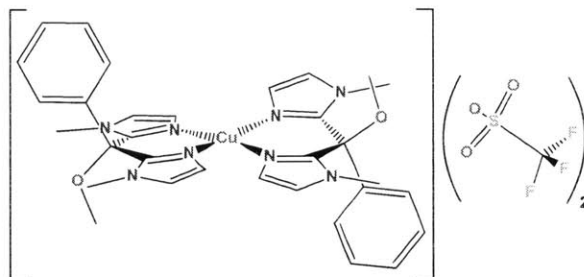


**2**

**Fe(BIPhMe)(MeCN)<sub>2</sub>(OTf)<sub>2</sub>, 2.** In a 20 mL vial Fe(MeCN)<sub>2</sub>(OTf)<sub>2</sub> (160 mg, 0.367 mmol) was dissolved in acetonitrile (6 mL) and solution of BIPhMe (108 mg, 0.381 mmol) in methylene chloride (4 mL) was added drop wise over the course of a minute. The solution was stirred overnight, the solvent evaporated in vacuo, and redissolved in acetonitrile (0.5 mL) to afford a colorless solution. This solution was filtered through glass filter paper in a Pasteur pipette. X-ray quality crystals of **2** were grown by vapor diffusion of diethyl ether into the product solution over the course of 7 days to afford colorless crystals. The product was collected and washed with diethyl ether (3 x 10 mL) to afford 191.5 mg (0.266 mmol, 75%) of **2**. Anal. Calc'd for Fe(BIPhMe)(OTf)<sub>2</sub>·(CH<sub>3</sub>CN)<sub>1.5</sub>·CH<sub>2</sub>Cl<sub>2</sub>: C, 33.75; H, 3.15; N, 9.84. Found: C, 33.70; H, 3.34; N, 9.71. ESI-MS (MeCN, m/z): 487.0 (calc'd [M-OTf-2MeCN]<sup>+</sup>: 487.0), 283.1 [calc'd [BIPhMe+H]<sup>+</sup>: 283.2), 251.1 (calc'd [BIPhMe-OMe]<sup>+</sup>: 251.1), 148.7 (calc'd [OTf]<sup>-</sup>: 149.0). <sup>1</sup>H NMR (400 MHz, CD<sub>3</sub>CN, ppm): 10.38 (s), 11.78 (s), 20.82 (s), 22.47 (s), 24.97 (s). <sup>19</sup>F{<sup>1</sup>H} NMR (376 MHz, CD<sub>3</sub>CN, ppm): -64.54 (s). FTIR (KBr, cm<sup>-1</sup>): 3141 (w), 3058 (w), 2997 (w), 2939 (w), 2837 (w), 2313 (ν(CN), m), 2284 (ν(CN), m), 1546 (w), 1503 (m), 1473 (w), 1450 (m), 1404 (w), 1308 (ν(SO<sub>3</sub>, asym), s), 1226 (s), 1217 (s), 1172 (ν(CF<sub>3</sub>), s), 1091 (w), 1072 (w), 1035 (ν(SO<sub>3</sub>, sym), s), 991 (m), 956 (w), 936 (w), 900 (s), 761 (s), 725 (m), 690 (m), 637 (s), 583 (w), 512 (m), 469 (w). <sup>57</sup>Mössbauer (mm/s) (80 K, δ mm/s, ΔE<sub>Q</sub> mm/s, Γ mm/s): 1.256(2), 4.344(2), 0.291(2).

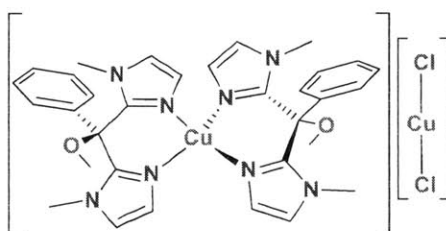


**[Fe(BIPhMe)(NO<sub>3</sub>)<sub>2</sub>]<sub>2</sub>O, 3.** This procedure was performed under aerobic and ambient moisture conditions. A 100 mL round bottom flask was charged with Fe(NO<sub>3</sub>)<sub>3</sub>·9H<sub>2</sub>O (600 mg, 1.487 mmol) and BIPhMe (421.1 mg, 1.487 mmol). The solid mixture was dissolved in tetrahydrofuran (30 mL) and stirred for 1 h. Over the course of the reaction a brown precipitate formed. The solvent was evaporated from the slurry and the product was extracted with methylene chloride (10 mL). X-ray quality crystals were grown by vapor diffusion of diethyl ether into the methylene chloride solution. The product was collected and washed with diethyl ether (3 x 20 mL) to afford 231 mg (0.416 mmol, 28 %) of **3**. FTIR (KBr, cm<sup>-1</sup>): 3139 (m), 3063 (w), 2957 (w), 2933 (w), 2834 (w), 2525 (w), 2293 (w), 1776 (w), 1723 (w), 1500 (s), 1448 (m), 1407 (w), 1381 (w), 1353 (w), 1296 (s), 1278 (s), 1186 (w), 1162 (w), 1162 (w), 1141 (m), 1089 (w), 1070 (m), 1028 (m), 989 (m), 957 (w), 900 (m), 861 (m), 806 (w), 758 (m), 723 (m), 703 (m), 643 (m), 557 (w), 508 (w), 470 (w). UV-Vis (MeCN, nm, M<sup>-1</sup>·cm<sup>-1</sup>): 268 (15270 ± 700), 310 (10790 ± 700), 365 (8450 ± 800). <sup>57</sup>Mössbauer (mm/s) (80 K, δ mm/s, ΔE<sub>Q</sub> mm/s, Γ mm/s): 0.562(2), 2.408(2), 0.284(2).



4

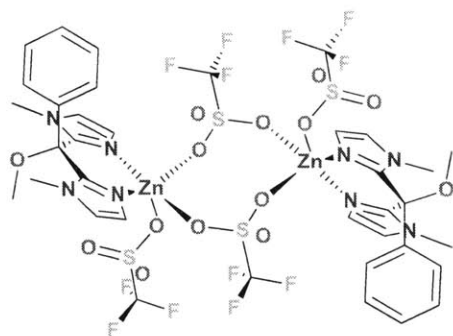
**[Cu(BIPhMe)<sub>2</sub>](OTf)<sub>2</sub>, 4.** To a 20 mL vial Cu(OTf)<sub>2</sub> (183.1 mg, 0.5062 mmol) and BIPhMe (297.7 mg, 1.051 mmol) was added. The mixture was dissolved in tetrahydrofuran (6 mL) and stirred for 1 h resulting in a green solution. To the solution diethyl ether (14 mL) was added, resulting in a green precipitate. The green precipitate was filtered on an F-grade frit, washed with pentanes (3 x 10 mL), and dried under vacuum for 6 hours, affording 320.7 mg (0.3456 mmol, 68 %) of **4**. X-ray quality crystals of **4** were grown by vapor diffusion of diethyl ether into a methylene chloride solution. Anal. Calc'd for C<sub>34</sub>H<sub>36</sub>F<sub>6</sub>CuN<sub>8</sub>O<sub>7</sub>S<sub>2</sub>: C, 44.08; H, 3.92; N, 12.10. Found: C, 43.76; H, 3.61; N, 11.88. ESI-MS (MeCN, m/z): 627.3 (calc'd [M-2OTf]<sup>+</sup>: 627.2), 776.2 (calc'd [M-OTf]<sup>+</sup>: 776.2), 148.7 (calc'd [OTf]<sup>-</sup>: 149.0). FTIR (KBr, cm<sup>-1</sup>): 3162 (w), 3130 (m), 3079 (w), 2972 (m), 2937 (w), 2889 (w), 2834 (w), 1638 (w), 1550 (m), 1505 (s), 1449 (s), 1408 (w), 1354 (w), 1259(v(SO<sub>3</sub>, asym), s), 1224(s), 1149 (v(CF<sub>3</sub>), s), 1090 (w), 1071 (s), 1030 (v(SO<sub>3</sub>, symm), s), 992 (s), 938 (w), 900 (s), 762 (s), 724 (s), 704 (s), 637 (s), 572 (m), 517 (m), 472 (w).



5

**[Cu(BIPhMe)<sub>2</sub>][CuCl<sub>2</sub>], 5.** To a 20 mL vial CuCl (42.5 mg, 0.430 mmol) and BIPhMe (121.0 mg, 0.427 mmol) was added. The mixture was dissolved in a mixture of methylene chloride (6

mL) and acetonitrile (0.5 mL), and stirred for an hour resulting in a turbid pale yellow solution. The solvent was evaporated *in vacuo* and the remaining pale yellow-green solid was dissolved in methylene chloride (1 mL). The pale yellow solution was filtered through glass filter paper in a Pasteur pipette. X-ray quality crystals were grown by vapor diffusion of diethyl ether into the methylene chloride solution. The pale yellow-green crystals were collected by filtration and washed with diethyl ether (3 x 5 mL) to afford 106.6 mg (0.230 mmol, 65 %) of **5**. Anal. Calcd for  $[\text{Cu}(\text{BIPhMe})_2][\text{CuCl}_2] \cdot (\text{CH}_2\text{Cl}_2)_{0.25}$ : C, 49.41; H, 4.69; N, 14.28. Found: C, 49.09; H, 4.71; N, 13.91.  $^1\text{H}$  NMR (400 MHz,  $\text{CDCl}_3$ , ppm): 3.15 (s), 4.03 (br), 7.28 (s), 7.33 (s), 7.52 (s). FTIR (KBr,  $\text{cm}^{-1}$ ): 3158 (w), 3140 (m), 3115 (m), 3067 (w), 3011 (w), 2952 (w), 2833 (w), 1692 (w), 1635 (w), 1603 (w), 1543 (w), 1501 (s), 1471 (m), 1449 (s), 1400 (m), 1349 (w), 1323 (w), 1385 (m), 1225 (w), 1211 (w), 1175 (m), 1152 (m), 1090 (m), 1071 (s), 992 (s), 941 (w), 898 (s), 847 (w), 759 (s), 723 (s), 703 (s), 688 (w), 645 (m), 628 (w), 558 (w), 512 (w), 465 (w).



**6**

**[Zn(BIPhMe)(OTf)( $\mu$ -OTf)]<sub>2</sub>, 6.** To a 125 mL Erlenmeyer flask  $\text{Zn}(\text{OTf})_2$  (362.5 mg, 0.997 mmol) and BIPhMe (284.2 mg, 1.007 mmol) was added. The mixture was dissolved in a mixture of tetrahydrofuran (6 mL) and methylene chloride (12 mL), and stirred for 2 days. The product was precipitated by addition of pentanes (100 mL) and collected by vacuum filtration to yield 330.7 mg (0.512 mmol, 51 %) of a white powder. X-ray quality crystals of **6** were grown by vapor diffusion of diethyl ether into a methylene chloride solution. Anal. Calcd for

$C_{36}H_{36}F_{12}N_8O_{14}S_4Zn_2$ : C, 33.47; H, 2.81; N, 8.67. Found: C, 33.44; H, 2.73; N, 8.45.  $^1H$  NMR (400 MHz,  $CDCl_3$ , ppm): 3.32 (s, 3H), 3.62 (s, 6H), 7.31–7.80 (m, 5H), 7.50 (d,  $J = 7.43$  Hz, 2H), 7.59 (d,  $J = 7.19$  Hz, 2H).  $^{19}F\{^1H\}$  NMR (376 MHz,  $CDCl_3$ , ppm): -77.72 (s). FTIR (KBr,  $cm^{-1}$ ): 3148 (m), 3134 (m), 3058 (w), 2951 (w), 2835 (w), 1632 (w), 1548 (w), 1507 (m), 1476 (w), 1450 (m), 1328 ( $\nu(SO_3, asymm)$ , s), 1312 ( $\nu(SO_3, asymm)$ , s), 1285 (s), 1259 (s), 1236 (s), 1207 (s), 1183 ( $\nu(CF_3)$ , s), 1167 ( $\nu(CF_3)$ , s), 1092 (m), 1074 (m), 1030 ( $\nu(SO_3, symm)$ , s), 994 (m), 943 (w), 901 (m), 768 (s), 727 (s), 704 (s), 638 (s), 590 (w), 573 (m), 515 (m), 469 (m).

**Reaction of  $[Zn(BIPhMe)(OTf)(\mu-OTf)]_2$  and  $(PPN)(SSNO)$ .** In a 20 mL vial,  $[Fe(BIPhMe)Cl_2]$  (24.3 mg, 59.4  $\mu mol$ ) was dissolved in acetonitrile (2 mL), resulting in a colorless solution. In a 5 mL vial, **6** (36.4 mg, 55.0  $\mu mol$ ) was dissolved in acetonitrile (2 mL), resulting in a colorless solution, and a stir bar was added. The 5 mL vial was placed into the 20 mL vial.  $(PPN)(SSNO)$  (37.1 mg, 58.6  $\mu mol$ ) was added to the Zn-containing solution and the reaction system was capped with a septum. The Zn-SSNO-containing solution turned from colorless to black to orange to colorless within 2 min. The solution of  $[Fe(BIPhMe)Cl_2]$  turned green indicating the release of  $NO(g)$ . The Zn-containing solution was poured into pentanes (100 mL) and resulted in the formation of a colorless precipitate.

**Reaction of  $[Zn(BIPhMe)(OTf)(\mu-OTf)]_2$  and  $(PPN)(SNO)$ .** In a 20 mL vial,  $[Fe(BIPhMe)Cl_2]$  (23.1 mg, 56.5  $\mu mol$ ) was dissolved in acetonitrile (2 mL), resulting in a colorless solution. In a 5 mL vial, **6** (39.8 mg, 60.1  $\mu mol$ ) was dissolved in acetonitrile (2 mL), resulting in a colorless solution, and a stir bar was added. The 5 mL vial was placed into the 20 mL vial.  $(PPN)(SNO)$  (39.0 mg, 64.9  $\mu mol$ ) was added to the Zn-containing solution and the reaction system was capped with a septum. The Zn-SNO-containing solution turned from colorless to dark green to orange to colorless within 2 min. The solution of  $[Fe(BIPhMe)Cl_2]$

turned green indicating the release of NO(g). The Zn-containing solution was poured into pentanes (100 mL) and resulted in the formation of a colorless precipitate.

### A.3 Results and Discussion

**Synthesis and spectroscopic characterization of M(BIPhMe) complexes.** The brown-purple compound Fe(BIPhMe)I<sub>2</sub>, **1**, is prepared by dissolving FeI<sub>2</sub> and BIPhMe in a mixture of tetrahydrofuran and acetonitrile. The complex is purified by stripping the reaction solvent, redissolving the product in methylene chloride, and layering with diethyl ether. This method yields brown-purple block crystals of **1** that can be further studied. The <sup>1</sup>H NMR spectrum of **1** is paramagnetically shifted similar to the related complexes having Cl<sup>-</sup> and Br<sup>-</sup> ligands (Figure A.1).

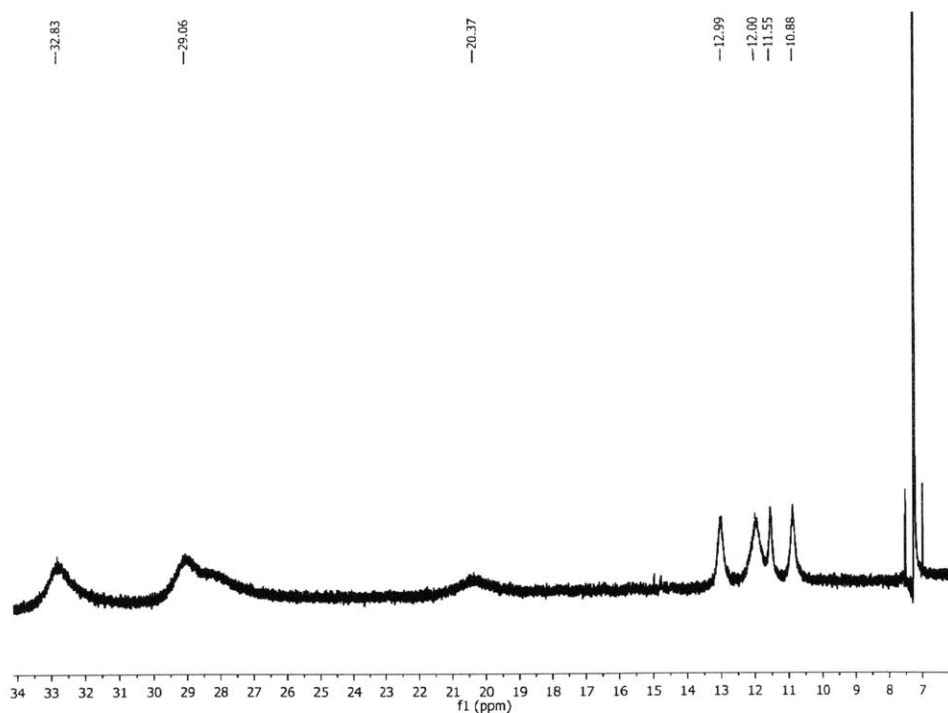


**Figure A.1.** <sup>1</sup>H NMR spectrum of **1** in CDCl<sub>3</sub> at 400 MHz.

Preparation of Fe(BIPhMe)(MeCN)<sub>2</sub>(OTf)<sub>2</sub>, **2**, is achieved by mixing Fe(OTf)<sub>2</sub>(MeCN)<sub>2</sub> and BIPhMe in acetonitrile. To obtain crystals of **2** we allowed diethyl ether to vapor diffuse into

the crude reaction solution, providing us with block crystals of **2** after two days. These crystals do not maintain their crystallinity overtime but slowly turn into a powder, suggesting that loss of acetonitrile may be occurring. The nitrile stretches of the bound acetonitrile molecules occur at  $2284\text{ cm}^{-1}$  and  $2313\text{ cm}^{-1}$ , indicating that the two acetonitriles are not equivalent (Figure A.2). The vibrational stretches at  $1308\text{ cm}^{-1}$  and  $1035\text{ cm}^{-1}$  are assigned as the asymmetric and symmetric stretches of the  $\text{SO}_3$  fragment, respectively. The band at  $1172\text{ cm}^{-1}$  is assigned as the symmetric  $\text{CF}_3$  vibrational mode. These assignments match literature values.<sup>10</sup>

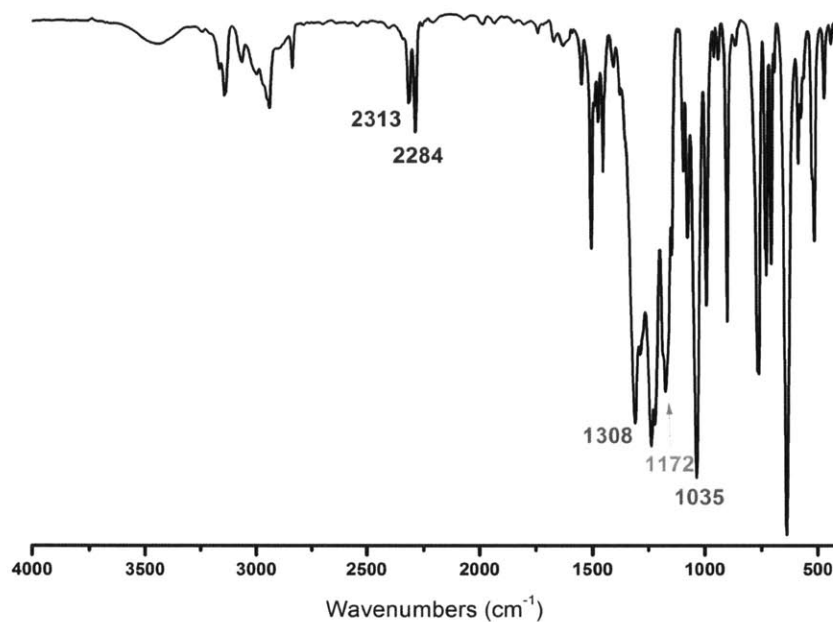


**Figure A.2.** FTIR of **2** collected as a KBr pellet. Nitrile stretches are indicated in blue.  $\text{SO}_3$  stretches are indicated in yellow. A  $\text{CF}_3$  stretch is indicated in green.

The  $^1\text{H}$  NMR spectrum of **2** (Figure A.3) has only five peaks that are downfield of the peaks of BIPhMe. The lack of the additional peaks is suspected to be due to the broadening of the peaks corresponding to the protons of the imidazole rings. The lack of peaks for the bound acetonitrile protons suggests that either the species is not six-coordinate in solution or the resonances were replaced by deuterium-labeled acetonitrile molecules to form

Fe(BIPhMe)(CD<sub>3</sub>CN)<sub>2</sub>(OTf)<sub>2</sub>. The <sup>19</sup>F{<sup>1</sup>H} NMR spectrum of **2** (Figure A.4) contains a single peak at -64.54 ppm which is down-field of the published value of -78.2 ppm.<sup>11</sup>

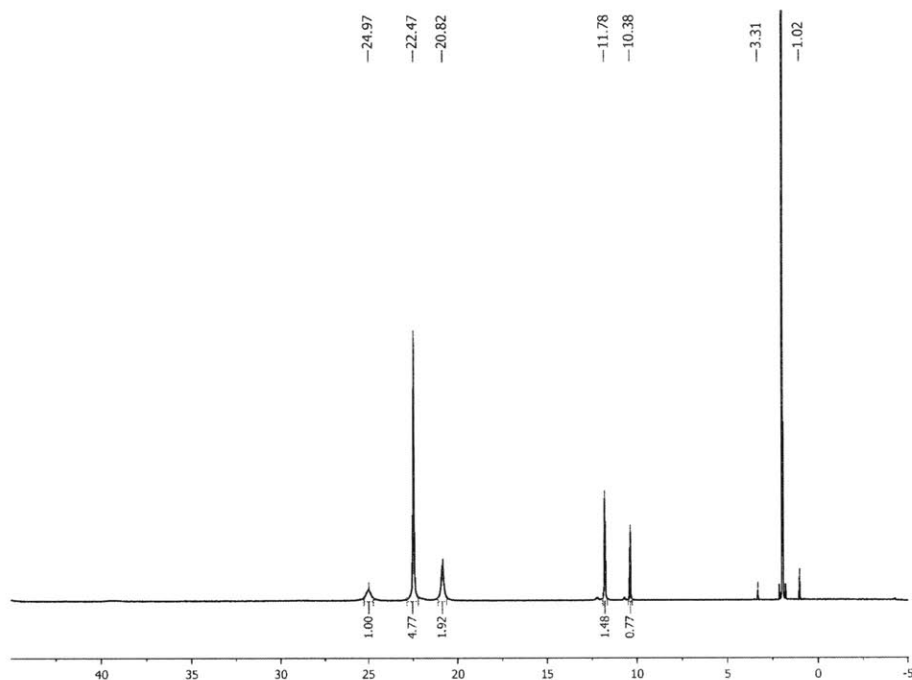


**Figure A.3.** <sup>1</sup>H NMR spectrum of **2** in CD<sub>3</sub>CN at 400 MHz.

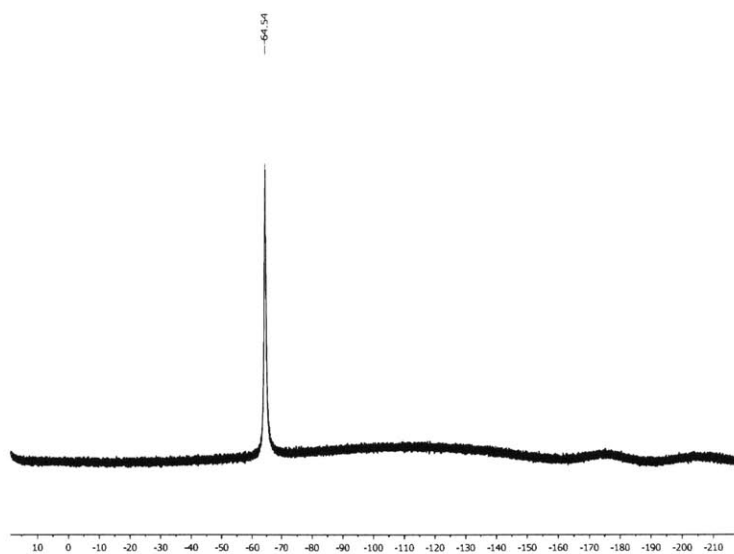


**Figure A.4.** <sup>19</sup>F{<sup>1</sup>H} NMR spectrum of **2** in CD<sub>3</sub>CN at 376 MHz.

The hept coordinate diiron compound [Fe(BIPhMe)(NO<sub>3</sub>)<sub>2</sub>]<sub>2</sub>O, **3**, is prepared by stirring a solution of Fe(NO<sub>3</sub>)<sub>3</sub>·9H<sub>2</sub>O and BIPhMe in tetrahydrofuran at ambient conditions. Loss of a



nitrate occurs by hydrolysis from adventitious water in the tetrahydrofuran to form nitric acid and the oxo-bridge between the irons. During the reaction an insoluble, brown solid is formed that is presumed to be an iron oxide hydroxide species. The intended product is separated from the side products by stripping the reaction mixture and then redissolving the product in methylene chloride. This methylene chloride solution can then be layered with diethyl ether to form crystals of **3**.

Copper binds two BIPhMe ligands. The preparation of  $[\text{Cu}(\text{BIPhMe})_2](\text{OTf})_2$ , **4**, is performed by adding two equivalents of BIPhMe to a solution of  $\text{Cu}(\text{OTf})_2$  in tetrahydrofuran, and forming a green solution. Adding a 2-fold excess of diethyl ether to the solution precipitates out **4**. Filtration, washing with pentanes, and drying under vacuum affords analytically pure **4**.

The Cu(I) complex  $[\text{Cu}(\text{BIPhMe})_2][\text{CuCl}_2]$ , **5**, is afforded by combining molar equivalents of CuCl and BIPhMe in a methylene chloride/acetonitrile mixture. The solvent is then stripped, leaving a yellow-green solid. This solid is dissolved in a minimal amount of methylene chloride and layered with diethyl ether to grow crystals of **5**.

The  $\text{Zn}(\text{OTf})_2$  binds an equivalent of BIPhMe to form a colorless solid. Crystallization of the product results in a triflate-bridged dizinc complex, but the  $^1\text{H}$  NMR spectrum has two full sets of ligand peaks (Figure A.5). These two sets are proposed to reflect an equilibrium between a mononuclear and dinuclear complex at 298 K. The  $^{19}\text{F}\{^1\text{H}\}$  NMR spectrum shows a single peak at -77.72 ppm, which is similar to the published value of free triflate.

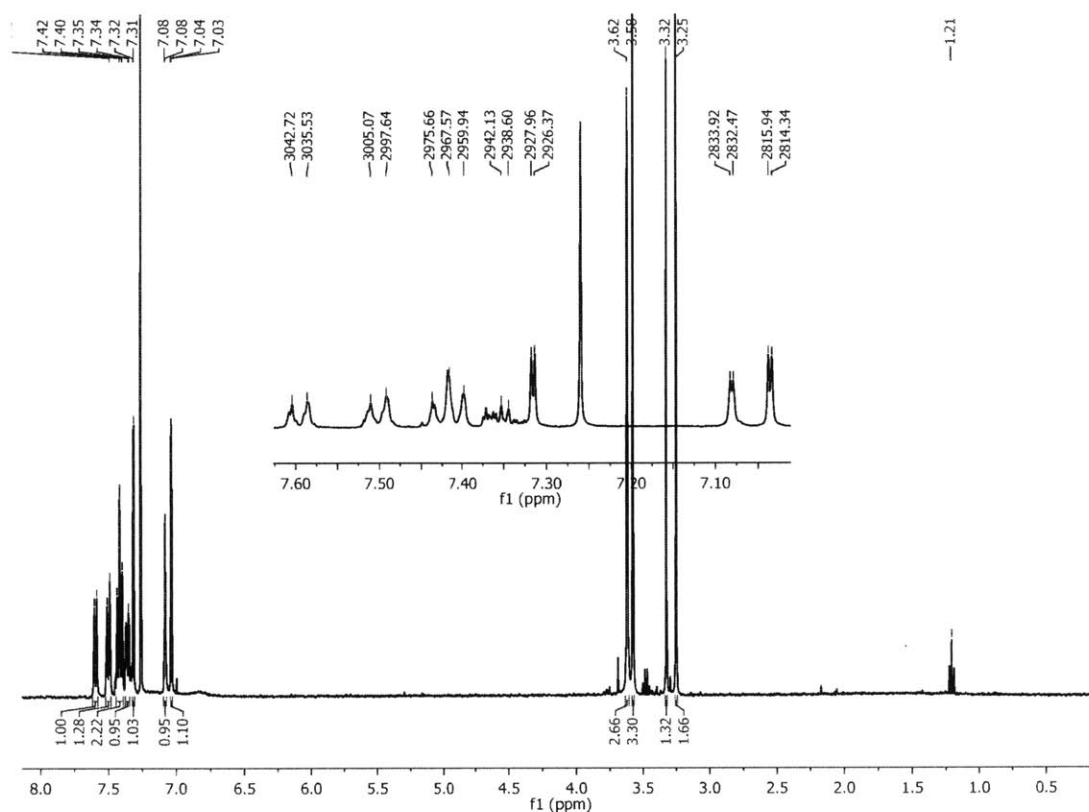


**Figure A.5.** <sup>1</sup>H NMR spectrum of **6** in CDCl<sub>3</sub> at 400 MHz at 298 K.

**Crystallographic characterization of M(BIPhMe) complexes.** Crystals of compound **1** were unstable below 140 K, at which point the crystal cracks and becomes unusable for X-ray diffraction studies. Diffraction spot frames were collected at varying temperatures to determine the lowest temperature that X-ray structural data could be collected (Figure A.6). Full data sets were collected at 296 K and 140 K, both consisting of the pseudo-tetrahedral complex **1**. No co-crystallized solvent or other species were observed at either temperature, suggesting that the cracking of the crystals is probably due to a change in the packing or rearrangement to another crystal system. Changes in bond distances and angles between the two structures are negligible (Table A.1).

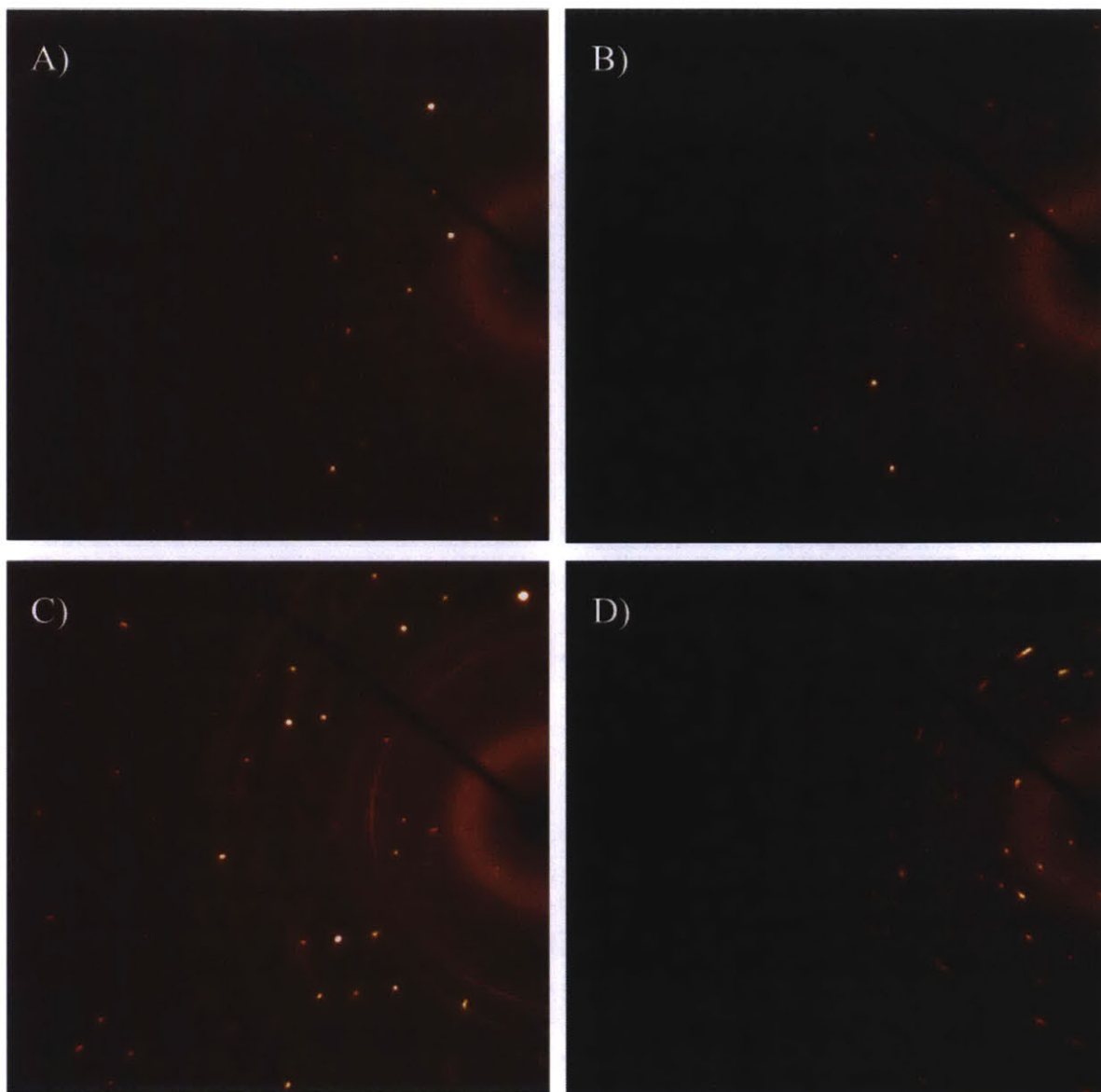


**Figure A.6.** Diffraction spot intensities of a single crystal of **1** at varying temperatures. A) 296 K, B) 250 K, C) 140 K, D) 120 K. The crystal undergoes a phase change in the 120–140 K temperature range resulting in loss of crystallinity.

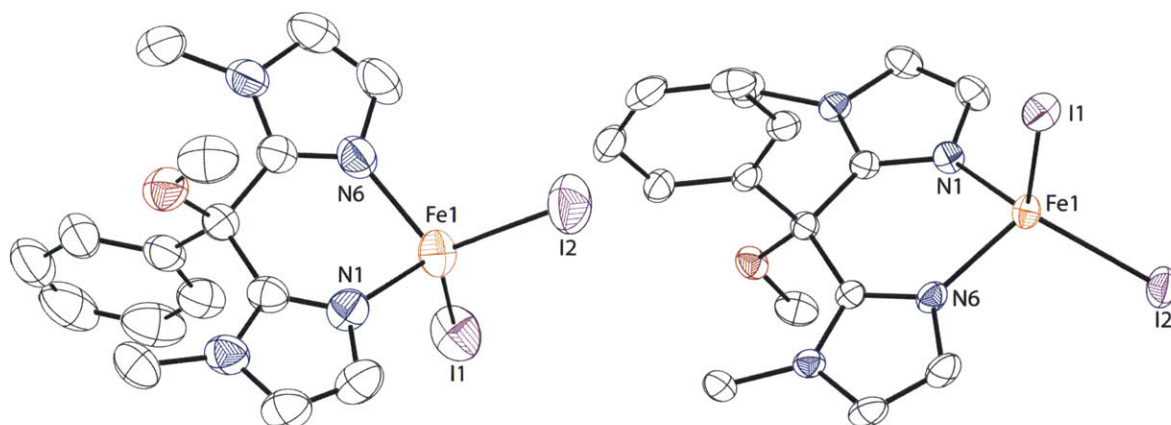


**Figure A.7.** Graphical representation of the X-ray crystal structures of **1** at 298 K (left) and 140 K (right), with ellipsoids shown at 50% probability. Hydrogen atoms are omitted for clarity. Color scheme: iron, orange; iodide, purple; nitrogen, blue; oxygen, red; carbon, colorless.

**Table A.1.** Selected bond distances for M(BIPhMe) complexes.

Complex	M–N, Å	N–M–N, °	M–X, Å	X–M–X, °	N–M–X, °
Fe(BIPhMe)I <sub>2</sub> , <b>1</b> at 140 K	2.0458(16)	8677(6)	2.5749(3)	116.711(12)	109.17(5)
	2.0551(16)		2.6040(3)		109.30(5)
Fe(BIPhMe)I <sub>2</sub> , <b>1</b> at 296 K	2.046(3)	86.82(12)	2.5713(6)	116.34(2)	111.70(5)
	2.055(3)		2.6021(6)		119.26(5)
					109.37(9)
					109.72(8)
					112.11(8)
Fe(BIPhMe)(OTf) <sub>2</sub> (MeCN) <sub>2</sub> , <b>2</b>	2.109(2)	86.21(9)	2.099(2)	171.53(9)	118.79(9)
	2.129(2)	94.63(9)	2.156(2)		91.64(9)
	Acetonitrile:	178.23(10)			94.98(9)
	2.169(3)	92.95(10)			90.66(9)
	2.205(3)	94.63(9)			93.31(9)
		174.49(10)			86.87(10)
		86.35(10)			90.95(10)
[Cu(BIPhMe) <sub>2</sub> (OTf)](OTf), <b>4</b>	1.9622(14)	90.45(5)	2.7074	N/A	81.24(9)
	1.9639(13)	90.60(5)			76.23
	1.9786(13)	93.33(5)			84.34
	1.9808(13)	99.04(5)			80.68
		149.52(6)			125.91
[Cu(BIPhMe) <sub>2</sub> ][CuCl <sub>2</sub> ], <b>5</b>	2.0178(13)	89.98(5)	2.1031(4)	180.0	N/A
	2.0337(13)	106.27(7)			
		109.03(7)			
		134.18(5)			

**Table A.2.** X-ray crystallographic data for **1** at 296 K and 140 K.

compounds	Fe(BIPhMe) <sub>2</sub> , <b>1</b> , 296 K	Fe(BIPhMe) <sub>2</sub> , <b>1</b> , 140 K
formula	C <sub>16</sub> H <sub>18</sub> I <sub>2</sub> FeN <sub>4</sub> O	C <sub>16</sub> H <sub>18</sub> I <sub>2</sub> FeN <sub>4</sub> O
formula weight	591.99	591.99
crystal system	monoclinic	monoclinic
space group	P2 <sub>1</sub> /n	P2 <sub>1</sub> /n
a, Å	10.7545(7)	10.7109(5)
b, Å	15.2080(10)	15.0257(7)
c, Å	13.5729(9)	13.4973(6)
β, deg	106.2520(10)	105.8210(10)
V, Å <sup>3</sup>	2131.6(2)	2089.95(17)
Z	4	4
ρ <sub>calcd</sub> , g/cm <sup>3</sup>	1.845	1.881
μ, mm <sup>-1</sup>	3.614	3.685
θ range, deg	2.06 to 27.54	2.07 to 30.95
completeness to θ, %	100.00	95.0
reflections collected	39731	45226
independent reflections	4915	6310
R(int)	0.0377	0.0242
restraints	0	0
parameters	220	220
Max., min. transmission	0.7456, 0.6359	0.7461, 0.6098
R1(wR2) [I>2σ(I)]	0.0397 (0.0866)	0.0238 (0.0622)
R1(wR2)	0.0602 (0.0926)	0.0291 (0.0636)
GoF(F <sup>2</sup> )	1.362	1.455
max, min peaks, e.Å <sup>-3</sup>	0.973, -0.852	0.968, -0.666

Compound **2** crystallized as a distorted octahedral complex with all N-donors in the equatorial plane and the two triflate anions bound by oxygen at the apical sites (Figure A.8). The coordination environment of this complex is similar to that in the published structure of Fe(OTf)<sub>2</sub>(MeCN)<sub>4</sub>, which is green, whereas these crystals are colorless. The asymmetric unit of the crystal contains two independent molecules with similar coordination and bonding, where one molecule is perpendicular to the other.

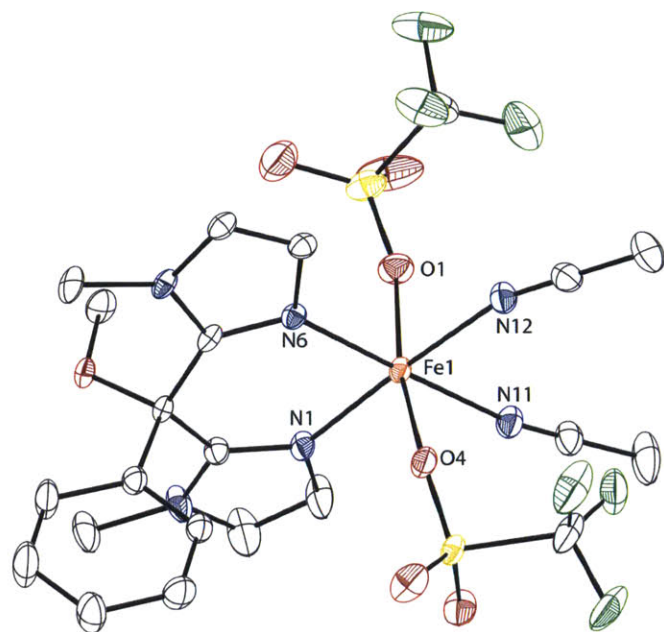


**Figure A.8.** Graphical representation of the X-ray crystal structure of one molecule of **2** from the asymmetric unit with ellipsoids shown at 50% probability. Hydrogen atoms are omitted for clarity. Color scheme: iron, orange; sulfur, yellow; fluorine, green; nitrogen, blue; oxygen, red; carbon, colorless.

**Table A.3.** X-ray crystallographic data for **2** and **3** at 100K.

compounds	Fe(BIPhMe)(OTf) <sub>2</sub> (MeCN) <sub>2</sub> , <b>2</b>	[Fe(BIPhMe)(NO <sub>3</sub> ) <sub>2</sub> ] <sub>2</sub> O, <b>3</b>
formula	C <sub>20</sub> H <sub>24</sub> F <sub>6</sub> FeN <sub>6</sub> O <sub>7</sub> S <sub>2</sub>	C <sub>34</sub> H <sub>40</sub> Cl <sub>4</sub> Fe <sub>2</sub> N <sub>12</sub> O <sub>15</sub>
formula weight	574.75	1110.28
crystal system	triclinic	monoclinic
space group	P $\bar{1}$	P2 <sub>1</sub> /c
a, Å	13.983(2)	19.2099(16)
b, Å	14.426(3)	16.7977(18)
c, Å	17.050(3)	14.919(2)
$\alpha$ , deg	71.015(3)	90
$\beta$ , deg	89.559(3)	109.3520(18)
$\gamma$ , deg	73.622(3)	90
V, Å <sup>3</sup>	3107.0(10)	4542.0(9)
Z	4	8
$\rho_{\text{calcd}}$ , g/cm <sup>3</sup>	1.229	1.624
$\mu$ , mm <sup>-1</sup>	0.705	0.954
$\theta$ range, deg	1.27 to 28.84	1.12 to 27.40
completeness to $\theta$ , %	99.0	99.7
reflections collected	63776	20336
independent reflections	16090	10284
R(int)	0.0402	0.0563
restraints	0	0
parameters	803	613
Max., min. transmission	0.7452, 0.6588	0.7455, 0.6796
R1(wR2) [ $I > 2\sigma(I)$ ]	0.0633 (0.1938)	0.0806 (0.2218)
R1(wR2)	0.0723 (0.1967)	0.0941 (0.2240)
GoF(F <sup>2</sup> )	1.785	2.791
max, min peaks, e.Å <sup>-3</sup>	2.265, -1.005	1.079, -2.064

Compound **3** crystallizes in a monoclinic space group with two molecules in the asymmetric unit. The two irons are seven-coordinate with the oxygen atoms of the two nitrates and a nitrogen of the BIPhMe forming the equatorial plane of a pentagonal bipyramid (Figure A.9). The Fe–O<sub>bridge</sub> bond distance is 1.7781(6) Å with a Fe–O<sub>bridge</sub>–Fe bond angle of 180.00(2)°. The Fe–O<sub>nitrate</sub> bond distances are 2.178(3) Å, 2.194(3) Å, 2.214(3) Å, and 2.249(4) Å. The O<sub>nitrate</sub>–Fe–O<sub>nitrate</sub> bond angles are 58.31(13)° and 58.37(12)° for the intra-nitrate oxygen atoms, and 77.72(12)°, 136.08(13)°, 135.77(12)°, and 165.13(13)° for the inter-nitrate oxygen atoms. The O<sub>bridge</sub>–Fe–O<sub>nitrate</sub> bond angles are 92.10(9)°, 92.51(8)°, 89.87(10)°, and 93.54(9)°. The Fe–N<sub>eq</sub> bond distance is 2.099(4) Å and the Fe–N<sub>ax</sub> distance is 2.112(3) Å. The N–Fe–N bond angle is 84.30(14)°. The N<sub>ax</sub>–Fe–O<sub>bridge</sub> angle is 177.09(10)° and the N<sub>eq</sub>–Fe–O<sub>bridge</sub> angle is 98.60(10)°. These geometrical parameters are very similar to the published values of the crystal structure of [Fe(bpy)(NO<sub>3</sub>)<sub>2</sub>]<sub>2</sub>O.<sup>12</sup>

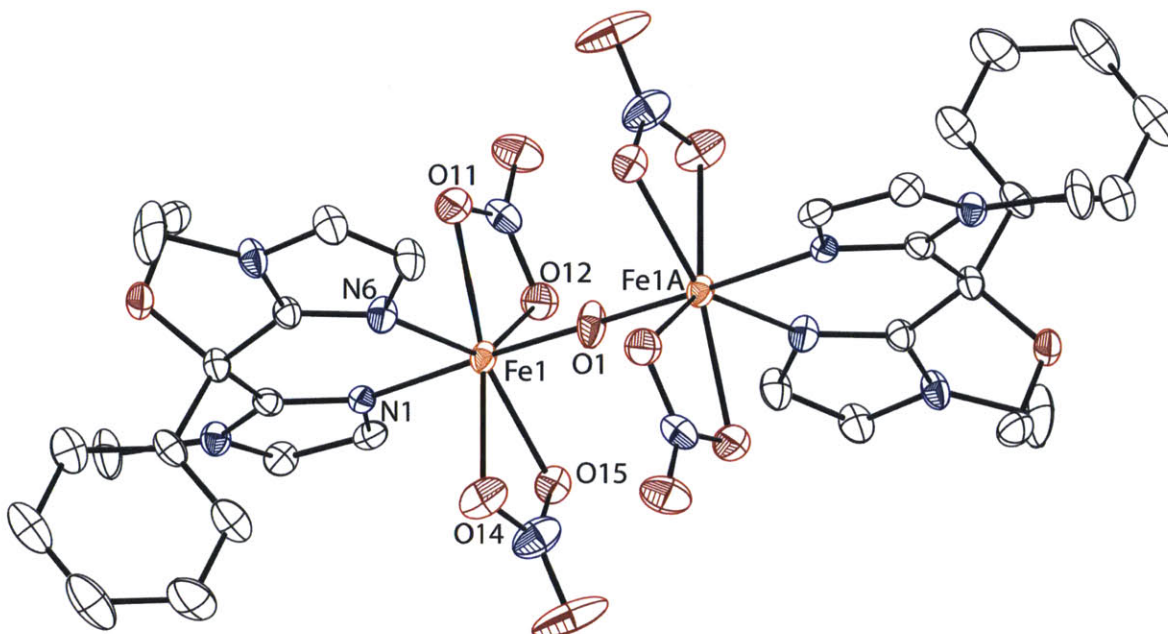


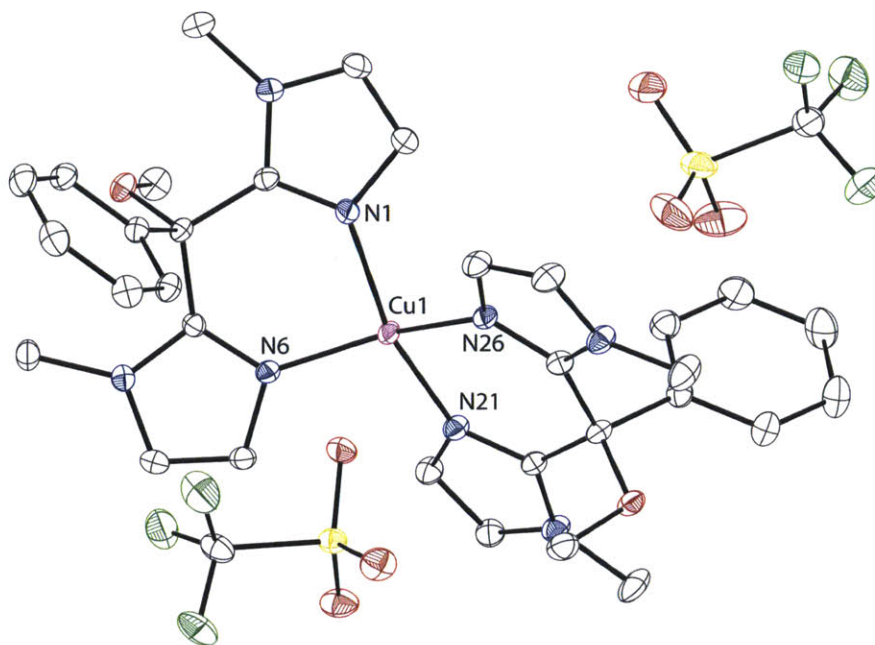
**Figure A.9.** Graphical representation of the X-ray crystal structure of one molecule of **3** from the asymmetric unit with ellipsoids shown at 50% probability. Hydrogen atoms are omitted for clarity. Color scheme: iron, orange; chloride, dark green; nitrogen, blue; oxygen, red; carbon, colorless.

**Table A.4** Selected geometrical parameters of hepta-coordinate,  $\mu$ -oxo diiron complexes.

	[Fe(BIPhMe)(NO <sub>3</sub> ) <sub>2</sub> ] <sub>2</sub> O, <b>3</b>		[Fe(bpy)(NO <sub>3</sub> ) <sub>2</sub> ] <sub>2</sub> O <sup>12</sup>	
<b>bond length, Å</b>				
Fe–O <sub>bridge</sub>	1.7781(6)		1.7755(4)	
Fe–O <sub>nitrate</sub>	2.249(4)	2.214(3)	2.159(2)	2.142(2)
	2.178(3)	2.194(3)	2.262(2)	2.203(2)
Fe–N	2.099(4)	2.112(3)	2.140(2)	2.178(2)
<b>bond angle, °</b>				
O <sub>nitrate</sub> –Fe–O <sub>nitrate</sub>	Intra:	Inter:	Intra:	Inter:
	58.31(13)	77.72(12)	57.97(7)	75.09(7)
	58.37(12)	136.08(13)	59.01(7)	
		135.77(12)		
		165.13(13)		
O <sub>nitrate</sub> –Fe–O <sub>bridge</sub>	92.10(9)	89.87(10)	96.32(5)	98.67(5)
	92.51(8)	93.54(9)	91.19(5)	93.44(6)
N–Fe–N	84.30(14)		75.02(8)	
N–Fe–O <sub>bridge</sub>	98.60(10)	177.09(10)	95.31(6)	169.19(6)
N <sub>eq</sub> –Fe–O <sub>nitrate</sub>	137.00(14)	85.73(14)	79.84(8)	86.92(8)
	142.42(14)	79.45(14)		
N <sub>ax</sub> –Fe–O <sub>nitrate</sub>	85.92(13)	90.08(13)		N/A
	84.99(12)	87.24(13)		
Fe–O–Fe	180.00(2)		180	

Complex **4** has a distorted square pyramidal geometry (Figure A.10). The two BIPhMe ligands are positioned in the equatorial plane with the oxygen atom of the triflate ligand interacting with the copper center at the apical position. The intra N–Cu–N bond angles of the BIPhMe ligands are 90.45(5)° and 90.60(5)°. The N–Cu–N bond angles of the *cis*–nitrogens is 93.33(5)° and 99.04(5)°, and 149.52(6)° and 154.02(6)° between the *trans*–nitrogens. The Cu–N bond distances are 1.9622(14) Å, 1.9639(13) Å, 1.9786(13) Å, and 1.9808(13) Å. The torsion angle between the two ligands is 46.15° out of plane. The apical triflate ligand does not form a perfect 90° angle with the equatorial nitrogen atoms, but is rather 84.34°, 76.23°, 80.68°, and 125.91°. An oxygen atom of the triflate ligands are 2.7074 Å and 2.9318 Å from the copper center, suggesting that they are not directly bound but rather only interacting with the  $d_{z^2}$  orbital of the metal.



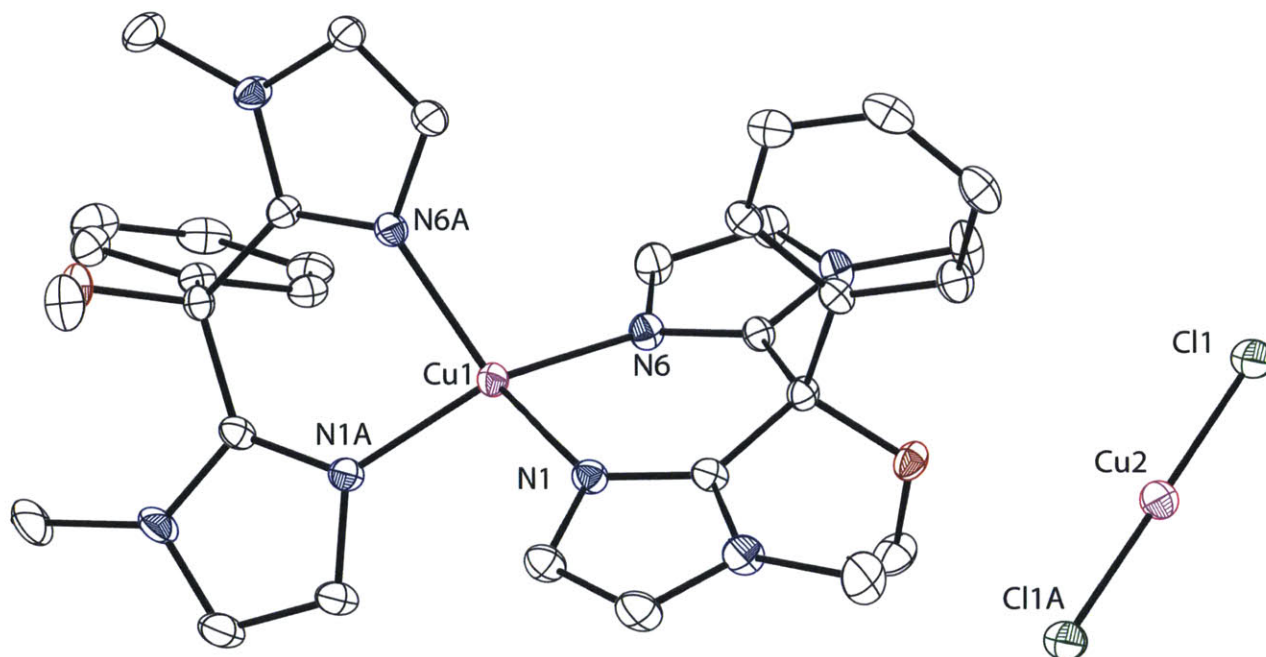


**Figure A.10.** Graphical representation of the X-ray crystal structure of **4** with ellipsoids shown at 50% probability. Hydrogen atoms are omitted for clarity. Color scheme: copper, magenta; sulfur, yellow; fluorine, green; nitrogen, blue; oxygen, red; carbon, colorless.

Complex **5** crystallizes with half a molecule in the asymmetric unit (Figure A.11). Generation of the other half of the molecule results in a linear  $[\text{Cu}^{\text{I}}\text{Cl}_2]^-$  and a pseudo-tetrahedral  $[\text{Cu}^{\text{I}}(\text{BIPhMe})_2]^+$  complex. The BIPhMe complex has an intra N–Cu–N angle of  $89.98(5)^\circ$ . The N–Cu–N angles between the symmetry generated nitrogen atoms are  $106.27(7)^\circ$  and  $109.03(7)^\circ$ , and  $134.18(5)^\circ$  for the *trans*-nitrogen atoms. The torsion angle between the two N–Cu–N planes is  $27.4^\circ$ . The Cu–N bond distances are  $2.0337(13) \text{ \AA}$  and  $2.0178(13) \text{ \AA}$ . The Cu–Cl bond distance is  $2.1031(4) \text{ \AA}$  and the bond angle of the symmetry equivalent chlorides is  $180^\circ$ . The structure does show that the geometry of the  $[\text{Cu}(\text{BIPhMe})_2]^{n+}$  complex changes dramatically from having more square planar character to tetrahedral upon reduction.

**Table A.5.** X-ray crystallographic data for **4**, **5**, and **6** at 100 K.

compounds	[Cu(BIPhMe) <sub>2</sub> ](OTf) <sub>2</sub> , <b>4</b> K	[Cu(BIPhMe) <sub>2</sub> ][CuCl <sub>2</sub> ], <b>5</b> K	[Zn(BIPhMe)(OTf)(μ-OTf)] <sub>2</sub> , <b>6</b>
formula	C <sub>34</sub> H <sub>36</sub> CuF <sub>6</sub> N <sub>8</sub> O <sub>8</sub> S <sub>2</sub>	C <sub>32</sub> H <sub>28</sub> Cl <sub>2</sub> Cu <sub>2</sub> N <sub>8</sub> O <sub>2</sub>	C <sub>18</sub> H <sub>18</sub> F <sub>6</sub> N <sub>4</sub> O <sub>8</sub> S <sub>2</sub> Zn
formula weight	926.37	754.60	661.85
crystal system	monoclinic	monoclinic	Monoclinic
space group	P2 <sub>1</sub> /c	C2/c	P2 <sub>1</sub> /c
a, Å	21.1854(9)	26.1032(11)	9.6948(4)
b, Å	13.1172(5)	7.9819(3)	22.6150(10)
c, Å	16.9684(7)	16.8627(7)	12.3263(5)
β, deg	111.3610(10)	107.6840(10)	110.3110(10)
V, Å <sup>3</sup>	4391.5(3)	3347.4(2)	2534.48(18)
Z	4	4	4
ρ <sub>calcd</sub> , g/cm <sup>3</sup>	1.401	1.497	1.735
μ, mm <sup>-1</sup>	0.673	1.473	1.229
θ range, deg	1.03 to 30.55	1.64 to 30.82	1.80 to 30.88
completeness to θ, %	97.3	95.3	94.7
reflections collected	93126	35190	53563
independent reflections	13094	5020	7569
R(int)	0.0299	0.0245	0.0251
restraints	0	0	78
parameters	538	213	355
Max., min. transmission	0.7461, 0.6735	0.7461, 0.6508	0.7461, 0.5733
R1(wR2) [I>2σ(I)]	0.0394 (0.1306)	0.0297 (0.1060)	0.0356 (0.1152)
R1(wR2)	0.0457 (0.1340)	0.0359 (0.1125)	0.0434 (0.1195)
GoF(F <sup>2</sup> )	1.913	1.734	1.884
max, min peaks, e.Å <sup>-3</sup>	1.310, -0.586	0.994, -0.251	1.157, -1.045

**Figure A.11.** Graphical representation of the X-ray crystal structure of **5** with ellipsoids shown at 50% probability. Hydrogen atoms are omitted for clarity. Color scheme: copper, magenta; chloride, green; nitrogen, blue; oxygen, red; carbon, colorless.

**Reactions of M(BIPhMe) complexes with RNOS.**  $[\text{Cu}(\text{BIPhMe})_2](\text{OTf})_2$  does not react with  $\text{NO}(\text{g})$  as measured by UV-vis spectroscopy, but upon addition of  $\text{NO}_2(\text{g})$  shows the formation of a shoulder at 350 nm and a minor decrease in intensity of the broad absorption bands at 610 nm and 746 nm (Figure A.12). This spectroscopic change does not result in a qualitative color change of the solution in methylene chloride.

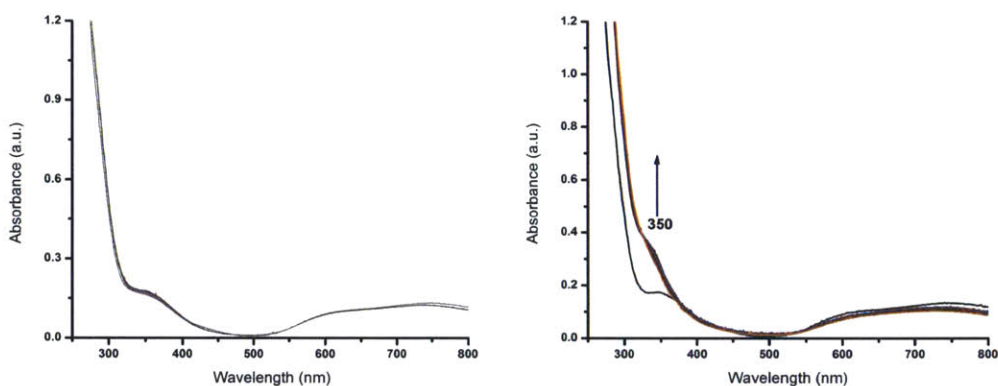


**Figure A.12.** The UV-Vis spectra of  $[\text{Cu}(\text{BIPhMe})_2](\text{OTf})_2$  and the reaction product with  $\text{NO}(\text{g})$  (left) and  $\text{NO}_2(\text{g})$  (right). In the reaction with  $\text{NO}(\text{g})$  no change is observed. In the reaction with  $\text{NO}_2(\text{g})$  only an increase in the band at 350 nm.

The reaction of **6** with  $(\text{PPN})(\text{SNO})$  was monitored by UV-Visible spectroscopy (Figure A.13). The band at 332 nm, associated with  $\text{SNO}^-$ , diminishes upon mixing with the solution of **6**. A new band at 440 nm forms along with an isosbetic point at 390 nm. We assign the formation of this band to the formation of  $\text{SSNO}^-$ . It has been previously reported that  $\text{SSNO}^-$  can be formed from  $\text{SNO}^-$  upon addition of elemental sulfur in solution.<sup>13</sup> The observance of  $\text{SSNO}^-$  formation suggests that **6** promotes the cleavage of the S–N bond to form elemental sulfur.

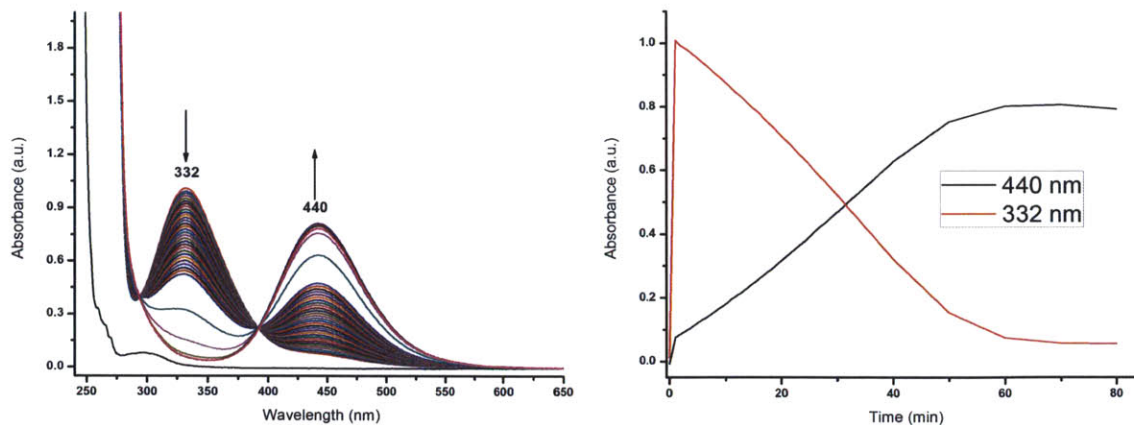


**Figure A.13.** The time-dependent UV-Visible spectroscopy in the reaction of **6** and (PPN)(SNO) in acetonitrile at 25° C.

Similar reactivity was observed during the reaction of **6** with (PPN)(SSNO), but only a decrease in the intensity of the band at 420 nm with the band shifting to 440nm (Figure A.14). This result suggests that **6** also promotes the cleavage of the S–N bond in SSNO<sup>-</sup>. The release of NO(g) from the reaction can be observed by using [Fe(BIPhMe)Cl<sub>2</sub>] as a colorimetric sensor (Figure A.16). The other reaction product is a zinc polysulfide.

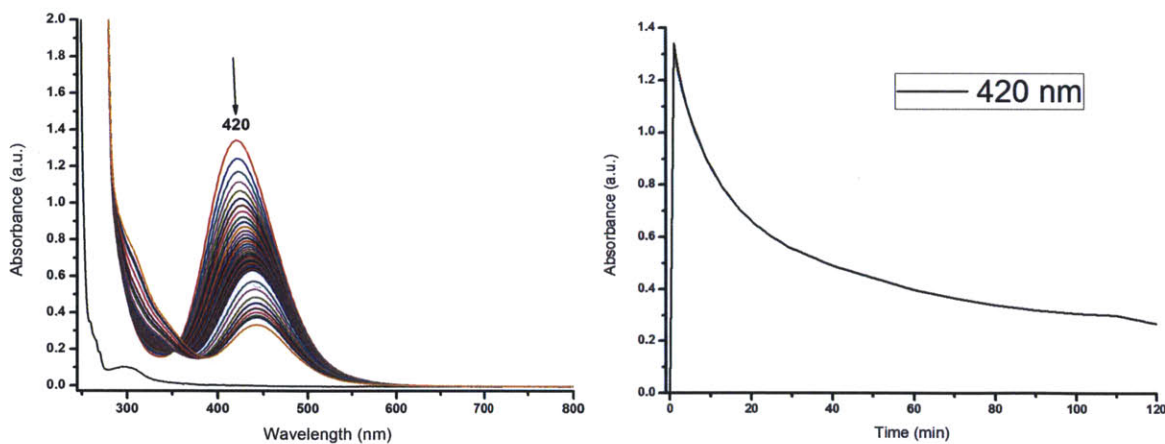


**Figure A.14.** The time-dependent UV-Visible spectroscopy in the reaction of **6** and (PPN)(SSNO) in acetonitrile at 25° C.



**Figure A.16.** Vial of **6** and  $\text{Fe}(\text{BIPhMe})\text{Cl}_2$  (left). After addition of  $(\text{PPN})(\text{SSNO})$  to the solution of **6**,  $\text{NO}(\text{g})$  is released and converts  $\text{Fe}(\text{BIPhMe})\text{Cl}_2$  to  $[\text{Fe}(\text{BIPhMe})_2(\text{NO})\text{Cl}][\text{Fe}(\text{NO})\text{Cl}_3]$  (middle) and  $\text{Zn}\{\text{S}\}$  (right).

#### A.4 Summary and Conclusions

We prepared additional metal-BIPhMe complexes using iron, copper, and zinc. These complexes were crystallographically characterized to have unique structures compared to the complexes reported in chapter 3. Initial reactivity studies of the complexes with different RNOS were performed, but further study would be needed to completely understand the chemistry observed.

## A.5 References

1. Lorkovic, I. M.; Ford, P. C., *Inorg Chem* **2000**, *39*, 632.
2. Pangborn, A. B.; Giardello, M. A.; Grubbs, R. H.; Rosen, R. K.; Timmers, F. J., *Organometallics* **1996**, *15*, 1518.
3. Kent, T. A. *WMOSS v. 2.5: Mössbauer Spectral Analysis Software*, WEB Research Co., WEB Research Co.: Minneapolis, MN, 1998.
4. APEX2 v2009 APEX2 v2009, Bruker AXS: Madison, WI, 2009.
5. Sheldrick, G. M. *SADABS: Area-Detector Absorption Correction*, University of Göttingen: Göttingen, Germany, 2008.
6. Sheldrick, G., *Acta Crystallographica Section A* **2008**, *64*, 112.
7. Sheldrick, G. M. *SHELXTL97: Program for Refinement of Crystal Structures*, University of Göttingen: Göttingen, Germany, 1997.
8. SHELXTL v. 6.10: *Program Library for Structure Solution and Molecular Graphics*, Bruker AXS, Madison, WI, 2001.
9. Dolomanov, O. V.; Bourhis, L. J.; Gildea, R. J.; Howard, J. A. K.; Puschmann, H., *J Appl Crystallogr* **2009**, *42*, 339.
10. Riedel, P. J.; Arulsamy, N.; Mehn, M. P., *Inorg. Chem. Commun.* **2011**, *14*, 734.
11. Martin, A.; Martinez-Espada, N.; Mena, M.; Yelamos, C., *Chem. Commun.* **2007**, 2983.
12. Taft, K. L.; Masschelein, A.; Liu, S.; Lippard, S. J.; Garfinkel-Shweky, D.; Bino, A., *Inorg. Chim. Acta* **1992**, *198–200*, 627.
13. Seel, F.; Kuhn, R.; Simon, G.; Wagner, M., *Zeitschrift fuer Naturforschung, Teil B: Anorganische Chemie, Organische Chemie* **1985**, *40b*, 1607

**APPENDIX B: MASS SPEC AND FTIR  
FIGURES OF THE REACTIONS NO(g) and  
Ph<sub>3</sub>CSNO WITH [Fe<sub>4</sub>S<sub>4</sub>(LS<sub>3</sub>)L']<sup>2-</sup>**

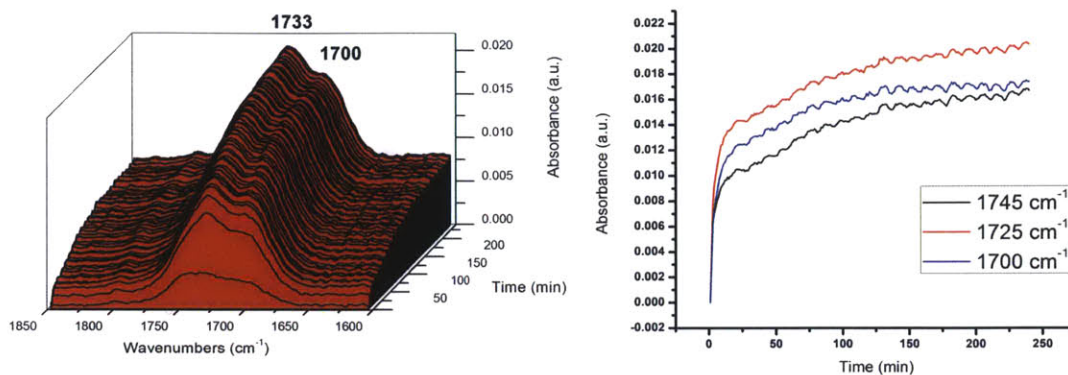


**Figure B.1.** Left: ReactIR spectra of  $(\text{Ph}_4\text{P})_2[\text{Fe}_4\text{S}_4(\text{LS}_3)(\text{SPh})]$  and one equivalent of  $\text{NO}(\text{g})$  in  $\text{CH}_2\text{Cl}_2$ . Right: The time-dependent absorbances at different wavenumbers were monitored to observe the concomitant formation of RBA and  $[\text{Fe}_4\text{S}_4(\text{NO})_4]^-$ .

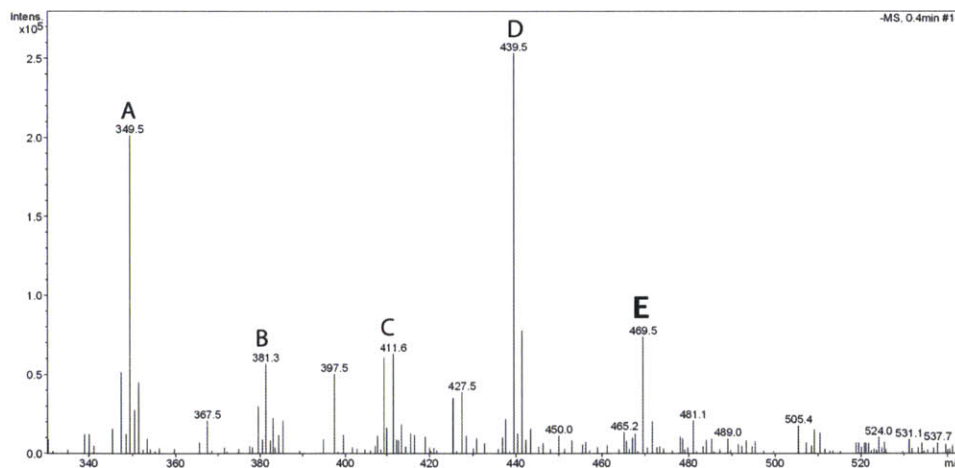


**Figure B.2.** Negative-mode ESI-MS spectrum (MeCN) of  $(\text{Ph}_4\text{P})_2[\text{Fe}_4\text{S}_4(\text{LS}_3)\text{Cl}]$  with one equivalent of  $\text{NO}(\text{g})$ . A)  $[\text{Fe}_4\text{S}_3(\text{NO})]^-$  (calculated: 349.6 m/z, observed: 349.5 m/z), B)  $[\text{Fe}_4\text{S}_4(\text{NO})]^-$  (calculated: 381.6 m/z, observed: 381.3 m/z), C)  $[\text{Fe}_4\text{S}_4(\text{NO})_2]^-$  (calculated: 411.6 m/z, observed: 411.6 m/z), D)  $[\text{Fe}_4\text{S}_3(\text{NO})_4]^-$  (calculated: 439.6 m/z, observed: 439.5 m/z), E)  $[\text{Fe}_4\text{S}_3(\text{NO})_5]^-$  (calculated: 469.6 m/z, observed: 469.5 m/z).



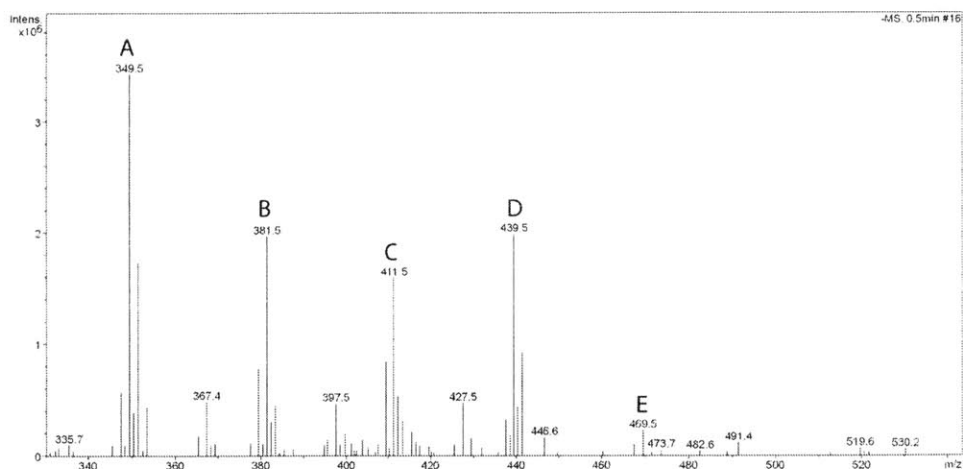


**Figure B.3.** Negative-mode ESI-MS spectrum (MeCN) of  $(\text{Ph}_4\text{P})_2[\text{Fe}_4\text{S}_4(\text{LS}_3)(\text{SEt})]$  with one equivalent of  $\text{NO}(\text{g})$ . A)  $[\text{Fe}_4\text{S}_3(\text{NO})]^-$  (calculated: 349.6 m/z, observed: 349.5 m/z), B)  $[\text{Fe}_4\text{S}_4(\text{NO})]^-$  (calculated: 381.6 m/z, observed: 381.5 m/z), C)  $[\text{Fe}_4\text{S}_4(\text{NO})_2]^-$  (calculated: 411.6 m/z, observed: 411.5 m/z), D)  $[\text{Fe}_4\text{S}_3(\text{NO})_4]^-$  (calculated: 439.6 m/z, observed: 439.5 m/z), E)  $[\text{Fe}_4\text{S}_3(\text{NO})_5]^-$  (calculated: 469.6 m/z, observed: 469.5 m/z).

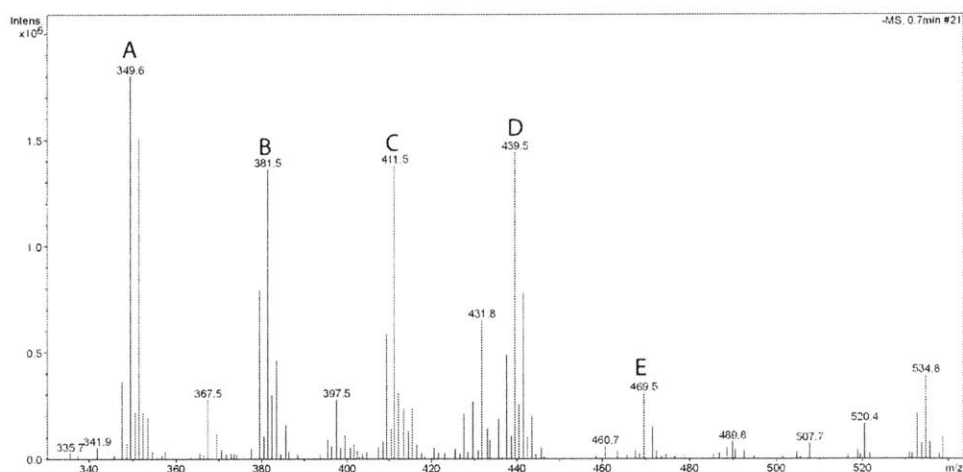


**Figure B.4.** Negative-mode ESI-MS spectrum (MeCN) of  $(\text{Ph}_4\text{P})_2[\text{Fe}_4\text{S}_4(\text{LS}_3)(\text{SPh})]$  with one equivalent of  $\text{NO}(\text{g})$ . A)  $[\text{Fe}_4\text{S}_3(\text{NO})]^-$  (calculated: 349.6 m/z, observed: 349.6 m/z), B)  $[\text{Fe}_4\text{S}_4(\text{NO})]^-$  (calculated: 381.6 m/z, observed: 381.5 m/z), C)  $[\text{Fe}_4\text{S}_4(\text{NO})_2]^-$  (calculated: 411.6 m/z, observed: 411.5 m/z), D)  $[\text{Fe}_4\text{S}_3(\text{NO})_4]^-$  (calculated: 439.6 m/z, observed: 439.5 m/z), E)  $[\text{Fe}_4\text{S}_3(\text{NO})_5]^-$  (calculated: 469.6 m/z, observed: 469.5 m/z).

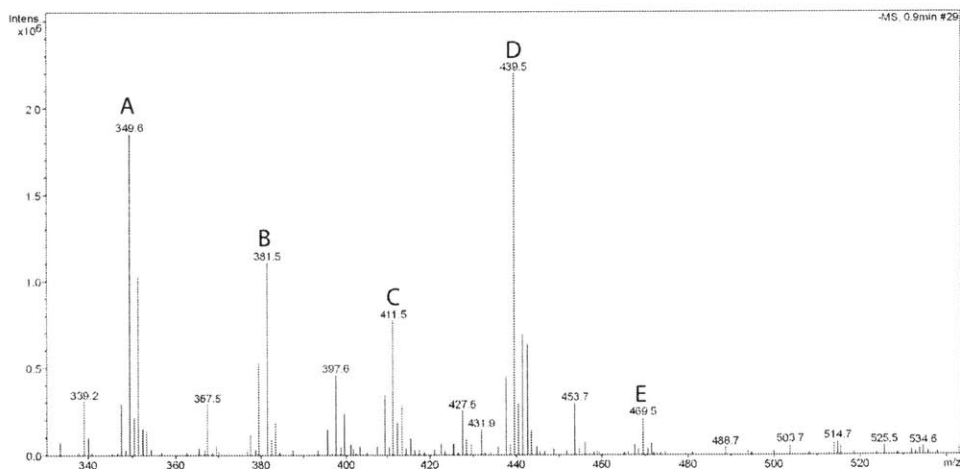


**Figure B.5.** Negative-mode ESI-MS spectrum (MeCN) of  $(\text{Ph}_4\text{P})_2[\text{Fe}_4\text{S}_4(\text{LS}_3)(\text{N}_3)]$  with one equivalent of  $\text{NO}(\text{g})$ . A)  $[\text{Fe}_4\text{S}_3(\text{NO})]^-$  (calculated: 349.6 m/z, observed: 349.6 m/z), B)  $[\text{Fe}_4\text{S}_4(\text{NO})]^-$  (calculated: 381.6 m/z, observed: 381.5 m/z), C)  $[\text{Fe}_4\text{S}_4(\text{NO})_2]^-$  (calculated: 411.6 m/z, observed: 411.5 m/z), D)  $[\text{Fe}_4\text{S}_3(\text{NO})_4]^-$  (calculated: 439.6 m/z, observed: 439.5 m/z), E)  $[\text{Fe}_4\text{S}_3(\text{NO})_5]^-$  (calculated: 469.6 m/z, observed: 469.5 m/z).

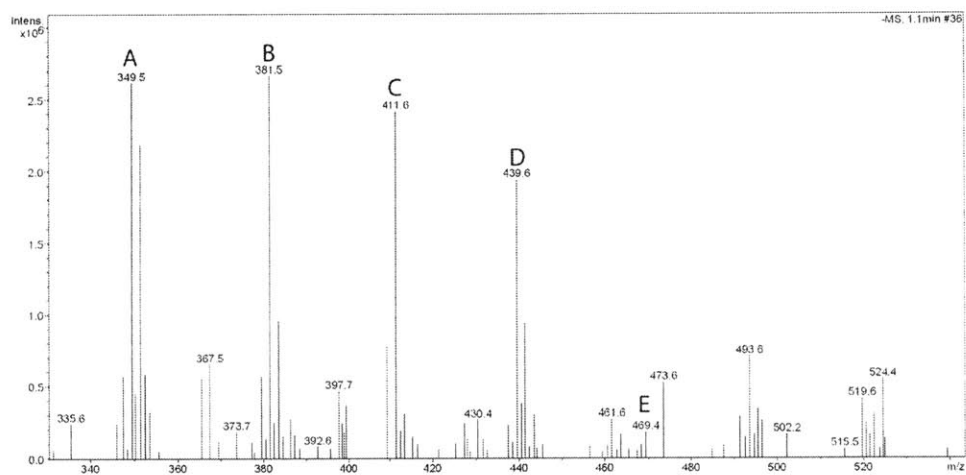


**Figure B.5.** Negative-mode ESI-MS spectrum (MeCN) of  $(\text{Ph}_4\text{P})_2[\text{Fe}_4\text{S}_4(\text{LS}_3)(\text{SPyr})]$  with one equivalent of  $\text{NO}(\text{g})$ . A)  $[\text{Fe}_4\text{S}_3(\text{NO})]^-$  (calculated: 349.6 m/z, observed: 349.5 m/z), B)  $[\text{Fe}_4\text{S}_4(\text{NO})]^-$  (calculated: 381.6 m/z, observed: 381.5 m/z), C)  $[\text{Fe}_4\text{S}_4(\text{NO})_2]^-$  (calculated: 411.6 m/z, observed: 411.6 m/z), D)  $[\text{Fe}_4\text{S}_3(\text{NO})_4]^-$  (calculated: 439.6 m/z, observed: 439.6 m/z), E)  $[\text{Fe}_4\text{S}_3(\text{NO})_5]^-$  (calculated: 469.6 m/z, observed: 469.4 m/z).

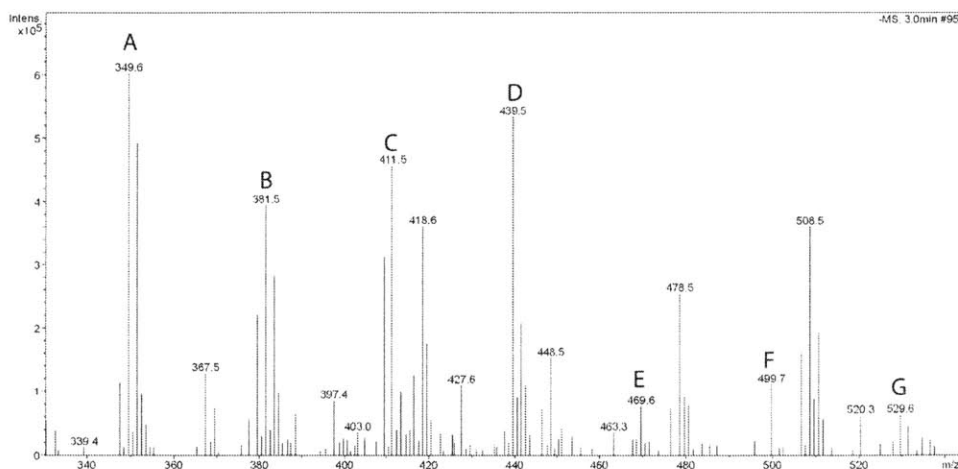


**Figure B.6.** Negative-mode ESI-MS spectrum (MeCN) of  $(\text{Ph}_4\text{P})_2[\text{Fe}_4\text{S}_4(\text{LS}_3)(\text{tpz})]$  with one equivalent of  $\text{NO}(\text{g})$ . A)  $[\text{Fe}_4\text{S}_3(\text{NO})]^-$  (calculated: 349.6 m/z, observed: 349.6 m/z), B)  $[\text{Fe}_4\text{S}_4(\text{NO})]^-$  (calculated: 381.6 m/z, observed: 381.5 m/z), C)  $[\text{Fe}_4\text{S}_4(\text{NO})_2]^-$  (calculated: 411.6 m/z, observed: 411.5 m/z), D)  $[\text{Fe}_4\text{S}_3(\text{NO})_4]^-$  (calculated: 439.6 m/z, observed: 439.5 m/z), E)  $[\text{Fe}_4\text{S}_3(\text{NO})_5]^-$  (calculated: 469.6 m/z, observed: 469.6 m/z), F)  $[\text{Fe}_4\text{S}_3(\text{NO})_6]^-$  (calculated: 499.6 m/z, observed: 499.7 m/z), G)  $[\text{Fe}_4\text{S}_3(\text{NO})_7]^-$  (calculated: 529.6 m/z, observed: 529.6 m/z).

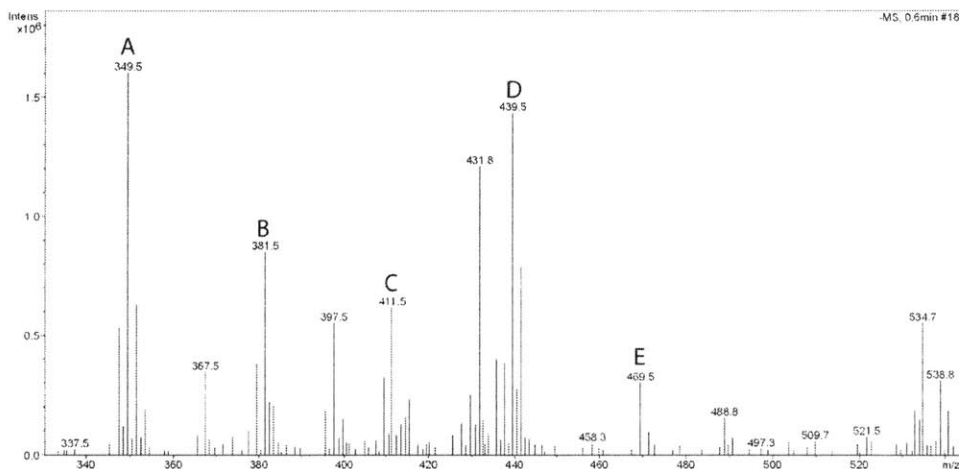


**Figure B.7.** Negative-mode ESI-MS spectrum (MeCN) of  $(\text{Ph}_4\text{P})_2[\text{Fe}_4\text{S}_4(\text{LS}_3)(\text{S}_2\text{CNET}_2)]$  with one equivalent of  $\text{NO}(\text{g})$ . A)  $[\text{Fe}_4\text{S}_3(\text{NO})]^-$  (calculated: 349.6 m/z, observed: 349.5 m/z), B)  $[\text{Fe}_4\text{S}_4(\text{NO})]^-$  (calculated: 381.6 m/z, observed: 381.5 m/z), C)  $[\text{Fe}_4\text{S}_4(\text{NO})_2]^-$  (calculated: 411.6 m/z, observed: 411.5 m/z), D)  $[\text{Fe}_4\text{S}_3(\text{NO})_4]^-$  (calculated: 439.6 m/z, observed: 439.5 m/z), E)  $[\text{Fe}_4\text{S}_3(\text{NO})_5]^-$  (calculated: 469.6 m/z, observed: 469.5 m/z).

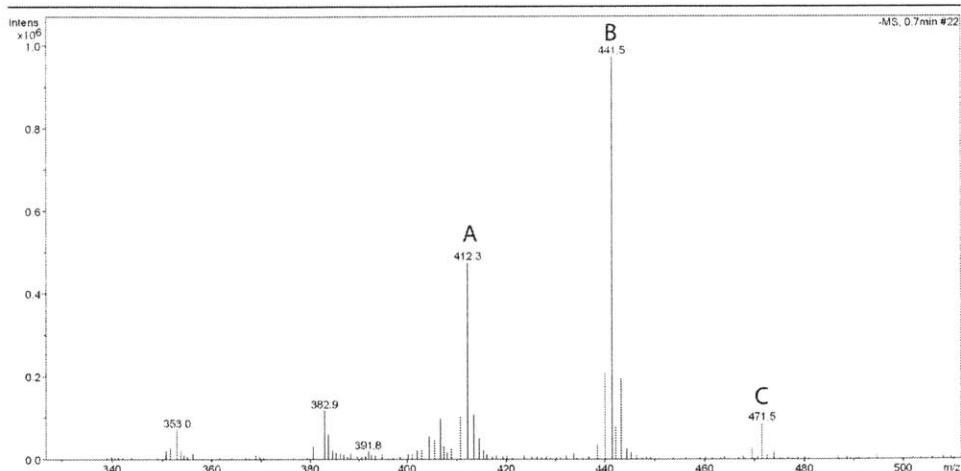


**Figure B.8.** Negative-mode ESI-MS spectrum (MeCN) of  $(\text{Ph}_4\text{P})_2[\text{Fe}_4\text{S}_4(\text{LS}_3)(\text{Cl})]$  with one equivalent of  $\text{Ph}_3\text{CSNO}$ . A)  $[\text{Fe}_4\text{S}_4(\text{NO})_2]^-$  (calculated: 411.6 m/z, observed: 412.3 m/z), B)  $[\text{Fe}_4\text{S}_4(\text{NO})_3]^-$  (calculated: 441.6 m/z, observed: 441.5 m/z), C)  $[\text{Fe}_4\text{S}_4(\text{NO})_4]^-$  (calculated: 471.6 m/z, observed: 471.5 m/z).

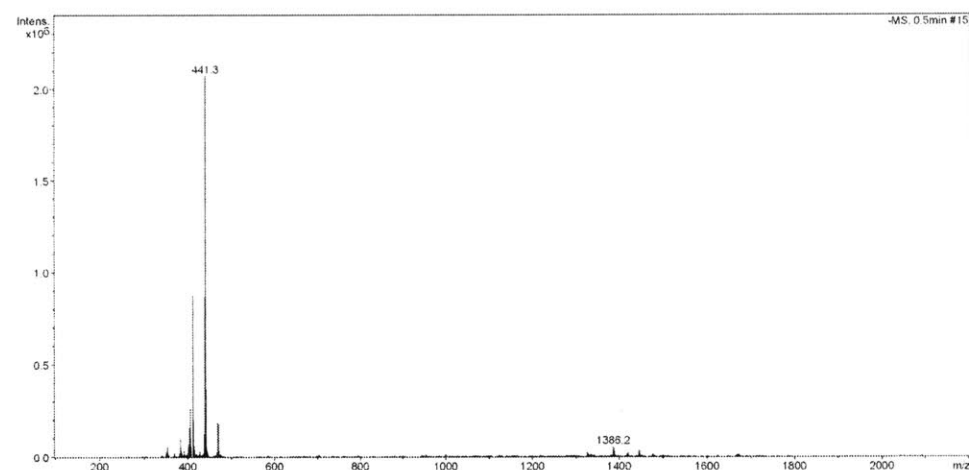


**Figure B.9.** Negative-mode ESI-MS spectrum (MeCN) of  $(\text{Ph}_4\text{P})_2[\text{Fe}_4\text{S}_4(\text{LS}_3)\text{Cl}]$  with four equivalents of  $\text{Ph}_3\text{CSNO}$ . The only product formed is  $[\text{Fe}_4\text{S}_4(\text{NO})_4]^-$  and all of  $(\text{Ph}_4\text{P})_2[\text{Fe}_4\text{S}_4(\text{LS}_3)\text{Cl}]$  is consumed.

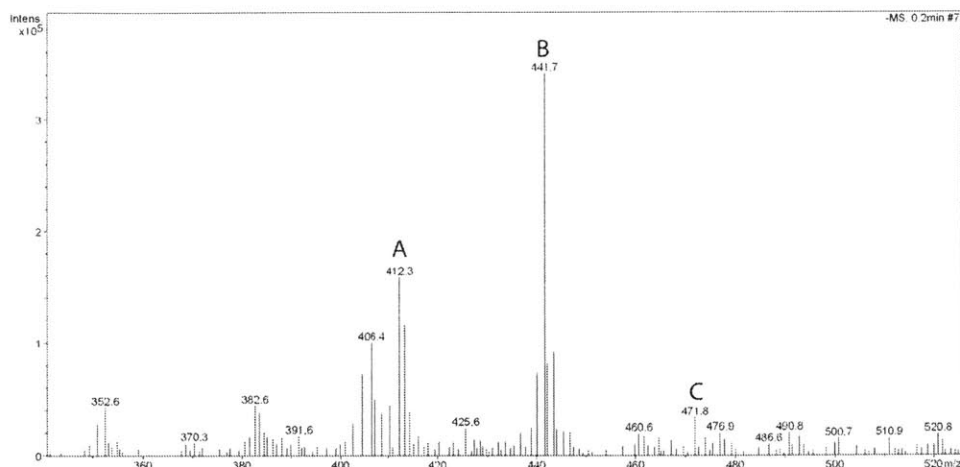


**Figure B.10.** Negative-mode ESI-MS spectrum (MeCN) of  $(\text{Ph}_4\text{P})_2[\text{Fe}_4\text{S}_4(\text{LS}_3)(\text{SPh})]$  with one equivalent of  $\text{Ph}_3\text{CSNO}$ . A)  $[\text{Fe}_4\text{S}_4(\text{NO})_2]^-$  (calculated: 411.6 m/z, observed: 412.3 m/z), B)  $[\text{Fe}_4\text{S}_4(\text{NO})_3]^-$  (calculated: 441.6 m/z, observed: 441.7 m/z), C)  $[\text{Fe}_4\text{S}_4(\text{NO})_4]^-$  (calculated: 471.6 m/z, observed: 471.8 m/z).

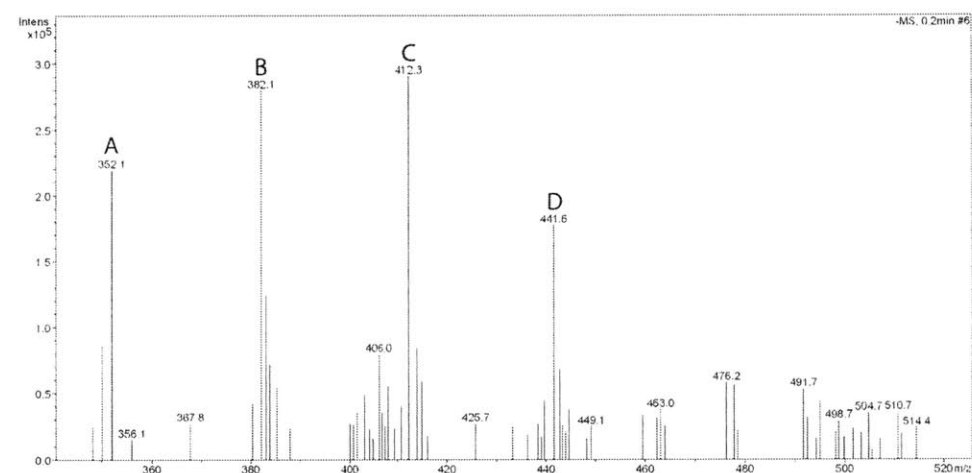


**Figure B.11.** Negative-mode ESI-MS spectrum (MeCN) of  $(\text{Ph}_4\text{P})_2[\text{Fe}_4\text{S}_4(\text{LS}_3)(\text{SPyr})]$  with one equivalent of  $\text{Ph}_3\text{CSNO}$ . A)  $[\text{Fe}_4\text{S}_4]^-$  (calculated: 351.6 m/z, observed: 352.1 m/z), B)  $[\text{Fe}_4\text{S}_4(\text{NO})]^-$  (calculated: 381.6 m/z, observed: 381.1 m/z), C)  $[\text{Fe}_4\text{S}_4(\text{NO})_2]^-$  (calculated: 411.6 m/z, observed: 412.3 m/z), D)  $[\text{Fe}_4\text{S}_4(\text{NO})_3]^-$  (calculated: 441.6 m/z, observed: 441.6 m/z).

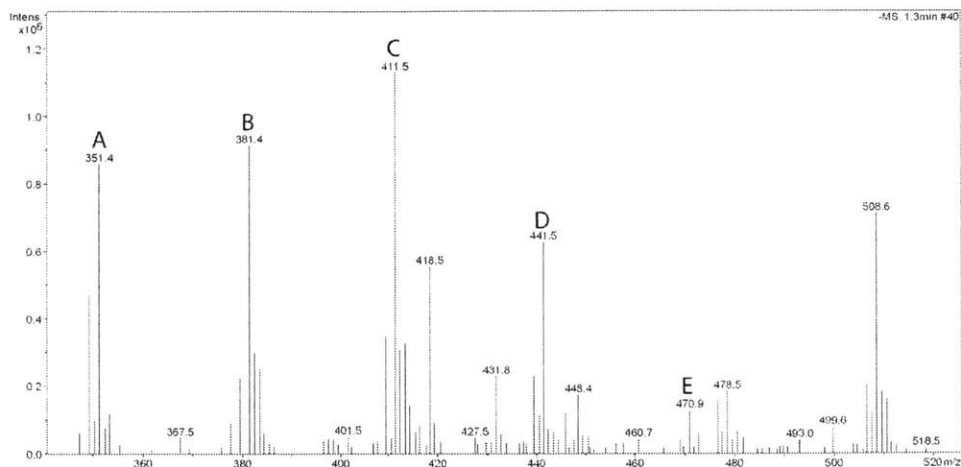


**Figure B.12.** Negative-mode ESI-MS spectrum (MeCN) of  $(\text{Ph}_4\text{P})_2[\text{Fe}_4\text{S}_4(\text{LS}_3)(\text{tpz})]$  with one equivalent of  $\text{Ph}_3\text{CSNO}$ . A)  $[\text{Fe}_4\text{S}_4]^-$  (calculated: 351.6 m/z, observed: 351.4 m/z), B)  $[\text{Fe}_4\text{S}_4(\text{NO})]^-$  (calculated: 381.6 m/z, observed: 381.4 m/z), C)  $[\text{Fe}_4\text{S}_4(\text{NO})_2]^-$  (observed: 411.6 m/z, observed: 411.5 m/z), D)  $[\text{Fe}_4\text{S}_4(\text{NO})_3]^-$  (calculated: 441.6 m/z, observed: 441.5 m/z), E)  $[\text{Fe}_4\text{S}_4(\text{NO})_4]^-$  (calculated: 471.6 m/z, observed: 470.9 m/z).

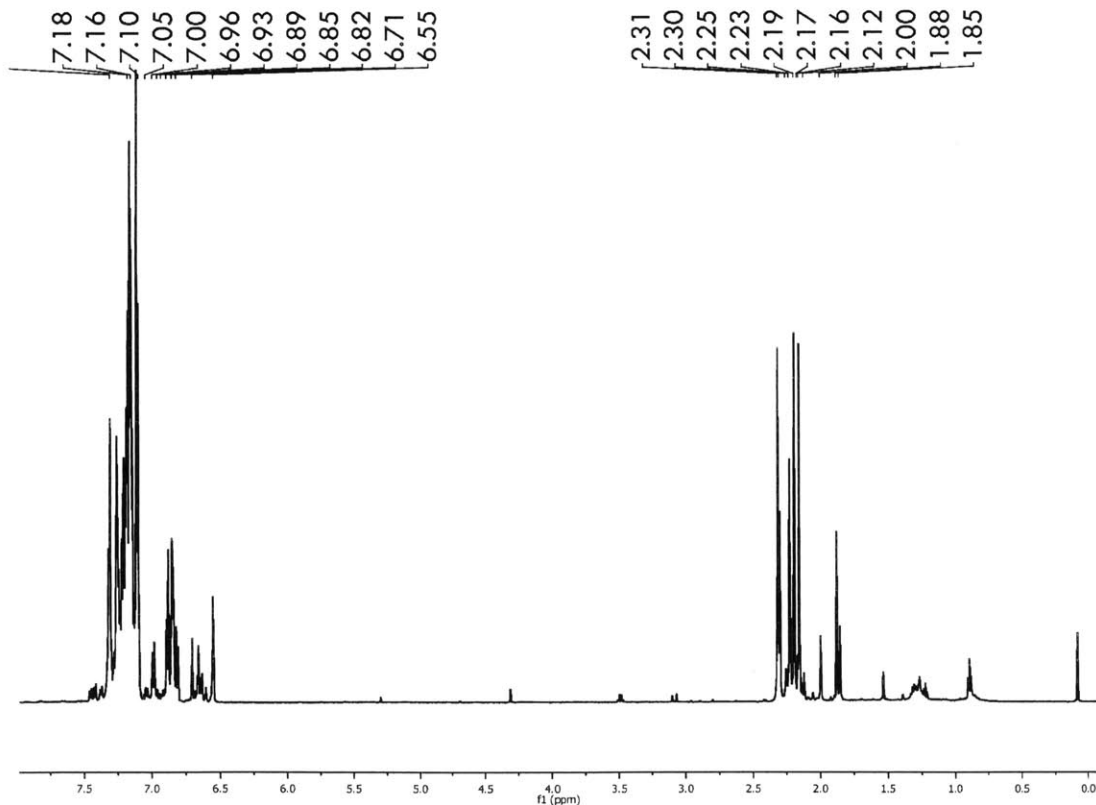


**Figure B.13.**  $^1\text{H}$  NMR spectrum of pentane extract of the reaction of  $(\text{Ph}_4\text{P})_2[\text{Fe}_4\text{S}_4(\text{LS}_3)\text{Cl}]$  with one equivalent of  $\text{Ph}_3\text{CSNO}$ . The spectrum shows multiple species that correspond to the  $\text{LS}_3$  ligand suggesting that ligand forms both intra- and intermolecular S-S bonds.

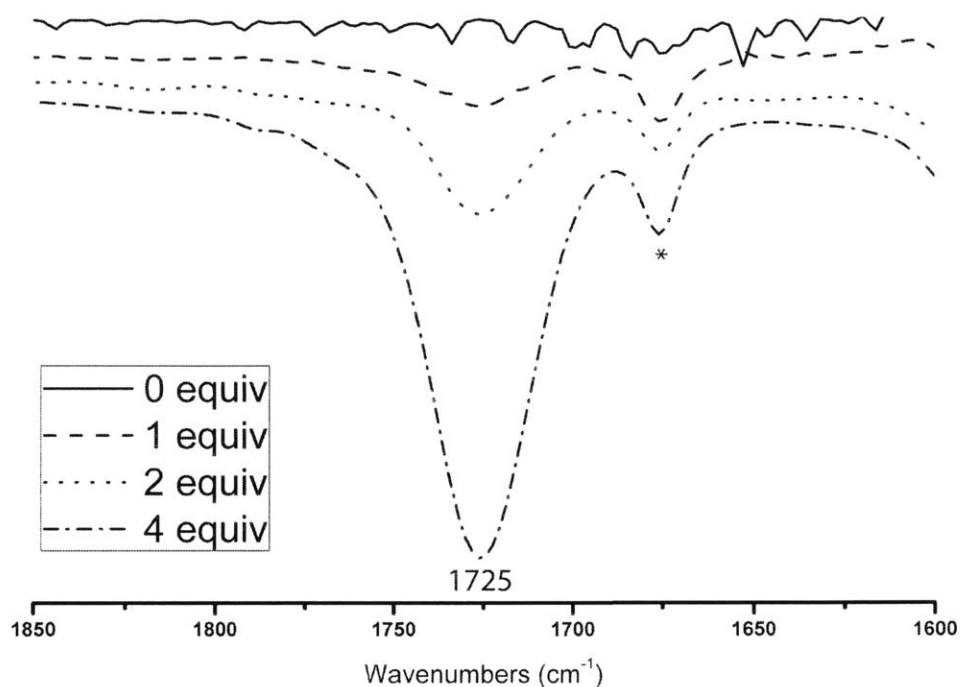


**Figure B.14.** FTIR spectroscopy (CH<sub>2</sub>Cl<sub>2</sub>) of (Ph<sub>4</sub>P)<sub>2</sub>[Fe<sub>4</sub>S<sub>4</sub>(LS<sub>3</sub>)Cl] with 1 – 4 equivalents of Ph<sub>3</sub>CSNO. The only product detected is [Fe<sub>4</sub>S<sub>4</sub>(NO)<sub>4</sub>]<sup>-</sup>. (\*) denotes a band associated with the LS<sub>3</sub> ligand.

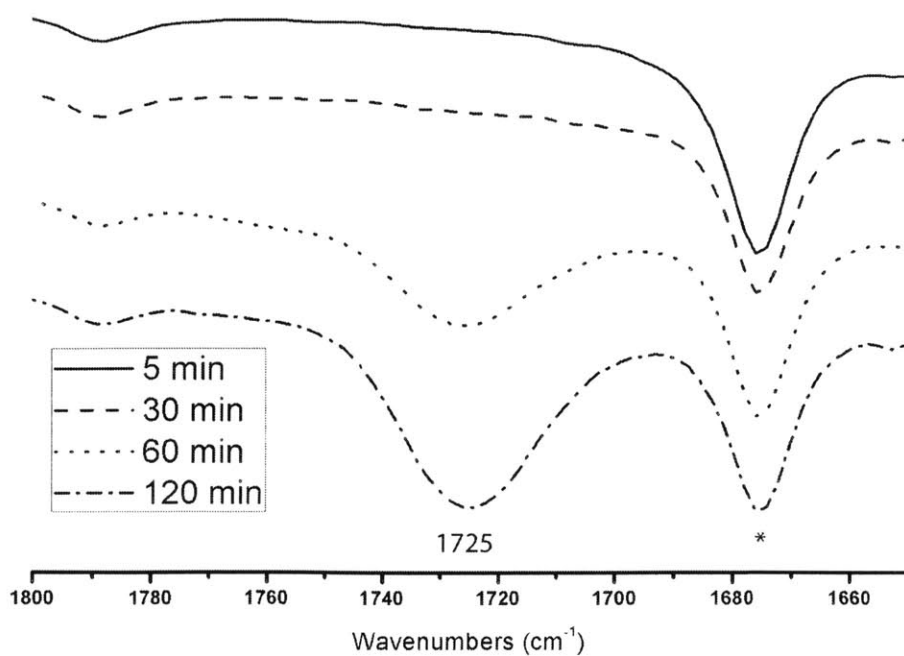


**Figure B.15.** TD-FTIR spectroscopy (CH<sub>2</sub>Cl<sub>2</sub>) of (Ph<sub>4</sub>P)<sub>2</sub>[Fe<sub>4</sub>S<sub>4</sub>(LS<sub>3</sub>)(SEt)] with one equivalent of Ph<sub>3</sub>CSNO. The only product detected is [Fe<sub>4</sub>S<sub>4</sub>(NO)<sub>4</sub>]<sup>-</sup>. (\*) denotes a band associated with the LS<sub>3</sub> ligand.

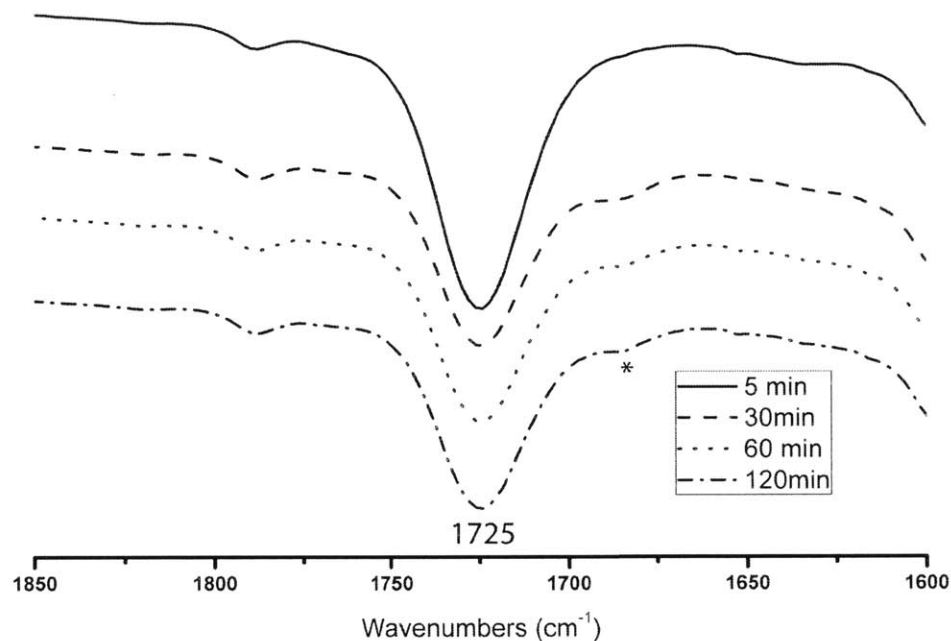


**Figure B.16.** TD-FTIR spectroscopy (CH<sub>2</sub>Cl<sub>2</sub>) of (Ph<sub>4</sub>P)<sub>2</sub>[Fe<sub>4</sub>S<sub>4</sub>(LS<sub>3</sub>)(SPh)] with one equivalent of Ph<sub>3</sub>CSNO. The only product detected is [Fe<sub>4</sub>S<sub>4</sub>(NO)<sub>4</sub>]<sup>-</sup>. (\*) denotes a band associated with the LS<sub>3</sub> ligand.

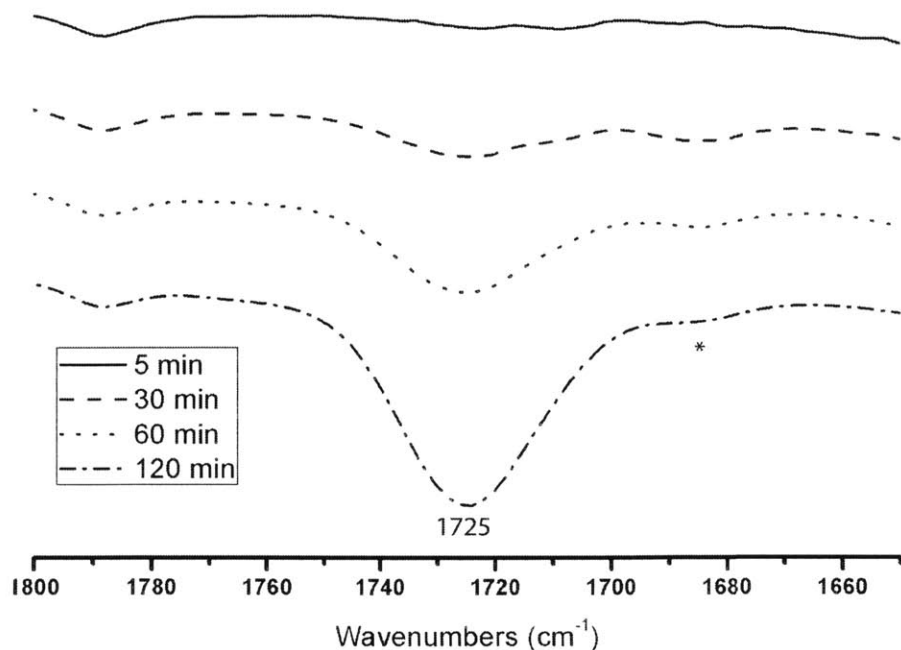


**Figure B.17.** TD-FTIR spectroscopy (CH<sub>2</sub>Cl<sub>2</sub>) of (Ph<sub>4</sub>P)<sub>2</sub>[Fe<sub>4</sub>S<sub>4</sub>(LS<sub>3</sub>)(N<sub>3</sub>)] with one equivalent of Ph<sub>3</sub>CSNO. The only product detected is [Fe<sub>4</sub>S<sub>4</sub>(NO)<sub>4</sub>]<sup>-</sup>. (\*) denotes a band associated with the LS<sub>3</sub> ligand.



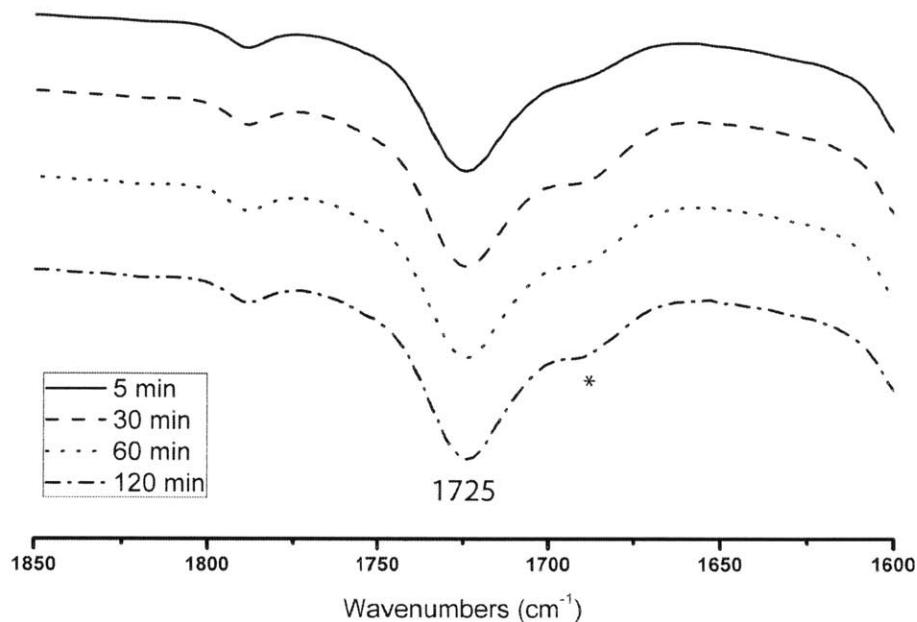


**Figure B.18.** TD-FTIR spectroscopy ( $\text{CH}_2\text{Cl}_2$ ) of  $(\text{Ph}_4\text{P})_2[\text{Fe}_4\text{S}_4(\text{LS}_3)(\text{SPyr})]$  with one equivalent of  $\text{Ph}_3\text{CSNO}$ . The only product detected is  $[\text{Fe}_4\text{S}_4(\text{NO})_4]^-$ . (\*) denotes a band associated with the  $\text{LS}_3$  ligand.

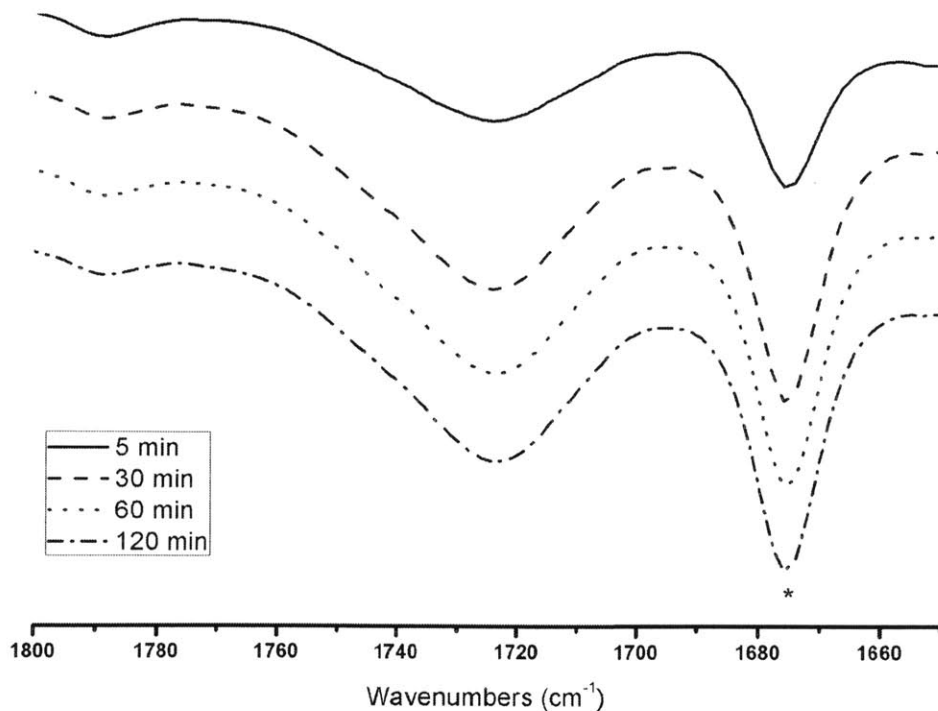


**Figure B.19.** FTIR spectroscopy ( $\text{CH}_2\text{Cl}_2$ ) of  $(\text{Ph}_4\text{P})_2[\text{Fe}_4\text{S}_4(\text{LS}_3)(\text{tpz})]$  with one equivalent of  $\text{Ph}_3\text{CSNO}$ . The only product detected is  $[\text{Fe}_4\text{S}_4(\text{NO})_4]^-$ . (\*) denotes a band associated with the  $\text{LS}_3$  ligand.

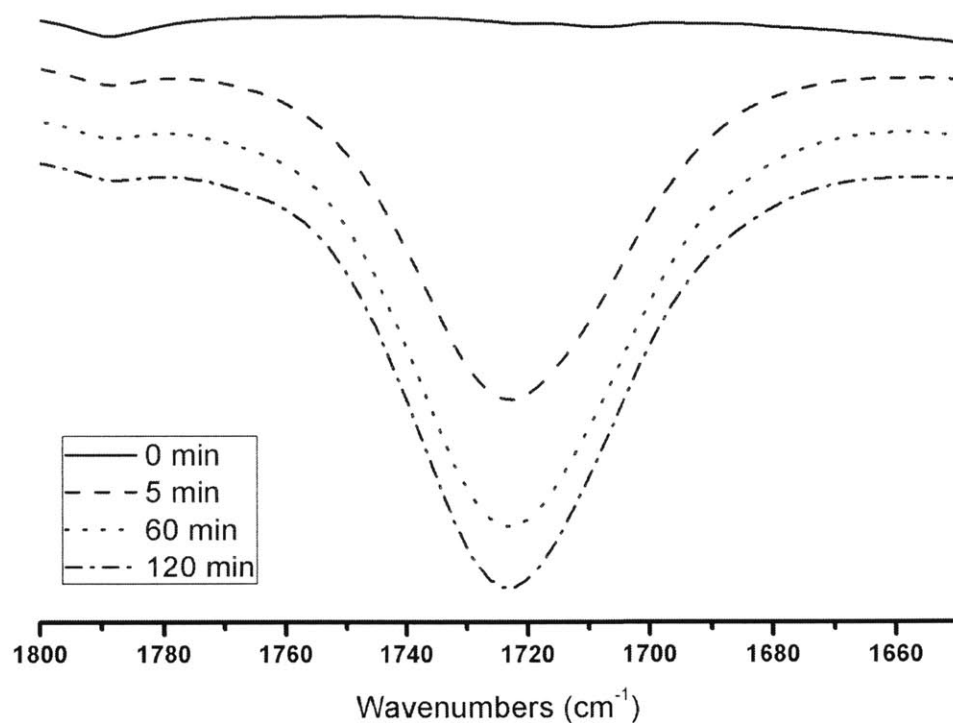


**Figure B.20.** FTIR spectroscopy ( $\text{CH}_2\text{Cl}_2$ ) of  $(\text{Ph}_4\text{P})_2[\text{Fe}_4\text{S}_4(\text{LS}_3)(\text{S}_2\text{CNET}_2)]$  with one equivalent of  $\text{Ph}_3\text{CSNO}$ . The only product detected is  $[\text{Fe}_4\text{S}_4(\text{NO})_4]^-$ . (\*) denotes a band associated with the  $\text{LS}_3$  ligand.

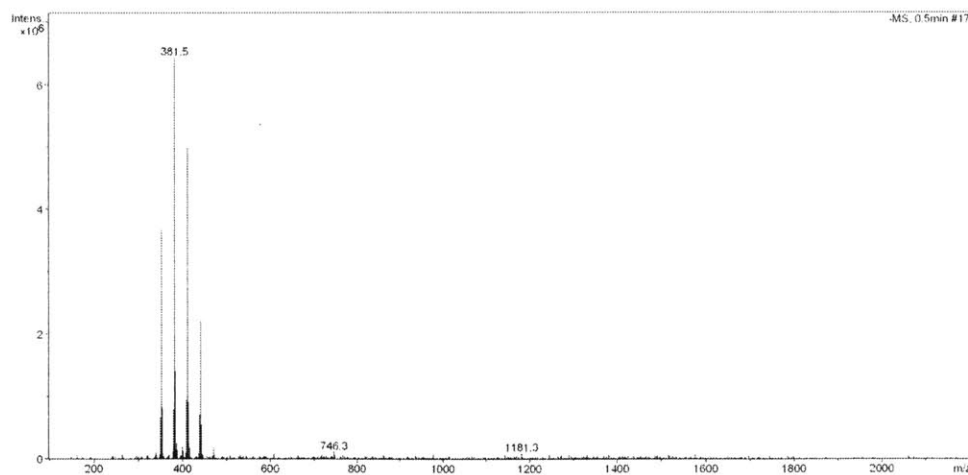


**Figure B.21.** Negative-mode ESI-MS spectrum ( $\text{MeCN}$ ) of  $[\text{Cp}^*_2\text{Fe}][\text{Fe}_4\text{S}_4(\text{NO})_4]$ .

## Biographical Note

The author was born on September 23, 1983 in El Paso, Texas to William Carney and Astrid Victor. Shortly thereafter he moved to Germany where he grew up in Worms and Karlsruhe. Eric graduated from Heidelberg American High School in 2002 and joined the US Army as a 54B – Chemical Operations Specialist. Eric deployed in support of Operation Iraqi Freedom in 2003 and 2005, being present for both the invasion and the first post-war government elections. Eric was honorably discharged from the Army in 2006 with the rank of Sergeant. He pursued undergraduate studies at the University of Wisconsin – Madison. At Madison the author worked in the lab of Professor John F. Berry on quadruply-bonded group six transition metals and their use as axial ligands for first row transition metals, in the lab of Professor Philipp W. Simon on genetic variations of the gene CHXE in *Daucus carota* (carrots), and on combining performance art with lecture demonstrations for Professor Bassam Shakhashiri. The author graduated from Madison with a B.Sc. with honors in Chemistry in 2009, and pursued graduate studies at MIT in the laboratory of Professor Stephen J. Lippard, where he studied the reactivity of nitric oxide and *S*-nitrosothiols towards bio-inspired iron, cobalt, zinc, and platinum complexes. After completing his graduate studies, the author will attend the World Cup tournament in Brazil and pursue a career in management or policy consulting.

## Curriculum Vitae

### Education

Massachusetts Institute of Technology, Cambridge, MA September 2014

Ph.D. Inorganic Chemistry

Thesis Topic: Reactions of *S*-nitrosothiols with biomimetic iron complexes and other transition metals

Thesis Advisor: Professor Stephen J. Lippard

University of Wisconsin – Madison, Madison, WI May 2009

B.Sc. Chemistry w/ Honors

### Publications

Victor, E.; Lippard, S. J. A tetranitrosyl [4Fe-4S] cluster forms en route to Roussin's Black Anion: Nitric Oxide reactivity of  $[\text{Fe}_4\text{S}_4(\text{LS}_3)\text{L}']^{2-}$  *Inorg. Chem.*, doi:10.1021/ic500586g.

Nippe, M.; Victor, E.; Berry, J. F. Oxidation Chemistry of Axially Protected Mo<sub>2</sub> and W<sub>2</sub> Quadruply Bonded Compounds *Inorg. Chem.*, **2009**, *48*, 11889-11895.

Nippe, M.; Victor, E.; Berry, J. F. Do Metal-Metal Multiply-Bonded Ligands Have a *trans* Influence? Structural and Magnetic Comparisons of Heterometallic CrCr···Co and MoMo···Co Interactions *Eur. J. Inorg. Chem.*, **2008**, *36*, 5569-5572.

### Presentations

Victor, E.; Lippard, S. J. Nitric Oxide reactivity of the site-differentiated cluster  $[\text{Fe}_4\text{S}_4(\text{LS}_3)\text{L}']^{2-}$ . 247<sup>th</sup> Meeting of the American Chemical Society, Dallas, TX; INOR-43.

Victor, E. NO reactivity of different irons: Site-differentiated multi-iron complexes and reactive nitrogen oxide species. MIT Department of Chemistry Inorganic Seminar Series; Cambridge, MA; March 6, 2013.

Victor, E. NO chemistry of site-differentiated multi-iron complexes. MIT Chemistry Student Seminar Series; Cambridge, MA; March 9, 2012.

Victor, E. Work towards biomimetic chemistry between site-differentiated iron-sulfur clusters and nitric oxide. MIT Chemistry Metals in Synthesis Seminar Series; Cambridge, MA; February 11, 2011.

Victor, E.; Schreiner, R.; Shakhashiri, B. Z. NO: Presenting real-world scientific research and problems in an artistic way. 240<sup>th</sup> Meeting of the American Chemical Society; Boston, MA; CHED-77.

Victor, E.; Simon, P. W. Sequencing and Subcloning of the CHXE gene in a Carrot (*Daucus Carota*) BAC. University of Wisconsin – Madison Undergraduate Symposium 2008; Madison,

WI; April 16, 2008.

**Awards**

MIT Department of Chemistry Awards for Outstanding Teaching by a Graduate Student (August 2010)

National Chemical and Starch Foundation Scholar (2008, 2009)

Edwin M. and Kathryn M. Larsen Scholar (2008)

Dean's List (December 2006)